

ENGINEERING GEOLOGICAL CHARACTERIZATION OF THE ROCK
MASSES AND THEIR EVALUATION BY SPATIAL ANALYSES,
DETERMINATION OF THE ROCK SLOPE FAILURE SUSCEPTIBILITY
ZONES AND HAZARD ASSESSMENT OF MUDURNU (BOLU)

A THESIS SUBMITTED TO
THE GRADUATE SCHOOL OF NATURAL AND APPLIED SCIENCES
OF
MIDDLE EAST TECHNICAL UNIVERSITY

BY

ARZU ARSLAN KELAM

IN PARTIAL FULFILLMENT OF THE REQUIREMENTS
FOR
THE DEGREE OF DOCTOR OF PHILOSOPHY
IN
GEOLOGICAL ENGINEERING

JULY 2022

Approval of the thesis:

ENGINEERING GEOLOGICAL CHARACTERIZATION OF THE ROCK
MASSES AND THEIR EVALUATION BY SPATIAL ANALYSES,
DETERMINATION OF THE ROCK SLOPE FAILURE SUSCEPTIBILITY
ZONES AND HAZARD ASSESSMENT OF MUDURNU (BOLU)

submitted by **ARZU ARSLAN KELAM** in partial fulfillment of the requirements
for the degree of **Doctor of Philosophy in Geological Engineering, Middle East
Technical University** by,

Prof. Dr. Halil Kalıpçılar
Dean, Graduate School of **Natural and Applied Sciences** _____

Prof. Dr. Erdin Bozkurt
Head of the Department, **Geological Engineering** _____

Prof. Dr. Haluk Akgün
Supervisor, **Geological Engineering, METU** _____

Prof. Dr. Antonio Bobet
Co-Supervisor, **Lyles School of Civil Eng., Purdue University** _____

Examining Committee Members:

Prof. Dr. Candan Gökçeoğlu
Geological Engineering, Hacettepe University _____

Prof. Dr. Haluk Akgün
Geological Engineering, METU _____

Prof. Dr. Tamer Topal
Geological Engineering, METU _____

Assoc. Prof. Dr. Kaan Sayıt
Geological Engineering, METU _____

Assoc. Prof. Dr. Mustafa Kerem Koçkar
Civil Engineering, Hacettepe University _____

Date: 20.07.2022

I hereby declare that all information in this document has been obtained and presented in accordance with academic rules and ethical conduct. I also declare that, as required by these rules and conduct, I have fully cited and referenced all material and results that are not original to this work.

Name Last name : Arzu Arslan Kelam

Signature :

ABSTRACT

ENGINEERING GEOLOGICAL CHARACTERIZATION OF THE ROCK MASSES AND THEIR EVALUATION BY SPATIAL ANALYSES, DETERMINATION OF THE ROCK SLOPE FAILURE SUSCEPTIBILITY ZONES AND HAZARD ASSESSMENT OF MUDURNU (BOLU)

Arslan Kelam, Arzu
Doctor of Philosophy, Geological Engineering
Supervisor : Prof. Dr. Haluk Akgün
Co-Supervisor: Prof. Dr. Antonio Bobet

July 2022, 215 pages

Mudurnu County, which is settled in a valley, is affected by regional rock slope instabilities especially due to precipitation, temperature changes, wind and earthquake activity. While units located on the eastern side of the valley are susceptible to rock falls, units at the western side are susceptible to planar, wedge or toppling failures. The presence of different rock mass properties makes Mudurnu an attractive and distinctive site for the investigation of rock mass failure. The rock slope failures tend to create an important hazard in and around the settlement area and generate regional risk due to exposure of the elements at risk (i.e., human life, houses, buildings and small industrial facilities) in Mudurnu. Moreover, instabilities create a risk to the historically valuable structures by which Mudurnu has been nominated as a candidate for the UNESCO World Heritage List. The purpose of this dissertation is to characterize the rock masses that have the potential to create a hazard in the Mudurnu county center through geomechanical evaluation of the slope instability problems under static and dynamic loading conditions and to identify the hazard zones in the Mudurnu Valley with a focus on the western side of the valley.

To that end, the engineering geological and geomechanical properties of the region were assessed through a 3D point cloud generated by an unmanned aerial vehicle (UAV) along with scan-line survey field studies of the physically accessible locations. Then, the data were evaluated statistically to define the discontinuous rock mass characteristics. Accordingly, the western side of the Mudurnu Valley was delineated into 11 geomechanical sectors. The stability analysis demonstrated that the rock mass is prone to planar, wedge, and toppling failures in the area. Moreover, the discontinuity sets can create complex kinematic failures that cause the study area to be a unique case study since it is difficult to separately identify the order or frequency of events originating from the different failure modes forming the complex failure. The hazard potential of the different modes of failures was assessed and hazard zonation maps were generated by considering the conditioning parameters (i.e., lithology, degree of weathering, block size, slope angle, aspect, surface water) along with travel distance and temporal frequency. In addition, the seismic loading was taken into account as a triggering factor. The combined hazard map composed of the planar, wedge and toppling failure potentials concluded that Sectors 6 and 8 were most critical in terms of high hazards. Under dynamic loading conditions, the most critical high-hazard sectors were determined as Sectors 2, 4, 6, 8, and 10.

Keywords: Rock Mass Characterization, Spatial Analysis, Rock Slope Failure Susceptibility, Hazard Assessment, Mudurnu

ÖZ

MUDURNU (BOLU) KAYA KÜTLELERİNİN MÜHENDİSLİK JEOLJİSİ AÇISINDAN KAREKTERİZASYONU, MEKANSAL ANALİZLERLE DEĞERLENDİRİLMESİ, KAYA ŞEVLERİN YENİLME YATKINLIK ZONLARININ BELİRLENMESİ VE TEHLİKE DEĞERLENDİRMESİ

Arslan Kelam, Arzu
Doktora, Jeoloji Mühendisliği
Tez Yöneticisi: Prof. Dr. Haluk Akgün
Ortak Tez Yöneticisi: Prof. Dr. Antonio Bobet

Temmuz 2022, 215 sayfa

Bir vadi içinde kurulmuş olan Mudurnu ilçesi; yağış, sıcaklık farklılıkları, rüzgar etkisi ve en önemlisi deprem sebebiyle bölgesel kaya şevi duraysızlıklarından etkilenmektedir. İlçenin doğu yakasındaki birimler kaya düşmesine sebep olurken, batı yakasındaki birimler düzlemsel, kamalanma ya da devrilme şeklinde kaymalar meydana getirmektedir. Farklı kaya kütlesi özelliklerinin varlığı, Mudurnu'yu kaya kütlesi yenilme çalışmaları için çekici ve ayırt edici bir alan haline getirmektedir. Mudurnu'daki kaya şevi yenilmeleri, yerleşim yeri ve etrafında insan hayatı, evler, binalar ve küçük sanayi tesisleri için önemli bir tehlike ve risk oluşturmaktadır. Buna ilave olarak, duraysızlıklar Mudurnu'nun UNESCO Dünya Mirası listesine aday olmasını sağlayan değerli tarihi yapılar için de risk oluşturmaktadır. Bu tez çalışmasının amacı, Mudurnu ilçe merkezinin batı yakasındaki tehlike oluşturma potansiyeline sahip kaya kütlelerinin şev duraysızlığı problemlerinin statik ve dinamik yük koşulları altında jeomekanik açıdan değerlendirilmesi yoluyla karakterize edilmesi ve Mudurnu Vadisi'ndeki tehlike zonlarının belirlenmesidir. Bu amaçla, bölgenin mühendislik jeolojisi ve jeomekanik özellikleri, bir insansız hava

aracı (İHA) kullanılarak oluşturulan 3 boyutlu nokta bulutu ve fiziksel olarak erişilebilir konumların hat etüdü çalışmaları ile değerlendirilmiştir. Ardından bu veriler, süreksiz kaya kütlesi özelliklerini tanımlamak amacıyla istatistiksel olarak değerlendirilmiştir. Buna göre, Mudurnu Vadisi'nin batı yakası 11 jeomekanik sektöre ayrılmıştır. Duraylılık analizleri, kaya kütlesinin bölgede düzlemsel, kama ve devrilme tipi yenilmelere yatkın olduğunu göstermiştir. Ayrıca, süreksizlik setleri, kompleks yenilmeyi oluşturan farklı yenilme modlarından kaynaklanan olayların sırasının veya sıklığının ayrı ayrı belirlenmesi meşakkatli olduğundan, çalışma alanının benzersiz bir vaka çalışması olmasına neden olan kompleks kinematik yenilmeler oluşturmaktadır. Farklı yenilme modlarının tehlike potansiyeli değerlendirilmiş ve belirlenen parametreler (litoloji, ayrışma derecesi, blok boyutu, eğim açısı, bakı, yüzey suyu) ile birlikte blokların ulaşabileceği mesafe ve zamansal frekans dikkate alınarak tehlike bölgeleme haritaları üretilmiştir. Buna ek olarak, sismik yük tetikleyici bir faktör olarak dikkate alınmıştır. Düzlemsel, kama ve devrilme tipi yenilme potansiyellerinden oluşan birleşik tehlike haritası, Sektör 6 ve 8'in yüksek tehlike açısından en kritik sektörler olduğunu göstermiştir. Dinamik yük koşulları altında en kritik yüksek tehlike sektörleri Sektör 2, 4, 6, 8 ve 10 olarak belirlenmiştir.

Anahtar Kelimeler: Kaya Kütlesi Karakterizasyonu, Mekânsal Analiz, Kaya Şevlerin Yenilme Yatkınlığı, Tehlike Değerlendirmesi, Mudurnu

To Abdullah

ACKNOWLEDGMENTS

I would like to express my gratitude to Prof. Haluk Akgün, my advisor, for his valuable mentoring and support. He has always inspired, encouraged, and guided me to improve myself. I am thankful to Prof. Antoni Bobet, my co-advisor, for his unwavering support, guidance, and the resources and opportunities he had shared. His guidance and advice have broadened my horizon. I would like to present my appreciation to Assoc. Prof. Mustafa Kerem Koçkar who was always there for me. I have always felt his precious support both on research-related issues and in my personal life. I am thankful to my thesis committee members Prof. Candan Gökçeoğlu, Prof. Tamer Topal, and Assoc. Prof. Kaan Sayıt for their invaluable comments, suggestions, and contributions.

I am thankful to my fellows at METU, in particular Dr. Kerim Yusufi, Selim Cambazoğlu, Dr. Kıvanç Okalp, Serdar Görkem Atasoy, Dr. Çidem Argunhan-Atalay and Kadir Yertutanol for their valuable friendship and support. I would like to thank Dr. Hala El-Fil, Amy Getchell, Dr. Osvaldo Vitali, SungSoo Park, Kanika Gupta, and Yu-Chung Lin for being friendly and supportive during my research studies at Lyles School of Civil Engineering at Purdue University. I am thankful to my dear friends Burcu Hızlı, Dr. Pınar Bulut, Elif Sarıgül Duman, and Hülya Salihoğlu who have never refrained their support, friendship, and patience for years.

I would like to express my thankfulness to my beloved family. Last but certainly not least, I would like to thank and express my appreciation to my partner, Mehmet Abdullah Kelam, for his endless support, encouragement, and patience.

This Ph.D. study was financially supported by the Scientific Research Projects Coordination Unit of METU (BAP-03-09-2017-005) and the Scientific and Technological Research Council of Turkey (TUBITAK)'s scholarship program entitled 'International Research Fellowship Program for Ph.D. Students'.

TABLE OF CONTENTS

ABSTRACT.....	v
ÖZ.....	vii
ACKNOWLEDGMENTS	xi
TABLE OF CONTENTS.....	xiii
LIST OF TABLES	xv
LIST OF FIGURES	xviii
CHAPTERS	
1 INTRODUCTION	1
1.1 Motivation and purpose of the study	1
1.2 The study area	9
1.2.1 Physiography and climate of the study area.....	11
2 GEOLOGICAL ASSESSMENT OF THE STUDY AREA	15
2.1 Regional geology of the study area.....	15
2.2 Seismotectonics of the study area	20
2.3 Local geology of the study area	23
3 SITE CHARACTERIZATION METHODOLOGY.....	25
3.1 Engineering geological assessment of the rock mass	25
3.2 Utilization of an Unmanned Aerial Vehicle (UAV).....	43
3.2.1 Discontinuity data identification from the 3D point cloud.....	48
3.3 Definition and delineation of the geomechanical sectors	55
3.4 Empirical classification of the rock slopes	73
4 STABILITY ASSESSMENT	83

4.1	Methods of rock slope stability assessment	83
4.2	Kinematic analysis.....	86
4.3	Back analysis	91
4.4	Limit equilibrium analysis.....	101
4.4.1	Pseudo-static analysis	112
4.5	Evaluation of the results of the rock slope stability assessment analysis...	121
5	HAZARD ASSESSMENT OF THE DISCONTINUOUS ROCK SLOPE INSTABILITY	125
6	CONCLUSIONS AND RECOMMENDATIONS FOR FUTURE RESEARCH	
	159	
	REFERENCES	167
	APPENDICES	
A.	Thin sections.....	181
B.	Field survey measurements	183
C.	Laboratory test sheets	189
D.	Rock mass classification system tables	195
E.	Back-calculated shear strength parameters	199
F.	Report obtained from the application of the Seismic Hazard Map of Turkey.....	203
G.	Hazard assessment flow chart	209
	CURRICULUM VITAE	211

LIST OF TABLES

TABLES

Table 1: Average, maximum, and minimum important meteorological parameters of Mudurnu for 1964-1997 (Turkish State Meteorological Service, 2021)	13
Table 2: Histograms of the bedding plane (BP) roughness and spacing distributions	30
Table 3: Histograms of the bedding plane (BP) aperture and infilling distributions	31
Table 4: Histograms of the Joint set 1 (J1) roughness and spacing distributions ...	32
Table 5: Histograms of the Joint set 1 (J1) aperture and infilling distributions	33
Table 6: Histograms of the Joint set 2 (J2) roughness and spacing distributions ...	34
Table 7: Histograms of the Joint set 2 (J2) aperture and infilling distributions	35
Table 8: Schmidt hammer rebound measurement locations and values	38
Table 9: Empirical relations between the Point Load Strength Index ($I_{s(50)}$) and Uniaxial Compressive Strength (UCS)	40
Table 10: Discontinuity orientations measured by scan-line survey and calculated from the point cloud	65
Table 11: Block sizes of sectors based on discontinuity spacing	73
Table 12: RMR basic and correction factor values used to calculate Slope Mass Rating (SMR) of different geomechanical sectors	75
Table 13: Slope Mass Rating (SMR) classes and their descriptions of different geomechanical sectors	77
Table 14: Values of the parameters used to calculate the Q-slope value of different geomechanical sectors	80
Table 15: Q-Slope values and stability conditions of the different geomechanical sectors	81
Table 16: Modes of slope failure (Hung et al., 2014 as modified from Varnes (1978))	84

Table 17: Possible modes of failure of the sectors identified by the kinematic analysis	91
Table 18: The friction angles calculated along the discontinuity sets J1 and J2 by using Equation 11 proposed by Barton and Choubey (1977).....	93
Table 19: Friction angle values calculated from Equation 11 of Barton and Choubey (1977) and obtained from the back-calculation.....	100
Table 20: Comparison of the probabilistic and deterministic analysis of planar failure	105
Table 21: Comparison of the probabilistic and deterministic analysis of wedge failure	110
Table 22: Comparison of the probabilistic and deterministic analysis results of planar failure under dynamic loading conditions	116
Table 23: Comparison of the probabilistic and deterministic analysis results of wedge failure under dynamic loading conditions	121
Table 24: Classification of the parameters employed in the hazard assessment...	129
Table 25: Weight of the parameters employed in the hazard assessment	142
Table 26: Hazard zones according to Swiss Federal Guidelines (Raetzo et al., 2002)	147
Table B 1: Field scan-line survey measurements	183
Table C 1: Density-Unit Weight Determination sheet of Sector 4, 6, and 10, respectively.....	189
Table C 2: Point Load Strength Index test sheet of Sector 4.....	191
Table C 3: Point Load Strength Index test sheet of Sector 10.....	191
Table C 4: Slake Durability test sheet of Sector 1, Sector 2, Sector 4, Sector 6, and Sector 8.....	193
Table D 1: Rock Mass Rating (RMR) system table (Bieniawski, 1989) along with the values used for the discontinuous limestone	195
Table D 2: Correction parameters and description of SMR classes (Romana, 1985)	196
Table D 3: Q-slope table (Barton and Bar, 2015)	197

Table E 1: c - ϕ pairs of Sector 5 back-calculated by the Mohr-Coulomb failure criterion	199
Table E 2: c - ϕ pairs of Sector 10 back-calculated by the Mohr-Coulomb failure criterion	199
Table E 3: c - ϕ pairs of Sectors 5 and 10 back-calculated by the limit equilibrium solution proposed by Hoek and Bray (1981)	201

LIST OF FIGURES

FIGURES

Figure 1: Number of landslide/rock slide events reported worldwide between 1903 and 2022 as of May 31, 2022 (EM-DAT, 2022)	2
Figure 2: Number of landslide/rock slide events reported in Turkey between 1945 and 2008 (Gökçe et al., 2008)	2
Figure 3: Examples of historical structures in Mudurnu. a) Yıldırım Bayazıt Mosque, b) Yıldırım Bayazıt Hammam, c) Sultan Suleiman Mosque, d-e) traditional Mudurnu houses, f) Wooden clock tower	4
Figure 4: Views from the rock mass of the east side of the Mudurnu valley which shows those houses that are under the threat of the large blocks	5
Figure 5: Views from the rock mass of the western side of the Mudurnu valley and houses under threat	6
Figure 6: a) Location map of Mudurnu, b) Google Earth image showing Mudurnu county center, c) General view of Mudurnu.....	10
Figure 7: Distribution of landslides and faults in the vicinity of the study region (modified from Emre et al., 2013 and Duman et al., 2011)	11
Figure 8: Monthly average precipitation and temperature values of Mudurnu between 1964-1997 (Turkish State Meteorological Service, 2021).....	14
Figure 9: The annual precipitation of Mudurnu (Turkish State Meteorological Service, 2021).....	14
Figure 10: Local geological map of the study region (MTA, 2002)	17
Figure 11: Simplified neotectonic map of Turkey (Bozkurt and Mittwede, 2001).21	
Figure 12: Distribution of the discontinuities and the identified sets of Sector 2 ...	27
Figure 13: Distribution of the discontinuities and the identified sets of Sector 4 ...	27
Figure 14: Distribution of the discontinuities and the identified sets of Sector 6 ...	28
Figure 15: Distribution of the discontinuities and the identified sets of Sector 8 ...	28
Figure 16: Distribution of the discontinuities and the identified sets of Sector 10.29	

Figure 17: A close-up view of discontinuous limestone. Note the 2 m long measuring tape as a scale.....	37
Figure 18: a) The surface drainage flow observed in the spring season, b) Schmidt hammer measurement in the field.....	37
Figure 19: Discontinuity wall compressive strength estimation from Schmidt hammer hardness (Deere and Miller, 1966)	39
Figure 20: A view of Point Load Strength testing	40
Figure 21: A view of the Slake Durability testing device.....	41
Figure 22: Slake Durability tested rock samples from Sectors 5 and 8. The first column shows a view of specimens before the test, whereas the second and third columns present the condition of the specimen following the 1 st and 2 nd cycles, respectively	42
Figure 23: UAV images showing details of the rock mass at higher elevations	45
Figure 24: UAV images showing the general appearance of the rock mass.....	46
Figure 25: 3D point cloud of the Mudurnu county center	47
Figure 26: Flow chart of the DSE methodology (Riquelme et al., 2014).....	49
Figure 27: Perspective of 3D point cloud for three coplanar clusters and the convex hull extracted (Riquelme et al., 2018).....	54
Figure 28: Delineated sectors defined as a result of a detailed evaluation of the rock mass characteristics.....	57
Figure 29: A view of Sectors 1 and 2 and the discontinuity sets identified by utilizing DSE.....	58
Figure 30: A view of Sectors 3 and 4 and the discontinuity sets identified by utilizing DSE.....	59
Figure 31: A view of Sectors 5 and 6 and the discontinuity sets identified by utilizing DSE.....	60
Figure 32: A view of Sectors 6 and 7 and the discontinuity sets identified by utilizing DSE.....	61
Figure 33: A view of Sector 8 and the discontinuity sets identified by utilizing DSE.....	62

Figure 34: A view of Sectors 9 and 10 and the discontinuity sets identified by utilizing DSE	63
Figure 35: A view of Sector 11 and the discontinuity sets identified by utilizing DSE	64
Figure 36: The distribution of bedding plane spacing for each sector	66
Figure 37: The distribution of J1 spacing for each sector	67
Figure 38: The distribution of J2 spacing for each sector	68
Figure 39: The distribution of bedding plane persistence for each sector.....	69
Figure 40: The distribution of J1 persistence for each sector.....	70
Figure 41: The distribution of J2 persistence for each sector.....	71
Figure 42: General views from the discontinuous rock mass on the western side of the Mudurnu valley.....	85
Figure 43: The distribution of discontinuity sets and the kinematic analysis results of Sectors 1, 2, 3, and 4 (i.e., planar failure analysis on the left, wedge failure analysis in the middle, and toppling failure analysis on the right).....	88
Figure 44: The distribution of discontinuity sets and the kinematic analysis results of Sectors 5, 6, 7, and 8 (i.e., planar failure analysis on the left, wedge failure analysis in the middle, and toppling failure analysis on the right).....	89
Figure 45: The distribution of discontinuity sets and the kinematic analysis results of Sectors 9, 10, and 11 (i.e., planar failure analysis on the left, wedge failure analysis in the middle, and toppling failure analysis on the right).....	90
Figure 46: Blocks identified in Sector 2 for the back analysis.....	94
Figure 47: Blocks identified in Sector 5 for the back analysis.....	95
Figure 48: Blocks identified in Sector 6 for the back analysis.....	95
Figure 49: Blocks identified in Sector 8 for the back analysis.....	96
Figure 50: Blocks identified in Sector 10 for the back analysis.....	96
Figure 51: Geometry of the blocks in Sector 2 analyzed by Swedge software through back analysis.....	97
Figure 52: Geometry of the blocks in Sector 5 analyzed by Swedge software through back analysis.....	97

Figure 53: Geometry of the blocks in Sector 6 analyzed by Swedge software through back analysis	97
Figure 54: Geometry of the blocks in Sector 8 analyzed by Swedge software through back analysis	98
Figure 55: Geometry of the blocks in Sector 10 analyzed by Swedge software through back analysis.....	98
Figure 56:2D and 3D view of the block generated in Sector 2 by Rocplane software	102
Figure 57: 2D and 3D view of the block generated in Sector 4 by Rocplane software	102
Figure 58: 2D and 3D view of the block generated in Sector 5 by Rocplane software	103
Figure 59: 2D and 3D view of the block generated in Sector 6 by Rocplane software	104
Figure 60: 2D and 3D view of the block generated in Sector 8 by Rocplane software	104
Figure 61: 3D view of the block generated in Sector 2 by Swedge software	106
Figure 62: 3D view of the block generated in Sector 3 by Swedge software	106
Figure 63: 3D view of the block generated in Sector 4 by Swedge software	107
Figure 64: 3D view of the block generated in Sector 5 by Swedge software	107
Figure 65: 3D view of the block generated in Sector 6 by Swedge software	108
Figure 66: 3D view of the block generated in Sector 8 by Swedge software	108
Figure 67: 3D view of the block generated in Sector 9 by Swedge software	109
Figure 68: 3D view of the block generated in Sector 10 by Swedge software	109
Figure 69: Sliding and toppling conditions of a block on an inclined plane (Hoek and Bray, 1981). Note that the condition of each sector were marked by a circle in different color.....	111
Figure 70: 2D view of the block generated for the pseudo-static analysis in Sector 2 by Rocplane software.....	113

Figure 71: 2D view of the block generated for the pseudo-static analysis in Sector 4 by Rocplane software	114
Figure 72: 2D view of the block generated for the pseudo-static analysis in Sector 5 by Rocplane software	114
Figure 73: 2D view of the block generated for the pseudo-static analysis in Sector 6 by Rocplane software	115
Figure 74: 2D view of the block generated for the pseudo-static analysis in Sector 8 by Rocplane software	115
Figure 75: 3D view of the block generated for the pseudo-static analysis in Sector 2 by Swedge software.....	117
Figure 76: 3D view of the block generated for the pseudo-static analysis in Sector 3 by Swedge software.....	117
Figure 77: 3D view of the block generated for the pseudo-static analysis in Sector 4 by Swedge software.....	118
Figure 78: 3D view of the block generated for the pseudo-static analysis in Sector 5 by Swedge software.....	118
Figure 79: 3D view of the block generated for the pseudo-static analysis in Sector 6 by Swedge software.....	119
Figure 80: 3D view of the block generated for the pseudo-static analysis in Sector 8 by Swedge software.....	119
Figure 81: 3D view of the block generated for the pseudo-static analysis in Sector 9 by Swedge software.....	120
Figure 82: 3D view of the block generated for the pseudo-static analysis in Sector 10 by Swedge software.....	120
Figure 83: Flowchart of the discontinuous rock slope hazard assessment	127
Figure 84: Lithology classes identified in the study area	130
Figure 85: Degree of weathering classes in the study area	131
Figure 86: Block size classes of the study area	132
Figure 87: Digital Elevation Model (DEM) of the study area generated from the 3D point cloud	133

Figure 88: Slope map of the study area extracted from the DEM	134
Figure 89: Aspect map of the study area extracted from the DEM	135
Figure 90: Surface water drainage pattern of the study area extracted from the DEM	136
Figure 91: Zones showing the distance to the drainage pattern.....	137
Figure 92: Planar failure-prone zones of the study area	138
Figure 93: Wedge failure-prone zones of the study area	139
Figure 94: Toppling failure-prone zones of the study area.....	140
Figure 95: Zones showing the distance to the sliding blocks from the discontinuous slope face	141
Figure 96: Hazard zonation map of planar failure on the western side of the Mudurnu valley.....	144
Figure 97: Hazard zonation map of wedge failure on the western side of the Mudurnu valley.....	145
Figure 98: Hazard zonation map of toppling failure on the western side of the Mudurnu valley.....	146
Figure 99: Example images for different failure types possible on the western side of the Mudurnu valley. a) Toppling (lower leftern side) and planar (upper part) failures, b) wedge failure	148
Figure 100: Combined rock slope failure hazard zonation map on the western side of the Mudurnu valley	149
Figure 101: Planar failure-prone zones of the study area under dynamic loading conditions.....	151
Figure 102: Wedge failure-prone zones of the study area under dynamic loading conditions.....	152
Figure 103: Toppling failure-prone zones of the study area under dynamic loading conditions.....	153
Figure 104: Hazard zonation map of planar failure under dynamic loading conditions	154

Figure 105: Hazard zonation map of wedge failure under dynamic loading conditions	155
Figure 106: Hazard zonation map of toppling failure under dynamic loading conditions	156
Figure 107: Combined rock slope failure hazard zonation map on the western side of the Mudurnu valley under dynamic loading conditions	158
Figure A 1: Thin sections of the pelagic limestone of Sector 4 (under PPL - plane polarized light).....	181
Figure A 2: Thin section of the pelagic limestone of Sector 10 (under PPL - plane polarized light).....	182
Figure C 1: The block samples of Sector 4 and Sector 10 before and after the Point Load Strength Index testing.....	190
Figure C 2: Slake Durability tested rock samples from Sectors 1, 2 and 4. The first column shows a view of specimens before the test, whereas the second and third columns present the condition of the specimen following the 1 st and 2 nd cycles, respectively.....	192
Figure D 1: Q-slope stability chart (Barton and Bar, 2015)	198
Figure E 1: Variation of the c- ϕ pairs in terms of the Mohr-Coulomb failure criterion where the intersection point identifies the back-calculated shear strength parameters of Sector 5.....	200
Figure E 2: Variation of the c- ϕ pairs in terms of the Mohr-Coulomb failure criterion where the intersection point identifies the back-calculated shear strength parameters of Sector 10.....	200
Figure G 1: Details of the process followed for the preparation of the hazard assessment layers in ArcGIS software	209

CHAPTER 1

INTRODUCTION

1.1 Motivation and purpose of the study

Slope instabilities are one of the most frequent natural hazards capable of causing severe failures both at regional and large scales. The number of slope instability cases has dramatically increased globally in the last decades. Figure 1 shows the number of landslide/rockslide events reported worldwide between 1903 and 2022 according to the International Disaster Database (EM-DAT 2022) database. Figure 2 gives the number of landslide/rock slide events that occurred in Turkey (Gökçe et al., 2008). The major triggering factors that contributed to the increasing cases are human interaction (Glade, 2003; Anderson and Holcombe, 2013; Froude and Petley, 2018) and climate change (Borgatti and Soldati, 2010; Gariano and Guzzetti, 2016). Hazard and risk analysis studies regarding mass movements have gained popularity in recent years due to population growth and the economic and environmental effects caused by the movements (UN, 2006). Researchers have conducted susceptibility, hazard, and risk assessment studies for slope instabilities at different scales both in Turkey and all around the world (Parise, 2002; Crosta and Agliardi, 2003; Ercanoğlu and Gökçeoğlu, 2004; Ayalew and Yamagishi, 2005; Çan et al., 2005; Gökçeoğlu et al., 2005; Cascini, 2008; Corominas and Moya, 2008; Fell et al., 2008; Das et al., 2012; Erener and Düzgün, 2010; Eker et al., 2015; Okalp and Akgün, 2016; Azarafza et al., 2018; Okalp and Akgün, 2022). Most of these studies have been applied in small (<1:100,000) or medium (1:100,000 to 1:25,000) scales rather than large (1:25,000 to 1:5,000) and detailed (>5,000) scales.

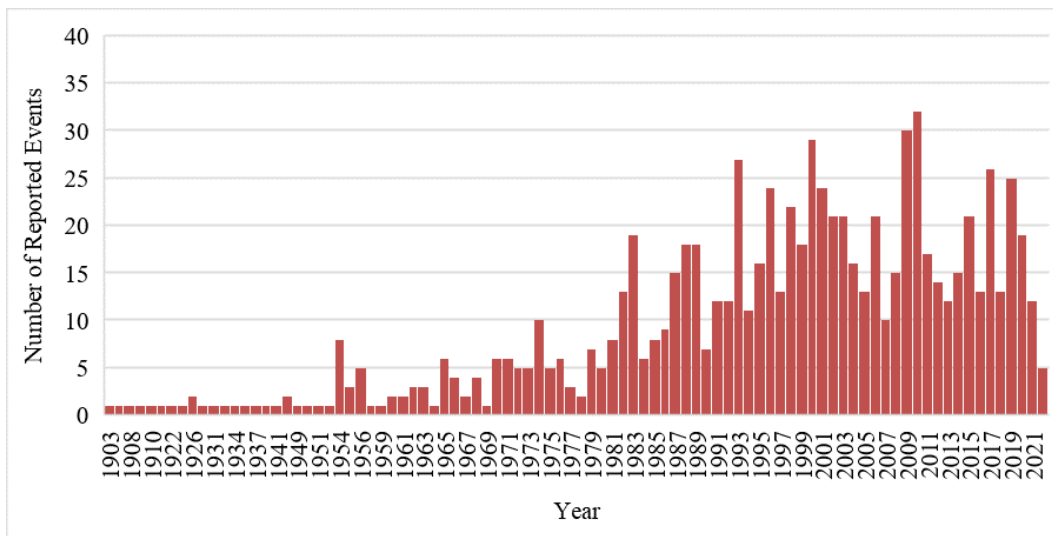


Figure 1: Number of landslide/rock slide events reported worldwide between 1903 and 2022 as of May 31, 2022 (EM-DAT, 2022)

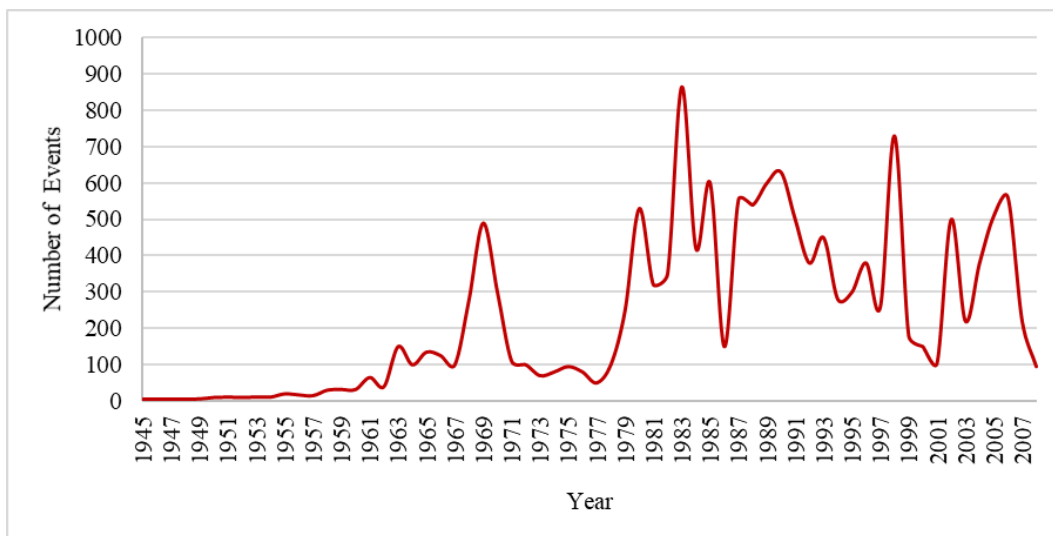


Figure 2: Number of landslide/rock slide events reported in Turkey between 1945 and 2008 (Gökçe et al., 2008)

Mudurnu is a county of Bolu located in northwestern Turkey. It is an important midpoint between the capital city, Ankara, and the largest city in the country, İstanbul. The county is located on the major trade routes (i.e. the Silk Road and the Crimean Road) and had served as a trading town and a military base in the Byzantine, Seljuk, and Ottoman periods. As a consequence, there are many historical buildings (traditional houses, mosques, a Turkish bath, and a clock tower) in Mudurnu (Figure 3). In 1991, a major part of the settlement area of the county was designated as an urban conservation site. Mudurnu has a total of 234 listed natural and cultural properties as of April 2014. The county center is in a valley that suffers from regional rock instabilities both on the eastern and western sides of the valley (Figure 4 and Figure 5). The instabilities are most likely the consequence of the combined effects of geology, topography, weathering, man-made activities, and seismicity. According to the inventory of Mudurnu Municipality, 84 of the damaging hazards that occurred between 1961 and 2016 were caused by rockfalls and mass movements due to precipitation, weathering, and secondary effects of earthquakes. The valley can be defined as a high-risk region, given the slope instability casualties that have occurred in the past and those that have the potential to occur. The instabilities throughout the valley tend to threaten human life, houses, buildings, and small industrial facilities. Moreover, instabilities create a risk to the historically important structures such as mansions, mosques, a Turkish bath from the Ottoman period, and a wooden clock tower by which Mudurnu has been nominated as a candidate for the UNESCO World Heritage List.



Figure 3: Examples of historical structures in Mudurnu. a) Yıldırım Bayazıt Mosque, b) Yıldırım Bayazıt Hammam, c) Sultan Suleiman Mosque, d-e) traditional Mudurnu houses, f) Wooden clock tower



Figure 4: Views from the rock mass of the east side of the Mudurnu valley which shows those houses that are under the threat of the large blocks

The slopes are prone to instability through modes of failure that are different on the western and eastern sides of the valley, as a consequence of the different rock mass properties which makes Mudurnu an attractive and distinctive site for the investigation of rock mass failure. Geological units outcropped in the Mudurnu county center are Quaternary alluvium, Late Cretaceous Üzümlü formation, and Değirmenözü member (Saner, 1980). The Üzümlü formation is composed of the alternation of thin-thick bedded volcanoclastic sandstone and thin-bedded shale. On the east side, the Üzümlü formation outcrops as volcanoclastic sandstone that is prone to rock falls. Volcanoclastic blocks are held in place by a less durable matrix that has low strength. As a result, the matrix decomposes due to weathering which

leads to the fall of rock blocks. The discontinuous limestone found in the study area belongs to the Late Cretaceous Değirmenözü member of the Yenipazar formation. The discontinuous Pelagic Limestone creates discontinuity-controlled complex kinematic failures (i.e., a combination of the planar, wedge, or toppling failures) on the western side of the Mudurnu valley.



Figure 5: Views from the rock mass of the western side of the Mudurnu valley and houses under threat

Since the study area lies in a tectonically active region, discontinuity sets having a non-homogeneous distribution have formed within the Pelagic Limestone. The presence of the different discontinuity sets together with the favorable orientation of the slope face at the center of the Mudurnu county has led to the development of kinematic failures. The discontinuity sets are capable of creating a combination of planar, wedge, and toppling failures (Arslan Kelam et al., 2018). Moreover, complex kinematic failures tend to make the study area a unique case study. In the area, planar and wedge failures tend to create large to very large unstable blocks that are very critical in terms of their consequences. In addition, it needs to be noted that their frequency of occurrence is lower than the frequency of occurrence of toppling failure in the region. The unstable blocks prone to toppling failure are almost always associated with small to medium-sized blocks with a higher frequency of occurrence. The combination of toppling-prone blocks with the planar and wedge blocks creates complex kinematic failures. Because of the rock mass complexity of the site and the distinct instability mechanisms identified, it is imperative to characterize the rock mass at the site.

The purpose of this dissertation is to characterize the rock masses that have the potential to create a hazard in the Mudurnu county center through geomechanical evaluation of the slope instability problems under static and dynamic loading conditions and identify the hazard zones in the Mudurnu Valley with a focus on the western side of the valley. The engineering geological and geomechanical properties of the region were assessed through a 3D point cloud generated by an unmanned aerial vehicle (UAV) along with scan-line survey field studies of the physically accessible locations. The data were evaluated statistically to define the discontinuous rock mass characteristics, identify the failure modes and susceptibility zones, and map the hazard zones on a detailed scale.

The studies completed within the scope of the dissertation were divided into chapters to better explain the theory related to the corresponding chapter, the methods applied and the results reached. Chapter 1 continues with the basic information regarding the study area, its location, topographical characteristics and climate. In Chapter 2, regional geology and seismotectonics of the study area are introduced. Then, the local geology of the study area is explained by combining the data gathered from the literature and field studies. Chapter 3 presents the methodology followed for the site characterization by explaining the scan-line field survey studies and the studies conducted by an Unmanned Aerial Vehicle (UAV). Also, the results of the laboratory tests performed on the samples collected from the field have been presented. Chapter 3 shows the discontinuity characteristics obtained from the UAV-generated data, their comparison and validation with the field measurements, and the delineation of the western side of the valley into 11 geomechanically uniform sectors. It should be noted that, throughout the dissertation, rock mass characteristics were considered on a sectoral basis. Hence, the stability and hazard assessments were performed based on the sectors. Moreover, empirical classification of the rock slopes was performed. Chapter 4 explains rock slope stability methods and the details and results of the analysis applied in Mudurnu. To that end, the stability conditions concluded by the kinematic analysis, back analysis and limit equilibrium analysis have been discussed. The limit equilibrium analyses have been performed in both static and dynamic loading conditions. Chapter 5 defines the parameters considered in the hazard assessment and the resultant hazard classes for different failure modes (i.e., planar, wedge, toppling, complex). The final chapter, Chapter 6, concludes the findings and gives recommendations regarding future research.

1.2 The study area

Mudurnu is a county of Bolu Province that is located in the Western Black Sea Part of the Black Sea Region. The county center was established in the valley between Hisar and Kulaklı Hills. The study area is in the county center (Figure 6). Mudurnu is bordered by Düzce Province in the north, Hendek County in the northwest, Bolu Province in the northeast, Seben County in the east, Nallıhan County in the south, and Göynük and Akyazı Counties in the west. The distance between the county to Bolu is 51 km, whereas Ankara is at a distance of 200 km and İstanbul is 260 km away (Figure 6). The county population is 18.880 and the number of people who live in the county center is 5.132 (TSI, 2019).

AFAD (2018) has reported the occurrence of a total of 145 landslide/rock slide events in Bolu between 1950 and 2018 which roughly indicates a frequency of 2 landslide/rock slide events in Bolu per year. As expected, the frequency becomes higher for the locations that are susceptible to slope instabilities such as Mudurnu. Moreover, the influence of triggering factors contributes to the number of cases. In Mudurnu, the major landslide triggering factor is expected to be an earthquake due to its proximity to the most active fault zone of Turkey: the North Anatolian Fault Zone (NAFZ). Therefore, seismic force should be considered as a major triggering mechanism of rock slides/rock falls that have occurred in Mudurnu. The distribution of landslides that have occurred around the study area and the active fault segments are given in Figure 7.



Figure 6: a) Location map of Mudurnu, b) Google Earth image showing Mudurnu county center, c) General view of Mudurnu

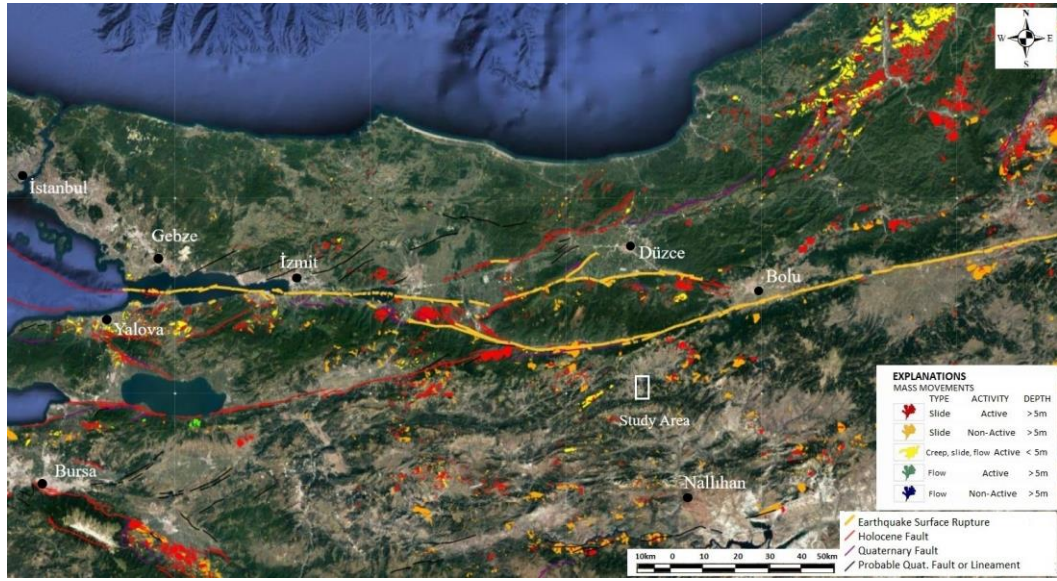


Figure 7: Distribution of landslides and faults in the vicinity of the study region (modified from Emre et al., 2013 and Duman et al., 2011)

1.2.1 Physiography and climate of the study area

Mudurnu County is on a rough terrain where the mountain ranges extend to the west and the elevation increases from west to east. The altitude of the county center is 840 m. There are three distinct mountain ranges in the region. The first one is the Abant Mountains, which pass through the northernmost part of the county and form the Düzce Province border. The second one begins at the Akyazı-Göynük border, and continues with Akkaya Hill (1628 m), Kuzgunkaya Hill (1651 m), and Alaçam Hill (1689 m) and merges with the Aladağ and Köroğlu mountain ranges. The third one is the range that comes through Göynük by the rise and enters the borders of Mudurnu in the southwest. This range extends to the east and then merges with the second range. Hisar Mountain (1384 m) located in the east and Şehriman Hill (1115m) located in the west of Mudurnu county center are the two topographically

high structures that draw attention at the entrance to Mudurnu. The most important stream around the county is Mudurnu Stream. In addition, there are Mudurnu Creek, Filibeli Creek, Karacakaya Creek, Ayı Creek, and Büyük Creek flow through the borders of the county.

In Mudurnu, neither the typical effects of the maritime climate nor the influences of the continental climate of Central Anatolia are fully observed. It has a transitional climate between these two climates, although the character of the continental climate is dominant. However, the climate is dissimilar to the Central Anatolian provinces in terms of average temperature, and seasonal and daily temperature differences. According to the Turkish State Meteorological Service (2021), the annual average temperature of 33 years is 9.2°C. January is the coldest month with an average temperature of -0.9°C and July is the warmest month with an average temperature of 18.8°C. The monthly average/maximum/minimum values of temperature, precipitation, wind speed, and the number of snowy and rainy days are given in Table 1. In addition, variations in the average monthly temperature and precipitation are presented in Figure 8. The annual precipitation values of Mudurnu are shown in Figure 9. Accordingly, the average annual precipitation is 505.4 mm. Meteorological data demonstrates that Mudurnu receives precipitation throughout the year. The monthly average precipitation is higher in December and January where the monthly values are 79.6 mm and 73.6 mm, respectively. Nonetheless, the precipitation amount in almost all of the other months is considerable, except in the summer. As a consequence, surface runoff may be expected to cause erosion of the rock masses. Hence, surface water should be eliminated by utilizing surface drainage system measures.

Table 1: Average, maximum, and minimum important meteorological parameters of Mudurnu for 1964-1997 (Turkish State Meteorological Service, 2021)

Month	Mean Monthly Temperature (°C)	Maximum Monthly Temperature (°C)	Minimum Monthly Temperature (°C)	Monthly Average of Cumulative Precipitation (mm)	Maximum Monthly Precipitation (mm)	Monthly Average of Number of Snowy Days	Monthly Average of Number of Rainy Days	Monthly Average Wind Speed (m/s)	Monthly Dominant Wind Direction
January	-0.9	4.0	-5.7	73.6	32.6	6.7	9.1	2.8	SW
February	0.2	5.7	-5.1	51.7	31.4	5.5	7.3	3.0	SW
March	3.5	10.0	-2.3	55.7	31.7	4.2	7.6	3.2	SW
April	8.4	15.2	2.0	50.7	24.8	1.6	8.4	3.2	SW
May	12.9	20.2	5.7	51.8	35.2	0.1	8.5	3.1	SW
June	16.3	23.7	8.5	38.0	36.3	-	5.9	3.2	SW
July	18.8	26.3	10.5	21.0	37.6	-	2.9	3.3	SW
August	18.6	26.4	10.3	24.7	50.6	-	2.7	3.3	SW
September	14.9	23.5	6.9	16.1	22.4	-	3.0	3.1	SW
October	10.3	18.1	3.7	34.5	35.5	0.3	5.4	2.9	SW
November	5.0	11.2	-0.3	50.0	30.5	2.5	7.7	2.8	SW
December	1.2	5.6	-3.1	79.6	72.8	5.6	9.6	2.8	SW

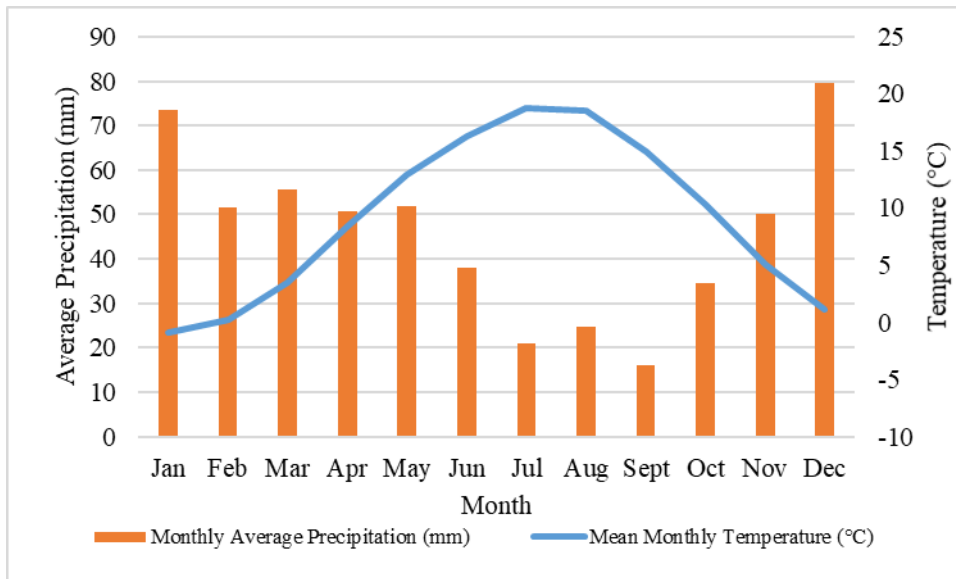


Figure 8: Monthly average precipitation and temperature values of Mudurnu between 1964-1997 (Turkish State Meteorological Service, 2021)

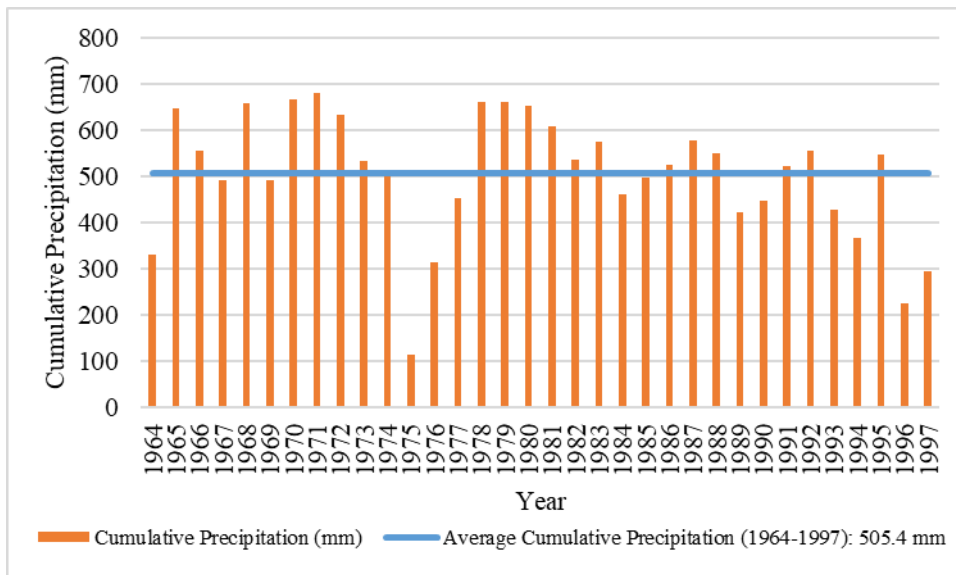


Figure 9: The annual precipitation of Mudurnu (Turkish State Meteorological Service, 2021)

CHAPTER 2

GEOLOGICAL ASSESSMENT OF THE STUDY AREA

2.1 Regional geology of the study area

Saner (1980) studied the units that outcrop in Mudurnu-Göynük Basin, which is bounded by Seben in the east, Bilecik in the west, Bolu in the north, and Nallıhan in the south, and presented the stratigraphic sequence of the basin for the units younger than Jurassic. According to Saner (1980), Mesozoic-Tertiary units in the region are deposited in the granitic basement. Although the Permian and older basement units outcrop in several locations within the basin, it is not observable in Mudurnu. Over the basement, the Lower Jurassic Bayırköy formation composed of sandstone was deposited discordantly by transgression. The stratigraphic section in Mudurnu Basin starts with the Middle-Upper Jurassic Mudurnu formation. This flysch-like formation is deposited in the deep marine environment and is composed of a sequence of tuff and volcanoclastic sandstone, tuff, agglomerate, and shale. It includes volcanic pebblestone layers at some points. A lava flow was observed in the formation. The deposition source is mainly volcanic and the unit is bonded by silica. Mudurnu formation is transitional with Soğukçam Limestone, which has started to deposit in a shelf environment in the Upper Jurassic-Lower Cretaceous. It is defined as clayey limestone, clayey micrite with definite layering. There is an Upper Cretaceous pelagic clayey limestone unit on Soğukçam Limestone. This unit may be observed as a transition to Soğukçam Limestone or can be observed as a unit named Değirmenözü member. In the Early Upper Cretaceous, marine environment conditions continued to be present and it became deeper. At that time, the Üzümlü formation composed of sandstone-shale alternation including volcanoclastic has been deposited. Üzümlü formation transits to shale-sandstone alternation of Yenipazar formation at Middle-Upper Cretaceous. These flysch facies include local

clayey limestone layers. Upper Cretaceous Yenipazar formation is observed in the entire Mudurnu-Göynük Basin covered by a deep sea. There are some structures and lithologies such as olistostromes that have developed as a result of submarine slumps in flysch deposits. On top of the Yenipazar formation, the deposited marls of the Seben formation have transited to the Taraklı formation (Saner, 1980). A geological map of the region is given in Figure 10.

The geological units of the study area consist of Jurassic Mudurnu formation, Late Cretaceous Yenipazar formation, Üzümlü formation, and Değirmenözü member and Quaternary Alluvium (Figure 10).

Mudurnu formation

The unit was formed by the alternation of volcanogenic sandstone, mudstone, shale, tuff, agglomerate, andesite, basalt, and limestone. The unit was first named as Jurassic dark green flysch by Abdüsselamoğlu (1959) and then redefined by Gözübol (1978) as Mudurnu formation. The dominant rock type of the formation was formed by the alternation of dark green colored thin to moderately bedded volcanogenic sandstone, shale, and mudstone. These lithologies representing the turbiditic facies were transitional to agglomerates and tuffs in horizontal and vertical directions. Andesitic and basaltic lava lenses are occasionally observed in the sequence. In the 30-40 cm sized pebbles of agglomerates, andesitic and basaltic (spilite) rocks are abundant. In addition, the sequence is locally cut by dolerite dykes. The dominant rock type in the upper levels of the unit is sandstone shale alternation. The lower contact of the formation has not been observed around Mudurnu, but it was assumed that it may have a lateral transition with the Bayırkoy formation. The age of the unit was considered Jurassic (Abdüsselamoğlu, 1959; Gözübol, 1978; Yılmaz et al., 1981), Middle-Upper Jurassic (Saner, 1980), Dogger (Altınır et al., 1991), Liassic-Lower Cretaceous (Göncüoğlu et al., 1996) by various researchers.

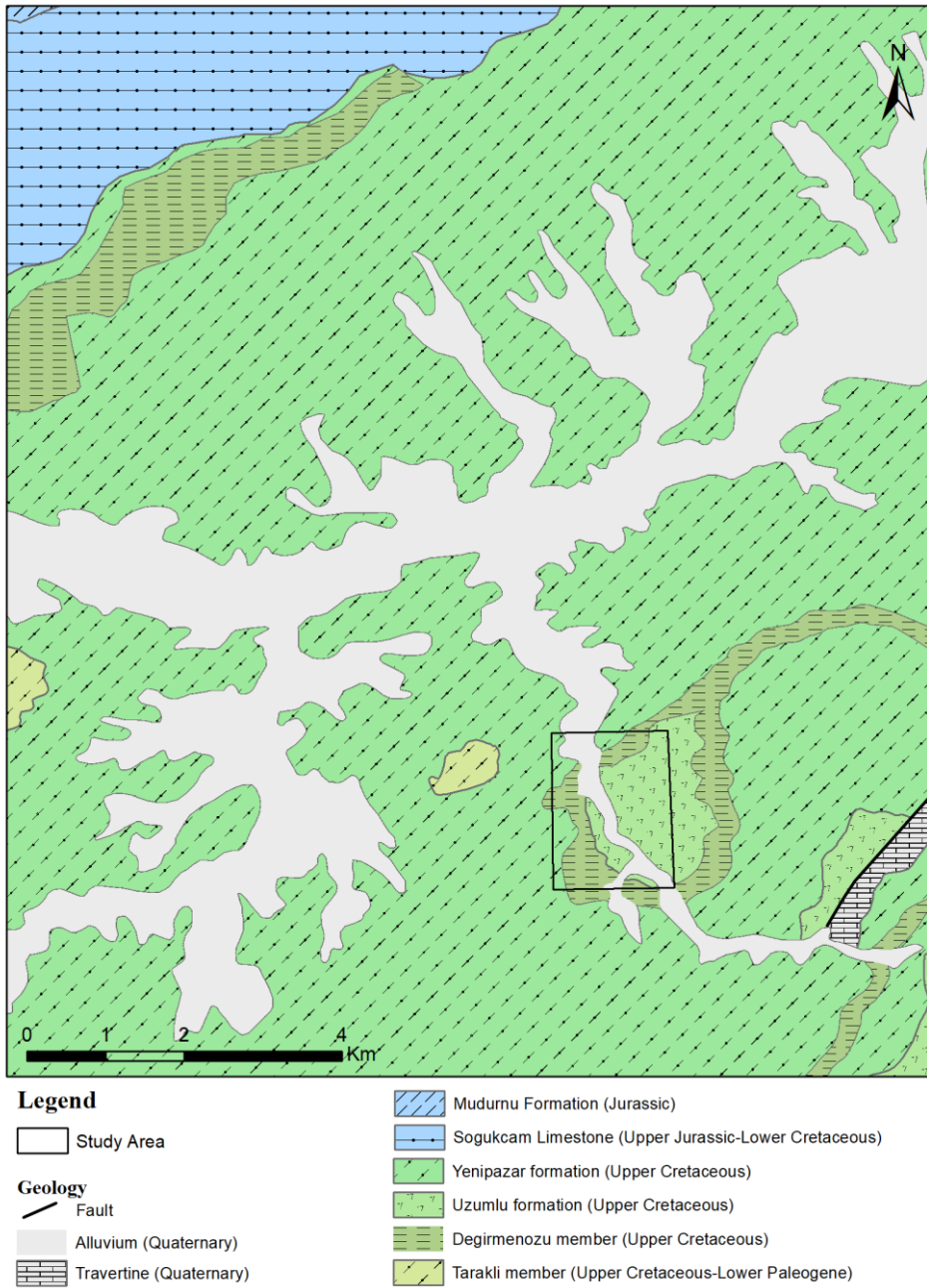


Figure 10: Local geological map of the study region (MTA, 2002)

Yenipazar formation

The name of the Yenipazar formation was used by Saner (1980) for the Late Cretaceous flysch facies sedimentary sequence consisting of volcanic blocky sandstone and shale alternation. Yenipazar formation starts with clastics overlying the Sogukcam formation. In the upper part, it reaches up to the Paleocene Selvipinar and Kızılcay formations, and where these formations do not exist (in the successions), it reaches up to the Lower Eocene Çataltepe formation. The formation is well observed alongside the banks of the road that ties the Yenipazar and Sarıcakaya districts. Yenipazar formation is mostly composed of grayish-green thin-medium bedded sandstone-shale alternation with green and brown colored volcanics, green-colored marl and white beige, red-pink colored thin-bedded micritic (pelagic-semipelagic) limestone, and a small amount of conglomerate.

Üzümlü formation

Demirkol (1973, 1977) named the unit consisting of mudstone, marl or clayey micrite, calcarenite, conglomerate, shale, sandstone (volcanogenic), and limestone as Üzümlü formation. The same name for this unit, which also includes basaltic lava and agglomerate, was used by Saner (1977, 1980) and Altiner et al. (1991). Göncüoğlu et al. (1996) examined this unit under the name of pyroclastic and lava member. According to Demirkol (1973), the unit is commonly composed of an alternation of brownish thin-thick bedded volcanoclastic sandstone and grayish-green thin-bedded shale. The member sparsely contains marl, conglomerate and limestone, metamorphics, serpentinite, and olistostrome derived from intra-basin lava. In addition, it contains white beige-colored, thin-medium bedded, unfossiliferous micritic limestone lenses. Although the limestones have a blocky appearance, they are gradually transitional with the shales in the unit (Saner, 1980). The member, which shows lateral variations and reaches a thickness of 800 m, is best seen around Üzümlü village in the south of Gölpazarı and the villages of

Karafakılar, Kayalıdere, Umurlar, and Susuz in the south of Göynük. The Late Cretaceous unit is gradually transitional with the Yenipazar formation.

Değirmenözü member

The name Değirmenözü member was used by Saner (1977, 1980) for the white beige, red-colored, Globotruncana bearing pelagic limestones. The unit was considered as a member of Yenipazar formation (Saner, 1977, 1980; Göncüoğlu et al., 1996). Late Cretaceous Değirmenözü member, located in the lower levels of the Yenipazar formation, is composed of pelagic-semipelagic clayey limestone. The member is generally white beige-colored at the bottom and red-colored at the top levels. It contains micrite, biomicritic limestone, intercalation of shale, sandstone, tuff, and monogenic olistostrome conglomerates derived from Bilecik limestone. The unit was observed well in Değirmenözü village in the north of Göynük and alongside the Yenipazar-Sarıcakaya road. At the bottom, the member is gradually transitional with Üzümlü member where it is present, and with the sandstone and shale units of the Yenipazar formation where Üzümlü member is missing. At the top, it is gradually transitional with the Yenipazar formation.

Alluvium

Quaternary alluvium consists of clay, silt, sand, gravel, and block-size materials carried by Mudurnu Stream, Filibeli Creek, Karacakaya Creek, Ayı Creek, and Büyük Creek.

2.2 Seismotectonics of the study area

Mudurnu is located in a tectonically active region as a consequence of one of the most important seismically active zones of Turkey, namely the North Anatolian Fault Zone (NAFZ). The NAFZ is a right-lateral strike-slip active fault with a length of approximately 1500 km. This major tectonic structure disconnects the Eurasia Plate from the Anatolian Plate (Figure 11). The NAFZ together with the East Anatolian Fault System shapes the neotectonic evolution and deformation of Anatolia (Şengör, 1979). The NAFZ has a relatively narrow zone from its east end (Karlıova) to Bolu and a wider zone in the west of Bolu in which Mudurnu is located (Şaroğlu et al., 1987; Barka, 1997). The NAFZ has created a 125-145 km long surface rupture as a result of the August 17, 1999, Kocaeli earthquake with a moment magnitude of 7.4 (Lettis et al., 2002; Barka et al., 2002). This surface rupture continues into the Marmara Sea (Emre et al., 1998; Barka et al., 2002; MTA, 2003; Harris et al., 2002; Duman et al., 2005; Emre et al., 2011). Another seismic source around the study area is the fault zone created on November 12, 1999, by the Düzce earthquake with a moment magnitude of 7.2. This fault zone has a length ranging from 30 to 45 km (Duman et al., 2005). In addition, there is another seismic source created by the Abant (May 26, 1957, $M_s=7.0$) and Mudurnu (June 22, 1967, $M_s=7.1$) earthquakes (Ambraseys and Zatopek, 1969). The Mudurnu earthquake has a 55 km long fault zone that overlaps 25 km of the Abant earthquake fault zone (Ambraseys and Zatopek, 1969). The 1957 Abant earthquake has a surface rupture with a length ranging from 30 km (Barka, 1996) to 40 km (Ambraseys and Zatopek, 1969) that extends between the Abant Lake and Dokurcun. The surface rupture of the Bolu earthquake (February 1, 1944, $M_w=6.8$) that occurred near the study area continues between the Abant Lake and Bayramören (Ketin, 1969; Öztürk et al., 1985).

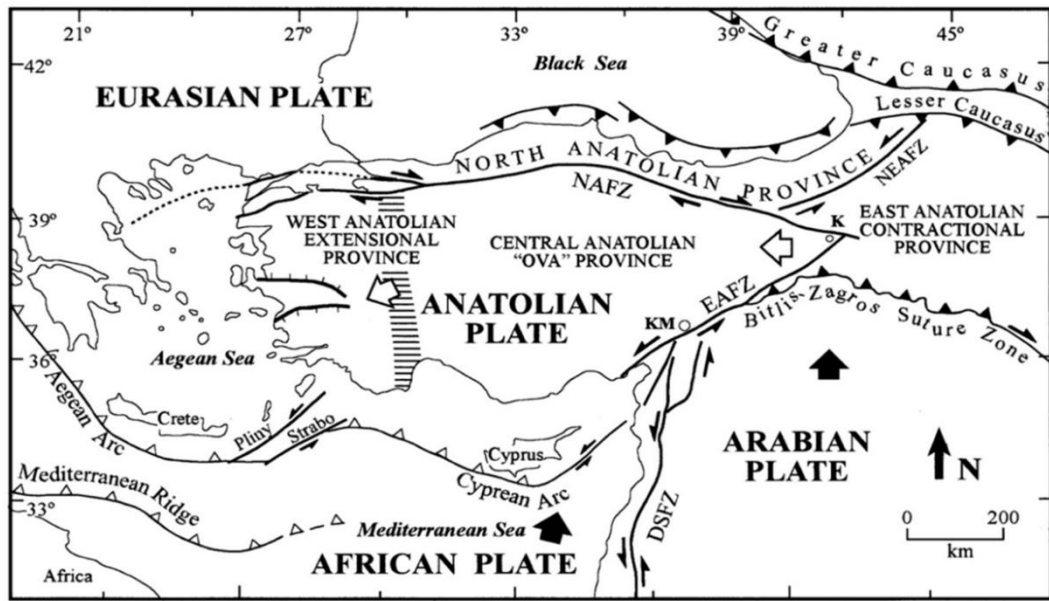


Figure 11: Simplified neotectonic map of Turkey (Bozkurt and Mittweide, 2001)

The NAFZ has created earthquakes both in historical and instrumental periods. The destructive earthquakes that have been reported during the historical period (B.C. 2100-1900) (Sipahioğlu, 1984) and that have been recorded during the instrumental period in the vicinity of the region of interest are listed below:

Historical period earthquakes

170, 268, 350 Earthquakes: Intensity: VIII, damage in İzmit and İznik

24.08.358 Earthquake: Intensity: IX, damage in Kocaeli, İznik, and İstanbul

467 and 500 Earthquakes: Intensity: VI, damage in İzmit

02.09.967 Earthquake: damage between Bolu-Çerkeş

03.05.1035 Earthquake: damage in Bayındır and Hamamlı

18.12.1036 Earthquake: damage in Bayındır and Hamamlı

18.07.1668 Earthquake: damage in Kastamonu, Gerede, and Bolu

24.11.1863 Earthquake: damage in Bolu

19.04.1878 Earthquake: damage and life loss between İzmit Adapazarı. Sapanca and Eşme were entirely destroyed.

Instrumental period earthquakes

20.06.1943 Adapazarı-Hendek Earthquake: Intensity=VIII (MSK), magnitude $M_s=6.4$ (Ambraseys, 1988).

01.02.1944 Bolu-Gerede Earthquake: Intensity:X (MSK) magnitude $M_s:7.2$ (Ergin et al., 1967).

05.04.1944 Mudurnu Earthquake is an aftershock of this earthquake ($M_s:5.6$). 30 people lost their lives and 900 houses were damaged (Ambraseys et al., 1968).

26.05.1957 Bolu-Abant Earthquake: Intensity=IX, magnitude $M_s=7.1$ (Gencoğlu, 1986).

22.07.1967 Mudurnu Valley earthquake: Intensity=9, magnitude $M_s=7.2$ (Bağcı et al., 2000). 89 people lost their lives and 235 people were injured. In addition, 5569 houses were highly damaged together with 5110 moderate and 3210 little damaged buildings.

17.08.1999 Gulf of İzmit Earthquake: Intensity=X, magnitude $M_s=7.8$

12.11.1999 Düzce Earthquake: Intensity=X, magnitude $M_s=7.2$

2.3 Local geology of the study area

The units that outcrop in the Mudurnu county center are Late Cretaceous Yenipazar formation, Üzümlü formation and Değirmenözü member, and Quaternary Alluvium. The characteristics of these units as observed in the study area are explained in the following paragraphs.

Yenipazar formation

The Yenipazar formation covers a wide area around the county center. It is a flysch facies deposited as an alternation of volcanoclastic, blocky sandstone and shale. In general, it is grayish-green colored thin medium bedded sandstone-shale intercalation. However, beige, green-colored marls, and white beige, thin-bedded limestones crop out in several locations such as the Mudurnu entrance and southwest of Mudurnu. The unit was generally observed as deformed and weathered.

Üzümlü formation

The Üzümlü formation crops out on the east side of the Mudurnu Valley. The formation consists of mudstone, marl, conglomerate, shale, sandstone, and limestone. Basaltic lavas and agglomerates are observed to the east of the Mudurnu Stream. The unit is gradually transitional with the rocks of the Yenipazar formation. In the study area, the unit is mainly composed of brownish thin sandstone with volcanoclastic materials, grayish-green colored thin and thick layered alternation of shales and agglomerates. The agglomerates are observable on the slope just behind the buildings that are located to the east of the Yıldırım Bayazit Mosque.

Değirmenözü member

Değirmenözü member forms the rock slopes to the west of the Mudurnu county center. The member crops out as a narrow band that consists of white beige clayey limestone. There are occasional shale, sandstone, and tuff intercalations in between limestone layers. In addition to field observations, thin sections were prepared from the samples collected from the western side of Mudurnu Valley, which is the focus of the dissertation, for the complete definition of the rock mass of the study site. The thin sections are presented in Appendix A. Based on the thin sections, the rock mass was identified as pelagic limestone deposited in a deep marine environment. More specifically, it was classified as planktonic foraminiferal packstone. A thin section of Sector 4 showed that the sample entails biotite, feldspar, glauconite, mica, and quartz. Micas and some of the quartz grains have an igneous origin. Globotruncana, echinoid fragments, benthic foraminifera, heterohelix, globicerinelloides, and calcified radiolaria were identified in the section. The thin section of Sector 10 has similar characteristics to that of Sector 4. However, it has a higher clay content, contains a higher proportion of microfractures, and smaller skeletal fragments as compared to the thin section of Sector 4. It can be concluded that Sector 10 may have been deposited in a deeper marine environment. In other words, the depositional marine environment may be deeper in the northern part of the valley. In Sector 10 dissolution cavities filled with vadosite silt and a matrix cemented by sparry calcite were observed.

CHAPTER 3

SITE CHARACTERIZATION METHODOLOGY

This chapter explains the procedure that has been followed to characterize the rock mass that forms the rock slopes of the western side of Mudurnu valley throughout the county center from an engineering geological point of view and aims to characterize the geomechanically-uniform sectors. The chapter is divided into four subchapters in an attempt to better explain the motivation behind the applied techniques and to discuss the findings in detail. To that end, studies that have been conducted in the field are described under two sub-headings as field rock mass characterization (i.e., scan-line survey) studies and Unmanned Aerial Vehicle (UAV) studies. The rock mass was characterized based on the data gathered from the scan-line survey and 3D point cloud. Moreover, by analyzing the rock mass characteristics, the valley slope was separated into geomechanically uniform sectors. After that, the rock slope sectors were classified empirically.

3.1 Engineering geological assessment of the rock mass

Rock material or intact rock can be defined as a continuum of polycrystalline solid composed of an aggregate of minerals or grains. Rock materials are commonly assumed homogenous, isotropic, continuous, linear, and elastic in solid mechanics (Goodman, 1989). However, in nature, this is not the case. Rocks have both micro and macro structures such as fissures, foliation, bedding planes, joints, folds, and faults. The general term used for joints, bedding planes, schistosity planes, weakness zones, and faults is ‘discontinuity’ (ISRM, 2007). Rock masses are non-

homogeneous, anisotropic, and discontinuous, unlike the other engineering materials. This entire structure which entails intact rock blocks separated by discontinuities, is referred to as 'rock mass' (Bieniawski, 1989). Discontinuities cause the tensile strength of rock mass to be reduced to nearly to zero in the perpendicular direction to the discontinuity plane and restrict shear strength in a parallel direction to the discontinuity plane (Goodman, 1989). Discontinuities have a controlling effect on the strength, permeability, and stability of rock masses (Hoek and Bray, 1981). It is crucial to characterize discontinuity properties since they have a major influence on the geomechanical behavior of the rock mass (Priest and Hudson, 1976; Palmstrom, 2001).

The discontinuity characteristics that need to be described according to ISRM (2007) are orientation, spacing, persistence, roughness, wall strength, aperture, infilling, seepage, number of joint sets, and block size. These properties were collected in the accessible parts of the study area utilizing the scan-line survey method by using a measuring tape (Figure 12). The data collected by the scan-line survey are given in Appendix B. It should be noted that the locations of measurements presented in Appendix B pertain to the assigned sectors. The details regarding the definition and delineation of the sectors are explained in Section 3.3. The collected discontinuity orientations of the physically accessible sectors (i.e., Sectors 2, 4, 6, 8, and 10) were plotted and the discontinuity sets were identified by Dips software (Rocscience, 2022). The distributions of the discontinuities and the discontinuity sets identified in Sectors 2, 4, 6, 8, and 10 are shown in Figures 12 through 16, respectively. As a consequence, three discontinuity sets were specified: a bedding plane (BP) and two discontinuity sets (Joint set 1: J1 and Joint set 2: J2).

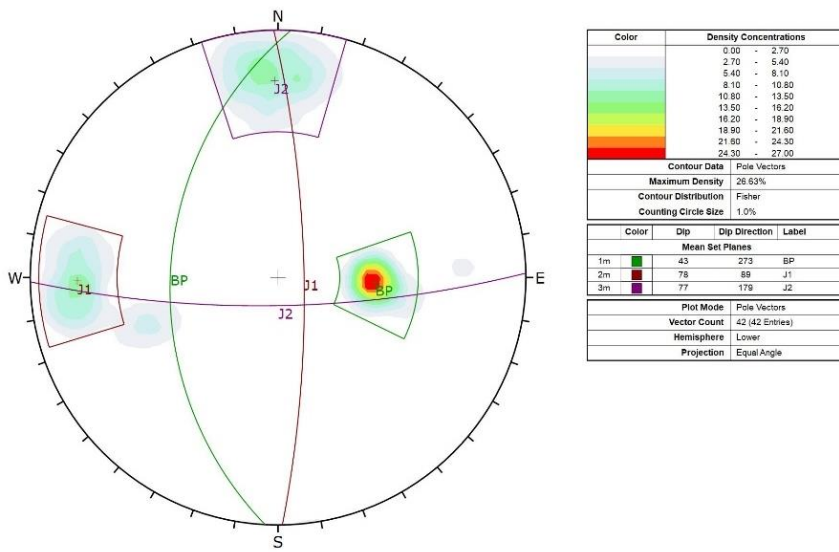


Figure 12: Distribution of the discontinuities and the identified sets of Sector 2

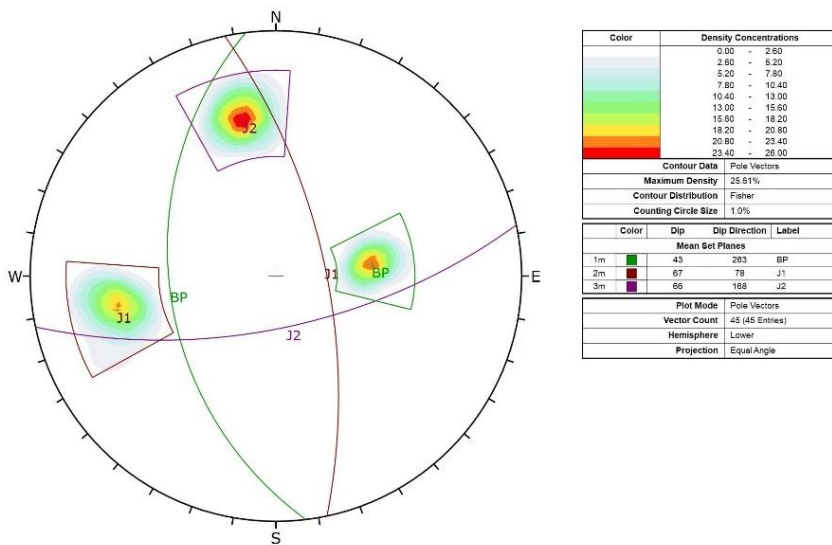


Figure 13: Distribution of the discontinuities and the identified sets of Sector 4

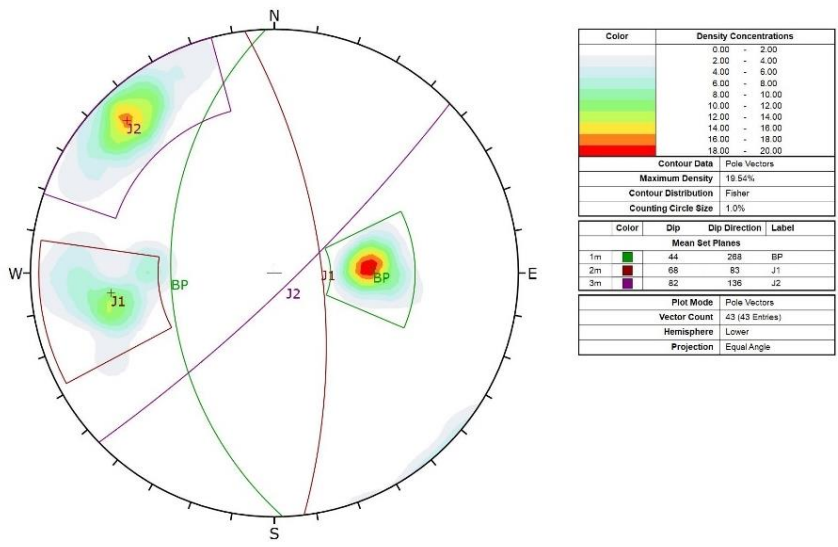


Figure 14: Distribution of the discontinuities and the identified sets of Sector 6

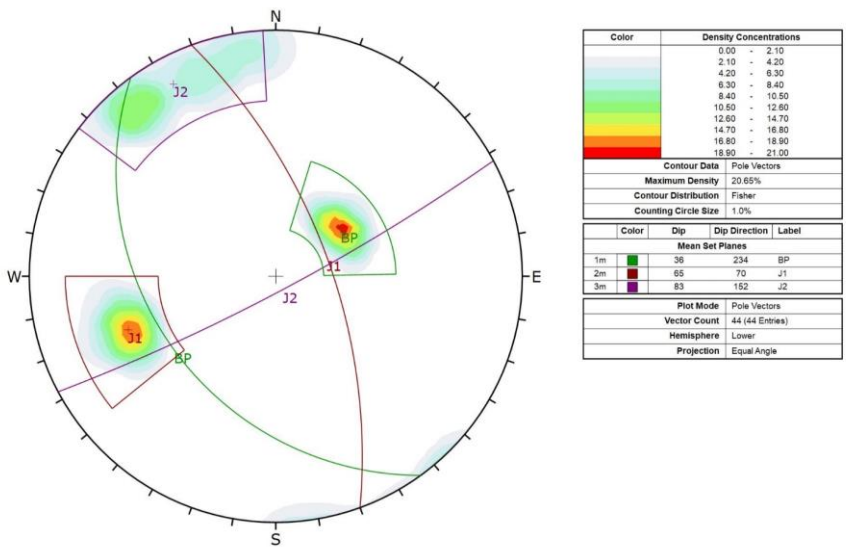


Figure 15: Distribution of the discontinuities and the identified sets of Sector 8

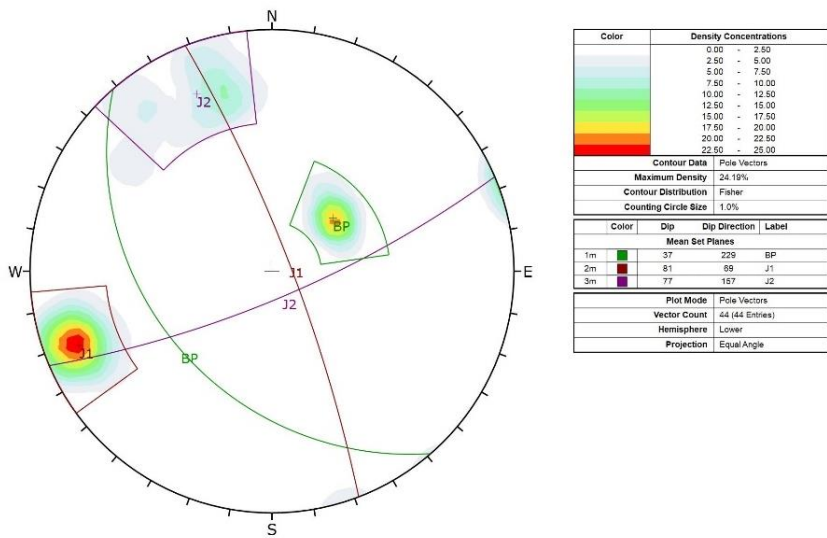


Figure 16: Distribution of the discontinuities and the identified sets of Sector 10

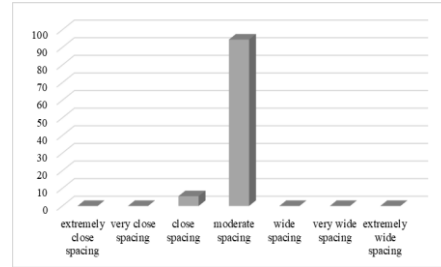
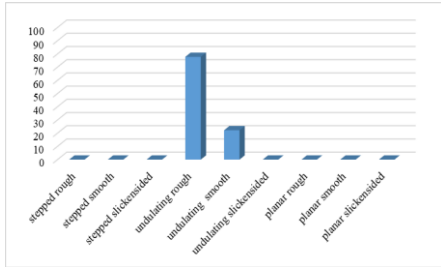
The discontinuity properties gathered by the scan-line survey were classified according to ISRM (2007) and histograms displaying the frequency of measurements in the corresponding classes were prepared for the accessible sectors (i.e., Sector 2, 4, 6, 8, and 10). Histograms were drawn separately for each sector. Histograms of bedding plane roughness and spacing are given in Table 2 and histograms of bedding plane aperture and infilling are presented in Table 3 for each sector. Similarly, histograms of Joint set 1 roughness and spacing are shown in Table 4, and histograms of Joint set 1 aperture and infilling are given in Table 5 for each sector. Histograms of Joint set 2 roughness and spacing are presented in Table 6 and histograms of Joint set 2 aperture and infilling are illustrated in Table 7 for each sector. In addition, Joint Roughness Coefficient (JRC) that was estimated in the field by observing the shape and waviness of the discontinuity surfaces, and by comparing the discontinuity surfaces with the standard profiles defined by Barton and Choubey (1977) is presented in Appendix B for each discontinuity set.

Table 2: Histograms of the bedding plane (BP) roughness and spacing distributions

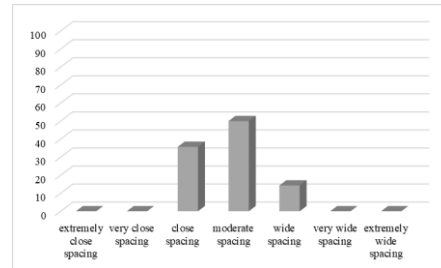
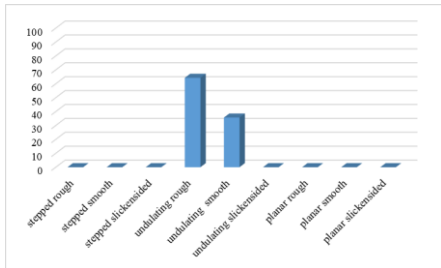
Sector BP Roughness

BP Spacing

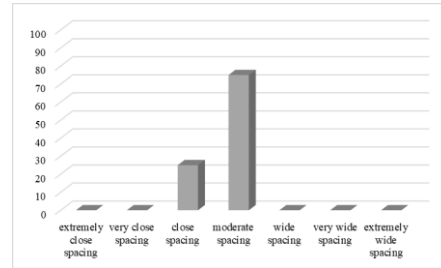
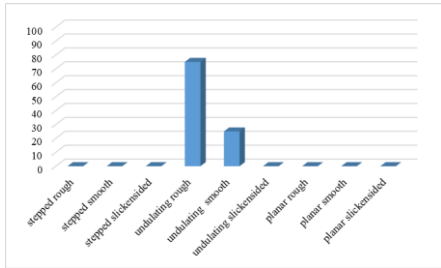
2



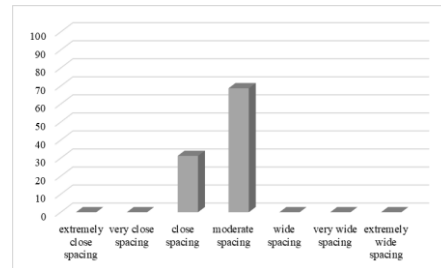
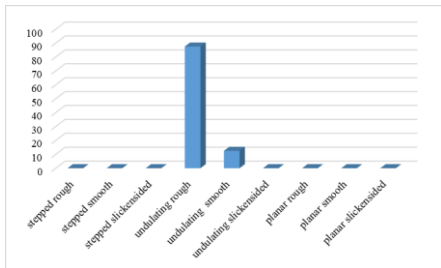
4



6



8



10

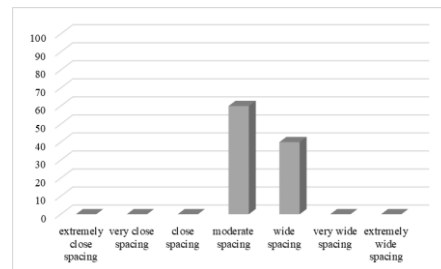
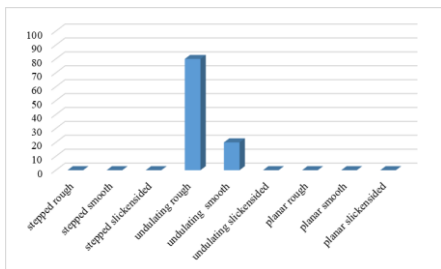


Table 3: Histograms of the bedding plane (BP) aperture and infilling distributions

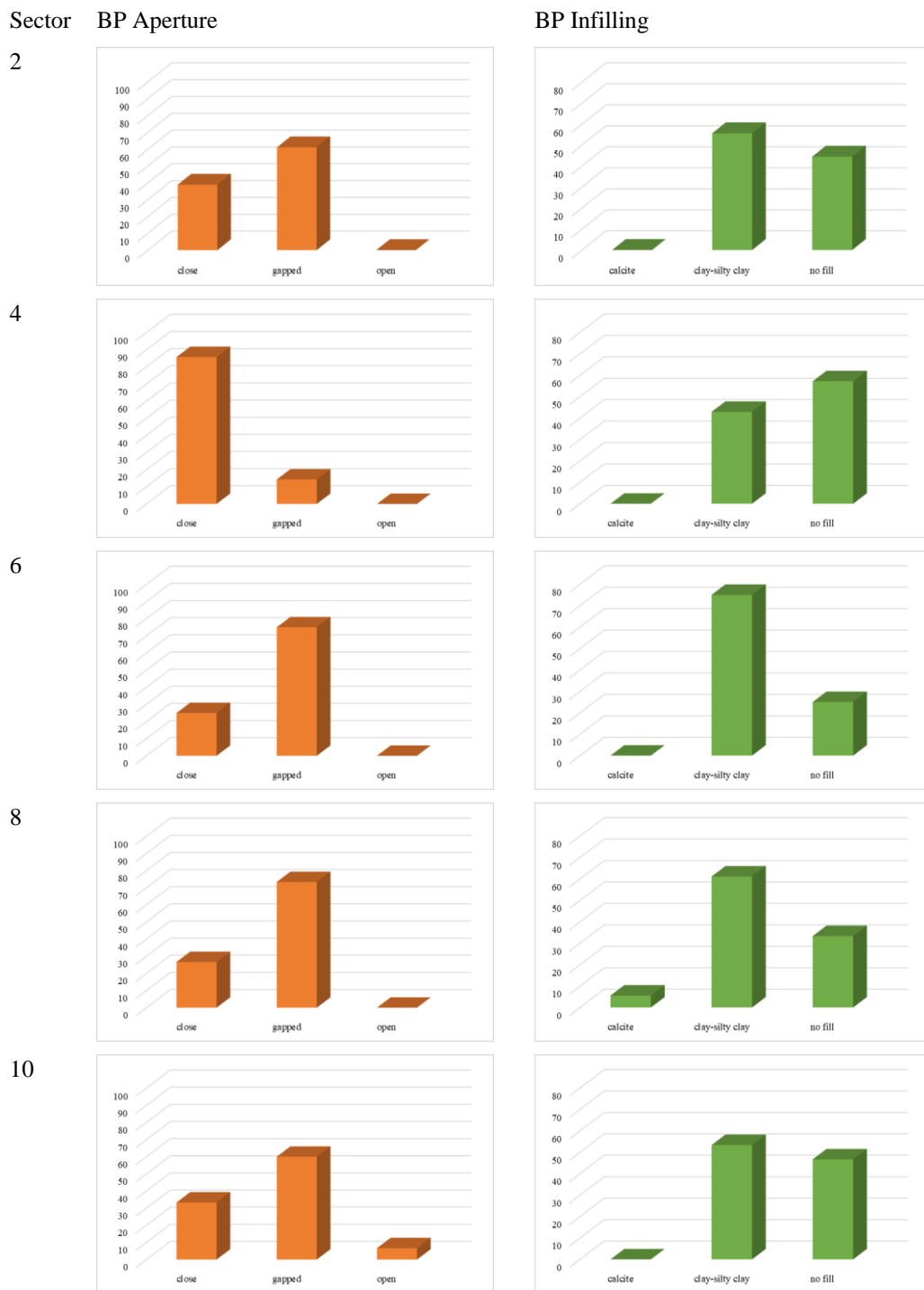
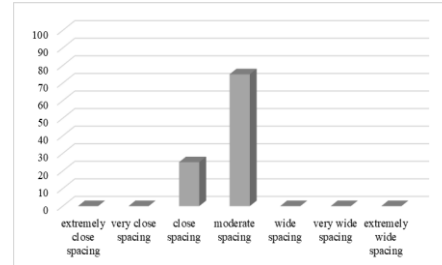
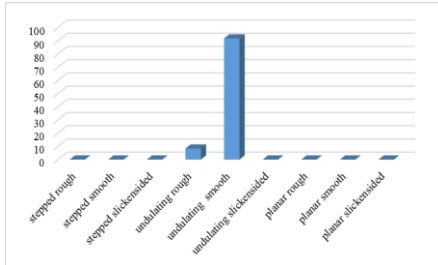


Table 4: Histograms of the Joint set 1 (J1) roughness and spacing distributions

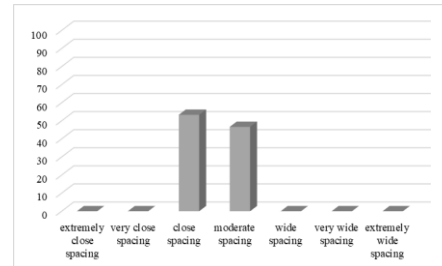
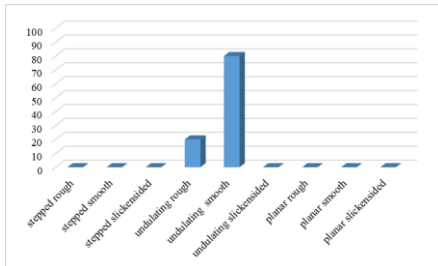
Sector J1 Roughness

J1 Spacing

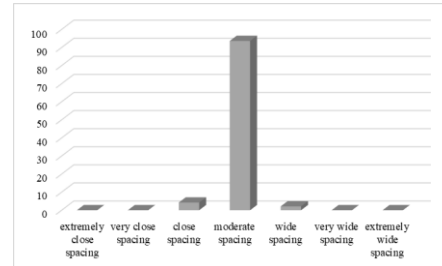
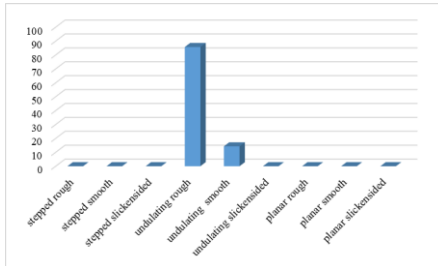
2



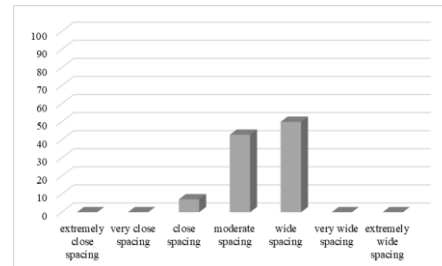
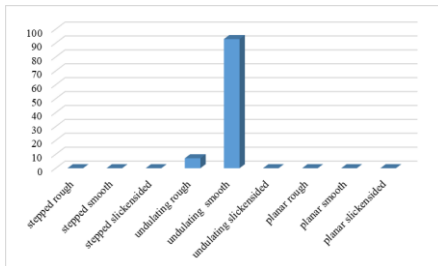
4



6



8



10

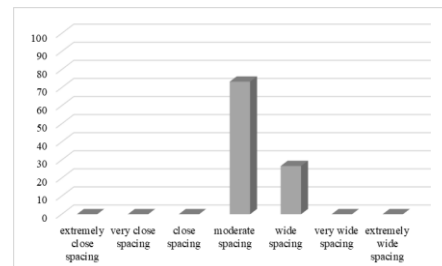
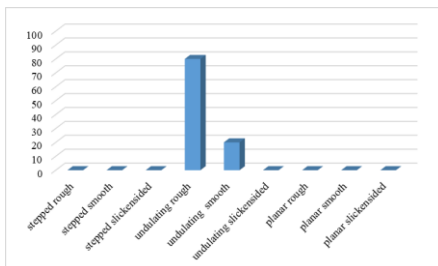


Table 5: Histograms of the Joint set 1 (J1) aperture and infilling distributions

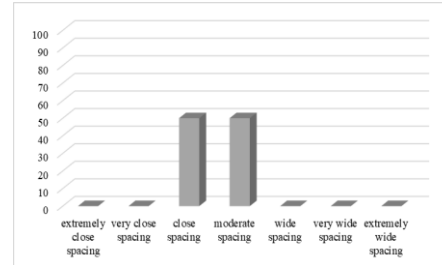
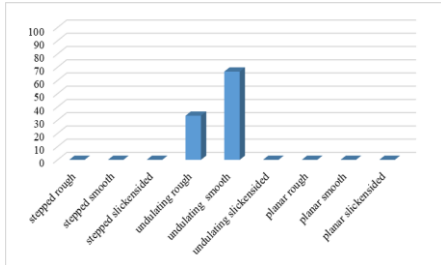


Table 6: Histograms of the Joint set 2 (J2) roughness and spacing distributions

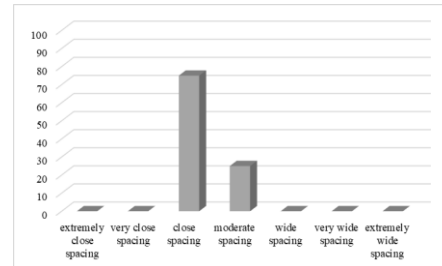
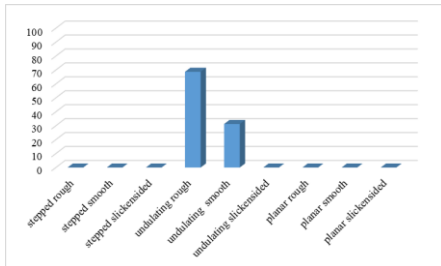
Sector J2 Roughness

J2 Spacing

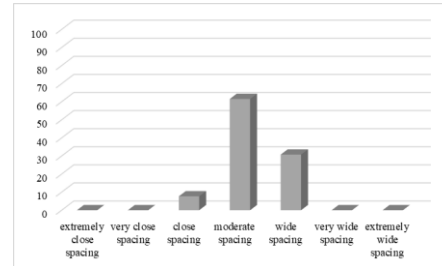
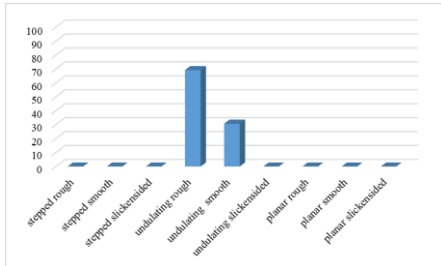
2



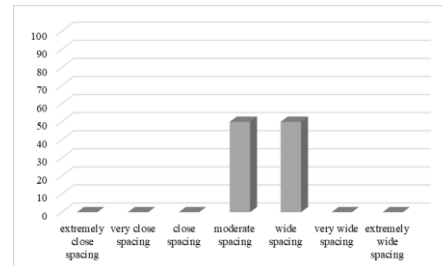
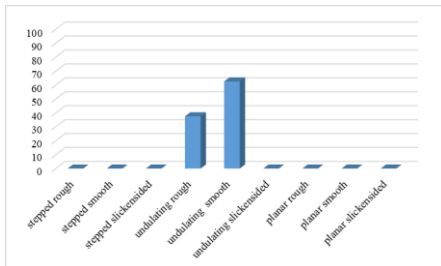
4



6



8



10

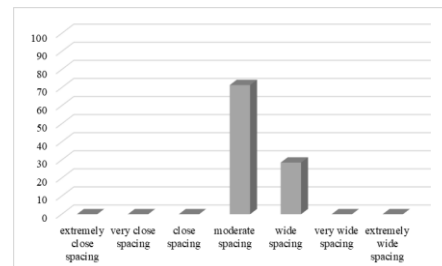
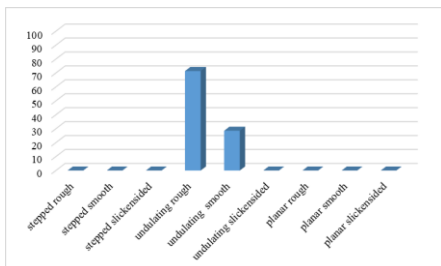
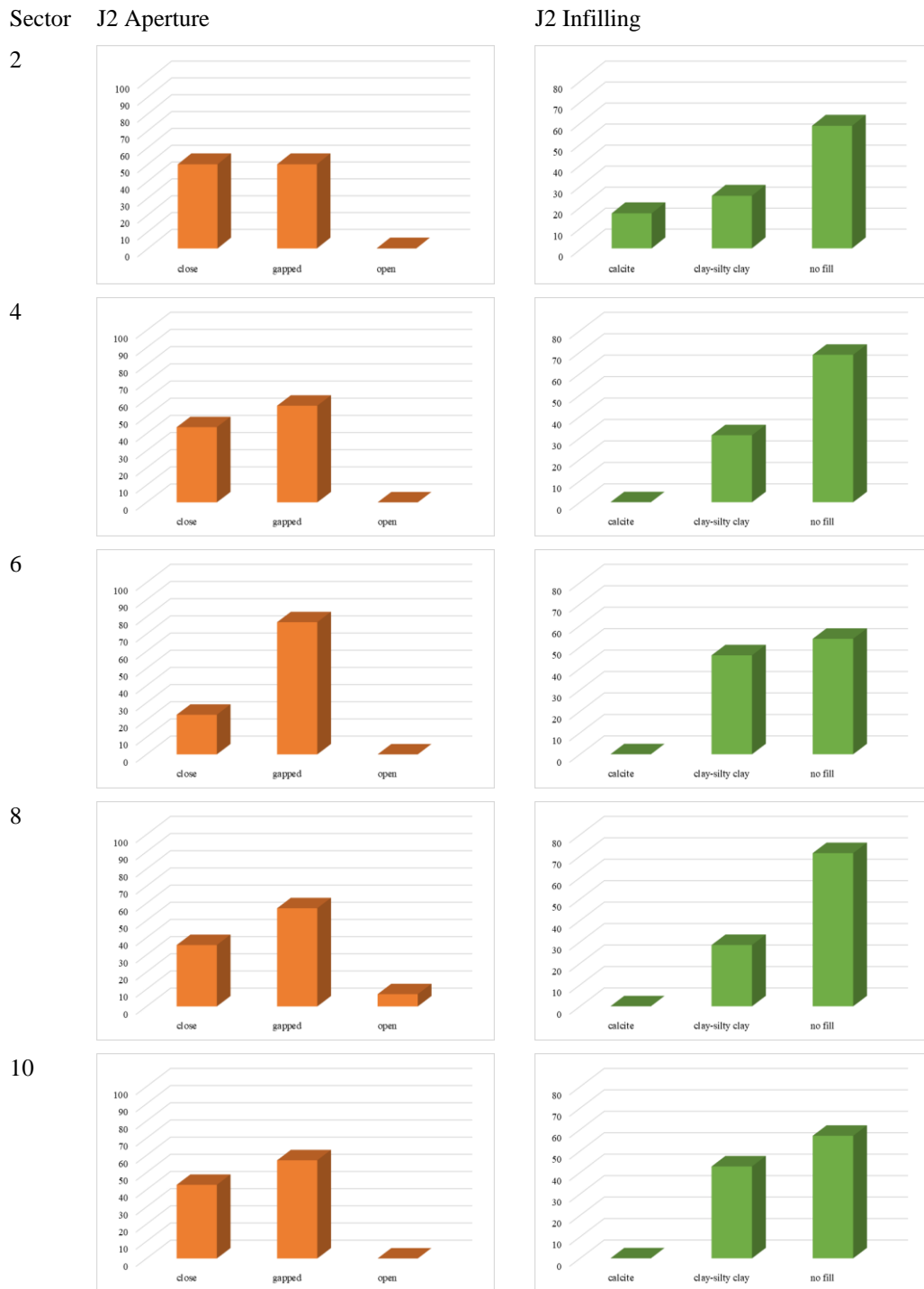


Table 7: Histograms of the Joint set 2 (J2) aperture and infilling distributions



The rock mass was characterized according to the field observations and the scan-line survey method as follows. The lithology was identified as limestone that is pinkish gray to light gray in color (Figure 17). The discontinuity orientation measurements collected by the scan-line survey revealed that there were three discontinuity sets (BP, J1, and J2). The discontinuity sets had strong to very strong strengths according to the field identification where several blows of a geological hammer were required to fracture the surfaces (ISRM, 2007). In general, the limestone was slightly weathered to moderately weathered at several locations. The discontinuity surfaces were described as undulating rough to undulating smooth, and the apertures were classified as closed in general, but there were moderately wide and open surfaces as well. Clay and silty clay infilling were observed in the apertures. The discontinuities were close to moderately spaced, in general. Persistence was high. Block sizes varied between medium to large. Water was not observed during any of the field studies conducted at different seasons of the year. However, some color changes were detected at several places. In addition, surface drainage flow through the slope face was encountered at one location (Figure 18a) in the spring season during snow melt. Hence, it is almost certain that surface drainage could affect the strength of rock masses, especially during the spring season when snow melt is encountered.



Figure 17: A close-up view of discontinuous limestone. Note the 2 m long measuring tape as a scale



Figure 18: a) The surface drainage flow observed in the spring season, b) Schmidt hammer measurement in the field

In addition to the field estimation of the discontinuity wall strength, a Schmidt hammer test was employed. To that end, Schmidt hammer rebound values were recorded in the field from the accessible locations (i.e., Sectors 2, 4, 6, 8, and 10) by an L-type hammer (Figure 18b) and the rebound values were calculated based on the recommendations of ISRM (2007). The measured and calculated Schmidt hammer rebound values are given in Table 8. In addition, the density and unit weight of the samples collected from Sectors 4, 6, and 10 are presented in Appendix C.

Table 8: Schmidt hammer rebound measurement locations and values

Sector	Discontinuity	Schmidt hammer rebound readings										Rebound value
2	Bedding plane	28	18	46	37	39	35	43	39	41	44	42.6
	Joint set 1	38	37	22	37	36	36	41	44	44	38	41.0
	Joint set 2	46	30	34	41	44	37	45	41	34	35	43.4
4	Bedding plane	19	30	42	38	42	35	46	43	37	41	42.8
	Joint set 1	20	23	38	42	37	41	40	37	44	42	41.8
	Joint set 2	35	44	36	40	43	38	46	37	45	42	44.0
6	Bedding plane	17	22	40	39	43	29	42	47	46	28	43.6
	Joint set 1	40	50	51	58	59	36	40	33	38	42	52.0
	Joint set 2	51	26	47	51	28	43	48	37	30	51	49.6
8	Bedding plane	39	38	38	33	24	36	30	48	37	44	41.4
	Joint set 1	50	55	49	52	58	53	48	40	51	58	55.2
	Joint set 2	47	46	47	45	30	50	49	42	54	53	50.6
10	Bedding plane	26	32	35	30	43	37	39	45	38	40	41.0
	Joint set 1	48	53	48	49	55	54	49	56	45	44	53.4
	Joint set 2	50	46	49	50	52	46	42	47	50	45	50.2

The mean density and mean unit weight of the limestone was measured as 2.65 g/cm^3 and 26 kN/m^3 , respectively. The uniaxial compressive strengths of the discontinuity walls of the bedding plane (BP), Joint set 1 (J1), and Joint set 2 (J2) were estimated as 100 MPa, 140 MPa, and 130 MPa, respectively (Figure 19). In addition, Point Load Strength Index (ASTM D5731-16) test was performed (Figure 20) to estimate

the Uniaxial Compressive Strength (UCS) where rock samples were available (i.e., Sector 4 and Sector 10). To that end, several empirical relations available in the literature (Table 9) utilized indicated that that these values were in good agreement with the strength estimated using the ISRM rock material strength for field identification (ISRM, 2007) for which the rock mass results have been determined to be classified as strong (Grade R4, uniaxial compressive strength = 50-100 MPa) to very strong rock (Grade R5, uniaxial compressive strength = 100-250 MPa).

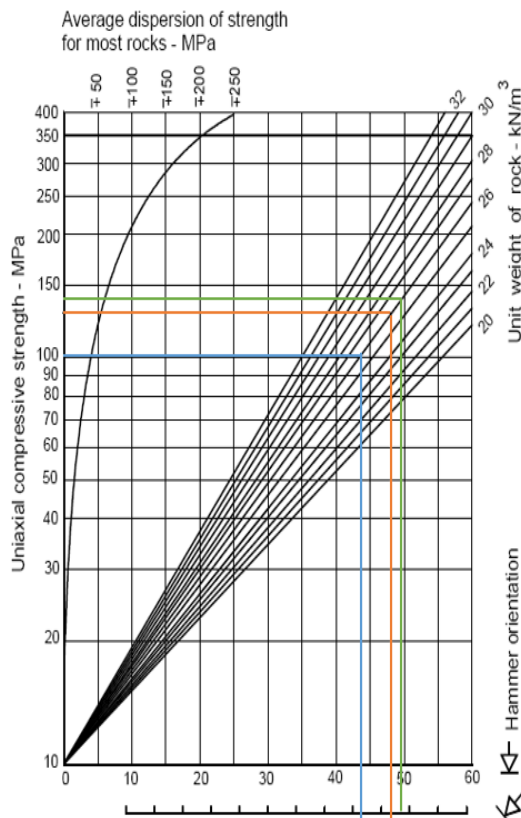


Figure 19: Discontinuity wall compressive strength estimation from Schmidt hammer hardness (Deere and Miller, 1966)



Figure 20: A view of Point Load Strength testing

Table 9: Empirical relations between the Point Load Strength Index ($I_{s(50)}$) and Uniaxial Compressive Strength (UCS)

Equation	Researcher	Estimated UCS Value (MPa)		
		Mean	Maximum	Minimum
$UCS=13.36I_{s(50)}+16.3$	D'Andrea et al. (1964)	109	189	64
$UCS=16I_{s(50)}$	Ghosh and Srivastava (1991)	97	180	49
$UCS=10.647I_{s(50)}+2.4736$	Topal (2000)	67	122	35
$UCS=11.6I_{s(50)}+22.5$	Gökçeoğlu and Zorlu (2004)	93	153	58
$UCS=10.92I_{s(50)}+24.24$	Kahraman and Günaydın (2009)	90	147	58
$UCS=16.4I_{s(50)}$	Kohno and Maeda (2012)	99	185	51
$UCS=13.36I_{s(50)}+18.66$	Kayabaşı and Gökçeoğlu (2022)	100	169	60

To investigate the durability against weakening and disintegration, Slake Durability Test (ASTM, D4644-16) was applied (Figure 21) on samples obtained from Sectors 1, 2, 4, 5, and 8 of the study area. A view of the rock samples obtained from Sectors 5 and 8 before and after the first and second cycles are given in Figure 22. The appearance of the rock samples for the rest of the sectors (i.e., Sectors 1, 2, and 4) along with a laboratory test sheet is presented in Appendix C. The Slake Durability tested samples obtained from various parts of the study area revealed that almost all of the rock samples remained virtually unchanged with a conclusion that the rock mass throughout the study area possesses a very high durability.

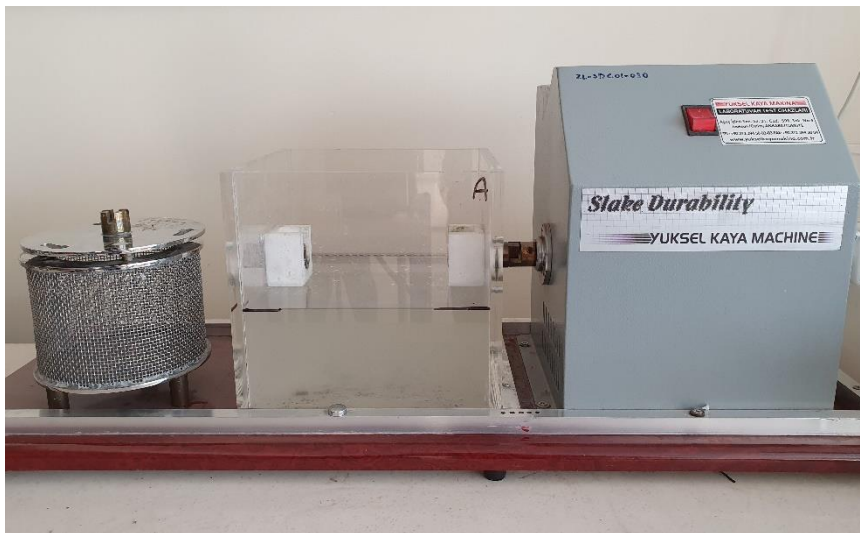


Figure 21: A view of the Slake Durability testing device

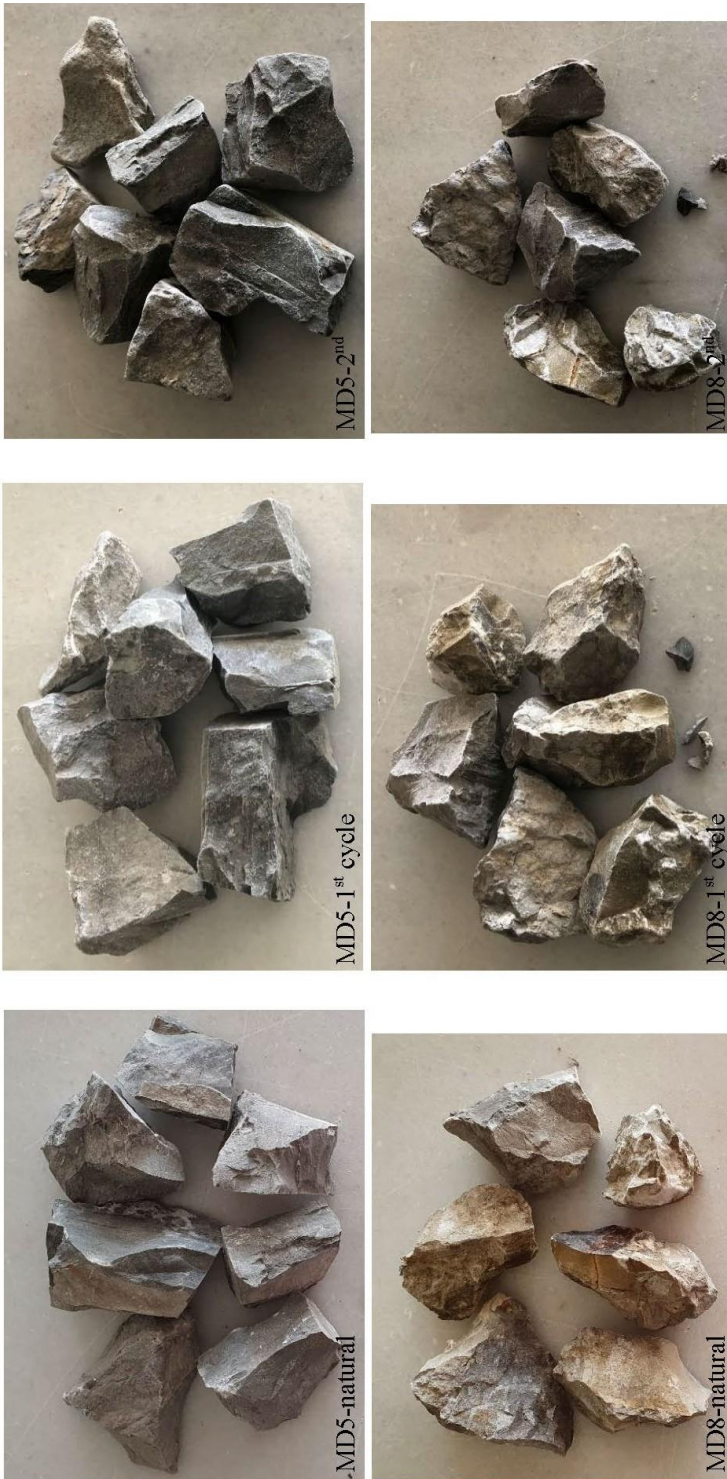


Figure 22: Slake Durability tested rock samples from Sectors 5 and 8. The first column shows a view of specimens before the test, whereas the second and third columns present the condition of the specimen following the 1st and 2nd cycles, respectively

3.2 Utilization of an Unmanned Aerial Vehicle (UAV)

Since the study area is located in a tectonically active area, the tectonic forces have led to a variation of the field stresses and have created structural features such as folds and faults. As a consequence, the bedding plane orientation has changed and two sets of systematic discontinuities have formed which implies that the rock mass properties were changed spatially. Therefore, to characterize the rock mass accurately, data gathered from each geomechanical sector needs to be reliable. Although this non-uniform nature of the rock mass requires it to be studied throughout the slope spatially, most parts of the valley, especially the higher elevations, were not possible to be investigated during the field study due to inaccessibility problems (i.e., the steep nature of the area and the rather high elevation of the valley slopes). Moreover, it was not deemed reasonable to assume that the rock mass properties were similar for the entire valley and hence, it was not fair to only evaluate the data gathered from the accessible parts since naturally, these characteristics are vital in identifying the strength, block size, failure modes, and stability. To overcome the physical limitations arising from performing the scan-line survey only at accessible locations and to overcome this bias as much as possible for rock mass characterization, an Unmanned Aerial Vehicle (UAV) was employed.

Nowadays, integration of structural analysis with remote sensing studies has become popular for rock mass characterization and many researchers have used these methods successfully in their studies (Sturzenegger and Stead, 2009; Riquelme et al., 2014; 2015; Greenwood et al. 2016; Manousakis et al., 2016; Riquelme et al., 2018; Öztürk et al., 2019; Bozkır et al., 2020; Yalçın et al., 2022). In this dissertation, a UAV was utilized to gather the characteristics of the rock mass in detail, particularly for inaccessible locations due to the steep nature of the Mudurnu valley. The UAV survey was planned by considering the weather conditions to be able to discard the effects of shadow and reflectance as much as possible. Moreover, the slope characteristics such as height, aspect, and slope degree were also considered. Instead

of placing specific targets, the structures that have already been in the area were used as ground control points. A total of 2053 images were collected by the flights of a two-day long field study in Mudurnu county center (Figures 23 and 24) that led to the generation of a high-density point cloud having 35192531 points for the western side of the valley (Figure 25). The resolution of the point cloud changes spatially as a consequence of the variations in the heights and the angles of the images taken. The overall resolution of the point cloud is 7.8 cm. The 3D point cloud was employed to obtain the orientation, spacing, and persistence of discontinuity sets by utilizing the Discontinuity Set Extractor (DSE) method (Riquelme et al., 2014). The DSE methodology is explained in the following paragraphs.



Figure 23: UAV images showing details of the rock mass at higher elevations



Figure 24: UAV images showing the general appearance of the rock mass

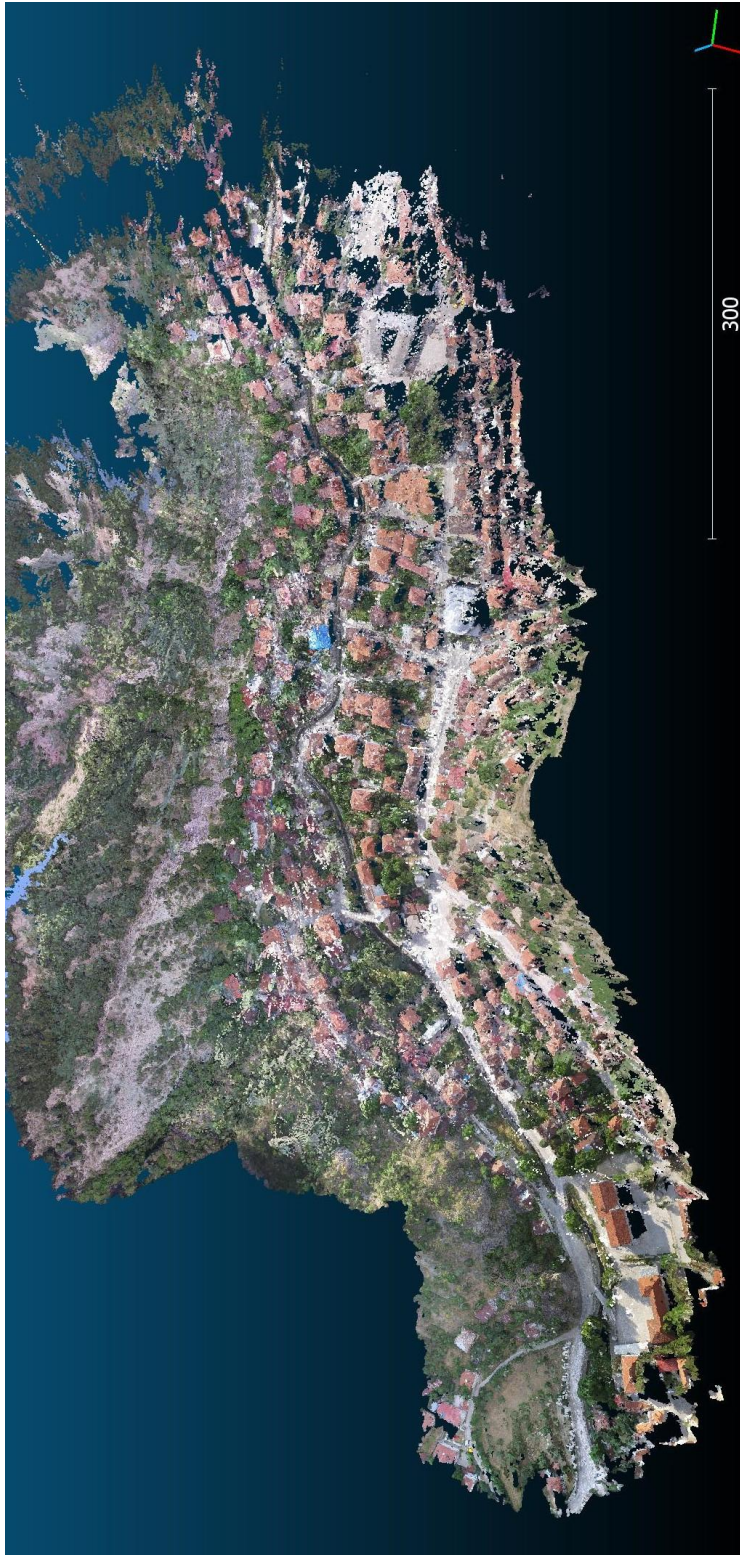


Figure 25: 3D point cloud of the Mudurnu county center

3.2.1 Discontinuity data identification from the 3D point cloud

Discontinuity Set Extractor (DSE) is a tool for the semi-automatic identification of the planar features of a rock mass through 3D point cloud data. The DSE methodology has been preferred as a tool in this dissertation study since it uses 3D data directly without applying any simplifications such as interpolated mesh surfaces. To this end, it is possible to identify local variations in slope geometry in detail which is important for the determination of the hazard potential of the rock mass. Moreover, this property makes obtaining information on non-accessible parts possible.

The DSE methodology uses raw data points (P_i) defined by X, Y, and Z coordinates and follows three main steps (Figure 26).

A-Local curvature calculation

This step calculates a normal vector for each point by the end of the three main phases.

i) Nearest neighbor searching

This phase defines a subset (Q_i) composed of K-nearest neighbors (knn) for each point. Nearest neighbors are calculated by *knnsearch* function of MATLAB and Euclidean distance where a fixed number of neighbors are considered.

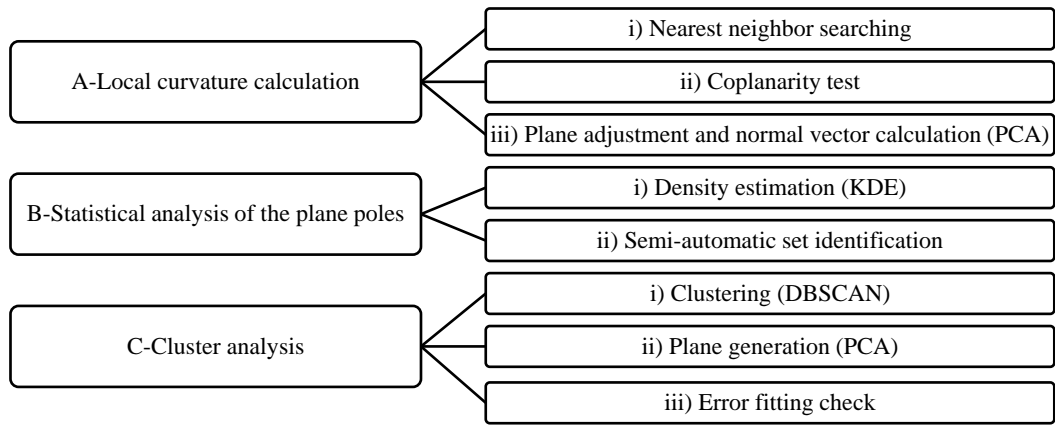


Figure 26: Flow chart of the DSE methodology (Riquelme et al., 2014)

ii) Coplanarity test

Coplanarity of subset Q_i is checked before applying normal vector calculation. Depending on the coplanarity check, the process is either continued or rejected. To check coplanarity, the method uses Principal Component Analysis (PCA) by applying the *princomp* function of MATLAB. This function determines eigenvalues and eigenvectors that will be used as an input for the calculation of the deviation parameter (η). Riquelme et al. (2014) suggest a tolerance (η_{\max}) of 20% since a set of principal components with a variance of 80% or higher represent the data properly (Rencher and Christensen, 2012). If $\eta > \eta_{\max}$ the subset is rejected.

iii) Plane adjustment and normal vector calculation

This phase is to set plane adjustments and to calculate its normal vector. The equation of a plane is given by Equation (1)

$$Ax+By+Cz+D=0 \quad [A,B,C,D] \in \mathbb{R} \quad (1)$$

where A, B, C are the unit normal vector components and D is the distance parameter measured perpendicular to the origin of the plane.

B-Statistical analysis of the planes

This step is composed of two phases and uses a stereographic projection of poles of planes to perform statistical analysis to identify the main discontinuity sets.

i) Density estimation

This phase is applied to calculate the densities of poles. For this purpose, Kernel Density Estimation (KDE), which is a non-parametric way of estimating the Probability Density Function (PDF) of a random variable, is used. The density estimation is applied by *kde* function of MATLAB.

ii) Semi-automatic set identification

In this phase, a principal orientation is assigned to every point. To define principal poles the method uses two different limiting parameters to get rid of reading errors and singular points: 1) cone filter (defines the minimum angle between two principal vectors), 2) the maximum number of poles filter (defines the maximum number of discontinuity sets). After these two filters are applied, the point cloud is segmented. In this step, principal families are checked by a defined minimum angle between the associated normal vector and the assigned principal plane normal vector. By this step, points having a different orientation to any principal pole are discarded.

C-Cluster analysis

In this step, discontinuity sets are assigned to subsets (R_i) of sets grouped by planar clusters. The Cluster analysis has three phases:

i) Clustering

This phase is applied to calculate spatial clusters for each discontinuity set. For the clustering, the Density-Based Scan Algorithm with Noise (DBSCAN) that needs two input parameters is employed. The input parameters are the maximum distance between neighbors and the minimum number of neighbor points to be considered.

ii) Plane generation

Plane equations are calculated by finding the best-fit plane of a set of points belonging to an identified cluster in the previous phase. Principal vectors are obtained by applying PCA and the values of A, B, and C are calculated. The parameter D is computed by the least-squares method.

iii) Error fitting check

After the definition of the plane equation, the quality of data fitting should be checked. The calculated error needs to be minimum and its standard deviation should be low.

Once the discontinuity sets are defined and the points are classified, this information can be used to obtain the spacing, persistence, and roughness. The DSE calculates the normal spacing between an exposed plane and a plane closest to it considering 3D relationships. The methodology computes spacing for both persistent and non-persistent discontinuities (Riquelme et al., 2015). Bedding planes tend to be fully persistent. In this dissertation, the bedding plane and the joint sets have been accepted to be persistent. ISRM (2007) defines spacing as mean fracture spacing between adjacent discontinuities that cut a traverse line of known length. However, Palmstorm (2001) states spacing as the minimum or normal distance between discontinuities within a set measured along an orthogonal scan-line. Measuring the normal spacing in field conditions may not be always possible or may only apply to a limited portion of the rock mass. This methodology uses 3D relationships between clusters to calculate the spacing by using orthogonal distance. Hence, the results obtained are expected to be more reliable compared to the field measurements.

This method uses a previously classified point cloud into discontinuity sets and clusters of the same discontinuity plane as an input. For this dissertation, DSE, which was used to reach discontinuity set orientations, has also been utilized for the classification of input data for every point. Required input data for the methodology are coordinates (X, Y, and Z), discontinuity set id, cluster id, the normal vector of the discontinuity set (A, B, C from Equation 1), the normal vector of the cluster (A, B, C from Equation 1) and plane position (D from Equation 1) of the cluster. Analytically, sets of points belonging to the same discontinuity plane have the same normal vector defined by A; B, C and varying plane positions represented by parameter D. At first, the distances of all points in every cluster are calculated and the distribution of distances having a mean value and standard deviation is obtained. Note that the density functions of different clusters are expected to have a major overlap when they belong to the same plane. To define the threshold value of the overlapping between two density functions, segments centered at their mean value with lengths of 2k times the standard deviation is computed for each cluster. Then, they are considered as the members of the same plane if segments $(\mu) \pm (k\sigma)$ of both distributions intersect. Hence, no spacing calculations are followed between the clusters belonging to the same plane. This is checked by Equation 2 which defines the condition when clusters are parts of the same plane. Otherwise, the spacing will be calculated between the clusters of different planes. Finally, an adjustment is applied once the clusters are determined to belong to the same plane. This adjustment re-defines the value of the D_b parameter as D_a .

$$k(\sigma_a + \sigma_b) \geq |D_a - D_b| \quad (2)$$

where σ_a =standard deviation of cluster a, σ_b = standard deviation of cluster b, D_a =position parameter of cluster a, D_b = position parameter of cluster b, k =parameter that controls how close two distributions must be to be considered as the same cluster.

After the spacing values are calculated, the non-parametric distribution is applied by the KDE technique. Min, max, mode, mean, maximum density value, and standard deviation are computed by statistical analysis. The normal spacing is calculated as the mean of the calculated distances.

For the persistence, the method uses a previously analyzed point cloud similar to the spacing methodology. This means that coordinates, discontinuity sets, clusters, and plane equations of clusters (Equation 1) are known for each point. Prior to persistence calculation, the coplanarity test is applied for clusters. Two planes are assumed to be coplanar when Equation 2 is satisfied and concluded that these clusters belong to the same discontinuity plane (Riquelme et al., 2015). At this stage, the D parameter of the cluster is modified and clusters are merged. After that, persistence measurement started with applying the transformation matrix given in Equation 3 (Riquelme et al., 2018).

$$R = \begin{bmatrix} \cos(\beta) \sin(\alpha) & -\cos(\alpha) & \sin(\beta) \sin(\alpha) \\ \cos(\beta) \cos(\alpha) & \sin(\alpha) & \sin(\beta) \cos(\alpha) \\ -\sin(\beta) & 0 & \cos(\beta) \end{bmatrix} \quad (3)$$

where β =dip angle and α =dip direction angle of the corresponding discontinuity set

Figure 27 shows the scheme of the transformation by which discontinuity persistence is measured in strike and dip orientations as suggested by ISRM (2007). Coordinates are transformed from OXYZ to O'X'Y'Z'. The persistence is extracted in the O'X direction for the dip and in the O'Y direction for the strike where these lengths are calculated by Equations 4 and 5.

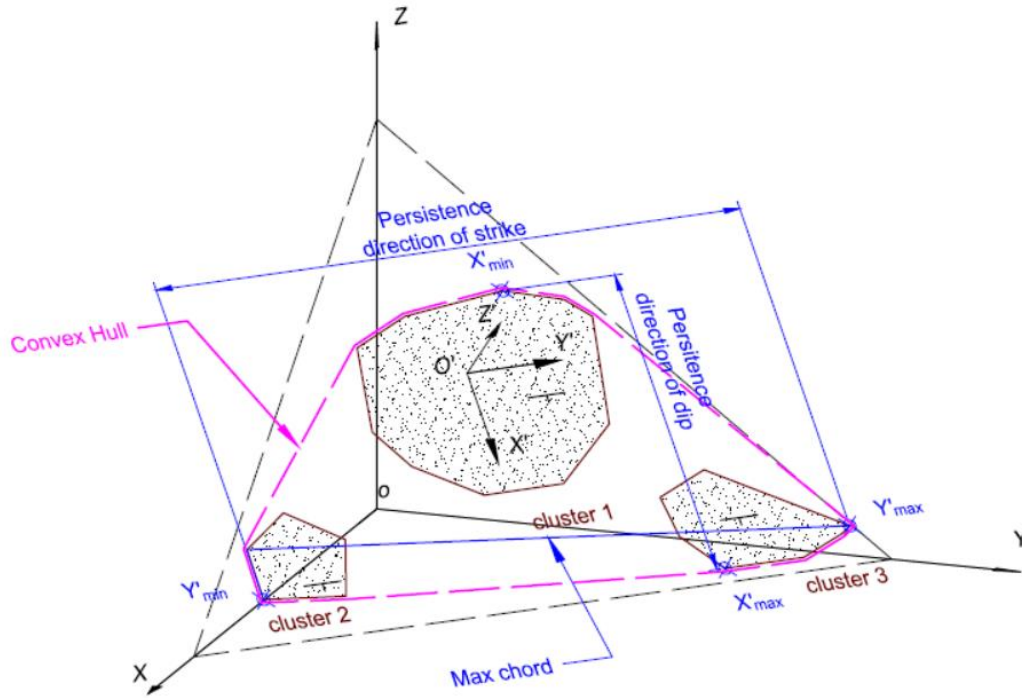


Figure 27: Perspective of 3D point cloud for three coplanar clusters and the convex hull extracted (Riquelme et al., 2018)

$$\text{Length-Persistence}_{\text{dip}}(i,j)=\max(x'(i,j))-\min(x'(i,j)) \quad (4)$$

$$\text{Length-Persistence}_{\text{strike}}(i,j)=\max(y'(i,j))-\min(y'(i,j)) \quad (5)$$

where $x'(i,j)$ and $y'(i,j)$ are the local coordinates of $X(i,j)$.

In addition, the area of the cluster is estimated by computing the convex hull ($\text{Ch}(X(i,j))$). The equation for the maximum length calculation is given by Equation 6 and the area estimation is given by Equation 7. To calculate the convex hull, cluster points are projected to the $O'X'Y'$ plane and then *convhull* function of MATLAB is applied.

$$\text{Length-Persistence}_{\max}(i,j)=\max \text{ length}(C_h(X(i,j))) \quad (6)$$

$$\text{Area-Persistence}(i,j)=\text{Area}(C_h(X(i,j))) \quad (7)$$

Note that, this method accepts intermittent discontinuities as a single persistent discontinuity, which results in higher persistence values and makes this method more conservative (Mauldon, 1994).

3.3 Definition and delineation of the geomechanical sectors

Remote sensing technologies have been utilized by many researchers for rock slope studies. These techniques are useful for obtaining accurate and dense information from a 3D point cloud. Although usage of remote sensing techniques enables the collection of information from a wider area, it is limited to the resolution of the image. It is possible to identify small discontinuities by high-resolution images but the small features may not be distinguished by the usage of low-resolution images (Sturzenegger and Stead 2009; Tuckey and Stead 2016). That is why methods applied should be used with caution and capabilities and limitations should be discussed. In this dissertation, at first, the data was gathered from the point cloud on the parts that had been studied in the field. Then, the gathered data were controlled and validated with field observations. Since the data gathered from the point cloud and the data collected from the field were comparable, the 3D analysis method was applied to the entire valley.

By gathering and combining all the available data (i.e., the geological and geomechanical rock mass properties, scan-line survey measurements, photos taken during field studies, UAV images collected, and 3D point cloud), the western side of the valley was divided into 11 sectors that had similar geomechanical properties. For the delineation, varying slope face orientations were determined through the valley. Then, the identified faces were subdivided into parts according to the characteristics of the discontinuity sets where necessary followed by defining the sectors. The sectors were numbered from south to north in ascending order as shown in Figure 28.

After the identification of the sectors, the discontinuity characteristics were gathered from the point cloud per sector. For the detection of discontinuity set orientations, the Discontinuity Set Extractor (DSE) method was utilized (Riquelme et al., 2014), as explained in Chapter 3.2.1. Afterwards, the results were compared with the field survey measurements. All the sectors were not physically accessible due to the steep nature of the slopes in the area; however, the DSE results were validated with data collected from Sectors 2, 4, 6, 8, and 10. The results obtained with DSE were comparable with those from the field observations. Thus, DSE results were accepted as reliable, and DSE was utilized to extract the discontinuity orientations of the inaccessible sectors. Discontinuity sets identified using DSE are given in Figures 29 through 35. In these figures, each set is represented by a different color. Table 10 gives the discontinuity orientations obtained from the field survey and the DSE method.

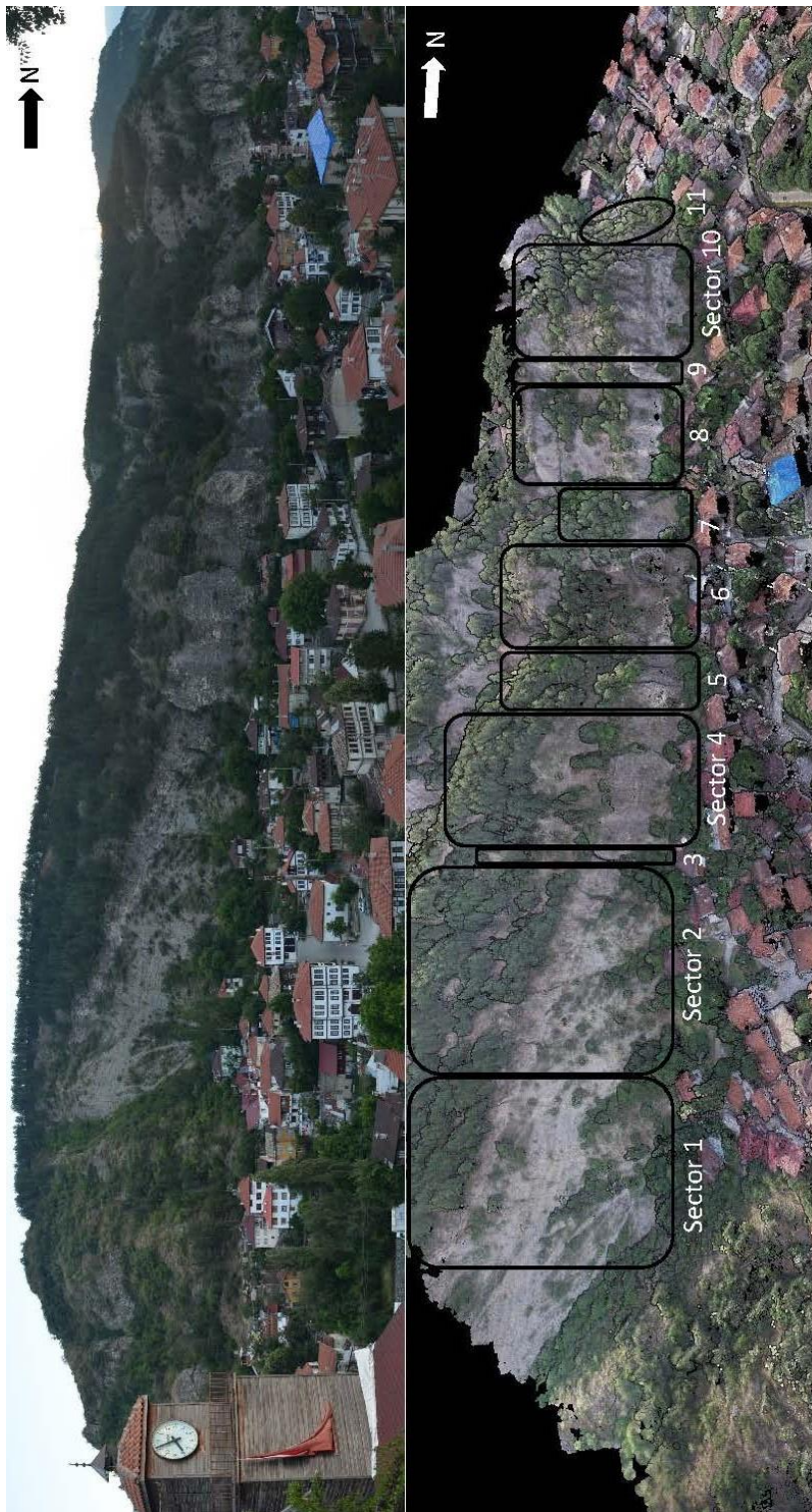


Figure 28: Delineated sectors defined as a result of a detailed evaluation of the rock mass characteristics

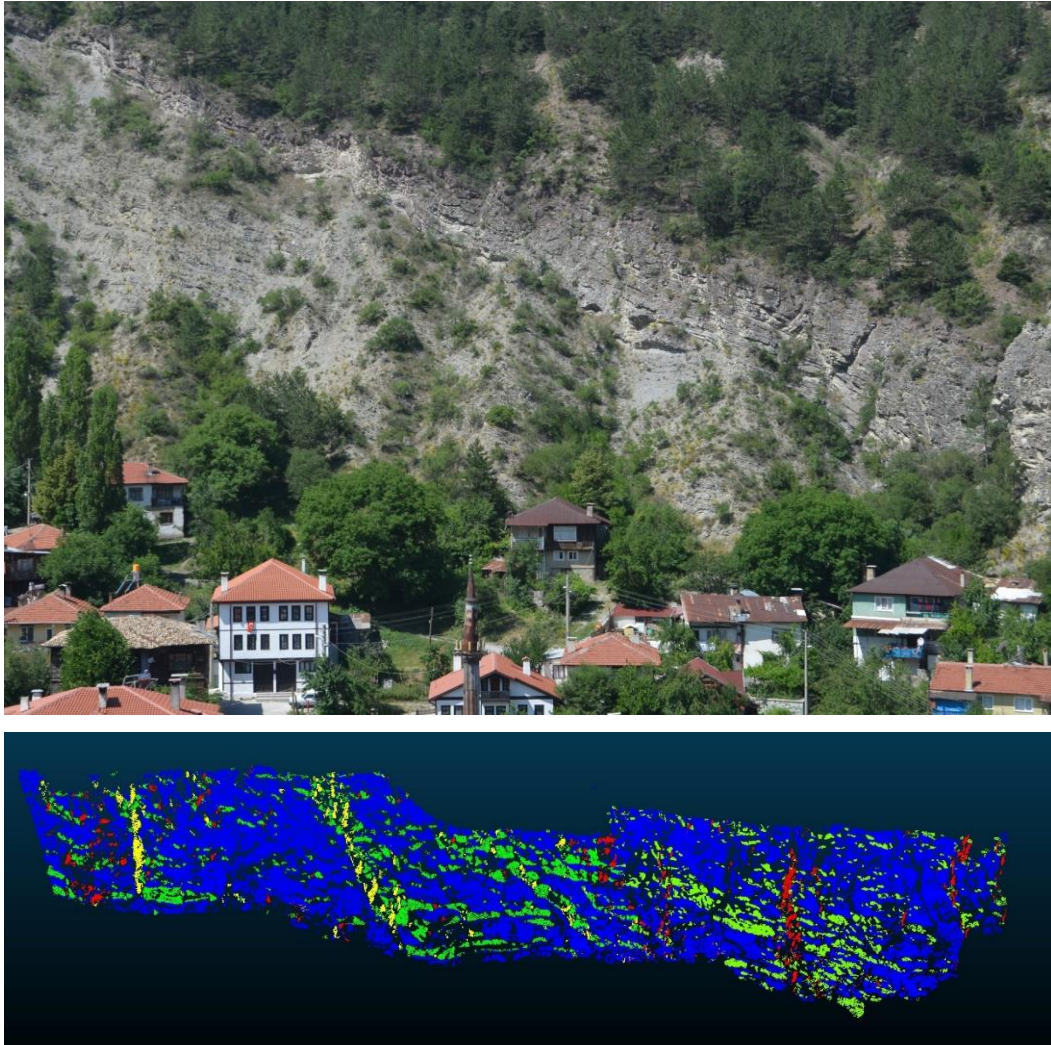


Figure 29: A view of Sectors 1 and 2 and the discontinuity sets identified by utilizing DSE

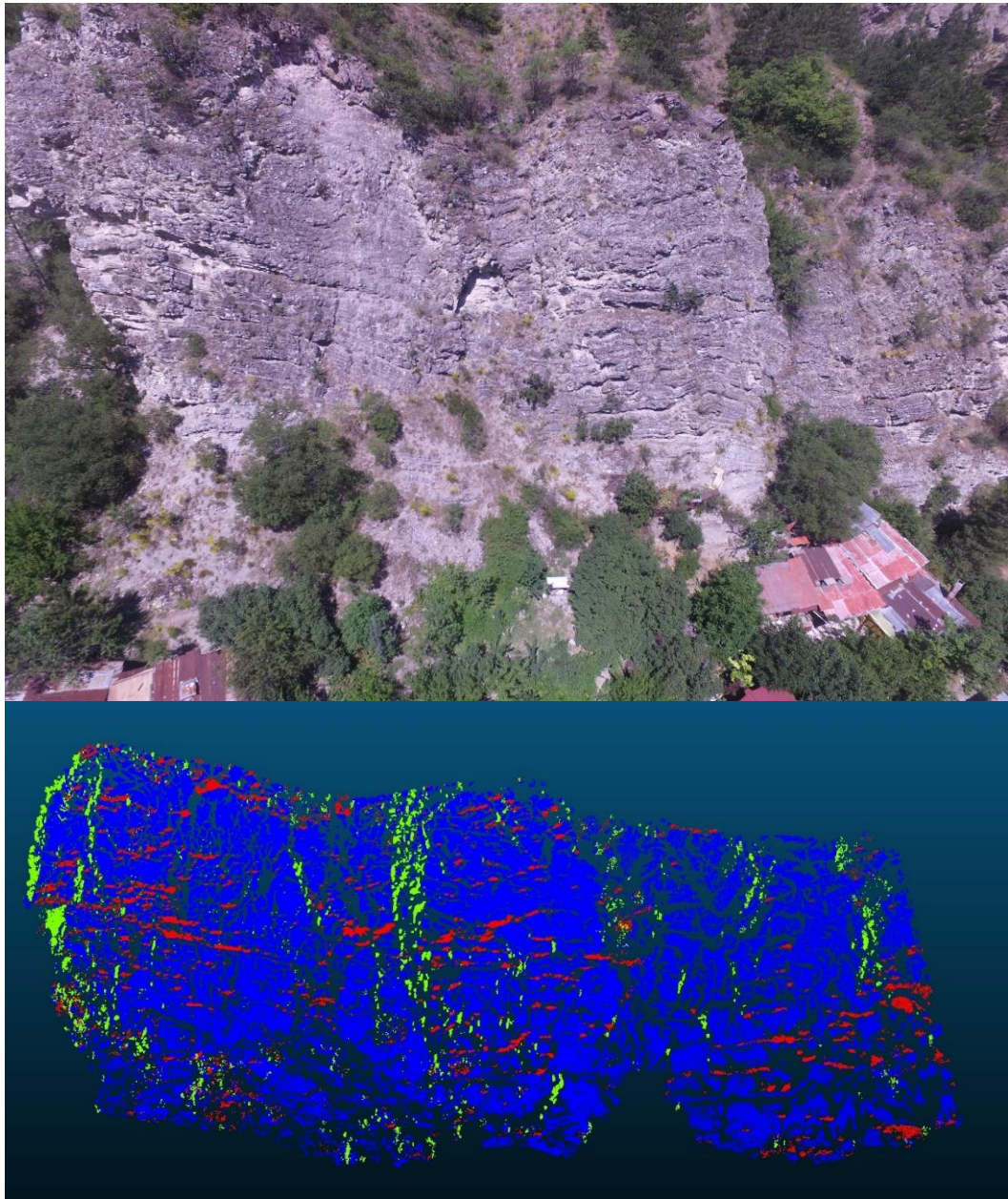


Figure 30: A view of Sectors 3 and 4 and the discontinuity sets identified by utilizing DSE

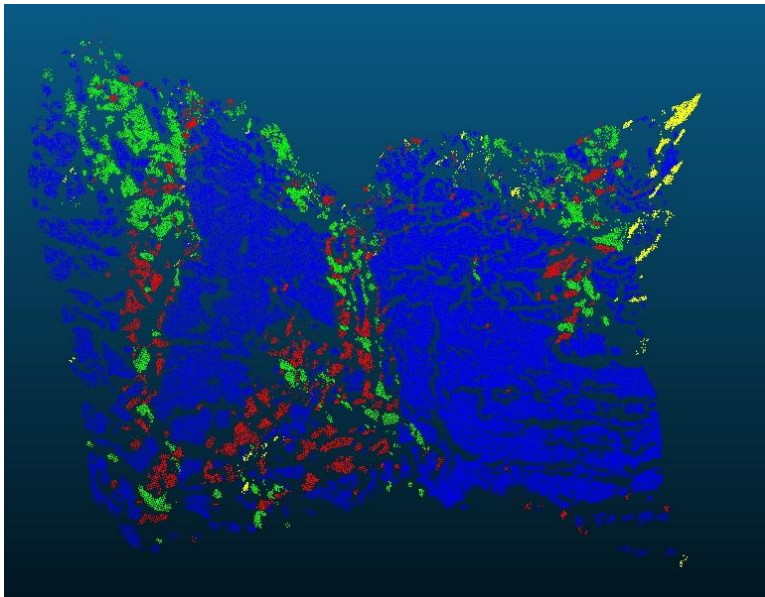


Figure 31: A view of Sectors 5 and 6 and the discontinuity sets identified by utilizing DSE

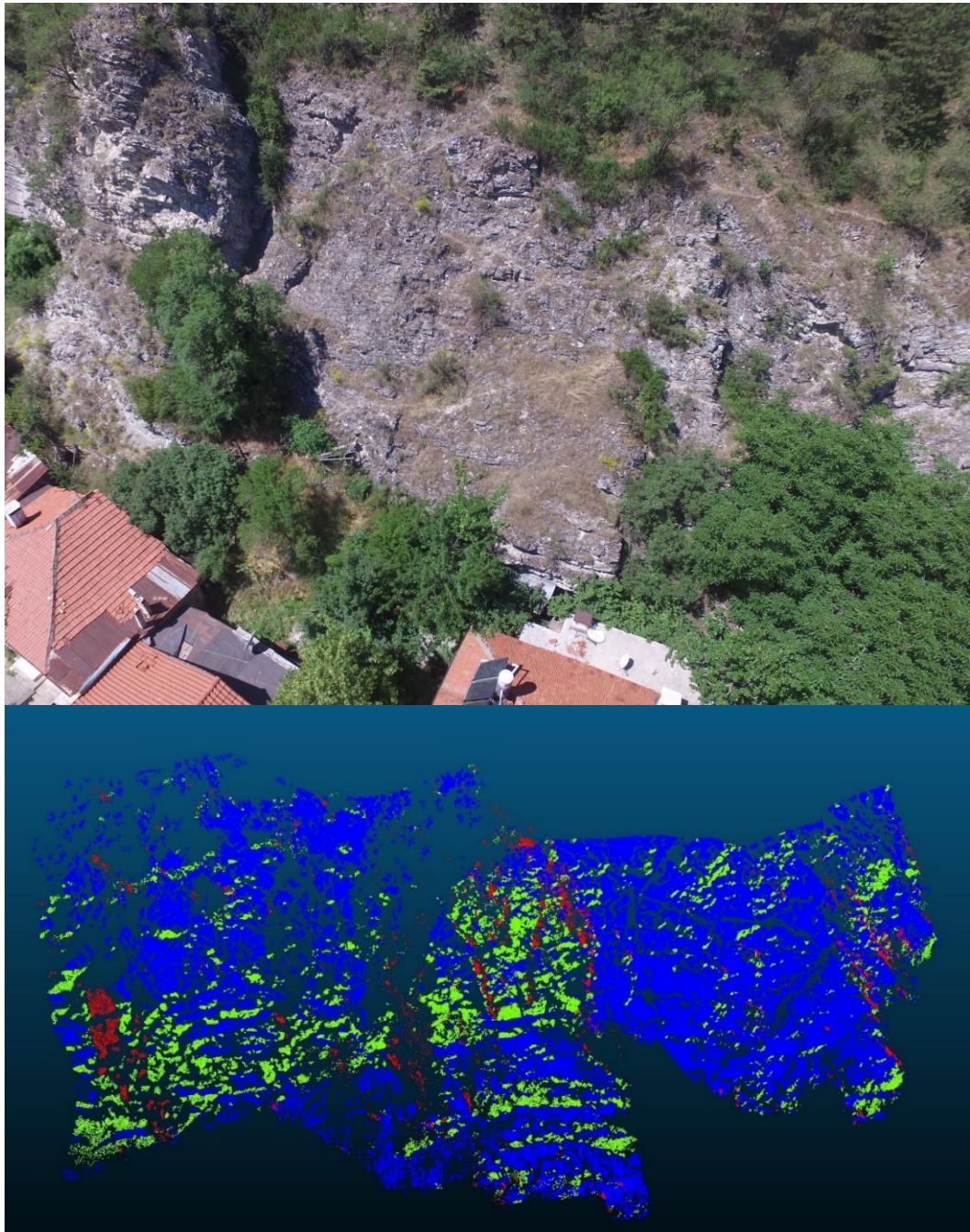


Figure 32: A view of Sectors 6 and 7 and the discontinuity sets identified by utilizing DSE

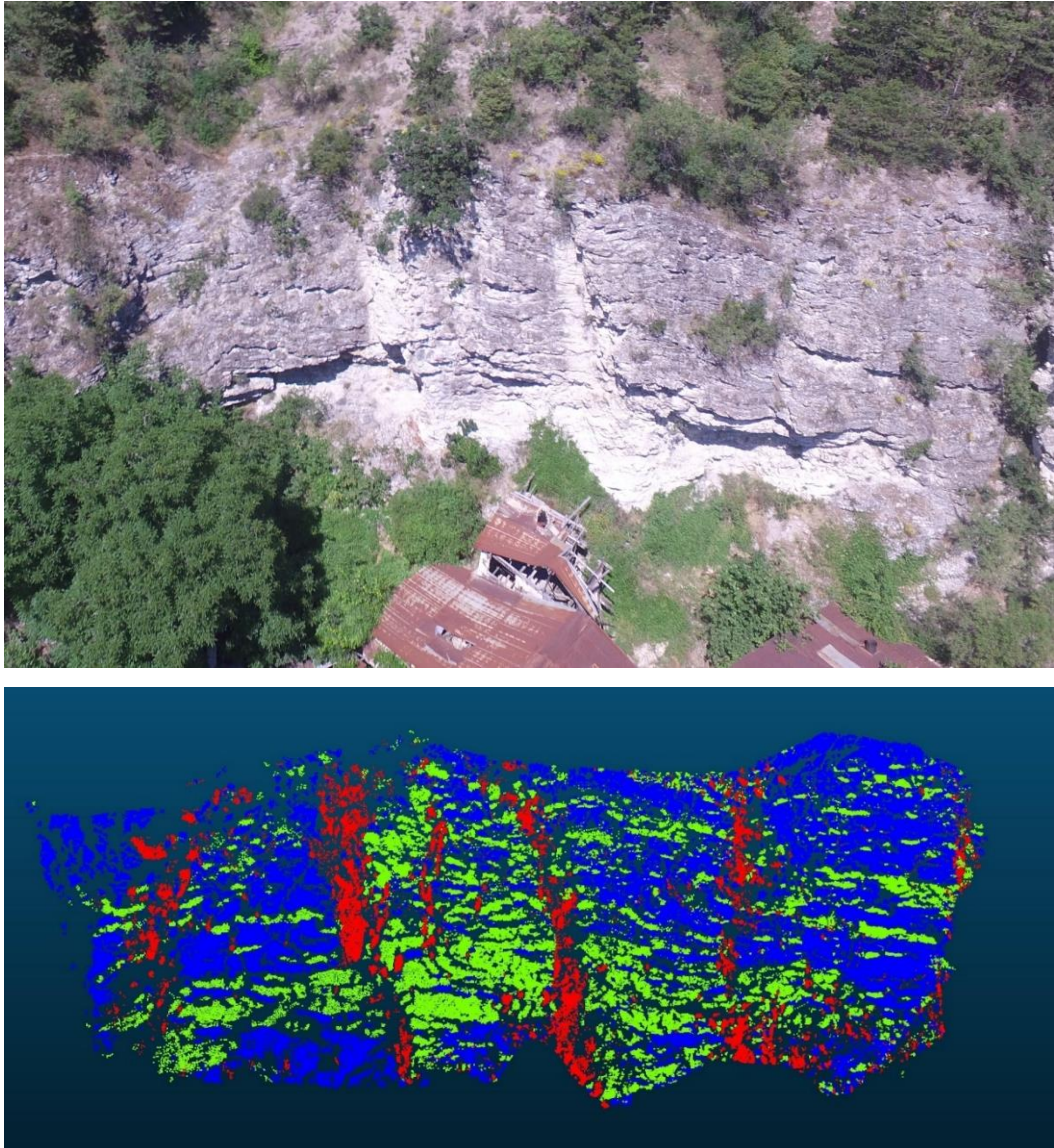


Figure 33: A view of Sector 8 and the discontinuity sets identified by utilizing DSE

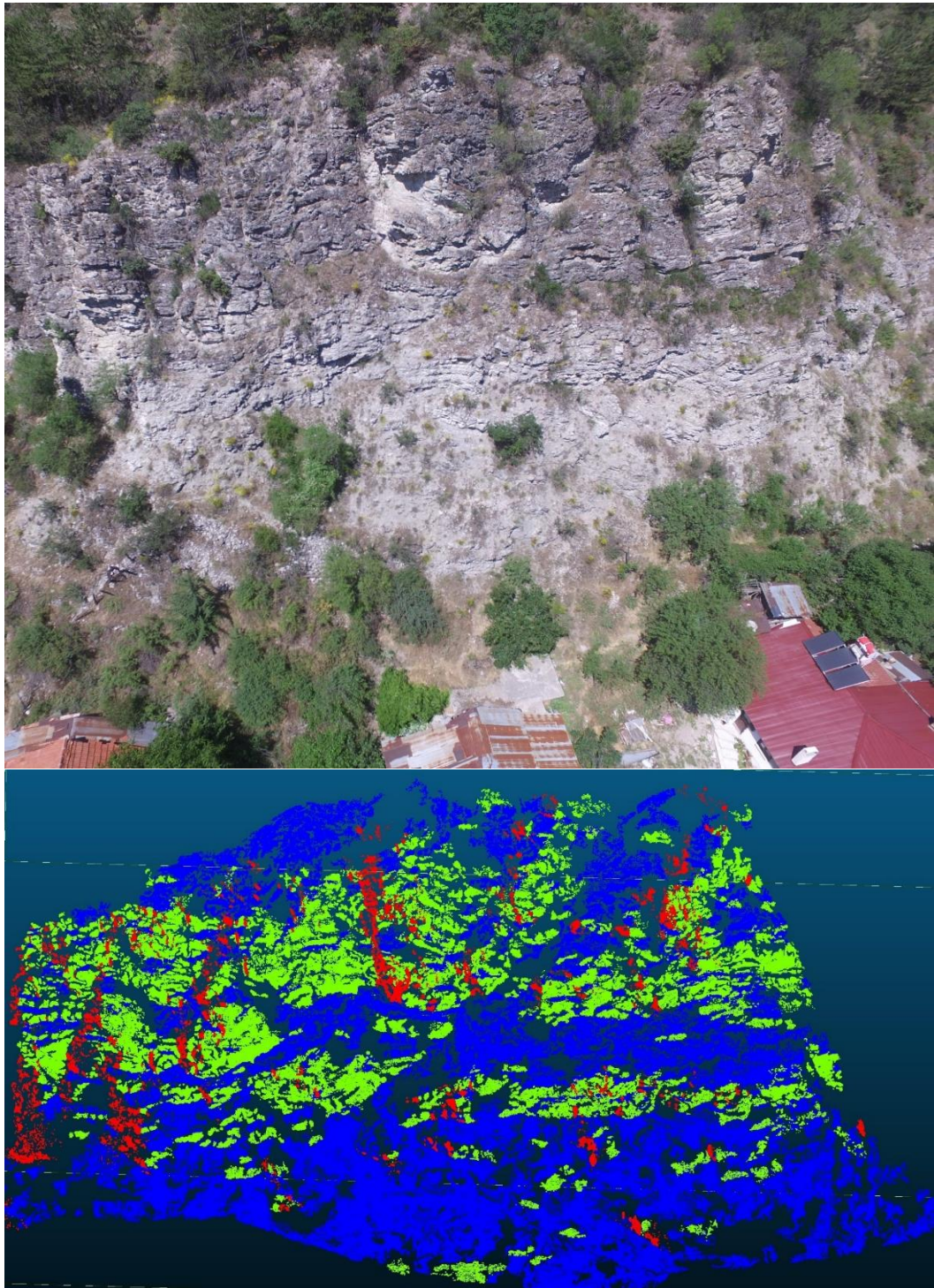


Figure 34: A view of Sectors 9 and 10 and the discontinuity sets identified by utilizing DSE

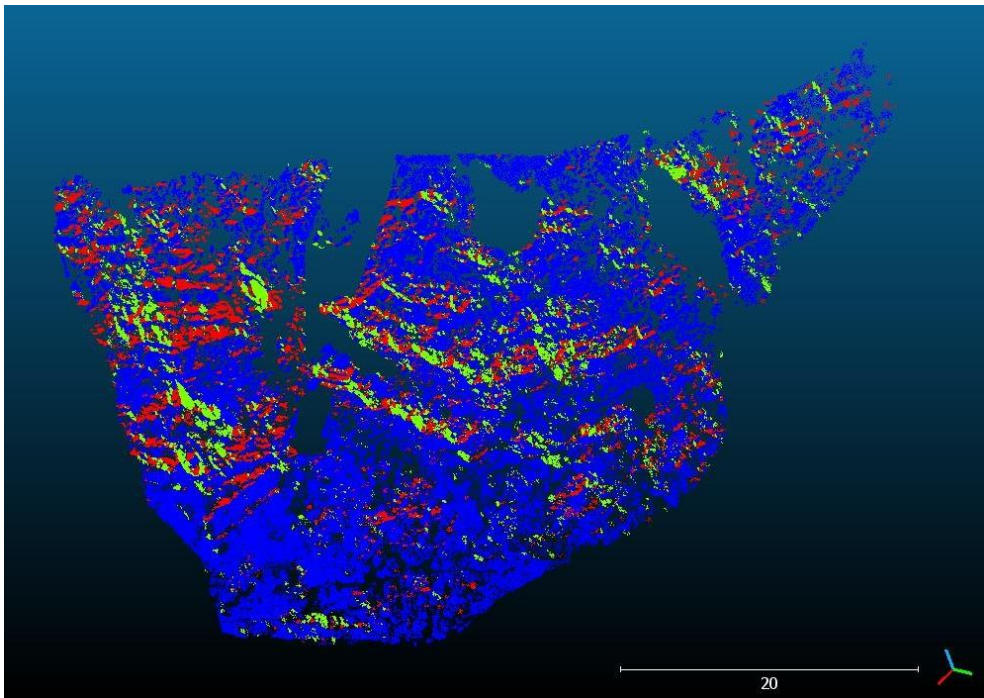


Figure 35: A view of Sector 11 and the discontinuity sets identified by utilizing DSE

Table 10: Discontinuity orientations measured by scan-line survey and calculated from the point cloud

Sector	Discontinuity Dip (Scan-line survey)			Discontinuity Dip (3D Point Cloud)			Discontinuity Dip Direction (Scan-line survey)			Discontinuity Dip Direction (3D Point Cloud)					
	Dip	Dip	Direction	BP	J1	J2	BP	J1	J2	BP	J1	J2	BP	J1	J2
1	66	084					56	81	68				259	108	156
2	76	105		43	78	77	52	74	58	273	089	179	260	098	176
3	84	235					56	68	67				271	083	167
4	72	096		43	67	66	56	68	67	263	078	168	271	083	167
5	76	064					61	55	56				255	084	178
6	78	092		44	68	82	55	76	78	268	083	136	272	091	153
7	48	070					46	84	63				256	058	156
8	80	104		36	65	83	44	79	80	234	070	152	255	083	141
9	85	185					38	78	85				268	75	145
10	80	075		37	81	77	42	78	85	229	069	157	250	75	145
11	75	045					45	78	88				225	51	166

The DSE results are accepted as reliable based on the comparison of results with the field measurements. For the sake of identifying discontinuity characteristics in a wider area, including the physically inaccessible locations, a 3D point cloud was employed and the DSE methodology was applied. The distributions of normal spacing and persistence of the discontinuity sets were obtained by the DSE methodology for each sector. The distributions of normal spacing of BP, J1 and J2 are presented in Figures 36, 37, and 38, respectively. Also, the distributions of persistence of BP, J1 and J2 are presented in Figures 39, 40, and 41, respectively.

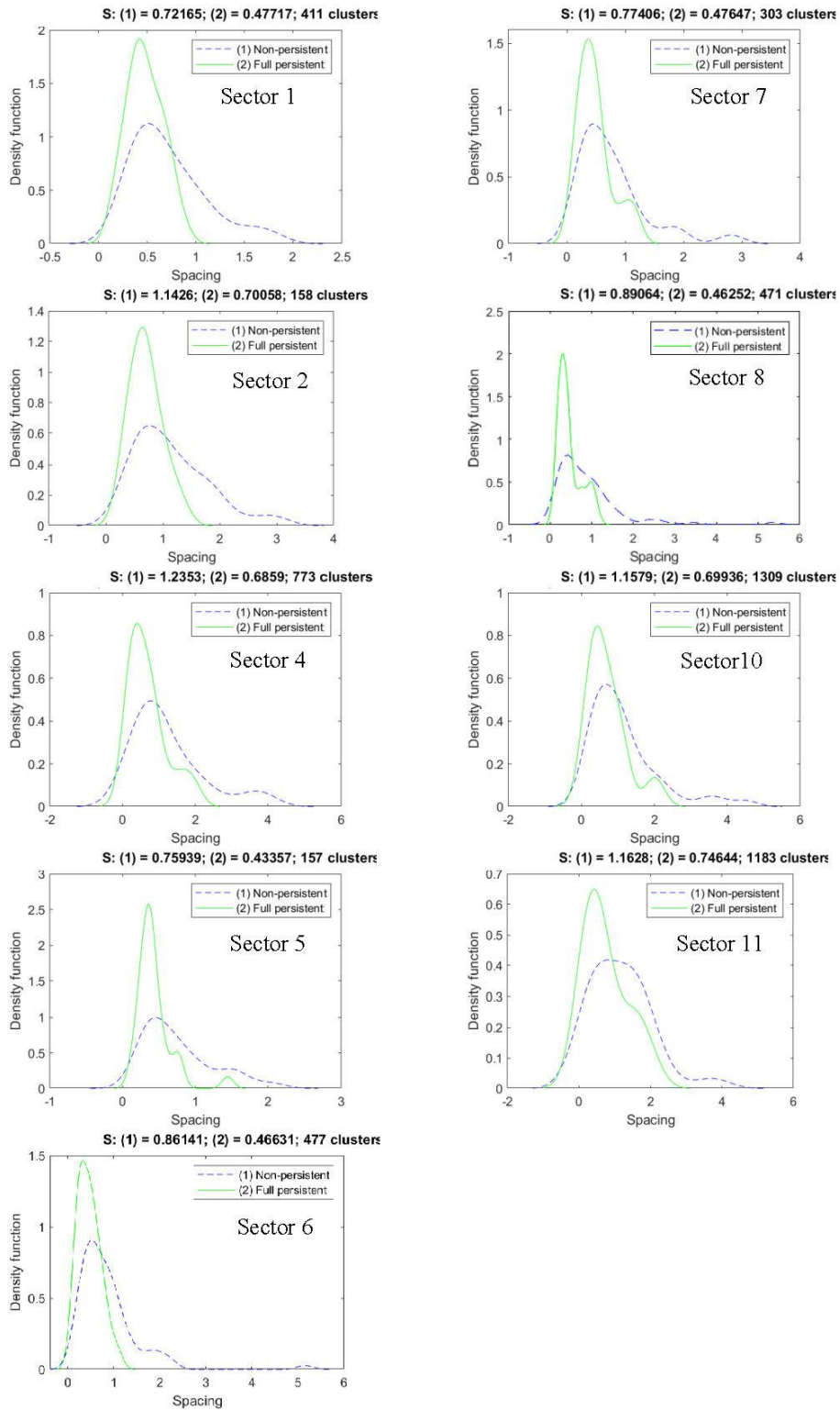


Figure 36: The distribution of bedding plane spacing for each sector

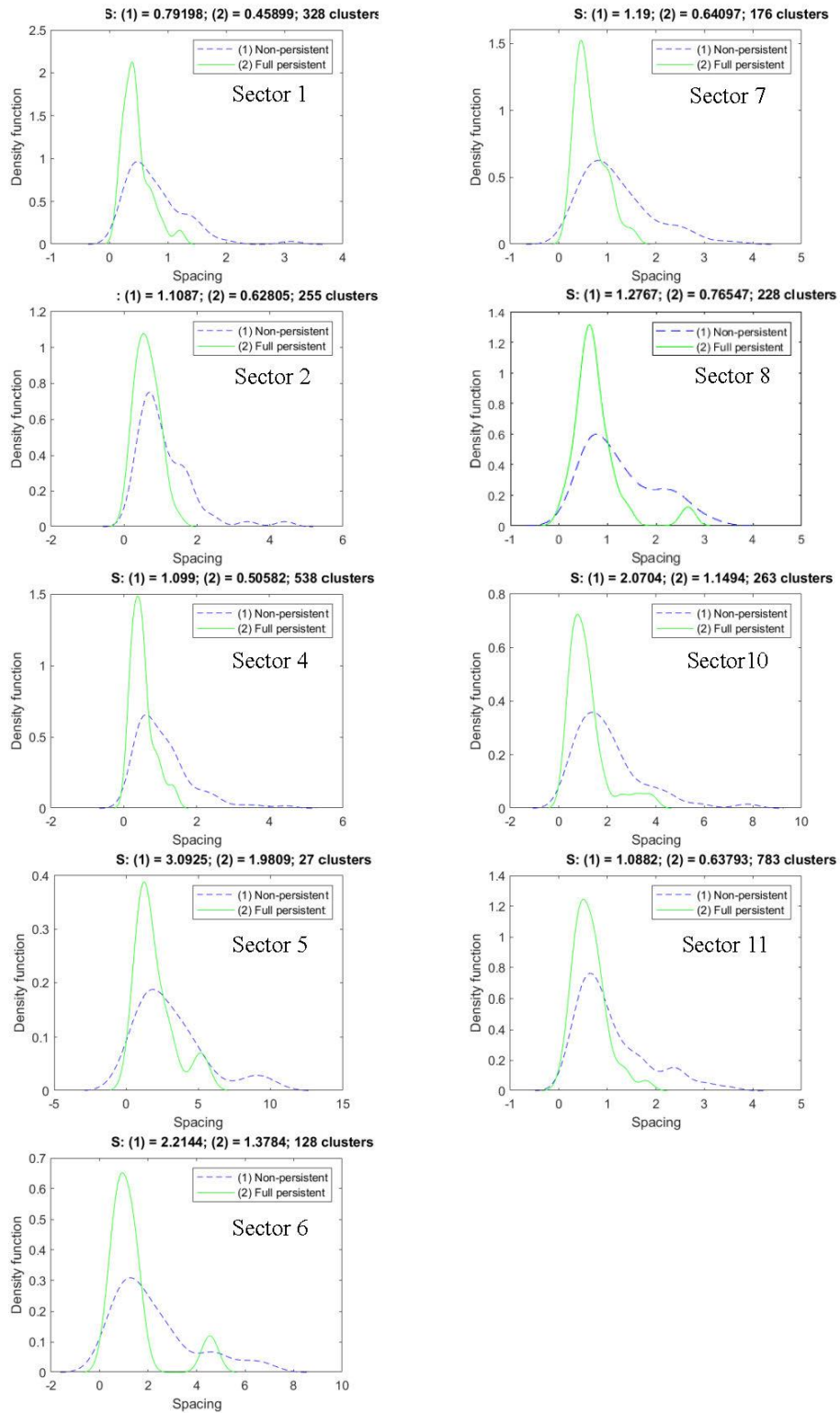


Figure 37: The distribution of J1 spacing for each sector

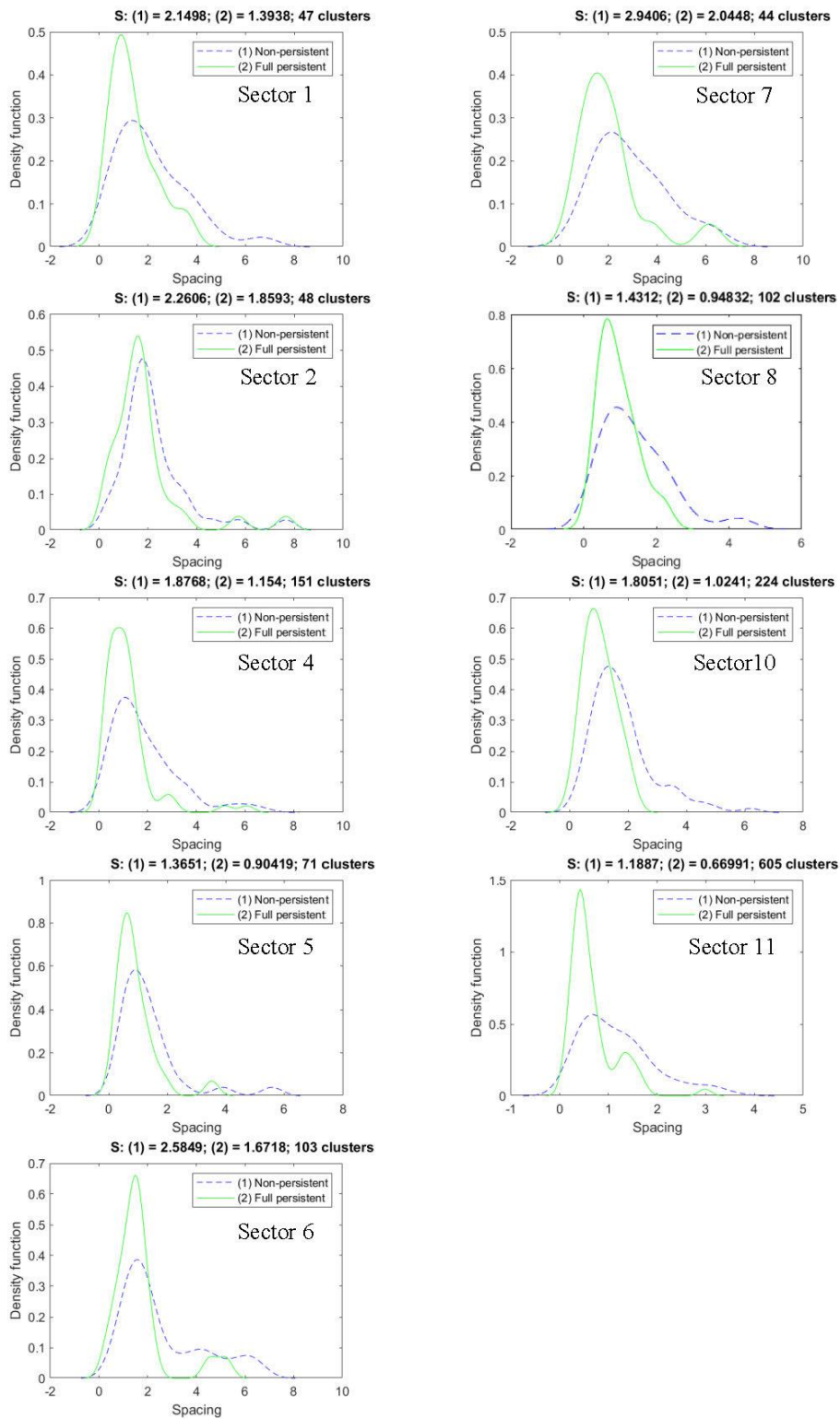


Figure 38: The distribution of J2 spacing for each sector

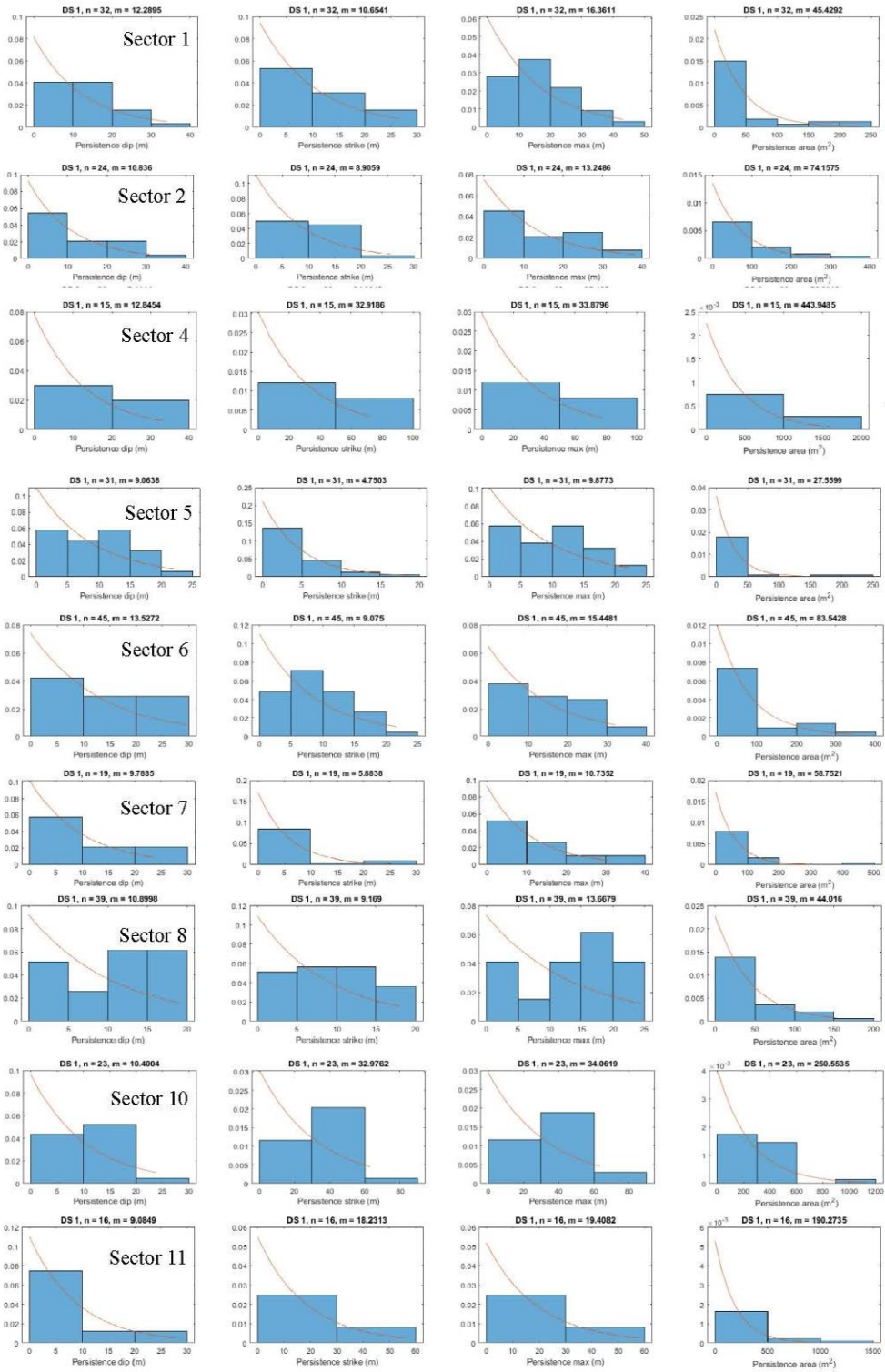


Figure 39: The distribution of bedding plane persistence for each sector

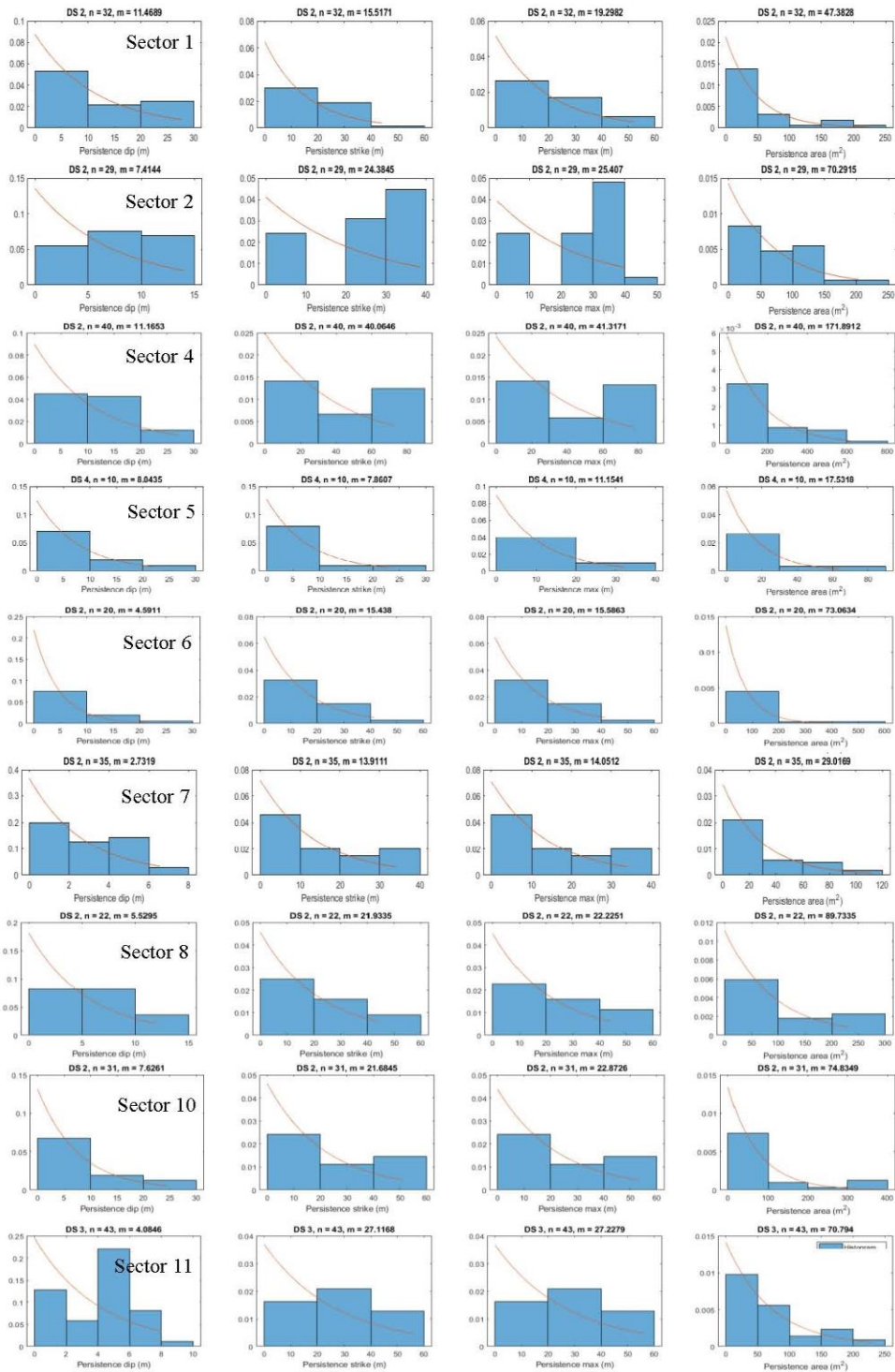


Figure 40: The distribution of J1 persistence for each sector

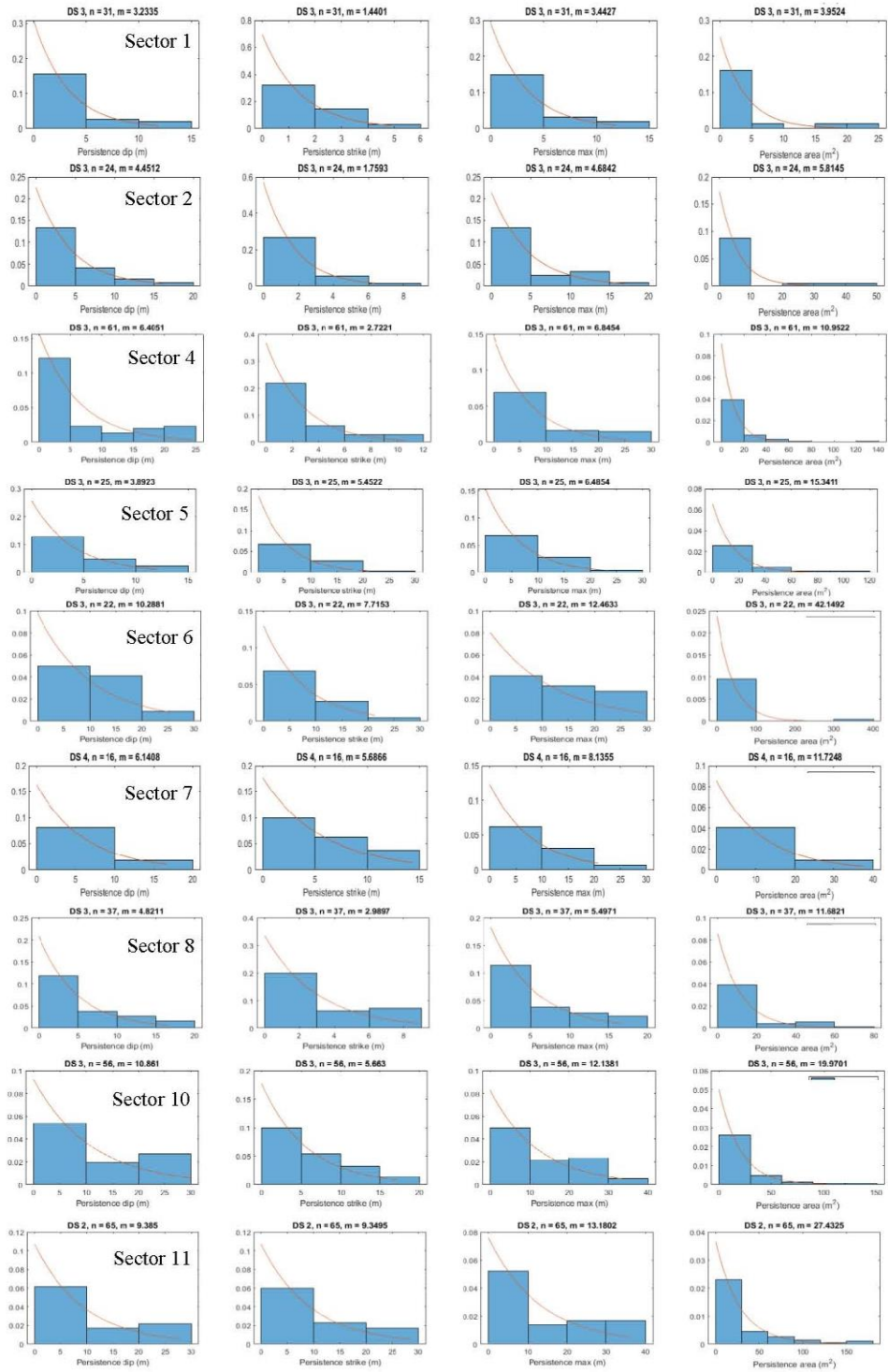


Figure 41: The distribution of J2 persistence for each sector

Block size is one of the most critical parameters of rock mass behavior and hence, of the hazard assessment. It defines the mechanical behavior of the rock mass together with the inter-block shear strength. Block size is a property that is controlled by the number of discontinuity sets, the orientation of discontinuities, discontinuity spacing, and persistence. The number of sets and orientation identify the shape of blocks. In the Mudurnu county center, the shape of the blocks created by the discontinuity sets is blocky according to ISRM (2007). Block size can be calculated by block size index (I_b), which describes the average dimension of the blocks, or volumetric joint count (J_v) which is defined as the total number of joints intersecting a unit volume of the rock mass. The block size index uses the average value of modal spacing of discontinuities (Equation 8). It is possible to find it correctly for sedimentary rocks having cubic or prismatic block shapes such as in the case of two mutually perpendicular joints and a bedding plane (ISRM, 2007). Considering the discontinuity spacing distributions obtained from the point cloud, the block size in the study area was calculated by block size index (I_b). The minimum, maximum, and mean values of block sizes of the sectors are given in Table 11.

$$I_b = \frac{S_1 + S_2 + S_3}{3} \quad (8)$$

where, I_b is the block size index.

According to the spacing and persistence of discontinuity sets obtained from the point cloud, block sizes of the sectors can be classified as follows:

Sector 1 is characterized by small blocks, Sector 2 can create medium to large blocks, Sector 3 and Sector 4 formed medium blocks, Sector 5 and Sector 6 are capable of creating large blocks, Sector 7 formed medium blocks, and Sector 8 is characterized by large blocks, Sector 9, Sector 10 and Sector 11 can create medium blocks. Note that, in the field, the block size was observed to be smaller in Sectors 9, 10, and 11

as compared to the other sectors; except Sector 1 where the limestone layers become thinner. The decrease in the block size in Sectors 9, 10, and 11 may be associated with the increasing clay content in the northern part of the valley that has been identified in the thin sections (Appendix A).

Table 11: Block sizes of sectors based on discontinuity spacing

Sector	BP Spacing (m)			J1 spacing (m)			J2 spacing (m)			Block Volume (m ³)		
	Minimum	Maximum	Mean	Minimum	Maximum	Mean	Minimum	Maximum	Mean	Minimum	Maximum	Mean
1	0.170	1.100	0.480	0.190	1.100	0.460	0.320	4.100	1.390	0.010	4.961	0.307
2	0.310	1.430	0.700	0.150	1.350	0.630	0.290	5.600	1.860	0.013	10.811	0.820
3	0.150	1.620	0.690	0.100	1.400	0.510	0.140	4.380	1.150	0.002	9.934	0.405
4	0.150	1.620	0.690	0.100	1.400	0.510	0.140	4.380	1.150	0.002	9.934	0.405
5	0.130	1.050	0.430	0.780	4.990	1.980	0.210	3.230	0.900	0.021	16.924	0.766
6	0.130	1.280	0.470	0.310	3.890	1.380	0.290	3.210	1.670	0.012	15.983	1.083
7	0.090	1.180	0.480	0.230	1.620	0.640	0.640	5.150	2.040	0.013	9.845	0.627
8	0.360	1.480	0.460	0.210	2.890	0.770	0.260	2.880	0.950	0.020	12.318	0.336
9	0.080	2.000	0.700	0.370	2.140	1.150	0.110	2.150	1.020	0.003	9.202	0.821
10	0.080	2.000	0.700	0.370	2.140	1.150	0.110	2.150	1.020	0.003	9.202	0.821
11	0.170	2.200	0.750	0.070	1.800	0.640	0.110	1.990	0.670	0.001	7.880	0.322

3.4 Empirical classification of the rock slopes

Rock mass classification systems are practical methods for the categorization of rock masses based on the geomechanical characteristics and the rough estimation of rock mass behavior. Since rock mass classification systems, in other words, the empirical methods, consider both the intact rock and the discontinuity parameters, they are useful in terms of directing users to examine the rock mass carefully and

systematically. There are several empirical methods utilized to classify rock slopes geomechanically as a preliminary assessment. In this study, Slope Mass Rating (SMR) and Q-Slope were considered to validate the instability and support requirements of the different sectors. Note that SMR and Q-Slope tables are given in Appendix D.

SMR is a classification system developed by Romana (1985). This method can be explained as a continuation of RMR for slopes. The method uses the basic Rock Mass Rating (RMR) value of Bieniawski (1989) and four correction factors depending on orientations of discontinuities and slope face, and the excavation method to calculate the SMR value according to Equation 9:

$$SMR = RMR_b + (F_1 F_2 F_3) + F_4 \quad (9)$$

where RMR_b is the basic RMR index of Bieniawski (Appendix D).

F_1 is a parameter that depends on the parallelism (A) between the discontinuity dip direction (α_j) and the slope dip direction (α_s). The value of A is calculated by $|\alpha_j - \alpha_s|$ for planar and wedge failures, and by $|\alpha_j - \alpha_s - 180|$ for toppling failure.

F_2 is a measure of the discontinuity shear strength. The value of this parameter (B) is equal to the discontinuity dip angle (β_j) for planar failure, the plunge of the line of intersection of discontinuities for wedge failure, and 1.00 for toppling failure.

F_3 is an expression of the probability of discontinuity to the outcrop on the slope face that depends on the dip angles of the discontinuity and the slope face. The value of this expression (C) is calculated by $\beta_j - \beta_s$ for planar failure, $\beta_I - \beta_s$ for wedge failure, and $\beta_j + \beta_s$ for toppling failure where β_j =discontinuity dip angle, β_I =plunge of line of intersection of discontinuities, and β_s =slope face dip angle.

F₄ is a correction factor depending on the excavation method.

Table 12 shows the RMR basic value and correction factors of each sector for planar (Romana, 1985), wedge (Anbalagan et al., 1992), and toppling (Romana, 1985) types of failures. The calculated SMR values of each sector and the corresponding rock mass classes, stability conditions, failures, and probability of failures for different modes are given in Table 13.

Table 12: RMR basic and correction factor values used to calculate Slope Mass Rating (SMR) of different geomechanical sectors

Sector	RMR basic	Planar							SMR
		A	F1	B	F2	C	F3	F4	
1	66	24	0.4	81	1	15	0	15	81
2	65	7	0.85	74	1	-2	-50	15	37.5
3	65	152	0.15	68	1	-16	-60	15	71
4	62	13	0.7	68	1	-4	-50	15	42
5	65	20	0.4	55	1	-21	-60	15	56
6	62	1	1	76	1	-2	-50	15	27
7	67	12	0.7	84	1	36	0	15	82
8	61	21	0.4	79	1	-1	-50	15	56
9	65	110	0.15	88	1	3	-6	15	79.1
10	65	0	1	78	1	0	-6	15	74
11	60	6	0.85	78	1	3	-6	15	69.9

Table 12 (continued): RMR basic and correction factor values used to calculate Slope Mass Rating (SMR) of different geomechanical sectors

Sector	RMR basic	Wedge							SMR
		A	F1	B	F2	C	F3	F4	
1	66	92	0.15	67	1	1	-6	15	80.1
2	65	108	0.15	57	1	-3	-50	15	72.5
3	65	93	0.15	61	1	-23	-60	15	71
4	62	31	0.15	61	1	-11	-60	15	68
5	65	56	0.15	38	0.85	-38	-60	15	72.35
6	62	75	0.15	78	1	17	0	15	77
7	67	67	0.15	62	1	14	0	15	82
8	61	3	1	78	1	-2	-50	15	26
9	65	43	0.15	85	1	0	-25	15	76.25
10	65	67	0.15	85	1	15	0	15	80
11	60	56	0.15	86	1	26	0	15	75

Sector	RMR basic	Toppling							SMR
		A	F1	B	F2	C	F3	F4	
1	66	5	0.85	-	1	122	-25	15	59.75
2	65	25	0.4	-	1	128	-25	15	70
3	65	144	0.15	-	1	140	-25	15	76.25
4	62	5	0.85	-	1	128	-25	15	55.75
5	65	11	0.7	-	1	137	-25	15	62.5
6	62	0	1	-	1	133	-25	15	52
7	67	6	0.85	-	1	94	0	15	82
8	61	29	0.4	-	1	124	-25	15	66
9	65	97	0.15	-	1	123	-25	15	76.25
10	65	5	0.85	-	1	120	-6	15	74.9
11	60	0	1	-	1	120	-6	15	69

Table 13: Slope Mass Rating (SMR) classes and their descriptions of different geomechanical sectors

Planar Failure					
Sectors	SMR	Class	Stability	Failures	Probability of Failure
1	81	I-Very good	Completely stable	None	0
2	37.5	IV-Bad	Unstable	Planar or big wedges	0.6
3	71	II-Good	Stable	Some blocks	0.2
4	42	III-Normal	Partially stable	Some joints or many wedges	0.4
5	56	III-Normal	Partially stable	Some joints or many wedges	0.4
6	27	IV-Bad	Unstable	Planar or big wedges	0.6
7	82	I-Very good	Completely stable	None	0
8	56	III-Normal	Partially stable	Some joints or many wedges	0.4
9	79.1	II-Good	Stable	Some blocks	0.2
10	74	II-Good	Stable	Some blocks	0.2
11	69.9	II-Good	Stable	Some blocks	0.2

Wedge Failure					
Sectors	SMR	Class	Stability	Failures	Probability of Failure
1	80.1	I-Very good	Completely stable	None	0
2	72.5	II-Good	Stable	Some blocks	0.2
3	71	II-Good	Stable	Some blocks	0.2
4	68	II-Good	Stable	Some blocks	0.2
5	72.35	II-Good	Stable	Some blocks	0.2
6	77	II-Good	Stable	Some blocks	0.2
7	82	I-Very good	Completely stable	None	0
8	26	IV-Bad	Unstable	Planar or big wedges	0.6
9	76.25	II-Good	Stable	Some blocks	0.2
10	80	II-Good	Stable	Some blocks	0.2
11	75	II-Good	Stable	Some blocks	0.2

Table 13 (continued): Slope Mass Rating (SMR) classes and their descriptions of different geomechanical sectors

Toppling Failure					
Sectors	SMR	Class	Stability	Failures	Probability of Failure
1	59.75	III-Normal	Partially stable	Some joints or many wedges	0.4
2	70	II-Good	Stable	Some blocks	0.2
3	76.25	II-Good	Stable	Some blocks	0.2
4	55.75	III-Normal	Partially stable	Some joints or many wedges	0.4
5	62.5	II-Good	Stable	Some blocks	0.2
6	52	III-Normal	Partially stable	Some joints or many wedges	0.4
7	82	I-Very good	Completely stable	None	0
8	66	II-Good	Stable	Some blocks	0.2
9	76.25	II-Good	Stable	Some blocks	0.2
10	74.9	II-Good	Stable	Some blocks	0.2
11	69	II-Good	Stable	Some blocks	0.2

Q-Slope is a method developed to estimate the stability of rock slopes (Barton and Bar, 2015). This system considers the same parameters as Barton et al. (1974)'s Q-System. In addition to these parameters, Q-Slope takes discontinuity orientation and environmental conditions into account to calculate the Q-Slope value according to Equation 10:

$$Q_{slope} = \frac{RQD}{J_n} \times \left(\frac{J_r}{J_a} \right)_0 \times \frac{J_{wice}}{SRF_{slope}} \quad (10)$$

where RQD is Rock Quality Designation

J_n is the number of joint sets

J_r is the joint roughness number

J_a is the joint alteration number

O-factor is the orientation factor for the ratio of J_r/J_a and provides adjustment for discontinuity orientations

J_{wice} is an environmental and geological condition number that considers the long-term exposure of slope to various conditions

SRF_{slope} is strength reduction factor. The most adverse factor among three categories are, namely, SRF_a =physical condition number, SRF_b =stress and strength number, and SRF_c =Major discontinuity number is chosen.

Table 14 shows the values of Q-slope parameters of each sector for planar and wedge type of failures. Table 15 presents the Q-Slope values and stability conditions of different sectors.

Table 14: Values of the parameters used to calculate the Q-slope value of different geomechanical sectors

Planar									
Sectors	RQD	J_n	J_r	J_a	O-factor	J_{wice}	SRF	Q-slope	
1	64	9	2	2	0.25	0.5	4	0.22	
2	68	9	2	2	0.25	0.5	4	0.24	
4	36	9	3	2	0.25	0.5	4	0.19	
5	70	9	3	3	0.25	0.5	4	0.24	
6	68	9	3	3	0.25	0.5	4	0.24	
7	59	9	3	3	0.25	0.5	4	0.20	
8	52	9	3	3	0.25	0.5	4	0.18	
10	35	9	3	2	0.25	0.5	4	0.18	
11	18	9	3	2	0.25	0.5	4	0.09	

Wedge									
Sectors	RQD	J_n	J_r	J_a	O-factor	O-factor	J_{wice}	SRF	Q-slope
1	64	9	2	2	0.25	0.8	0.5	4	0.18
2	68	9	2	2	0.25	0.8	0.5	4	0.19
4	36	9	3	2	0.25	0.8	0.5	4	0.23
5	70	9	3	3	0.25	0.8	0.5	4	0.19
6	68	9	3	3	0.25	0.8	0.5	4	0.19
7	59	9	3	3	0.25	0.8	0.5	4	0.16
8	52	9	3	3	0.25	0.8	0.5	4	0.14
10	35	9	3	2	0.25	0.8	0.5	4	0.22
11	18	9	3	2	0.25	0.8	0.5	4	0.11

Table 15: Q-Slope values and stability conditions of the different geomechanical sectors

Sectors	Slope Dip	Planar		Wedge	
		Q-slope	Stability	Q-slope	Stability
1	66	0.22	Unstable	0.18	Unstable
2	60	0.24	Unstable	0.19	Unstable
4	72	0.19	Unstable	0.23	Unstable
5	76	0.24	Unstable	0.19	Unstable
6	61	0.24	Unstable	0.19	Unstable
7	48	0.2	Stable	0.16	Stable
8	80	0.18	Unstable	0.14	Unstable
10	70	0.18	Unstable	0.22	Unstable
11	60	0.09	Unstable	0.11	Unstable

SMR concluded that all the sectors are capable of creating failures up to some degree except Sector 7. According to rock mass classes and the probability of failures, the most critical sectors are evaluated as Sectors 8 and 6. Sector 8 is critical, especially in terms of a wedge failure probability of 0.6 and a planar failure probability of 0.4. Sector 6 is critical in terms of a planar failure probability of 0.6 and a toppling failure probability of 0.4. This is followed by, Sector 4 and Sector 5, where partially stable blocks are found for planar and toppling type failures. The Q-Slope classification shows that all the sectors are unstable except Sector 7. Although the discontinuity orientations are unfavorable, Sector 7 is determined to be stable due to its lower overall slope angle (Arslan Kelam et al., 2021).

CHAPTER 4

STABILITY ASSESSMENT

4.1 Methods of rock slope stability assessment

Slope stability terminology is described by Kliche (2018) as “the resistance of any inclined surface, as the wall of an open pit or cut, to failure by sliding or collapsing”. Different rock masses and geological structures are associated with different sorts of slope instability. There are classification systems that categorize types of movement based on the rock masses. The most recent of these classification systems, a new version of the widely used Varnes classification system (Varnes, 1978), has been proposed by Hungr et al. (2014). The updated modes of failure are given in Table 16. According to this table, the possible modes of failure on the western side of Mudurnu county center are toppling and sliding of discontinuous rock masses.

Rock slope stability deals with a slope formed in rock by utilizing rock mechanics and structural geology principles. Assessment of a rock slope stability is not a straightforward process since rock mechanics is a challenging subject due to the heterogeneous and anisotropic nature of rock materials, difficulties in identifying the strength parameters of rock masses, the complexity of the rock behavior theories and models, difficulty to represent field conditions in the laboratory and complexity of field testing (Brawner and Milligan, 1971). In general, slope failure originates from a combination of causes that occur simultaneously. These causes can be grouped under two categories, namely, the ones that contribute to increased shear stress and the ones that lead to reduced shear strength (Varnes, 1978). On the western side of the Mudurnu county center, an increase in shear stress may be attributed to the removal of lateral support utilizing previous slides, removal of underlying support as a consequence of the weathering of the discontinuous rock mass, or the

undermined geometry because of human activity, and earthquake forces. Besides, a decrease in shear strength can be attributed to inherent characteristics of the material such as the presence and favorable orientation of discontinuities and slope face orientation on the western side of the Mudurnu Valley (Figure 42).

Table 16: Modes of slope failure (Hungri et al., 2014 as modified from Varnes (1978))

Type of movement	Rock	Soil
Fall	1. Rock/ice fall*	2. Boulder/debris/silt fall*
Topple	3. Rock block topple* 4. Rock flexural topple	5. Gravel/sand/silt topple*
Slide	6. Rock rotational slide 7. Rock planar slide* 8. Rock wedge slide* 9. Rock compound slide 10. Rock irregular slide*	11. Clay/silt rotational slide 12. Clay/silt planar slide 13. Gravel/sand/debris slide* 14. Clay/silt compound slide
Spread	15. Rock slope spread	16. Sand/silt liquefaction spread* 17. Sensitive clay spread*
Flow	18. Rock/ice avalanche*	19. Sand/silt/debris dry flow 20. Sand/silt/debris flowslide* 21. Sensitive clay flowslide* 22. Debris flow* 23. Mud flow* 24. Debris flood 25. Debris avalanche* 26. Earthflow 27. Peat flow
Slope deformation	28. Mountain slope deformation 29. Rock slope deformation	30. Soil slope deformation 31. Soil creep 32. Solifluction

*Movement types that usually reach extremely rapid velocities as defined by Cruden and Varnes (1996). The other landslide types are most often (but not always) extremely slow to very rapid

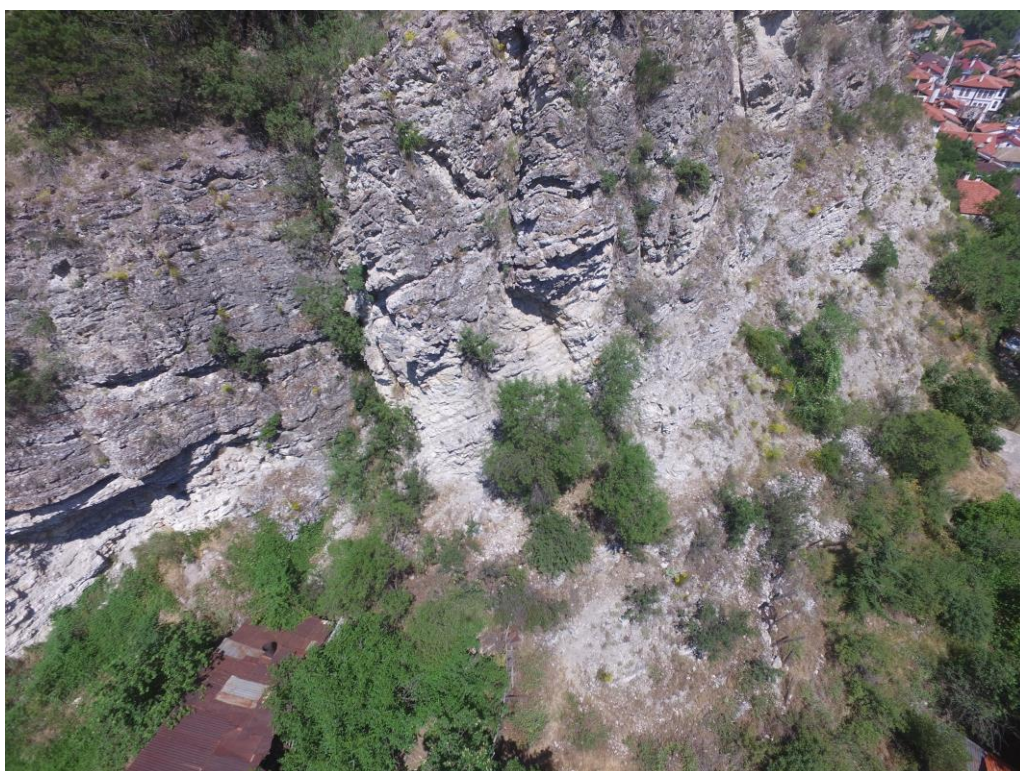


Figure 42: General views from the discontinuous rock mass on the western side of the Mudurnu valley

When the size of blocks formed by intersecting discontinuities is in the same order as the scale of the slope, the stability should be analyzed by considering the sliding and rotation of the blocks (Hoek and Karzulovic 2001). Since the rock mass under question is discontinuous limestone, a two-step process has been followed for the stability assessment in Mudurnu. First, kinematic analysis has been applied to identify possible modes of failure (Piteau and Peckover, 1978). Then, limit equilibrium analysis has been employed for the sectors that have a potential for failure based on the kinematic analysis.

4.2 Kinematic analysis

The kinematic analysis explores the slope geometrically with the aid of stereographic projection to pinpoint possible modes of slope failures. It considers the orientation of discontinuities and the slope face under investigation by taking the friction angle into account. The orientation is the attitude of a plane (discontinuity or slope face) represented by dip direction and dip. Dip direction is the angle showing the dipping direction of a plane that is measured from true north and dip is the steepest angle measured from the horizontal (ISRM, 2007). Orientation is a significant characteristic since it affects the failure type and kinematic instability. Engineering characteristics of the rock mass are influenced by the discontinuity set orientations and degree of clustering of the sets (Park et al., 2005). The influence of orientation becomes more important when other characteristics are favorable for deformation (Zhang, 2005).

In this dissertation, the DSE methodology has been explained in Chapter 3.2 and Chapter 3.3 in an attempt to obtain the clusters and distributions of the discontinuity sets. The discontinuity orientations were determined by Fisher distribution which is

commonly used to model 3D distributions because of its simplicity and flexibility (Priest, 1993). Fisher distribution gives an angular distribution of orientations about a mean orientation (Fisher, 1953). For the kinematic analysis, the strength parameters of the discontinuity surfaces were employed. In the preliminary analysis of stability, Hunt (1996) suggests the common strength values (i.e., internal friction angle) of rock mass discontinuities for smooth and unweathered surfaces as 30°-35° for granite, basalt, gneiss, sandstone, limestone and 25°-30° for shale, phyllite, micaschist. According to Hunt (1996), 5°-15° is advised to be added to these values whenever the discontinuity surfaces are rough and undulated or have an average roughness. 5°-10° is recommended to be subtracted from these values if the discontinuity surfaces are highly weathered and decomposed. The lower bound of the suggested internal friction angle values for limestone, namely, 30° was utilized in the kinematic analysis for the sake of not missing any possible failures that can form due to the uncertainties of discontinuity characteristics. This value is consistent with the results obtained through the RMR classification. The possibility of kinematic failure was examined by using the Dips software (Rocscience, 2022). The distributions of the discontinuity sets, as well as the kinematic analysis results of the sectors, are given in Figures 43 through 45. Note that each row presents the analysis of a particular sector for planar, wedge, and toppling types of failures.

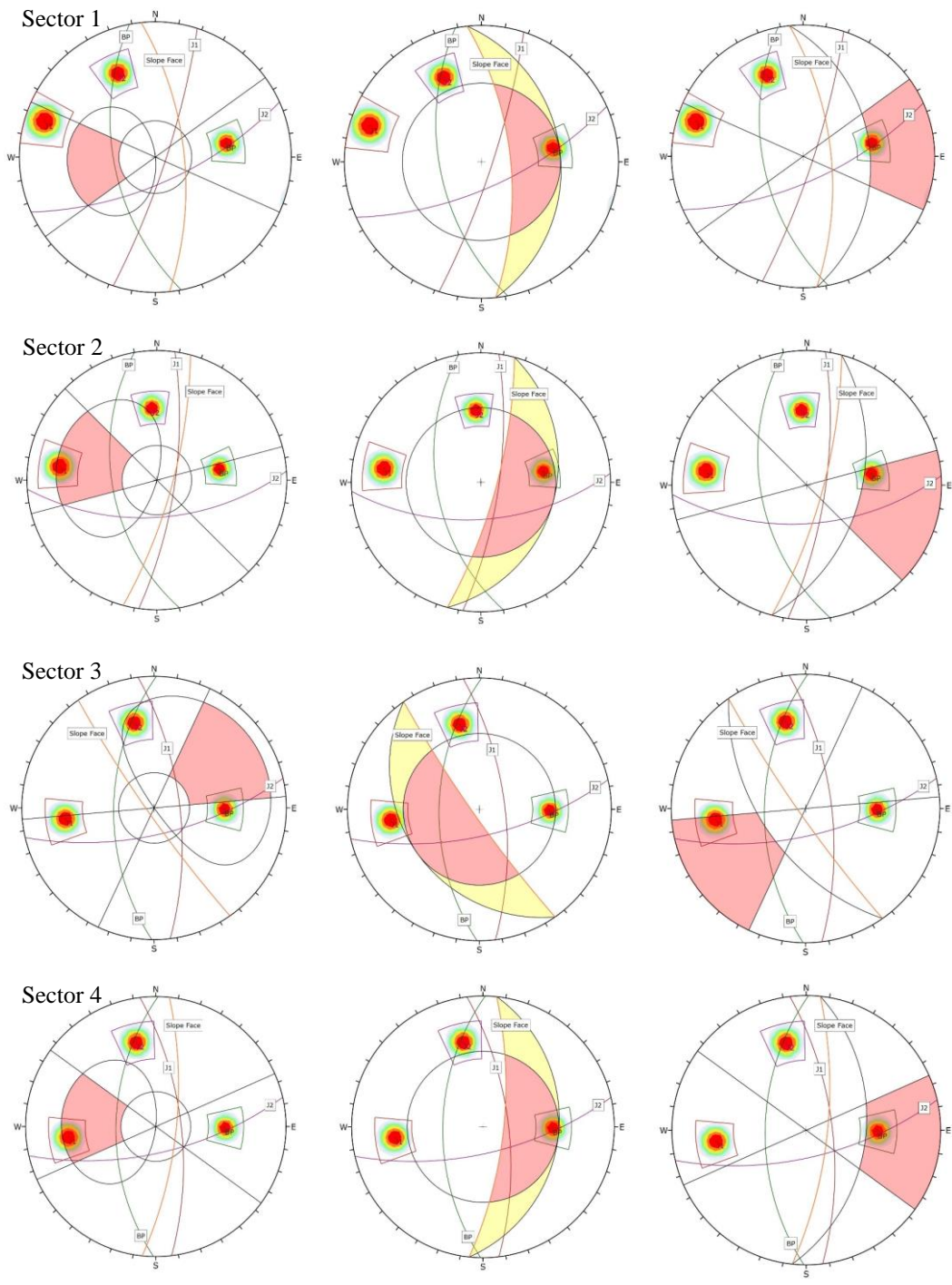


Figure 43: The distribution of discontinuity sets and the kinematic analysis results of Sectors 1, 2, 3, and 4 (i.e., planar failure analysis on the left, wedge failure analysis in the middle, and toppling failure analysis on the right)

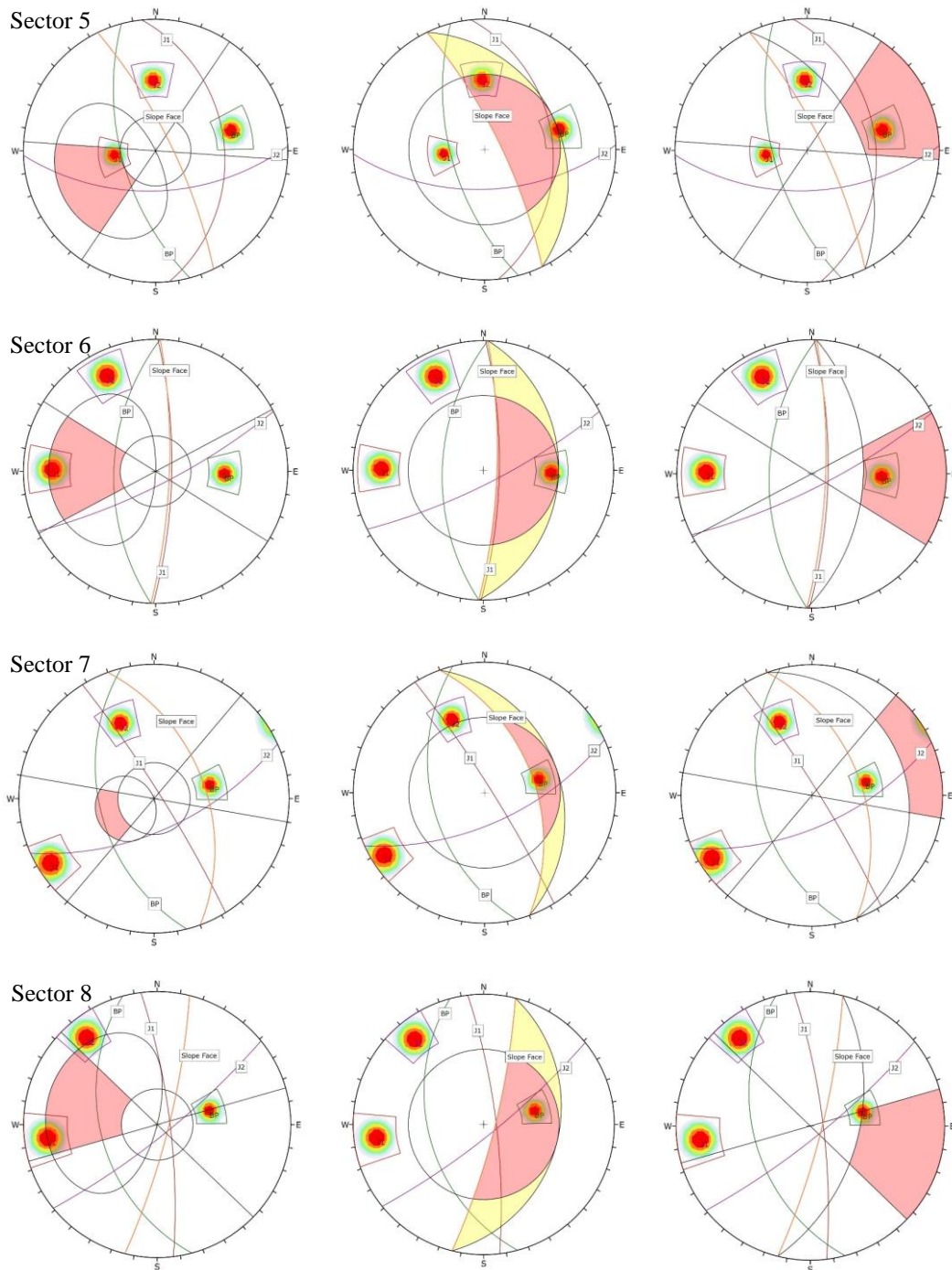


Figure 44: The distribution of discontinuity sets and the kinematic analysis results of Sectors 5, 6, 7, and 8 (i.e., planar failure analysis on the left, wedge failure analysis in the middle, and toppling failure analysis on the right)

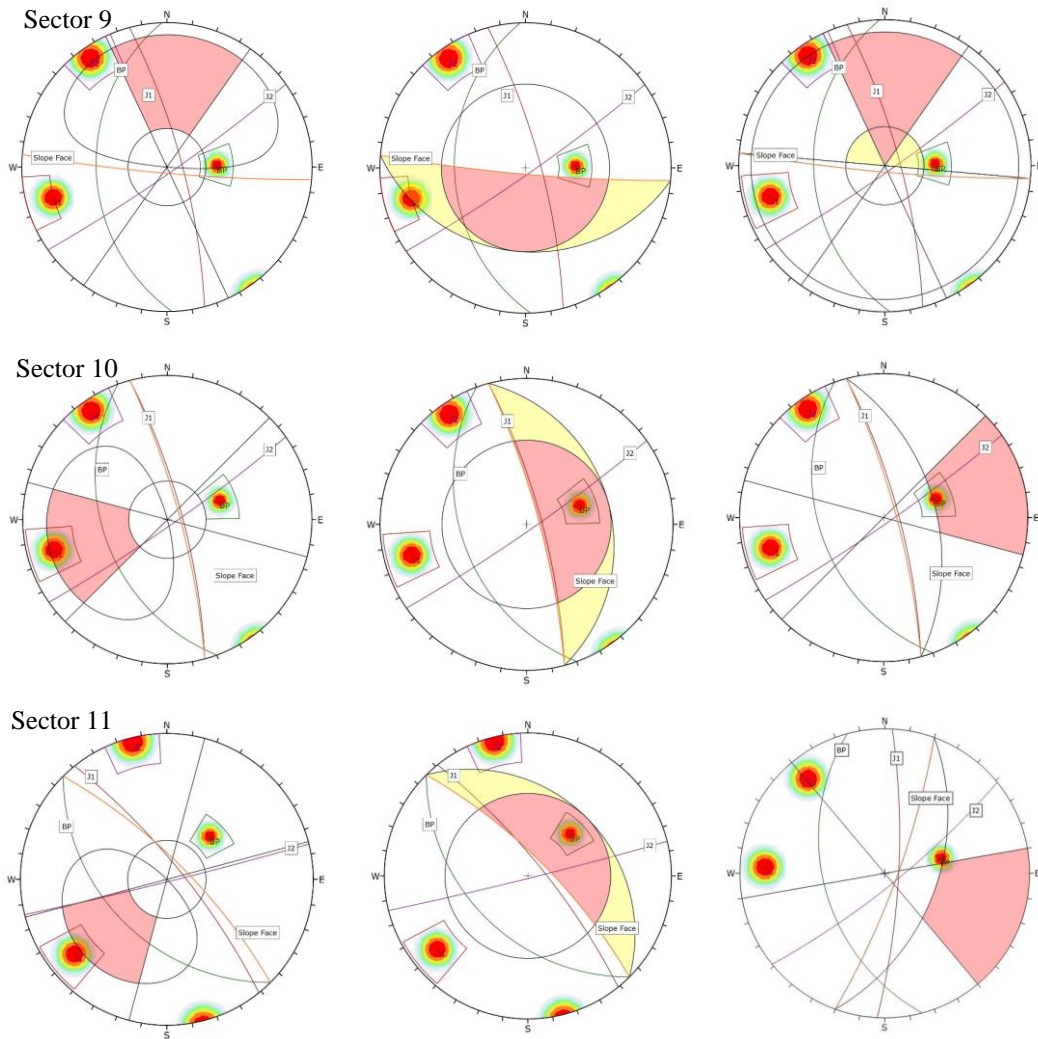


Figure 45: The distribution of discontinuity sets and the kinematic analysis results of Sectors 9, 10, and 11 (i.e., planar failure analysis on the left, wedge failure analysis in the middle, and toppling failure analysis on the right)

The kinematic analyses revealed that planar, wedge and toppling failures were possible throughout the study area. In the area, Joint set 1 (J1) can cause planar failures, the intersection of Joint set 1 (J1) and Joint set 2 (J2) may produce wedge failures and the Bedding Plane (BP) is capable of inducing toppling failure (Arslan

Kelam et al., 2018). Possible modes of failure identified in each sector by the kinematic analysis are summarized in Table 17.

Table 17: Possible modes of failure of the sectors identified by the kinematic analysis

Sector	Slope Face Orientation	Discontinuity Orientation			Possibility of*								
					Planar Failure			Wedge Failure			Toppling Failure		
		BP	J1	J2	BP	J1	J2	I _{BP,1}	I _{BP,2}	I _{1,2}	BP	J1	J2
1	084/66	259/56	108/81	156/68	N	N	N	N	N	N	Y	N	N
2	105/76	260/52	098/74	176/58	N	Y	N	N	N	Y	Y	N	N
3	235/84	271/56	083/68	167/67	N	N	N	N	Y	N	Y	N	N
4	096/72	271/56	083/68	167/67	N	Y	N	N	N	Y	Y	N	N
5	064/76	255/61	084/35	178/56	N	Y	N	N	N	Y	Y	N	N
6	092/78	272/55	091/76	153/78	N	Y	N	N	N	Y	Y	N	N
7	070/48	256/46	058/84	156/63	N	N	N	N	N	N	N	N	N
8	104/80	255/44	083/79	141/80	N	Y	N	N	N	Y	Y	N	N
9	185/85	268/38	075/88	145/85	N	N	N	N	Y	N	N	N	N
10	075/80	250/42	075/78	145/85	N	N	N	N	N	Y	Y	N	N
11	045/75	225/45	051/78	166/88	N	N	N	N	N	N	Y	N	N

*Y=Yes, failure is possible. N=No, failure is not possible.

4.3 Back analysis

Stability analysis is performed to reach a factor of safety or probability of failure. However, it is also possible to perform stability analysis to determine the mobilized shear strength parameters of a failed slope. This methodology is named as back analysis. In the case of back analysis, the stability analysis is performed using a factor of safety of 1 that represents the limiting equilibrium condition at the time of failure (Bromhead, 1992). Back analysis provides information about the shear strength parameters of a slope that could not be reached by conventional laboratory tests

(Abramson et al., 2002). To consult a back analysis and to investigate the stability of the slopes as well, a failure criterion that is reasonable for the expected modes of failure (i.e. discontinuity-controlled) in the study area was need to be determined. The behavior of natural rock joints can be estimated by using Equation 11 suggested by Barton and Choubey (1977):

$$\tau = \sigma_n \tan \left(\phi_r + JRC \log_{10} \left(\frac{JCS}{\sigma_n} \right) \right) \quad (11)$$

where JRC is the joint roughness coefficient

JCS is the joint wall compressive strength

ϕ_r is the residual friction angle

σ_n is the normal stress

The estimation of JRC was employed based on the field observations and the JCS was estimated according to field measurements and laboratory test results. Detailed information regarding these parameters has been given in Section 3.1. In the field, observations and measurements have been made in the accessible yet relatively limited parts of the valley slopes. However, it is expected that these measurements represent the entire slope face. Barton and Bandis (1982) suggest that JRC and JCS are affected by the scale effect where these values decrease as the size of the discontinuity increases. Therefore, the values from the field were corrected to account for the scale effects by using Equations 12 and 13 proposed by Barton and Bandis (1982):

$$JRC_n = JRC_0 \left(\frac{L_n}{L_0} \right)^{-0.02JRC_0} \quad (12)$$

where, JRC_0 is the joint roughness measured on a $L_0 = 100$ mm sample and JRC_n is the joint roughness of an in-situ block having a size of L_n

$$JCS_n = JCS_0 \left(\frac{L_n}{L_0} \right)^{-0.03JRC_0} \quad (13)$$

where, JCS_0 is the average joint wall compressive strength of a $L_0 = 100$ mm sample and JCS_n is the average joint wall compressive strength of an in-situ block having a size of L_n

The corrected values of JRC and JCS were employed in Equation 11 proposed by Barton and Choubey (1977) to estimate the friction angles along the discontinuity sets J1 and J2. The friction angles calculated are given in Table 18.

Table 18: The friction angles calculated along the discontinuity sets J1 and J2 by using Equation 11 proposed by Barton and Choubey (1977)

Sector	1	2	3	4	5	6	7	8	9	10	11
ϕ_{J1}	42°	42°	42°	43°	48°	47°	47°	45°	45°	46°	46°
ϕ_{J2}	42°	42°	44°	46°	50°	49°	49°	49°	46°	46°	46°

It should be noted that due to the inherent variability of natural rock masses, there is a significant amount of uncertainty in these estimates. Therefore, back analysis was performed on the failed blocks in Mudurnu to determine the mobilized shear strength

parameters at the time of failure. The failed blocks identified for back analysis in Sectors 2, 5, 6, 8, and 10 are shown in Figures 46, 47, 48, 49 and 50, respectively. Note that two identifiable blocks have been used in back analysis per sector. In the following figures, these blocks were specified through color-coding, where Block 1 was marked by a red circle and Block 2 by a dark blue circle. Several images of the same block were provided where images from different angles have been available.

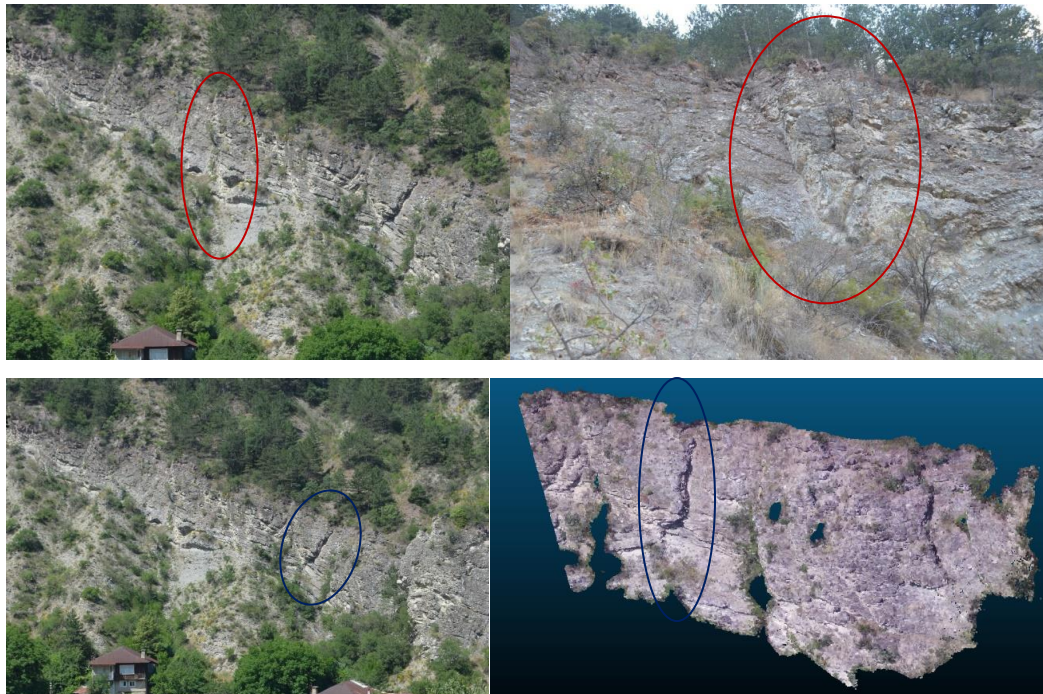


Figure 46: Blocks identified in Sector 2 for the back analysis



Figure 47: Blocks identified in Sector 5 for the back analysis



Figure 48: Blocks identified in Sector 6 for the back analysis



Figure 49: Blocks identified in Sector 8 for the back analysis



Figure 50: Blocks identified in Sector 10 for the back analysis

The geometry of the blocks analyzed by the back analysis in Sectors 2, 5, 6, 8, and 10 are given in Figures 51, 52, 53, 54 and 55, respectively. Back calculation of observed failures in the study area was performed to independently estimate the strength parameters of the rock mass discontinuities. Swedge software (Rocscience, 2022) was utilized for the analysis.

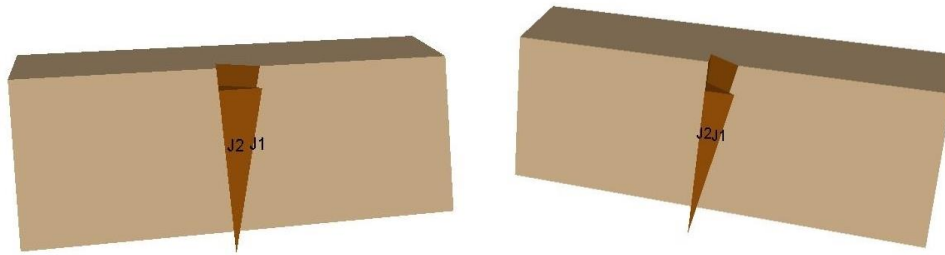


Figure 51: Geometry of the blocks in Sector 2 analyzed by Swedge software through back analysis

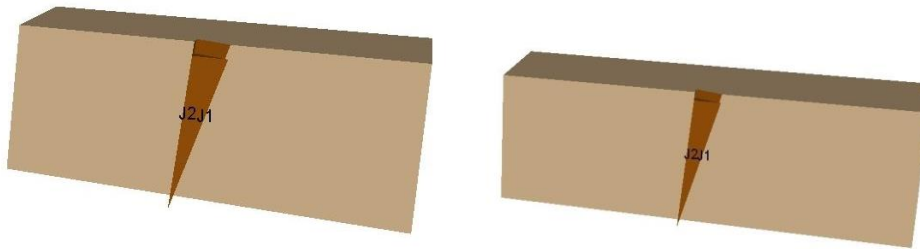


Figure 52: Geometry of the blocks in Sector 5 analyzed by Swedge software through back analysis

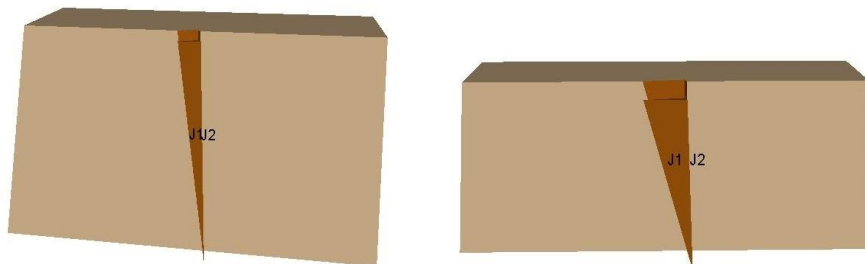


Figure 53: Geometry of the blocks in Sector 6 analyzed by Swedge software through back analysis

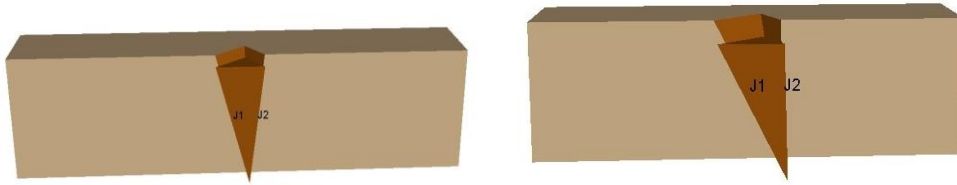


Figure 54: Geometry of the blocks in Sector 8 analyzed by Swedge software through back analysis

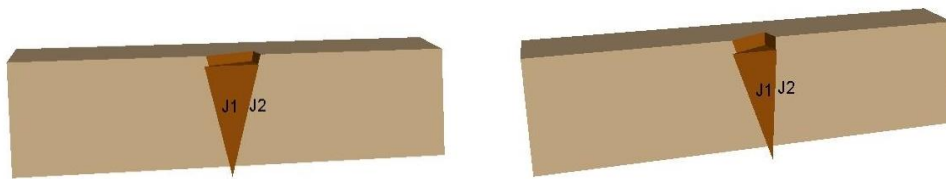


Figure 55: Geometry of the blocks in Sector 10 analyzed by Swedge software through back analysis

The shear strength parameters obtained in each sector as the result of the back analysis are given in Table 19. Accordingly, the back-calculated internal friction angles are lower than the values calculated from Equation 11 of Barton and Choubey (1977). The difference may arise from the influences of local changes in weathering degree, water condition, or JRC even though the values were corrected for scale effect. Although the Barton-Bandis failure criterion was reasonable due to the strong and slightly weathered nature of the rock mass and mostly no infilled discontinuities

(Choi and Chung, 2004; Zhao et al., 2016; Zhao et al., 2020; Zuo et al., 2021), soft infilling (i.e., clay or silty-clay) is occasionally available. Thus, a sensitivity study was applied for the back analysis by utilizing numerical and analytical solutions for the sake of revealing the impact of cohesion. Numerical analyses were performed in two sectors (i.e., Sectors 5 and 10) where intersections of the wedges were identifiable (Figures 47 and 50). The cohesion and internal friction angle pairs that satisfy the factor of safety of unity were estimated by considering the Mohr-Coulomb failure criterion. The estimated values of c - ϕ pairs for wedges 1 and 2 as well as the graph showing their variation are given in Appendix E. As a result, ϕ and c values were obtained from the back analysis as 46° and 1.8 kPa in Sector 5, and 44° and 1.9 kPa in Sector 10, respectively. In addition, the shear strength values were also estimated via the analytical solution proposed by Hoek and Bray (1981) based on Equation 14 by using the angles determined from stereonet plots. The c - ϕ pairs obtained from the analytical solution are given in Appendix E. It can be concluded that the analyses applied by the Mohr-Coulomb failure criterion and Hoek and Bray solution results in friction angles that are in good agreement with the values obtained by utilizing the Barton-Bandis failure criterion. Moreover, the analyses showed that the influence of the cohesion is insignificant. Therefore, the parameters back-calculated by the Barton-Bandis failure criterion can be satisfactorily applied for the stability analysis of the rock mass on the western side of the Mudurnu valley.

$$F = \frac{3}{\gamma H} (c_A X + c_B Y) + \left(A - \frac{\gamma_w}{2\gamma} X \right) \tan \phi_A + \left(B - \frac{\gamma_w}{2\gamma} Y \right) \tan \phi_B \quad (14)$$

where c_A and c_B are the cohesive strengths of planes A and B

ϕ_A and ϕ_B are the internal friction angles of planes A and B

γ is the unit weight of the rock mass

γ_w is the unit weight of water

H is the total height of the wedge

X, Y, A and B are dimensionless factors that depend on the wedge geometry:

$$X = \frac{\sin\theta_{24}}{\sin\theta_{45}\cos\theta_{2.nA}}$$

$$Y = \frac{\sin\theta_{13}}{\sin\theta_{35}\cos\theta_{1.nB}}$$

$$A = \frac{\cos\Psi_A - \cos\Psi_B\cos\theta_{nA.nB}}{\sin\Psi_5\sin^2\theta_{nA.nB}}$$

$$B = \frac{\cos\Psi_B - \cos\Psi_A\cos\theta_{nA.nB}}{\sin\Psi_5\sin^2\theta_{nA.nB}}$$

where Ψ_A and Ψ_B are the dips of planes A and B

Ψ_5 is the plunge of the line of intersection of planes A and B.

Table 19: Friction angle values calculated from Equation 11 of Barton and Choubey (1977) and obtained from the back-calculation

Block	Sector 2		Sector 5		Sector 6		Sector 8		Sector 10	
	S2-1	S2-2	S5-1	S5-2	S6-1	S6-2	S8-1	S8-2	S10-1	S10-2
ϕ_{J1}	42°	42°	48°	49°	48°	46°	45°	46°	47°	46°
ϕ_{J2}	42°	43°	50°	50°	50°	49°	49°	49°	46°	44°
Back calculated	36	36	45	46	43	43	43	44	41	40
ϕ_{J1} Back calculated	42	39	45	44	45	45	42	48	44	42
ϕ_{J2}										

4.4 Limit equilibrium analysis

In rock slope engineering, the natural phenomena have been explained by mathematical models using geomechanical parameters that represent a simplified form of rock mass behavior. Despite the simplifications, rock slope analysis includes a significant amount of uncertainty due to the nature of the rock masses. Also, determining a representative value for the analysis is challenging for rock slopes. The stability of the rock slopes may be analyzed by deterministic or probabilistic approaches. For the deterministic analysis, a single representative value is used for each parameter, while the parameters are identified by the statistical evaluation of available data for the probabilistic analysis. Therefore, the probabilistic approach considers the uncertainty and variability of rock mass parameters (Park et al., 2005). Within the scope of this dissertation, the limit equilibrium analysis has been applied in terms of planar and wedge types of failures for the kinematically possible failure sectors. For the analysis, the probabilistic approach was used along with the deterministic analysis.

The kinematic analysis concluded that Joint set 1 (J1) can cause planar failures in Sectors 2, 4, 5, 6, and 8 of the study area. The deterministic and probabilistic analyses were applied by using the Rocplane software. The 2D and 3D views of the blocks and the calculated results for deterministic (i.e., factor of safety) and probabilistic (i.e., probability of failure) analysis are given in Figures 56, 57, 58, 59, and 60. For the probabilistic analysis of planar failure, the parameters introduced based on their statistical distribution are slope face dip angle, failure plane dip angle, JRC and JCS.

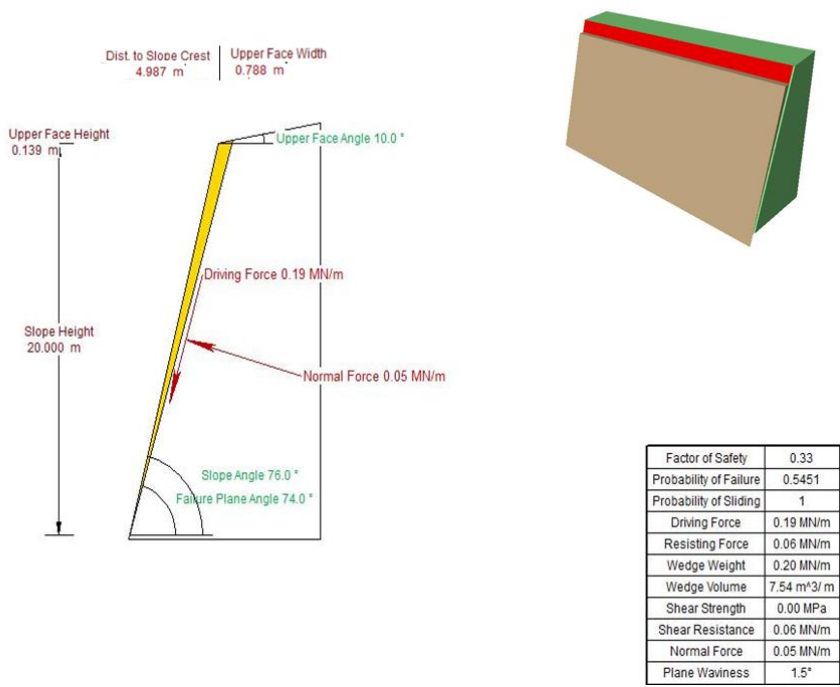


Figure 56: 2D and 3D view of the block generated in Sector 2 by Rocplane software

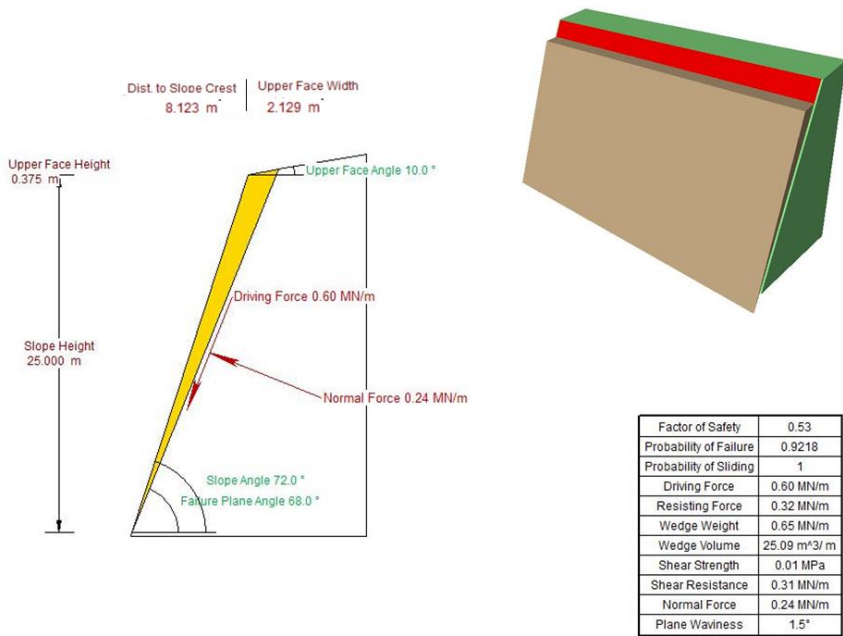


Figure 57: 2D and 3D view of the block generated in Sector 4 by Rocplane software

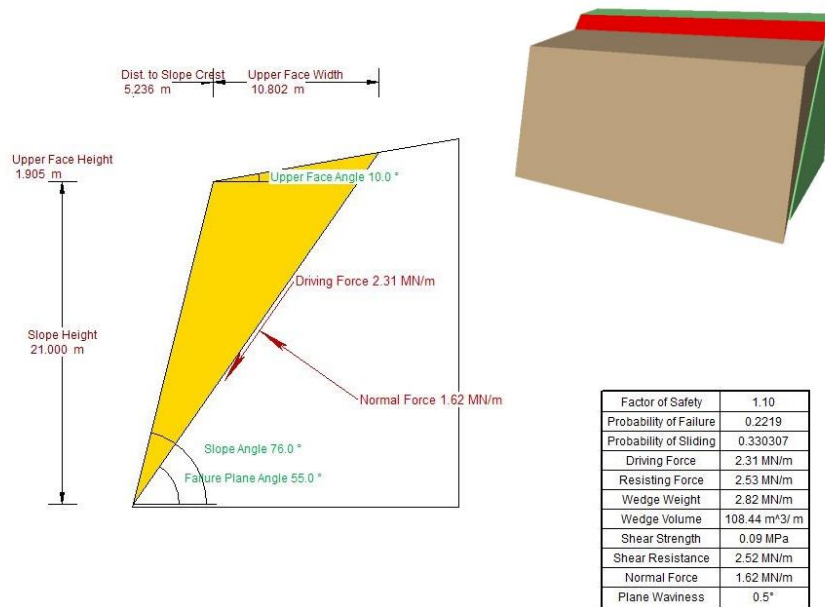


Figure 58: 2D and 3D view of the block generated in Sector 5 by Rocplane software

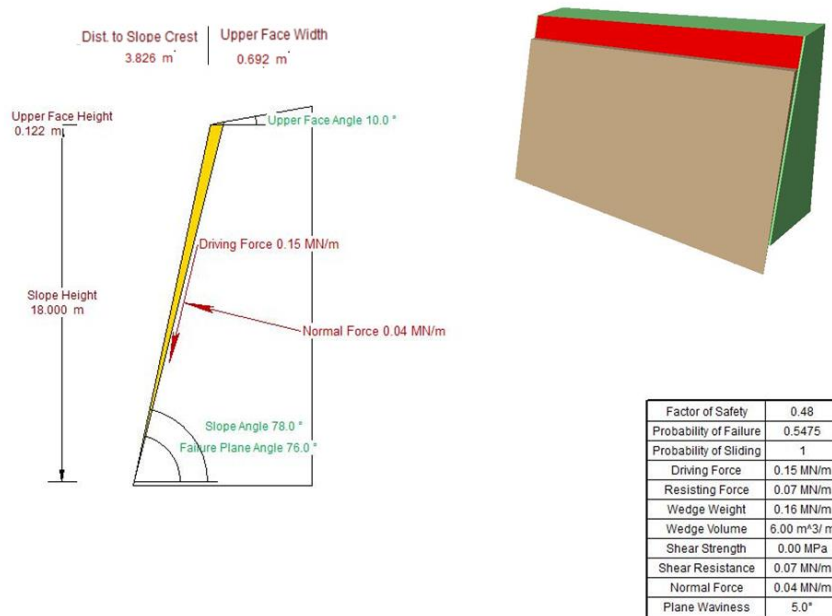


Figure 59: 2D and 3D view of the block generated in Sector 6 by Rocplane software

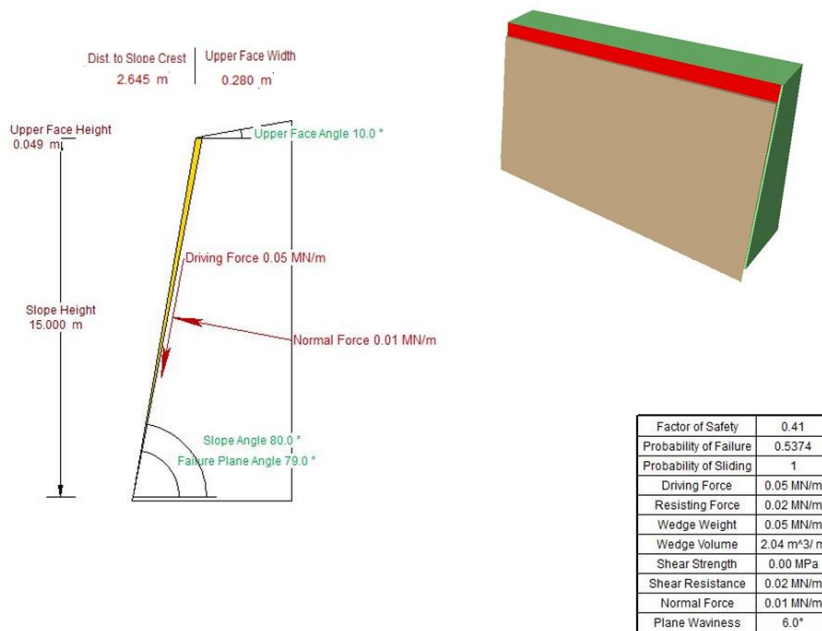


Figure 60: 2D and 3D view of the block generated in Sector 8 by Rocplane software

The probability of failure and the factor of safety values of the kinematically possible sectors of planar failure are given in Table 20.

Table 20: Comparison of the probabilistic and deterministic analysis of planar failure

	Planar failure					
	Probability of failure			Factor of safety		
	BP	J1	J2	BP	J1	J2
2	0	0.55	0	0	0.33	0
4	0	0.92	0	0	0.53	0
5	0	0.22	0	0	1.10	0
6	0	0.55	0	0	0.48	0
8	0	0.54	0	0	0.41	0

The kinematic analysis revealed that the intersection of Joint set 1 (J1) and Joint set 2 (J2) may produce wedge failures in Sectors 2, 4, 5, 6, 8, and 10 of the study area. In addition, the intersection of the Bedding plane and Joint set 2 (J2) is capable to cause wedge failures in Sectors 3 and 9. The deterministic and probabilistic analyses were applied by using Swedge software. The 3D views of the blocks and the calculated results for deterministic (i.e., the factor of safety) and the probabilistic (i.e., probability of failure) analysis are given in Figures 61 to 68. For the probabilistic analysis of wedge failure, the parameters introduced based on their statistical distribution are slope face dip direction, slope face dip angle, dip directions of joint planes 1 and 2, dip angles of joint planes 1 and 2, JRC of set 1 and 2 and JCS of set 1 and 2.

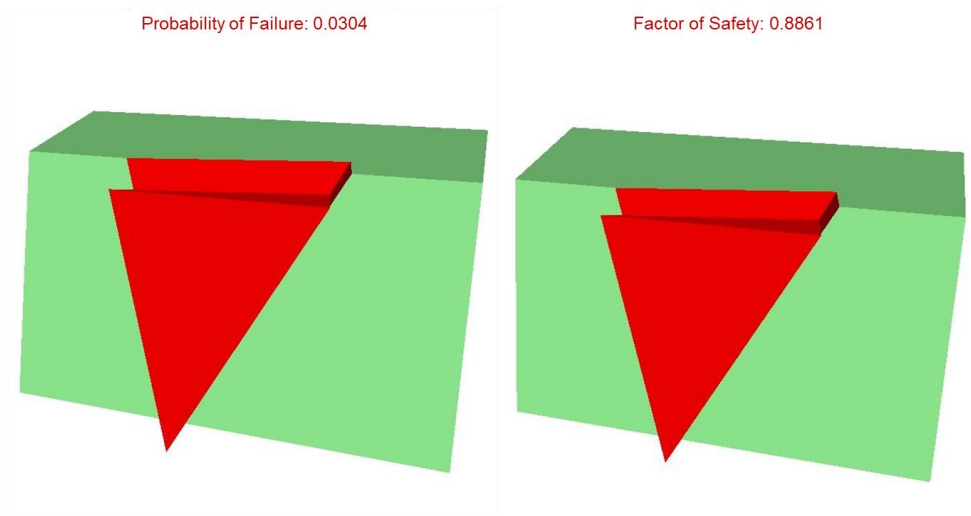


Figure 61: 3D view of the block generated in Sector 2 by Swedge software

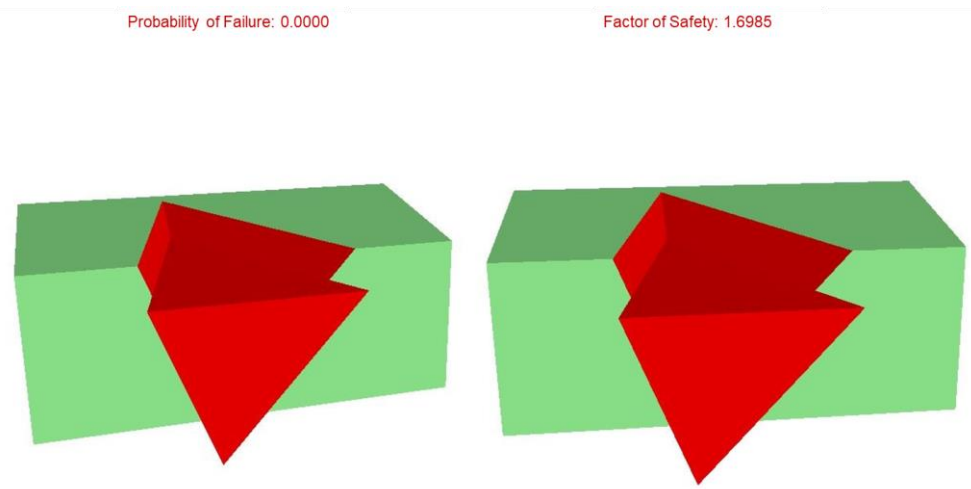


Figure 62: 3D view of the block generated in Sector 3 by Swedge software

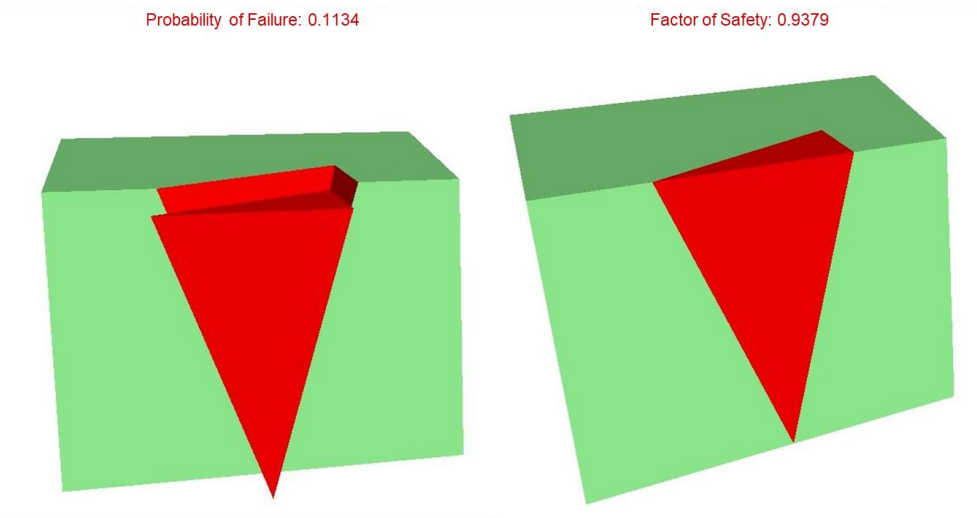


Figure 63: 3D view of the block generated in Sector 4 by Swedge software

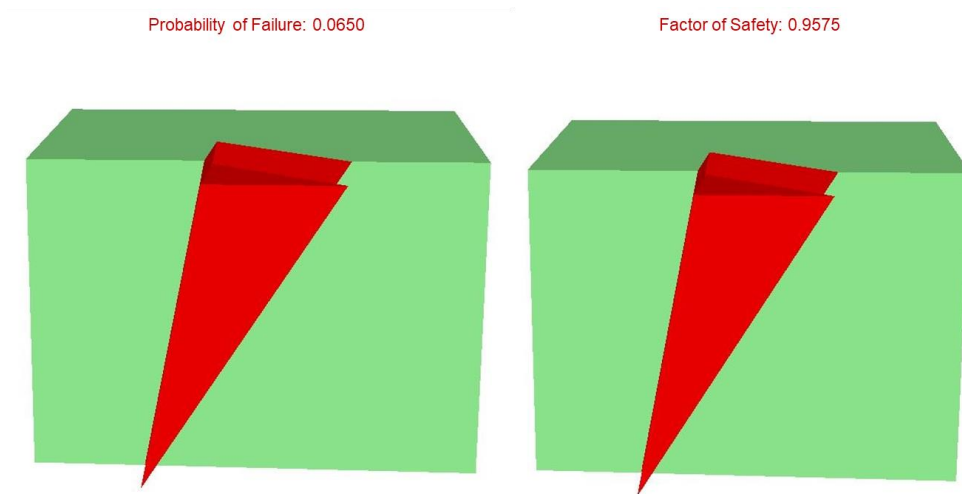


Figure 64: 3D view of the block generated in Sector 5 by Swedge software

Probability of Failure: 0.0605

Factor of Safety: 0.6250

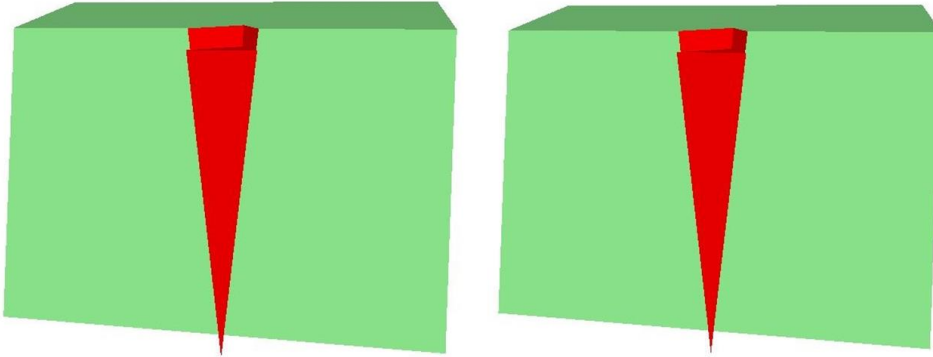


Figure 65: 3D view of the block generated in Sector 6 by Swedge software

Probability of Failure: 0.0605

Factor of Safety: 0.5259

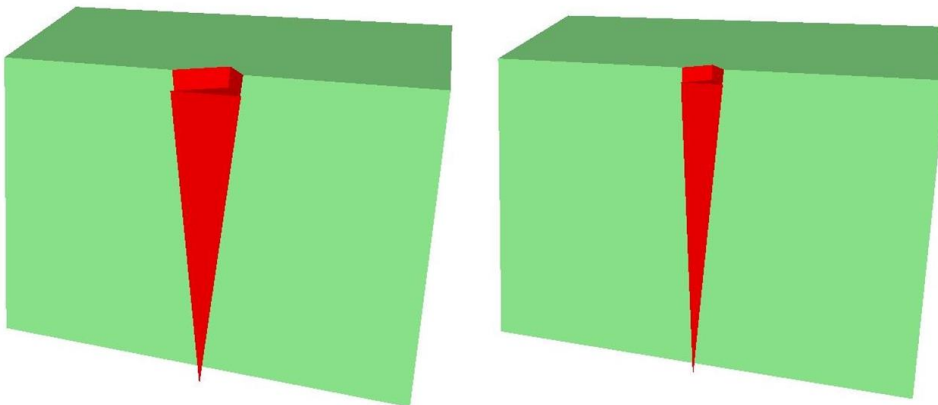


Figure 66: 3D view of the block generated in Sector 8 by Swedge software

Probability of Failure: 0.0000

Factor of Safety: 3.1148

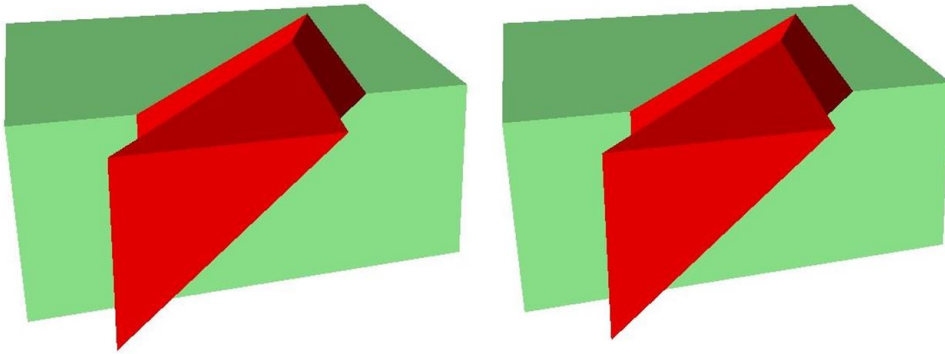


Figure 67: 3D view of the block generated in Sector 9 by Swedge software

Probability of Failure: 0.0576

Factor of Safety: 0.3865

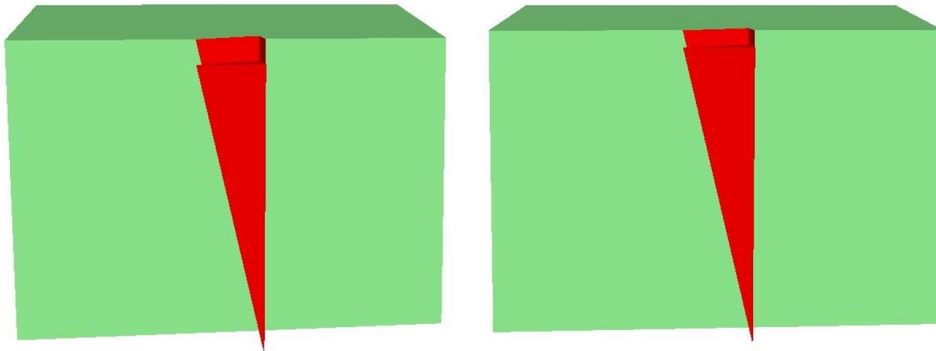


Figure 68: 3D view of the block generated in Sector 10 by Swedge software

The probability of failure and the factor of safety values of the kinematically possible sectors of wedge failure are given in Table 21.

Table 21: Comparison of the probabilistic and deterministic analysis of wedge failure

	Wedge failure					
	Probability of failure			Factor of safety		
	$I_{BP,1}$	$I_{BP,2}$	$I_{1,2}$	$I_{BP,1}$	$I_{BP,2}$	$I_{1,2}$
2	0	0	0.03	0	0	0.89
3	0	0	0	0	1.70	0
4	0	0	0.11	0	0	0.94
5	0	0	0.07	0	0	0.96
6	0	0	0.06	0	0	0.63
8	0	0	0.06	0	0	0.53
9	0	0	0	0	3.12	0
10	0	0	0.06	0	0	0.39

Unlike planar and wedge types of failures, a toppling failure entails rock columns or blocks rotating about a fixed point. Toppling failure occurs when the center of gravity of a block falls outside the dimension of its base (Norrish and Wyllie, 1996). The toppling failure potential of a block can be measured by its slenderness ratio which is the thickness (t) to height (h) ratio. The location of the resultant force of a block is controlled by this ratio (Kliche, 2018). Figure 69 shows the conditions required for sliding and toppling failure to develop. According to this figure, toppling failure can arise when $t/h < \tan\beta$.

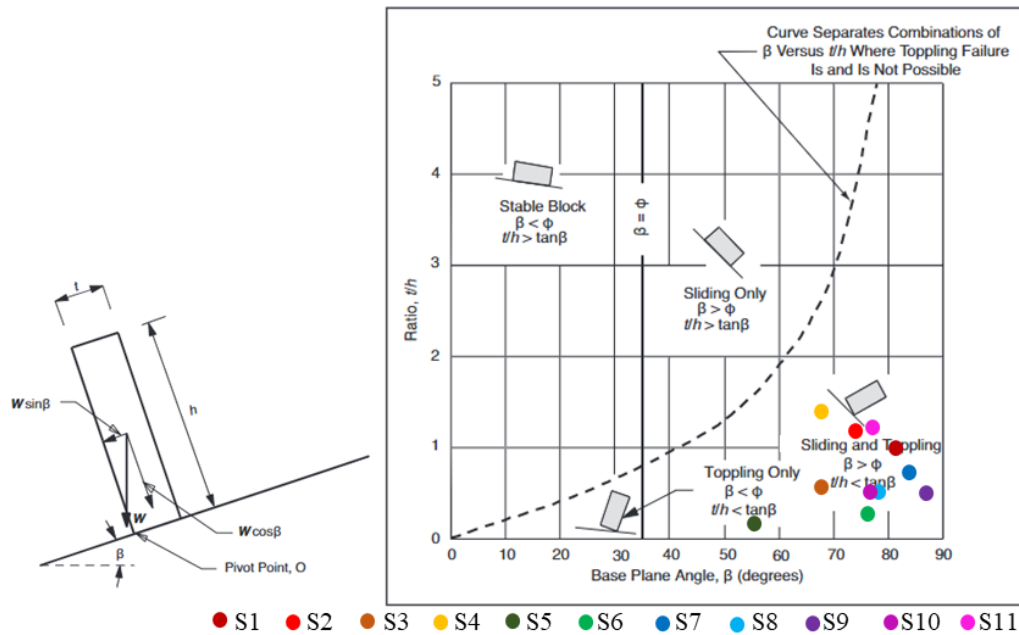


Figure 69: Sliding and toppling conditions of a block on an inclined plane (Hoek and Bray, 1981). Note that the condition of each sector were marked by a circle in different color

In the study area, Joint set 1 forms the base inclination and controls the height of the block. In addition, the Bedding plane defines the thickness of the block. This condition is applicable for all kinematically favorable sectors except Sector 3 where the base inclination and the height of the block are controlled by Joint set 2. By considering the block geometry and base plane angle, it has been defined that $t/h < \tan \beta$ and $\beta > \phi$ through out the valley slopes (Figure 69). Therefore, the movement type of the blocks has been identified as a “sliding and toppling” condition, which is concordant with the rock mass characteristics along the western side of the Mudurnu valley (Figures 42, 46, 47, 48, 49, 50, etc.).

4.4.1 Pseudo-static analysis

As it has been previously explained in Chapter 2.2, Mudurnu is located in a seismically active region. Therefore, the dynamic conditions of the stability analysis are crucial. In this dissertation, the dynamic force due to earthquakes was considered by pseudo-static analysis based on the TBEC (2019). The pseudo-static analysis is a modification of limit equilibrium analysis that has been developed to evaluate the stability of slopes under dynamic loading. Pseudo-static limit equilibrium of slopes incorporates the ground motion as a force that is effective out of the face direction (Wyllie, 2018). The magnitude of the horizontal force for the pseudo-static analysis is expressed by Equation 15 according to TBEC (2019):

$$F_H = Wk_h = 0.5W(0.4S_{DS}S_T) \quad (15)$$

where:

W is the weight of the block

k_h is the horizontal seismic load coefficient in terms of g

S_{DS} is the short period design spectral acceleration coefficient

S_T is the topographical amplification factor.

According to the Seismic Hazard Map of Turkey (TEHM, 2018) and Turkish Building Earthquake Code (TBEC, 2019), for a return period of 475 years (i.e., the probability of exceedance in 50 years is 10%) of a ZB class of material, S_{DS} was determined to be 0.87 and S_T was accepted as 1.4 since the slope face dip angle is greater than 30°. The details of the input parameters and the corresponding accelerations estimated based on the Seismic Hazard Map of Turkey and the Turkish Building Earthquake Code (TEHM, 2018 and TBEC, 2019) are given in Appendix

F. As a result, the seismic load coefficient (k_h) of the study area was estimated as 0.24g to evaluate the dynamic condition in the stability analysis.

The pseudo-static stability analysis of planar failure was applied by using both the deterministic and probabilistic options of the Rocplane software. The 2D views of the blocks and the calculated results for deterministic (i.e., the factor of safety) and probabilistic (i.e., probability of failure) analyses are given in Figures 70, 71, 72, 73, and 74. For the probabilistic analysis of planar failure, the parameters introduced based on their statistical distribution are slope face dip angle, failure plane dip angle, JRC and JCS. These parameters were found to be normally distributed based on the DSE methodology for the dip angles and field measurements for JRC and JCS. The normal distribution was used along with the mean, standard deviation, relative minimum and relative maximum values of each parameter to perform the probabilistic analysis.

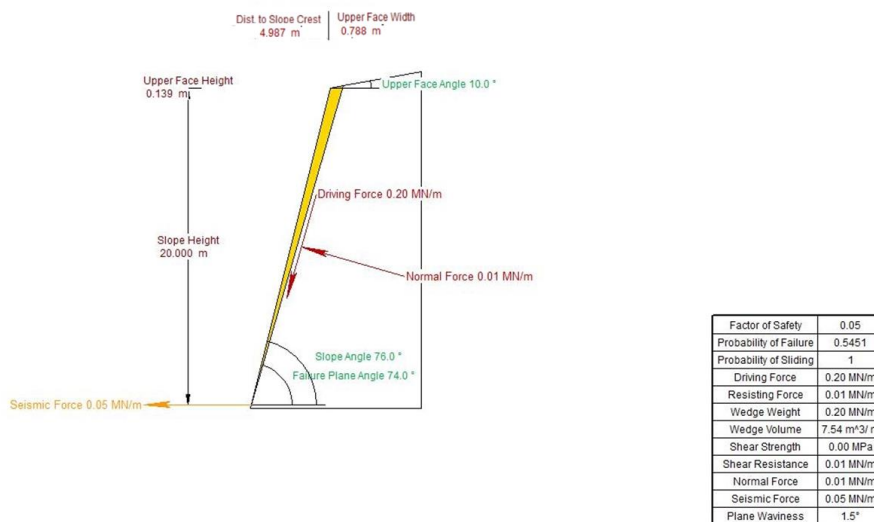


Figure 70: 2D view of the block generated for the pseudo-static analysis in Sector 2 by Rocplane software



Figure 71: 2D view of the block generated for the pseudo-static analysis in Sector 4 by Rocplane software

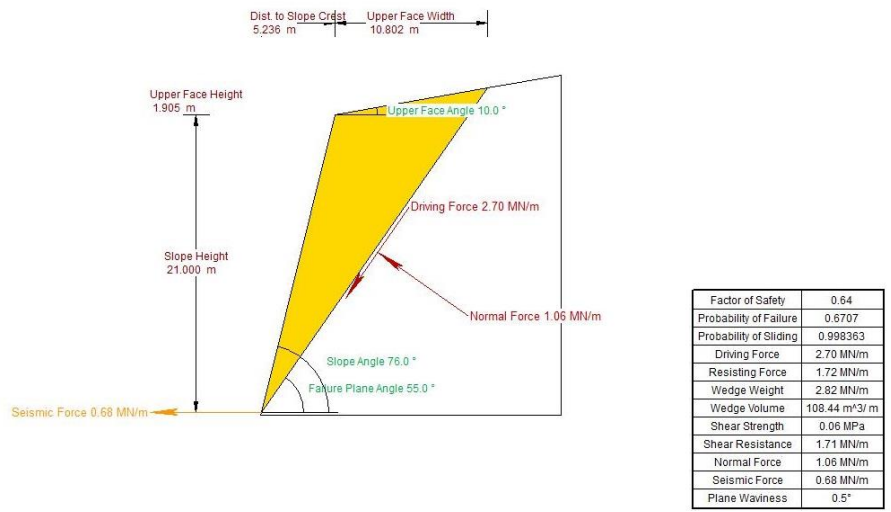


Figure 72: 2D view of the block generated for the pseudo-static analysis in Sector 5 by Rocplane software

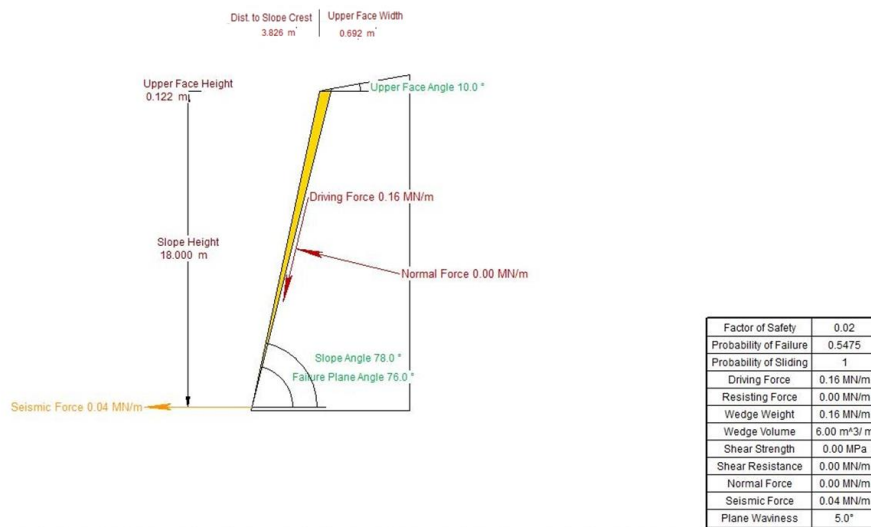


Figure 73: 2D view of the block generated for the pseudo-static analysis in Sector 6 by Rocplane software



Figure 74: 2D view of the block generated for the pseudo-static analysis in Sector 8 by Rocplane software

The probability of failure and the factor of safety values of the kinematically possible sectors of planar failure under dynamic loading conditions are given in Table 22.

Table 22: Comparison of the probabilistic and deterministic analysis results of planar failure under dynamic loading conditions

	Planar failure					
	Probability of failure			Factor of safety		
	BP	J1	J2	BP	J1	J2
2	0	0.55	0	0	0.05	0
4	0	0.92	0	0	0.20	0
5	0	0.67	0	0	0.64	0
6	0	0.55	0	0	0.02	0
8	0	0.54	0	0	0	0

The dynamic (i.e., pseudo-static) stability analysis of wedge failure was implemented by using Swedge software by both deterministic and probabilistic approaches. The 3D views of the blocks and the calculated results for deterministic (i.e., the factor of safety) and probabilistic (i.e., probability of failure) analysis are given in Figures 75 to 82. For the probabilistic analysis of the wedge failure, the parameters introduced based on their statistical distribution are slope face dip direction, slope face dip angle, dip directions of joint planes 1 and 2, dip angles of joint planes 1 and 2, JRC of set 1 and 2, and JCS of set 1 and 2. These parameters were found to be normally distributed based on the DSE methodology for the dip directions and dip angles, and field measurements for JRC and JCS. The normal distribution was used along with the mean, standard deviation, relative minimum and relative maximum values of each parameter to perform the probabilistic analysis.

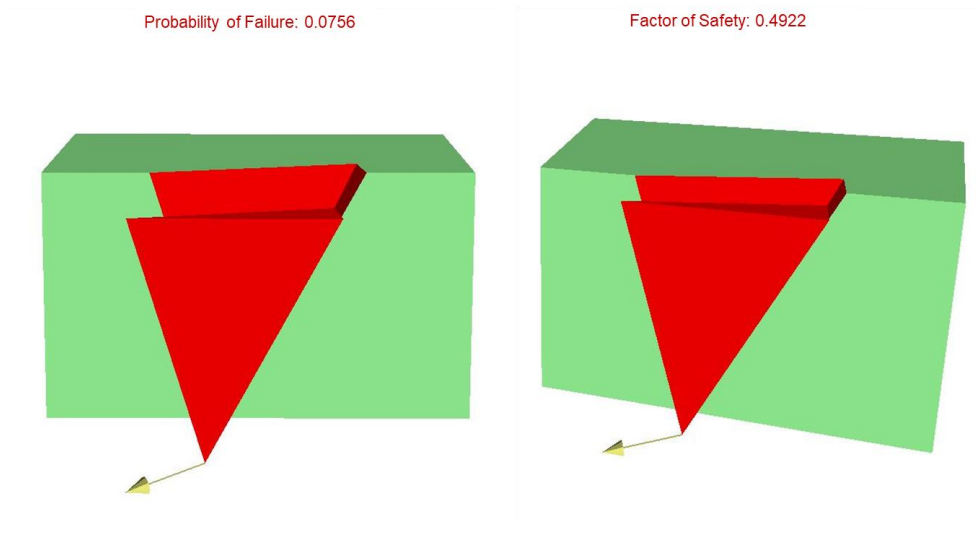


Figure 75: 3D view of the block generated for the pseudo-static analysis in Sector 2 by Swedge software

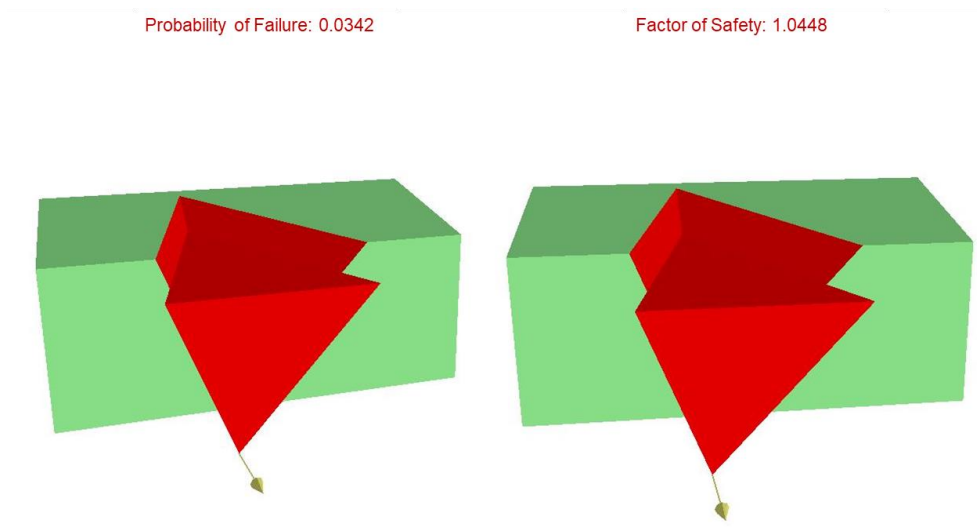


Figure 76: 3D view of the block generated for the pseudo-static analysis in Sector 3 by Swedge software

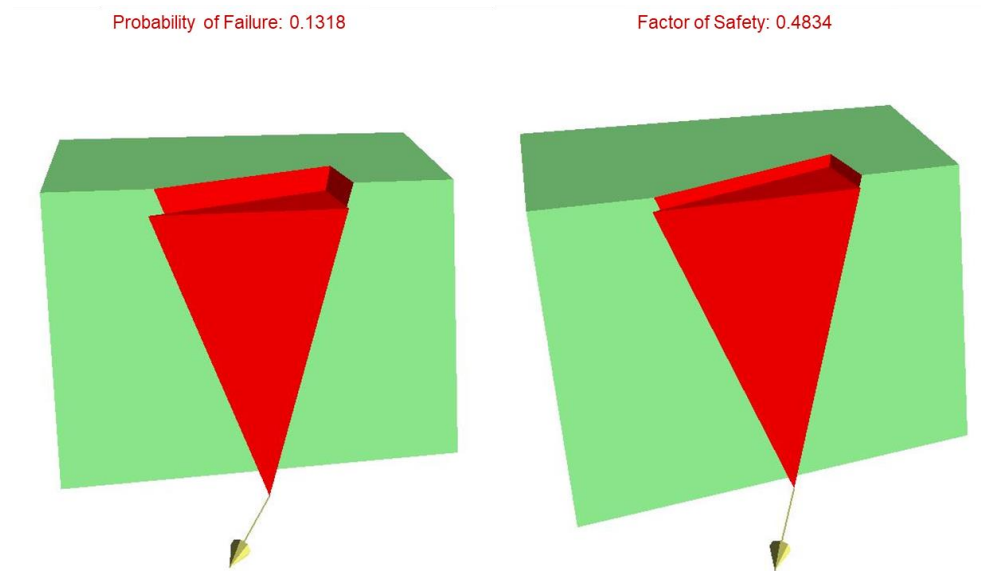


Figure 77: 3D view of the block generated for the pseudo-static analysis in Sector 4 by Swedge software

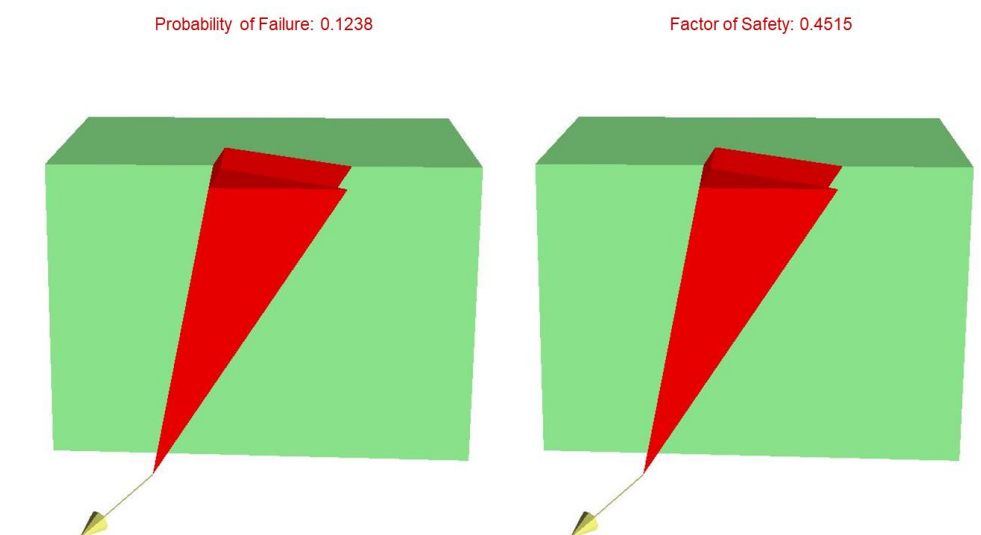


Figure 78: 3D view of the block generated for the pseudo-static analysis in Sector 5 by Swedge software

Probability of Failure: 0.0605

Factor of Safety: 0.0762

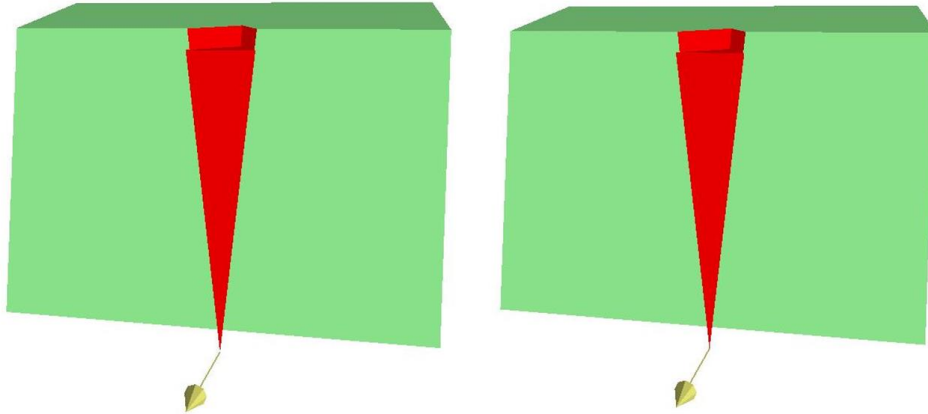


Figure 79: 3D view of the block generated for the pseudo-static analysis in Sector 6 by Swedge software

Probability of Failure: 0.0605

Factor of Safety: 0.0000

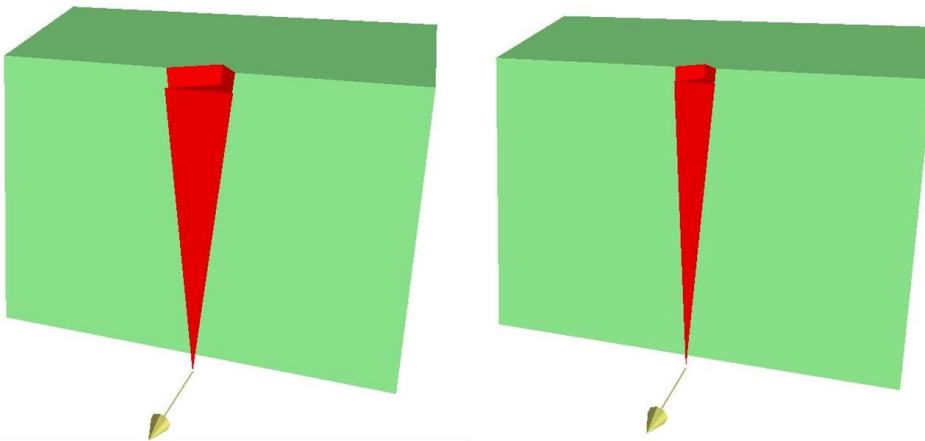


Figure 80: 3D view of the block generated for the pseudo-static analysis in Sector 8 by Swedge software

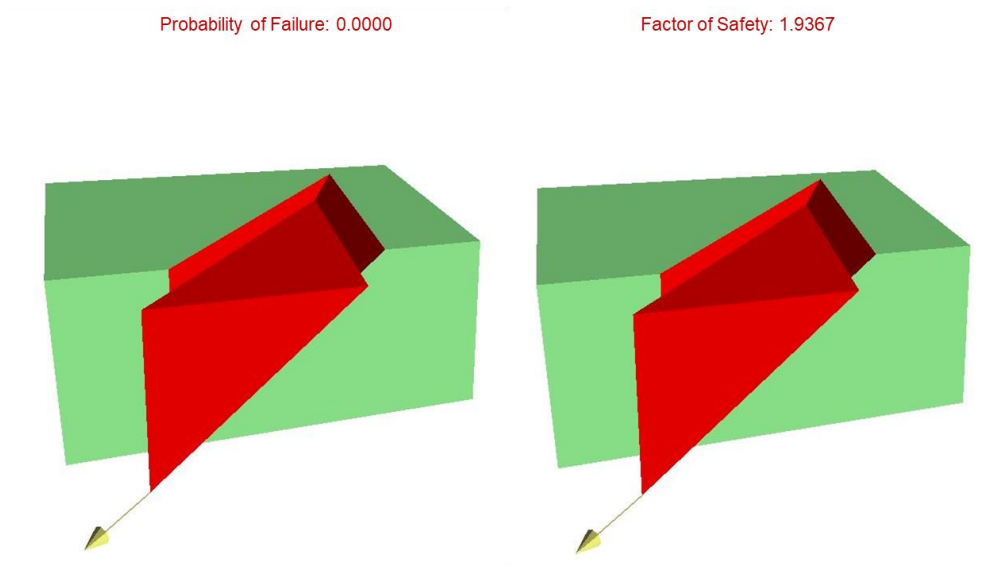


Figure 81: 3D view of the block generated for the pseudo-static analysis in Sector 9 by Swedge software

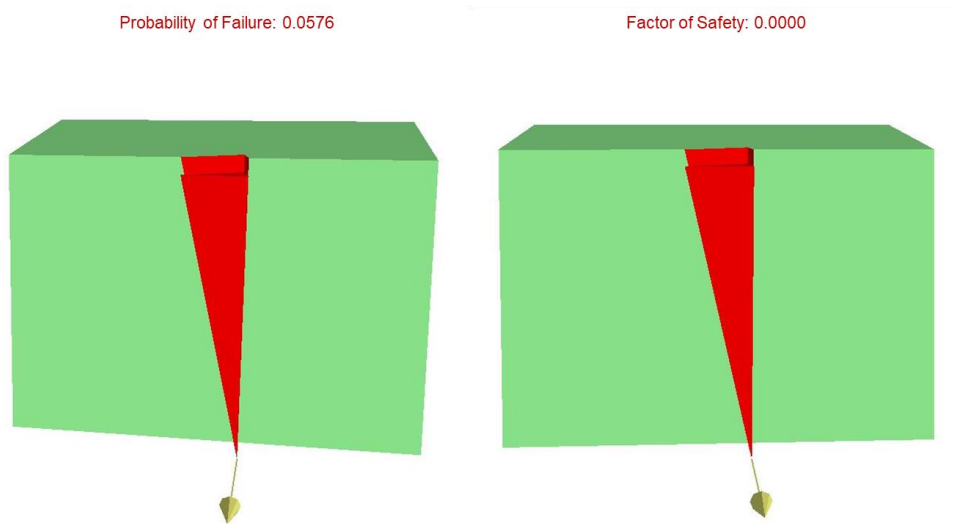


Figure 82: 3D view of the block generated for the pseudo-static analysis in Sector 10 by Swedge software

The probability of failure and the factor of safety values of the kinematically possible sectors of wedge failure under dynamic loading conditions are given in Table 23.

Table 23: Comparison of the probabilistic and deterministic analysis results of wedge failure under dynamic loading conditions

	Wedge failure					
	Probability of failure			Factor of safety		
	$I_{BP,1}$	$I_{BP,2}$	$I_{1,2}$	$I_{BP,1}$	$I_{BP,2}$	$I_{1,2}$
2	0	0	0.08	0	0	0.49
3	0	0.03	0	0	1.04	0
4	0	0	0.13	0	0	0.48
5	0	0	0.12	0	0	0.45
6	0	0	0.06	0	0	0.08
8	0	0	0.06	0	0	0
9	0	0	0	0	1.94	0
10	0	0	0.06	0	0	0

4.5 Evaluation of the results of the rock slope stability assessment analysis

The identified rock slope sectors on the west of Mudurnu county center were classified empirically by Q-slope and SMR. According to the Q-slope classification, all of the sectors along the valley were unstable except Sector 7. In terms of planar failure, SMR analysis revealed that Sectors 1 and 7 were stable; whereas Sectors 3, 9, 10, and 11 were stable with local block failures; Sectors 4, 5, and 8 were partially stable with failures along some joints; and Sectors 2 and 6 were unstable. Based on the kinematic analysis, planar failure was possible through Joint set 1 in Sectors 2,

4, 5, 6, and 8. The partially stable and unstable sectors identified by SMR were concordant with the kinematically possible sectors. Limit equilibrium analyses revealed that the blocks were unstable in all kinematically probable failure sectors. In general, the probability of failure (POF) obtained from limit equilibrium analyses were in good agreement with the empirical results. However, limit equilibrium analyses resulted in a higher POF in Sector 4 and a lower POF in Sector 5.

Concerning wedge failure, SMR revealed that most of the sectors possessed a probability of failure of 0.2. Specifically, according to SMR, Sectors 1 and 7 were completely stable; Sectors 2, 3, 4, 5, 6, 9, 10, and 11 were stable with local block failures; and Sector 8 was unstable. Based on the kinematic analysis, wedge failure was possible along the intersection of Joint set 1 and Joint set 2 in Sectors 2, 4, 5, 6, 8, and 10. In addition, in Sectors 3 and 9, wedge failure was determined to be kinematically possible along the intersection of the Bedding plane and Joint set 2. The failure-prone sectors identified by SMR were concordant with the kinematically possible sectors except Sector 11. Kinematic analysis showed that there is no wedge failure in Sector 11. Limit equilibrium analyses revealed that the blocks were unstable in Sectors 2, 4, 5, 6, 8, and 10. From a kinematical point of view, Sectors 3 and 9 were stable in static conditions but unstable in Sector 3 under dynamic loading conditions. In general, the probability of failures (POF) obtained from limit equilibrium analyses was lower than the empirical results.

In the case of toppling failure, SMR revealed that Sector 7 was completely stable; Sectors 2, 3, 5, 8, 9, 10, and 11 were stable with some local block failures; Sectors 1, 4, and 6 were partially stable with the possibility of failure along some joints. Based on the kinematic analysis, toppling failure was possible along the Bedding plane in Sectors 1, 2, 3, 4, 5, 6, 8, 10, and 11. Although according to SMR, Sector 9 had a probability of failure of 0.2, the kinematic analysis showed no possibility of toppling failure for this sector. In addition, the toppling failure potential of the blocks was

evaluated by considering block geometry. Accordingly, the movement types of all the blocks have been identified as sliding and toppling.

The probability of failure and the factor of safety values obtained from the limit equilibrium analysis revealed that the stability of the slopes changed under dynamic loading conditions. In general, when the seismic force was introduced, the analyses resulted in a higher probability of failure and a lower factor of safety. In terms of planar failure, Sector 5 tends to become more susceptible to dynamic loading. In the case of wedge failure, the failure susceptibility of Sectors 2, 4, and 5 tended to increase. Moreover, by the effect of the seismic force, wedge failure became possible in Sector 3, which was stable under static conditions. Therefore, it was concluded that the influence of the dynamic load was more intense for wedge failure as compared to planar failure. Moreover, the dynamic load has also been expected to change the stability of toppling blocks significantly due to the geometry of blocks and the presence of the undermining effect. In conclusion, introducing dynamic force in the stability analysis tends to increase the susceptibility to planar, wedge, and toppling failures as expected. Thus, the hazard potential originating from these failures is expected to be higher.

CHAPTER 5

HAZARD ASSESSMENT OF THE DISCONTINUOUS ROCK SLOPE INSTABILITY

Susceptibility is the tendency of a location to experience a certain event such as rock sliding (Glade et al., 2005). Rock slope susceptibility is a function of the combined effects of the inherent stability of the slope and other factors capable to reduce the strength or increase the stress. Hazard can be stated as the probability of occurrence of an event with a given magnitude that has damage potential to occur in a unit of time (Glade et al., 2005). It is important to identify the magnitude since the probability is controlled by the magnitude of the event. In general, small events tend to develop more frequently than large ones. Within the scope of this dissertation, rock slope failure susceptibility zones in terms of different failure types (i.e., planar, wedge, toppling) and the related hazard zones have been identified.

There are several qualitative and quantitative methods that have been proposed for the spatial analysis of slope instabilities. GIS-based hazard assessment methods can be classified into four approaches such as i) inventory-based analysis, ii) heuristic analysis, iii) statistical analysis and iv) deterministic approach (Soeters and Van Westen, 1996; Van Westen et al., 2006). In the Mudurnu region, a number of previous failures (i.e., rock instabilities, seismic events) that occurred in the area have been reported. However, in general, reports do not include the exact location and time of the events. Therefore, a proper magnitude-frequency relation that needs to be considered for hazard assessment is not available. Although quantitative values were available for the stability conditions of the sectors along with some of the other parameters considered in the hazard assessment in Mudurnu, a heuristic model has been employed due to the lack of a well-documented inventory as mentioned above. This approach is a method based on prior knowledge in which local experiences and

expert judgment are included. This approach uses spatial information of topographic, hydrological, geological, geotechnical, geomorphological factors, and land use when considered (Glade et al., 2005). The importance of different factors was identified and weighted according to personal knowledge and experience which tends to provide an initial assessment of susceptibility. Note that using qualitative weighting is a limitation of the heuristic method since the weightings depend on the experience of the researcher. However, the heuristic approach is capable to be accurate and applicable, especially for the initial approximations of susceptibility if the expert has detailed knowledge of the area under question and has a deep understanding of the processes (Glade et al., 2005). Since the scale of the study area was suitable and the engineering geological characteristics, as well as the stability, were considered in detail along the entire valley, using the heuristic approach in Mudurnu seemed reasonable. As a result, susceptibility zones for planar, wedge, and toppling failures were directly identified. According to Corominas et al. (2014), it is also possible to apply heuristics methods indirectly through utilizing GIS together with several factor maps that need to be considered for failure. To include the influence of all the possible factors that can be effective in the study area, and hence, to accomplish a complete hazard assessment, the heuristic method has been indirectly employed through utilizing maps of different parameters which are explained in the following paragraphs.

By considering the parameters proposed by previous researchers (Parise, 2002; Ercanoğlu and Gökçeoğlu, 2004; Ayalew and Yamagishi, 2005; Çan et al., 2005; Gökçeoğlu et al., 2005; Erener and Düzgün, 2010; Syafril et al., 2020; Omran et al., 2021) and by adopting the suitable parameters for the study area in terms of failure type, the scale of the study and available data, major factors required for the hazard assessment in the study area were selected. These factors were geological and engineering geological parameters (i.e., lithology, degree of weathering, block size) and topographical parameters (i.e., slope angle, aspect, surface water) along with

travel distance and temporal frequency. In addition, the seismic loading conditions were taken into account as a triggering factor (Figure 83).

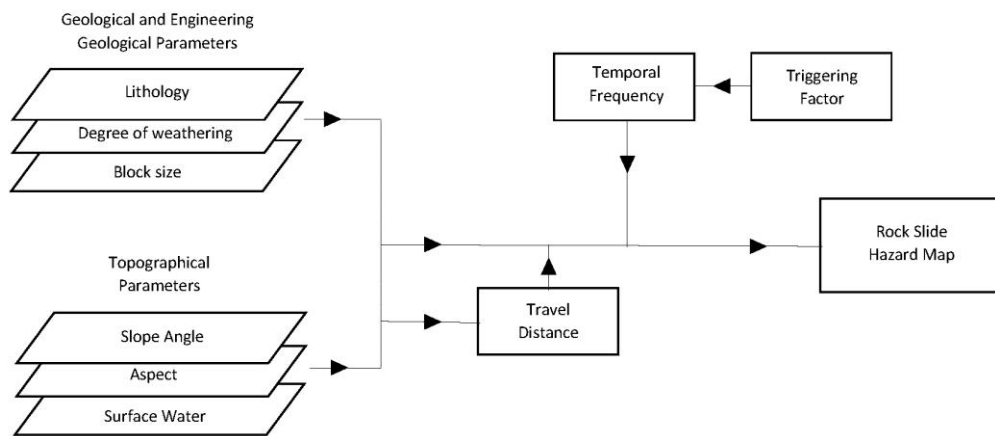


Figure 83: Flowchart of the discontinuous rock slope hazard assessment

The parameters and explanation of classes attributed to these parameters are given in Table 24. Lithologies that outcrop in the study area were identified in the field by consulting the H26 - Adapazari sector of 1/100.000 scaled geological maps prepared by MTA (2002). Figure 84 shows the boundaries of the lithologies as observed in the field. The degree of weathering was classified according to the field studies and UAV images. The degree of weathering classes assigned to sectors are given in Figure 85. Block sizes are based on the discontinuity spacing distributions obtained from the 3D point cloud and field observations. Block sizes attributed to the sectors are shown in Figure 86. Topographical factors such as slope and aspect were

extracted from the DEM (Figure 87) that is generated from the 3D point cloud. Figures 88 and 89 give the slope and aspect maps generated by the ArcGIS software (ESRI, 2022), respectively. Similar to the other topographical parameters, surface water drainage pattern was generated from the DEM in the ArcGIS software (ESRI, 2022). In addition, field observations regarding surface water drainage were taken into account. The generated surface water drainage pattern is given in Figure 90 and the buffer zones that define the distance from the drainage lines are shown in Figure 91. As mentioned, a well-documented inventory for the rock slope failures is not available for the area. Therefore, the temporal frequency was decided qualitatively by considering the failure stability analysis results together with the events reported to AFAD, experiences of local people, field observations, and changes detected between the field studies. Since 2017, when Mudurnu had been decided as the study area, at least a couple of field studies have been conducted each year, except in 2020. The rock masses and failures were observed, measured spatially, and photographed during these field studies. Consequently, the possible number of events was estimated qualitatively per sector. Since the temporal frequency of different failure types varies, a separate layer was prepared for each failure type (i.e., planar, wedge and toppling). Figures 92, 93, and 94 show the zones that are prone to planar, wedge, and toppling failures, respectively. The travel distance of the blocks was estimated from the field studies and UAV images. The buffer zones introduced to classify the distance from the discontinuous slope faces are given in Figure 95.

Table 24: Classification of the parameters employed in the hazard assessment

Factor	Parameter	Attribute	Relative value
Geology and engineering Geology	Lithology	Limestone	High
		Flysch	Moderate
		Alluvium	Low
	Degree of weathering	Highly weathered	High
		Moderately weathered	Moderate
		Slightly weathered	Low
	Block size (m ³)	>10 (Large)	High
		5-10 (Medium)	Moderate
		1-5 (Small)	Low
Topography	Slope angle (°)	>70	High
		45-70	Moderate
		<45	Low
	Aspect (Slope face orientation)	075-105	High
		045-074	Moderate
		185-220	Low
	Surface water (m) (Distance to drainage lines)	<2	High
		2-5	Moderate
		>5	Low
Slide occurrences	Temporal frequency (Probability of failure)	greater than 2	High
		1 to 2	Moderate
	Travel (runout) distance of sliding blocks (m)	0.1 to 1	Low
		>40	High
		20-40	Moderate
	<20	Low	

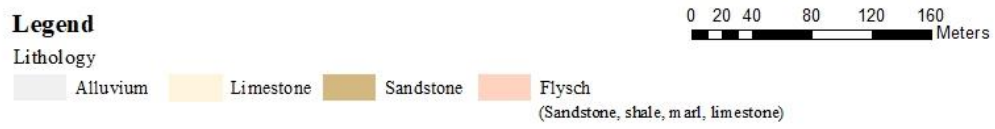





Figure 84: Lithology classes identified in the study area



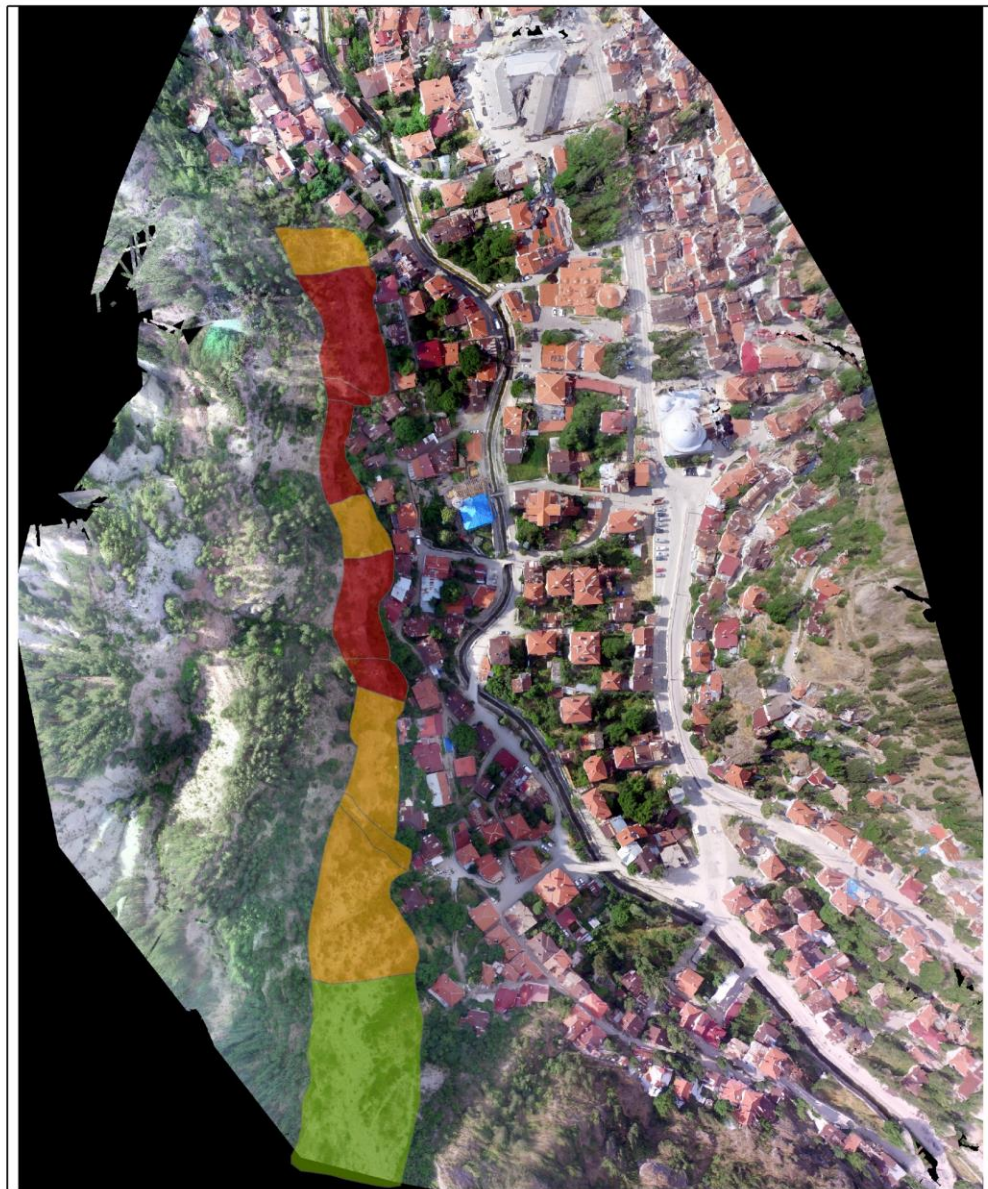
Legend

Degree of weathering

 Slightly weathered	 Moderately weathered	 Highly weathered
--	--	---

0 15 30 60 90 120 Meters

Figure 85: Degree of weathering classes in the study area



Legend

Block size

- Large Medium Small

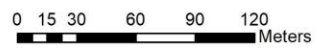
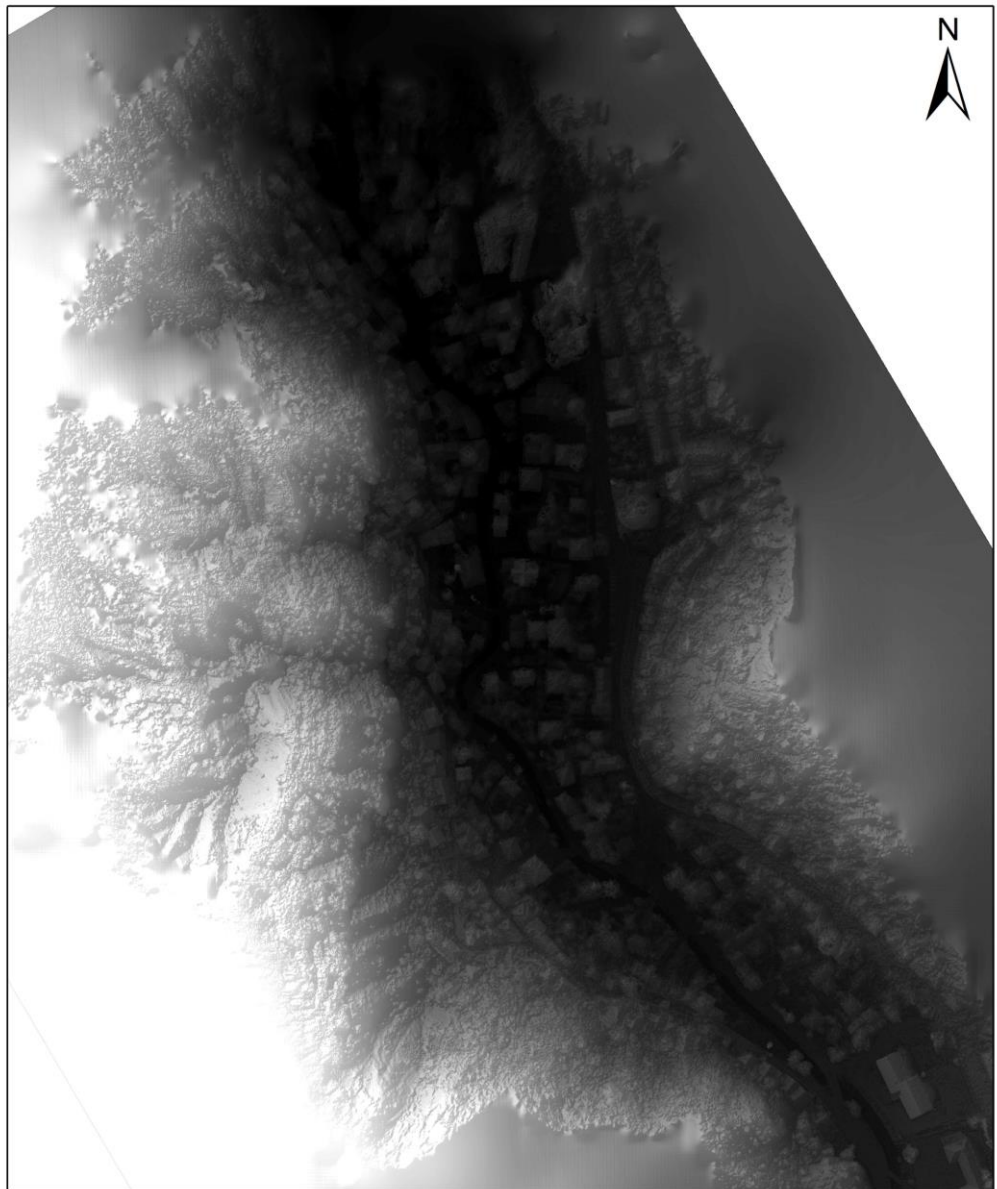


Figure 86: Block size classes of the study area

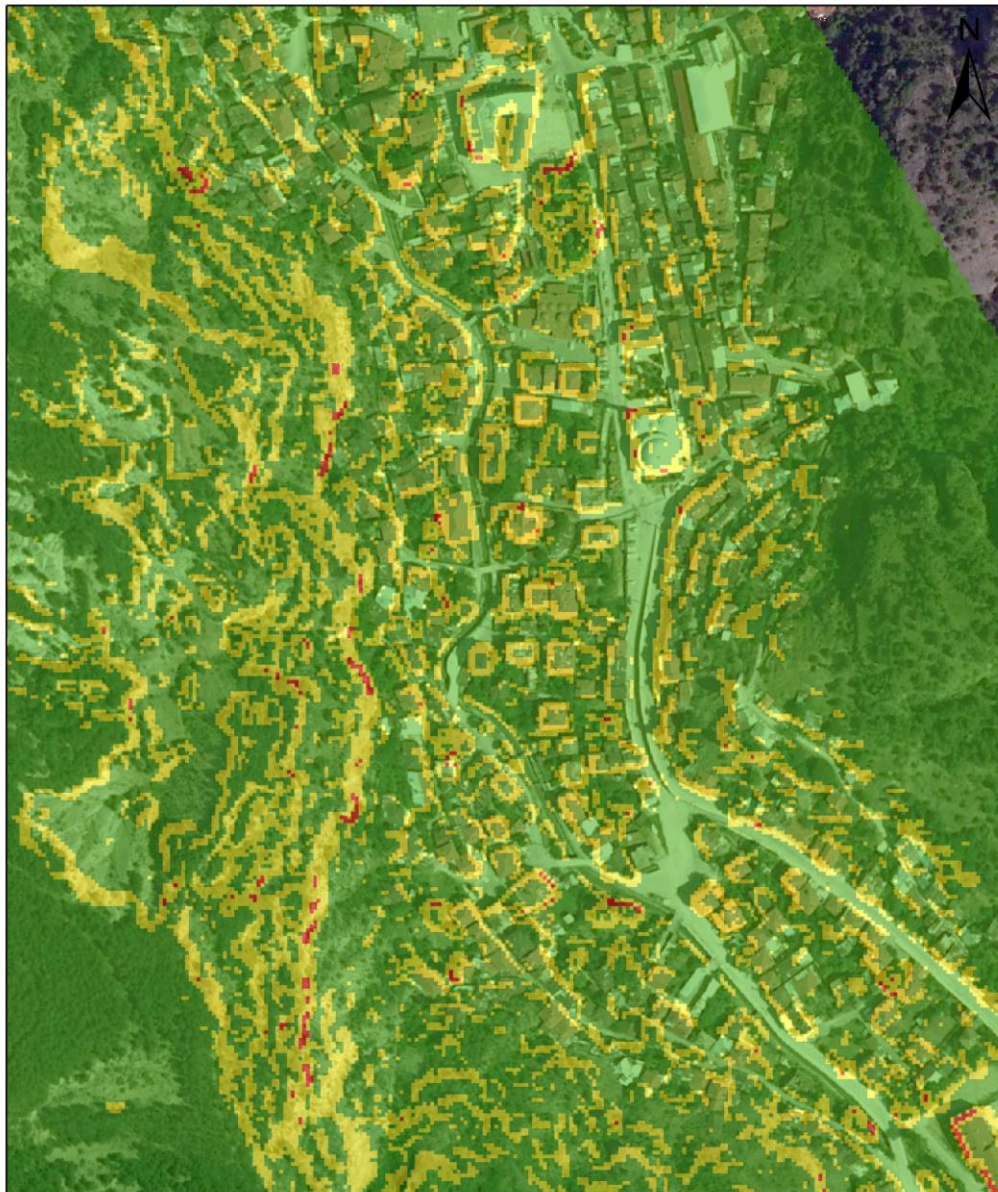


Legend

DEM
High : 1000 m
Low : 844 m

0 20 40 80 120 160 Meters

Figure 87: Digital Elevation Model (DEM) of the study area generated from the 3D point cloud



Legend

Slope (Degree)

0 - 45 45 - 70 70 - 90

0 15 30 60 90 120
Meters

Figure 88: Slope map of the study area extracted from the DEM

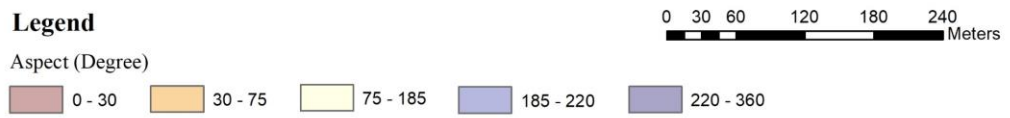
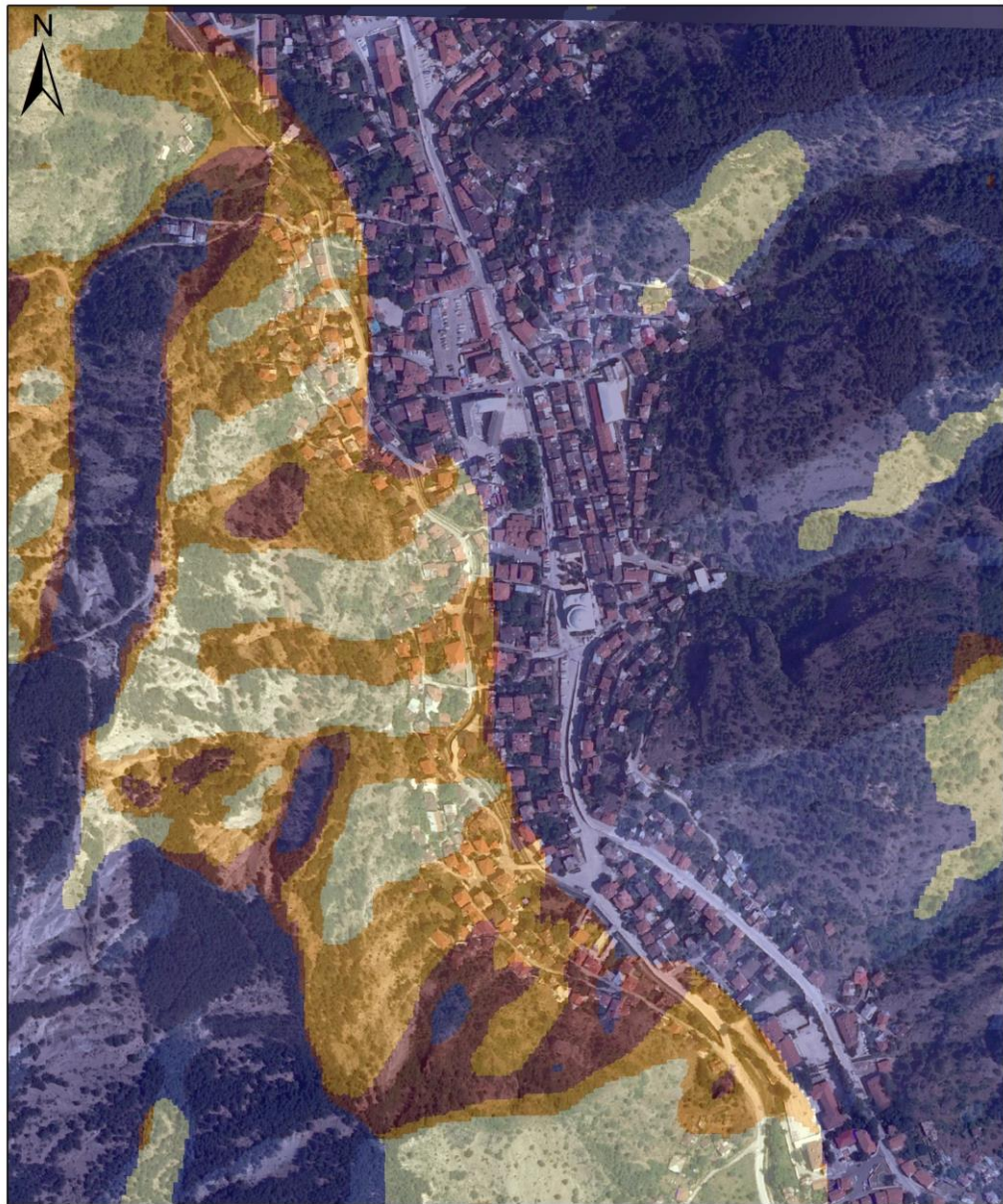


Figure 89: Aspect map of the study area extracted from the DEM

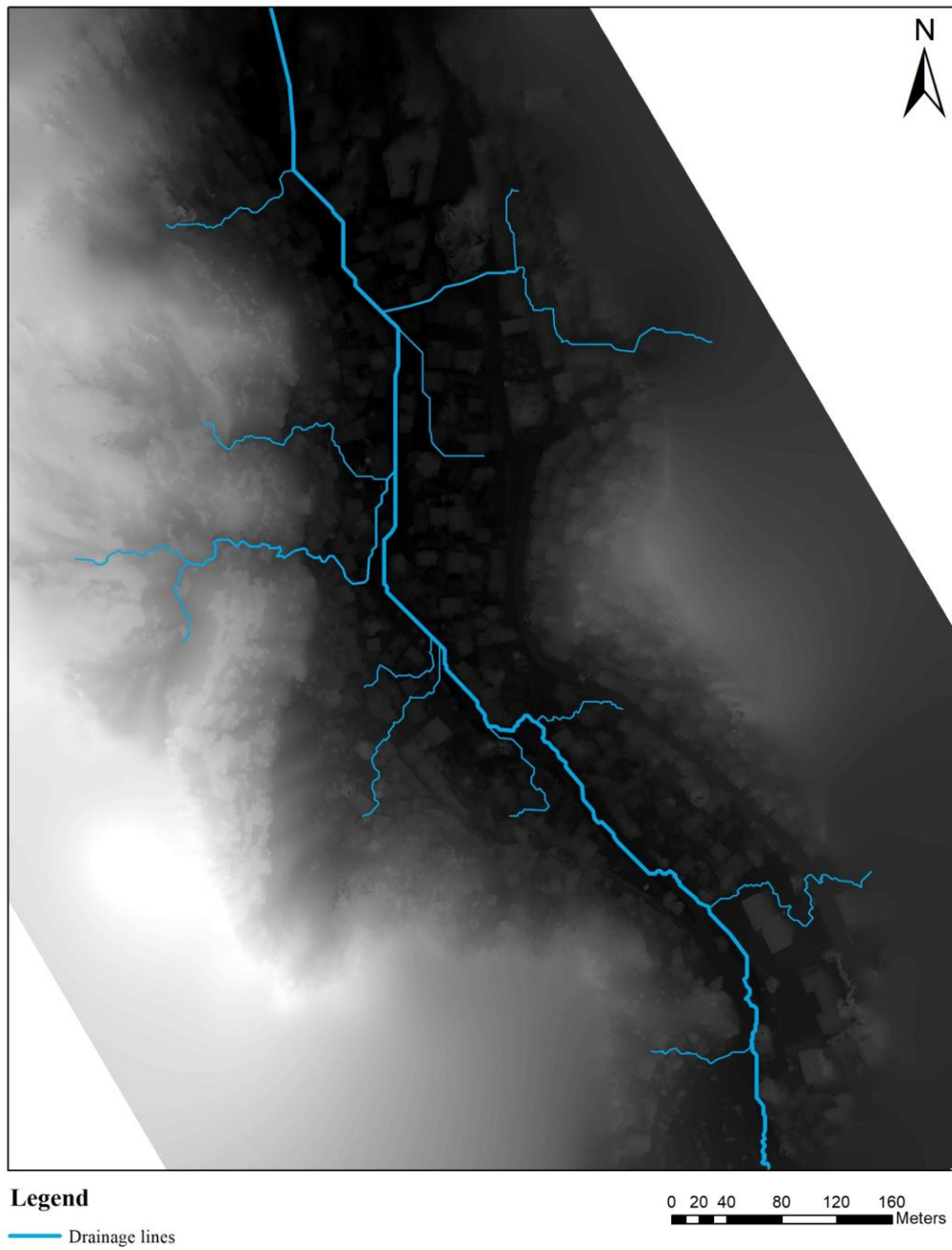
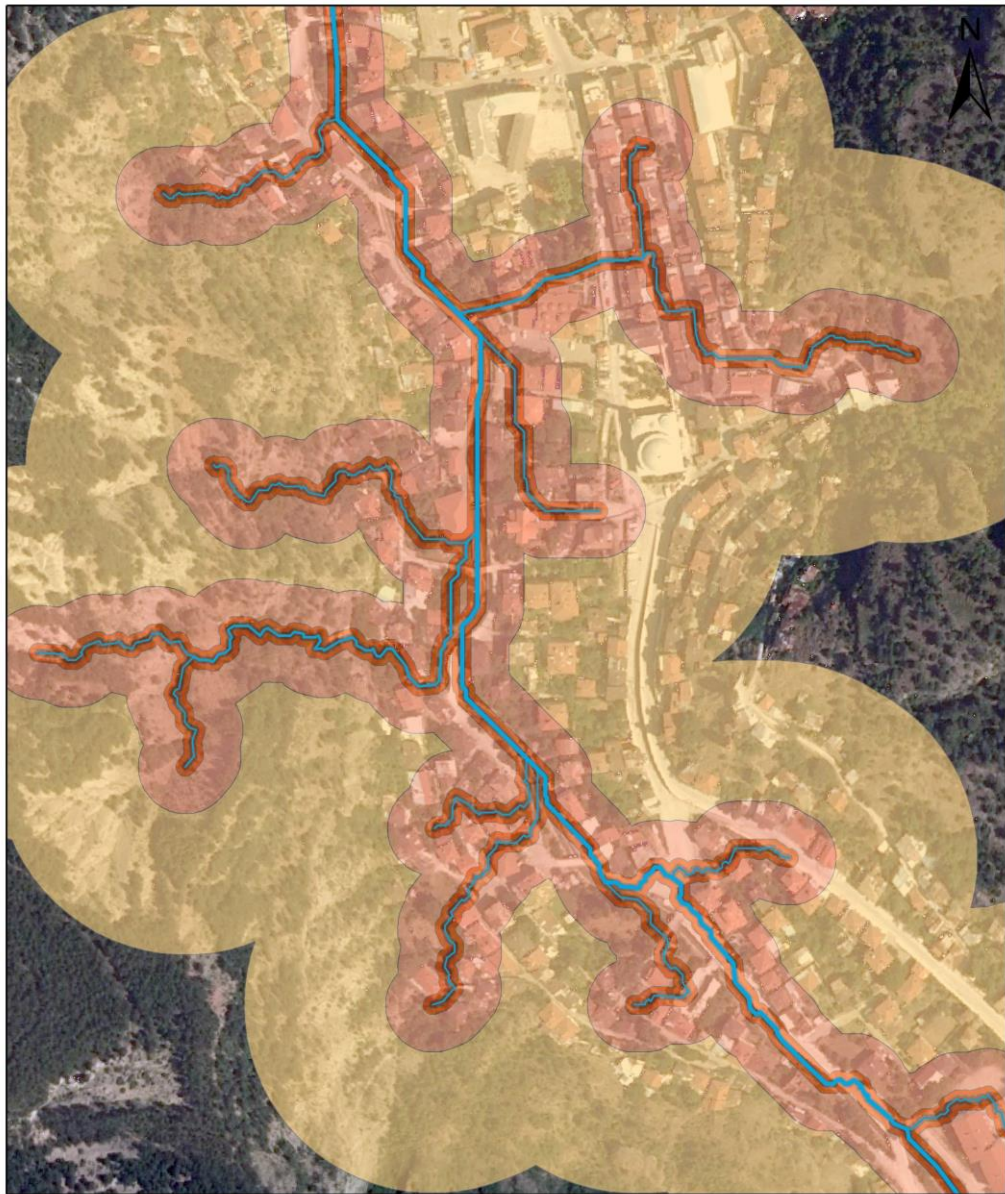


Figure 90: Surface water drainage pattern of the study area extracted from the DEM



Legend

— Drainage lines

Distance to drainage lines

2 m

2 m - 5 m

5 m - 25 m

>25 m

0 15 30 60 90 120 Meters

Figure 91: Zones showing the distance to the drainage pattern

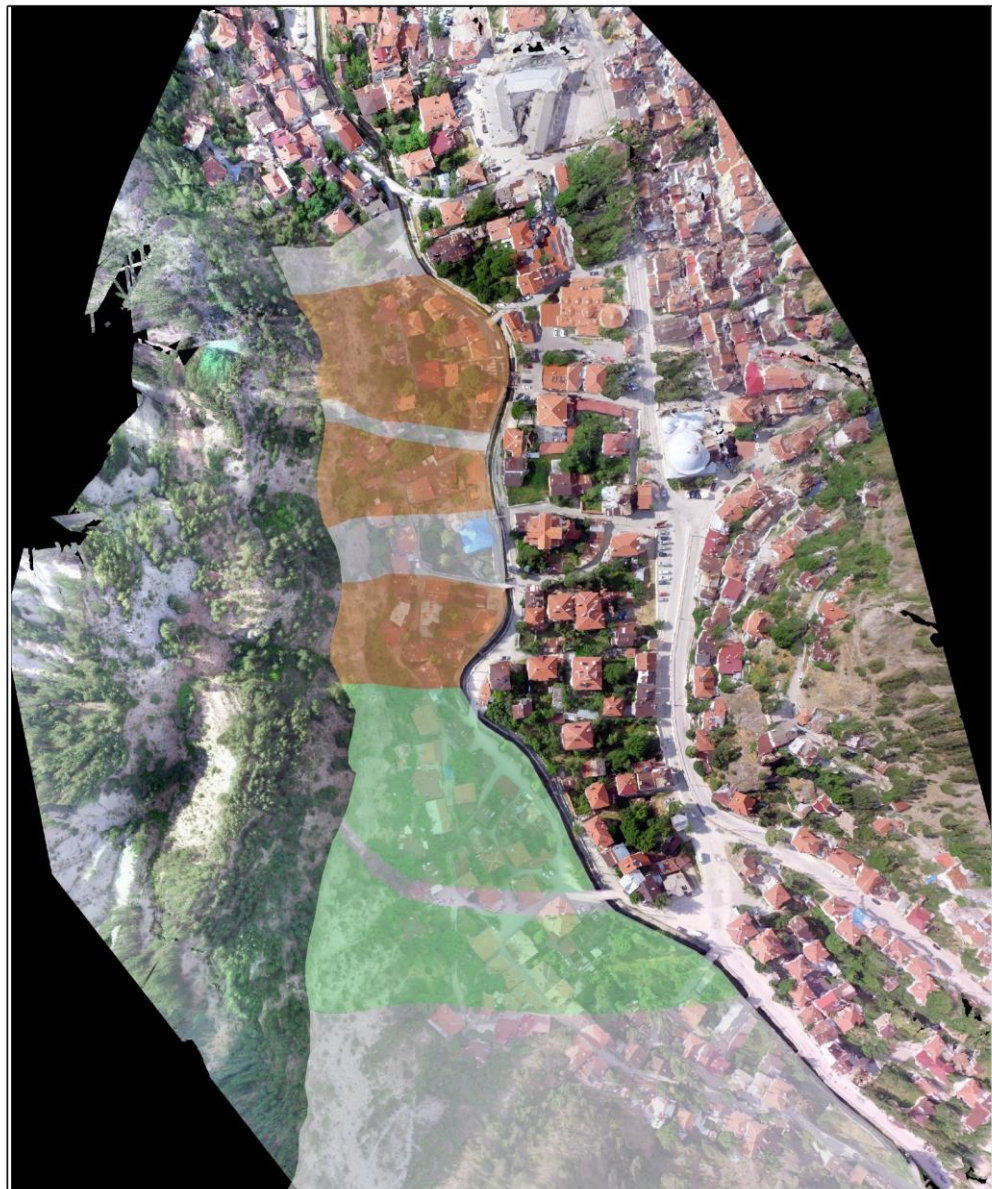


Legend

High Medium None

0 15 30 60 90 120 Meters

Figure 92: Planar failure-prone zones of the study area



Legend

Medium Low None

0 15 30 60 90 120 Meters

Figure 93: Wedge failure-prone zones of the study area



Legend

- High
- Medium
- Low
- None

0 15 30 60 90 120
Meters

Figure 94: Toppling failure-prone zones of the study area

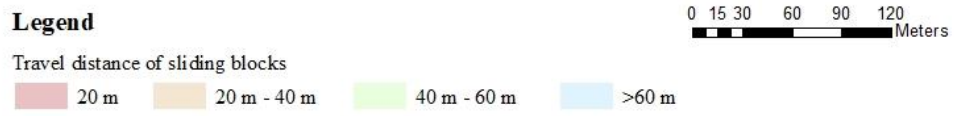


Figure 95: Zones showing the distance to the sliding blocks from the discontinuous slope face

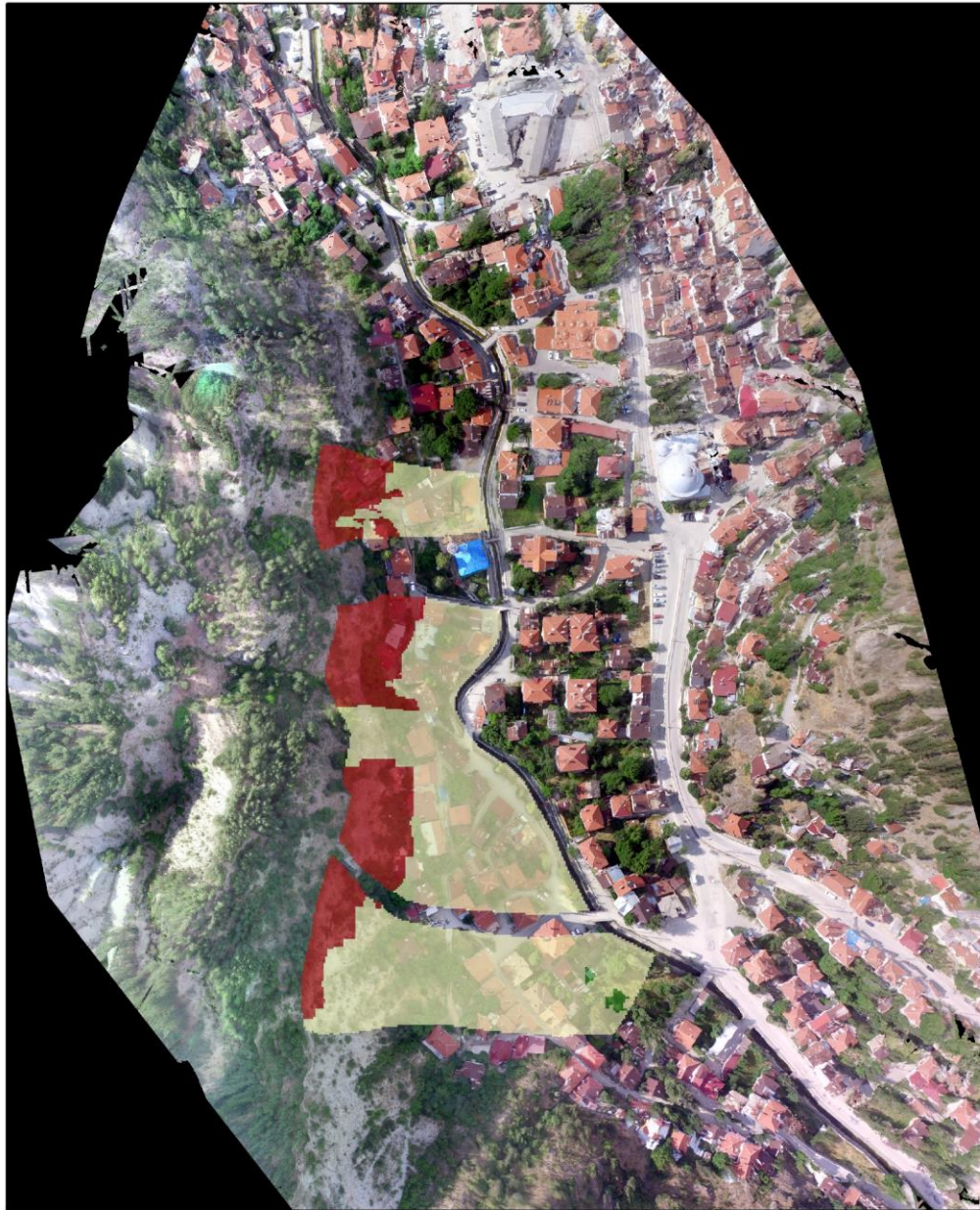
A relative weighting value assigned to each parameter map employed in hazard assessment is given in Table 25. The highest weight was assigned to aspect that controls the failure possibility of kinematically controlled rock slides. This was followed by the travel distance which defines the damage potential by considering the locations where people or buildings may be affected. Block size and temporal frequency had the third order of importance. The parameter that followed them was slope angle. It should be noted that the slope angle is a significant factor that needs to be considered in slope stability-related assessments. However, slope angles on the western side of Mudurnu county center did not change dramatically between the sectors. Therefore, this parameter was assigned a weight high enough to show its importance in the Mudurnu region. Lithology, degree of weathering, and surface drainage parameters had the lowest weight. Lithology was also assigned a low weight since the failure mechanism in the study area is related to rock mass discontinuities. Besides, all the sectors have the same lithology, which is limestone. The weight of the degree of weathering was assigned based on the field observations and the Slake Durability test results. Surface drainage was given a low weight because of the field observations. Surface water drainage was primarily encountered at only one location during the spring season due to snow melt.

Table 25: Weight of the parameters employed in the hazard assessment

Parameter	Weight
Lithology	1
Degree of weathering	1
Block size	3
Slope angle	2
Aspect (Slope face orientation)	5
Surface water	1
Temporal frequency	3
Travel distance	4

Hazard assessment was implemented by the Spatial Analyst toolbox of ArcGIS software (ESRI, 2022). To process the hazard assessment, all the parameter maps were converted into a raster format. The layers generated from DEM (i.e., slope, aspect, and surface drainage) were already in raster format. The rest of the layers, which were presented as vector polygons, have been rasterized. After that, the raster layers were re-classified into three categories having relative values named as high, moderate, and low (Table 24). Finally, the layers were processed with a weighted overlay analysis to identify the hazard zones. A detailed workflow of the process followed for the layers in the ArcGIS software (ESRI, 2022) is given in Appendix G.

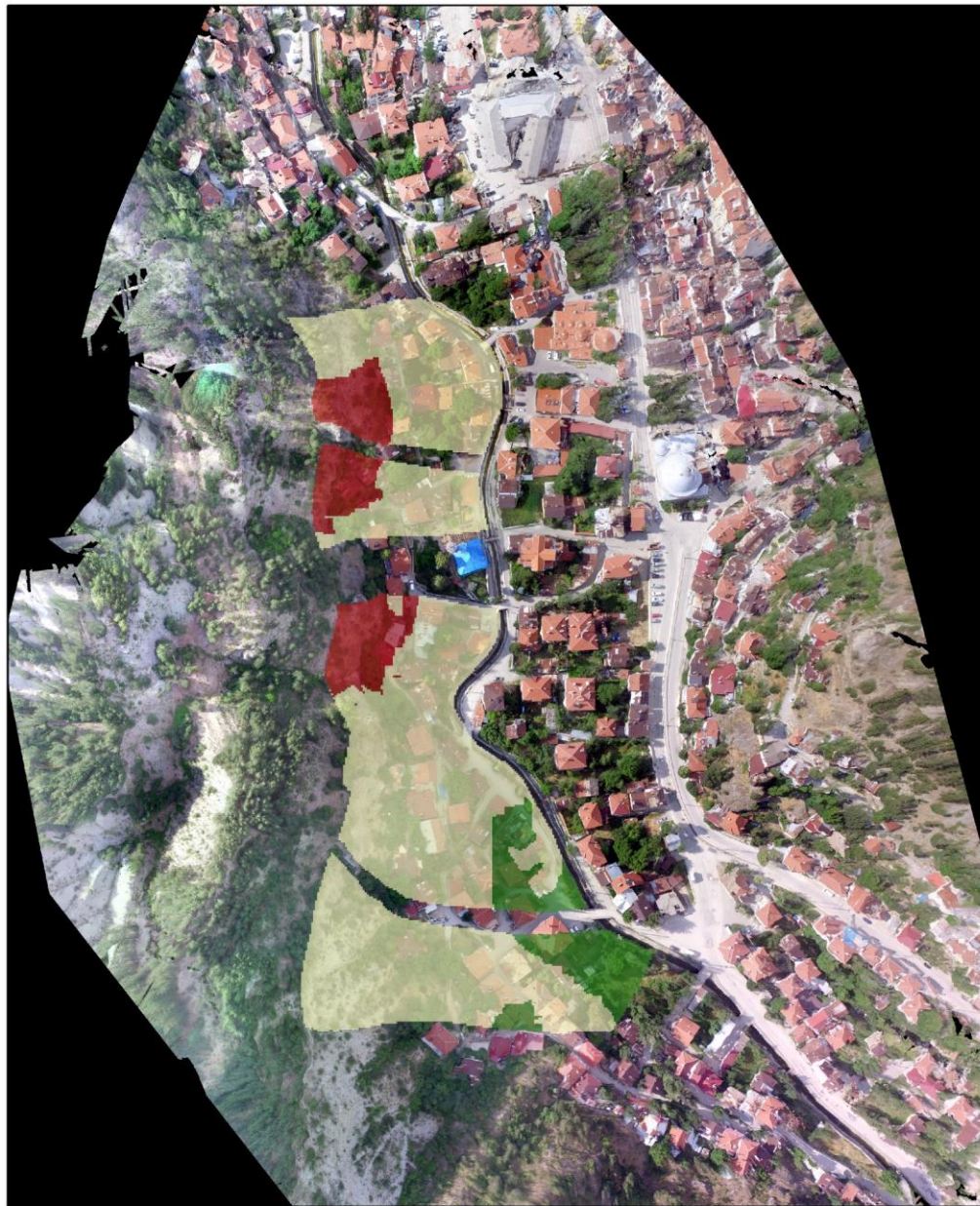
Hazard zonation maps identified for planar, wedge, and toppling failures are given in Figures 96, 97, and 98, respectively. Note that the hazard classes were defined qualitatively by following the Swiss Federal Guidelines. The meaning of the hazard classes is presented in Table 26.



Legend
 Planar failure hazard zone
 High Moderate Low

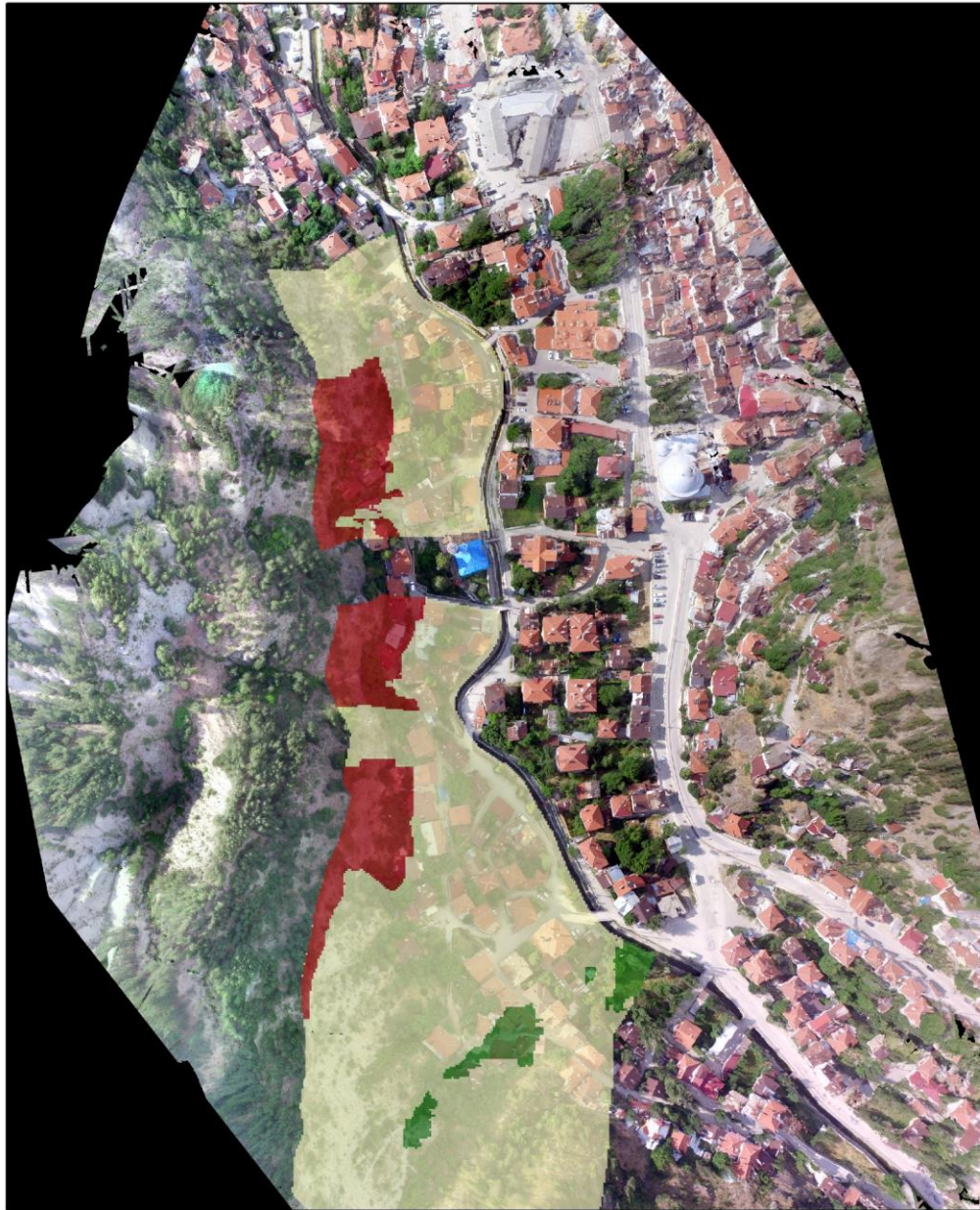
0 20 40 80 120 160 Meters

Figure 96: Hazard zonation map of planar failure on the western side of the Mudurnu valley



Legend
 Wedge failure hazard zone
 High Moderate Low

Figure 97: Hazard zonation map of wedge failure on the western side of the Mudurnu valley



Legend
Toppling failure hazard zone
High Moderate Low

Figure 98: Hazard zonation map of toppling failure on the western side of the Mudurnu valley

Table 26: Hazard zones according to Swiss Federal Guidelines (Raetzo et al., 2002)

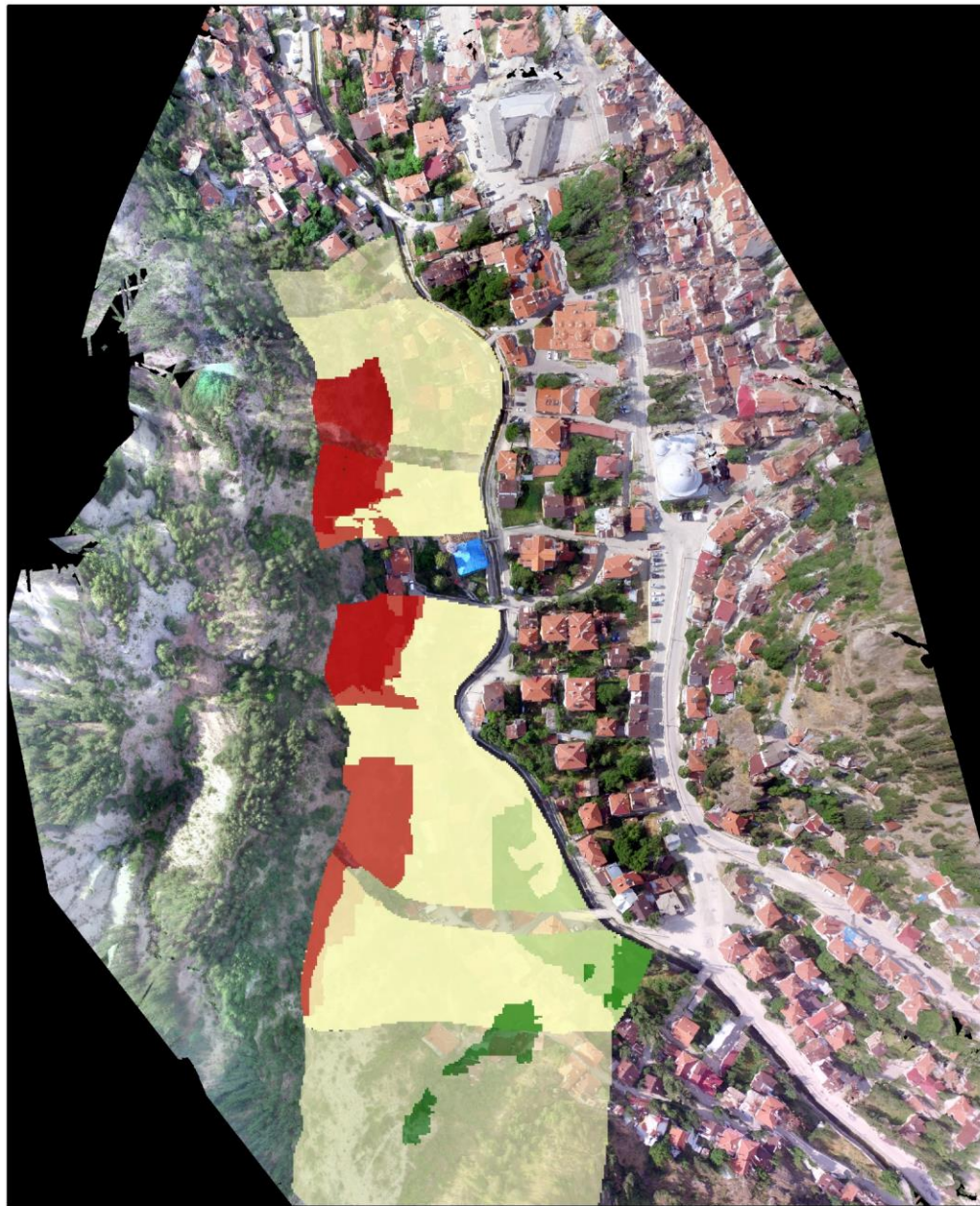
Hazard class	Meaning
High hazard	-People at risk of injury both inside and outside buildings -A rapid destruction of the building is possible -or: Events with a lower intensity, but having a higher probability of occurrence. In this case, people are mainly at risk outside buildings, or buildings can no longer house people
	-People are at risk of injury outside buildings. Risk is considerably lower inside buildings
Moderate hazard	-Damage to buildings should be expected, but not rapid destruction as long as the destruction type has been adapted to the present conditions
Low hazard	-People are at slight risk of injury -Slight damage to buildings is possible
Residual danger	-An alerting domain for a low probability of a high-intensity event
No/negligible danger	-No danger according to currently available information

In general, high hazard zones concentrate in the middle of the valley while the southern and northern parts are mostly represented by moderate hazards and no hazards. The resultant hazard zonation maps conclude that toppling failure covers the largest area in terms of high hazard. It is followed by planar failure that covers a relatively smaller area. Wedge failure has relatively the smallest area of high hazard zones. Note that toppling failure is almost always associated with small to medium-sized blocks while planar and wedge failures are correlated with large to very large unstable blocks (Figure 99). Moreover, the combination of toppling-prone blocks with the planar and wedge blocks creates complex kinematic failures. Therefore, planar and wedge failures are more critical in terms of the risks regarding their consequences. For the sake of evaluating complex failures, a combined hazard map was prepared by utilizing planar, wedge and toppling failure maps as combined layers (Figure 100). Accordingly, Sectors 6 and 8 are the most critical in terms of

high hazard. These sectors are followed by Sectors 2 and 4. Sectors 1 and 11 that possess moderate hazard potential, while Sector 7 is free from rock slope failure.



Figure 99: Example images for different failure types possible on the western side of the Mudurnu valley. a) Toppling (lower leftern side) and planar (upper part) failures, b) wedge failure

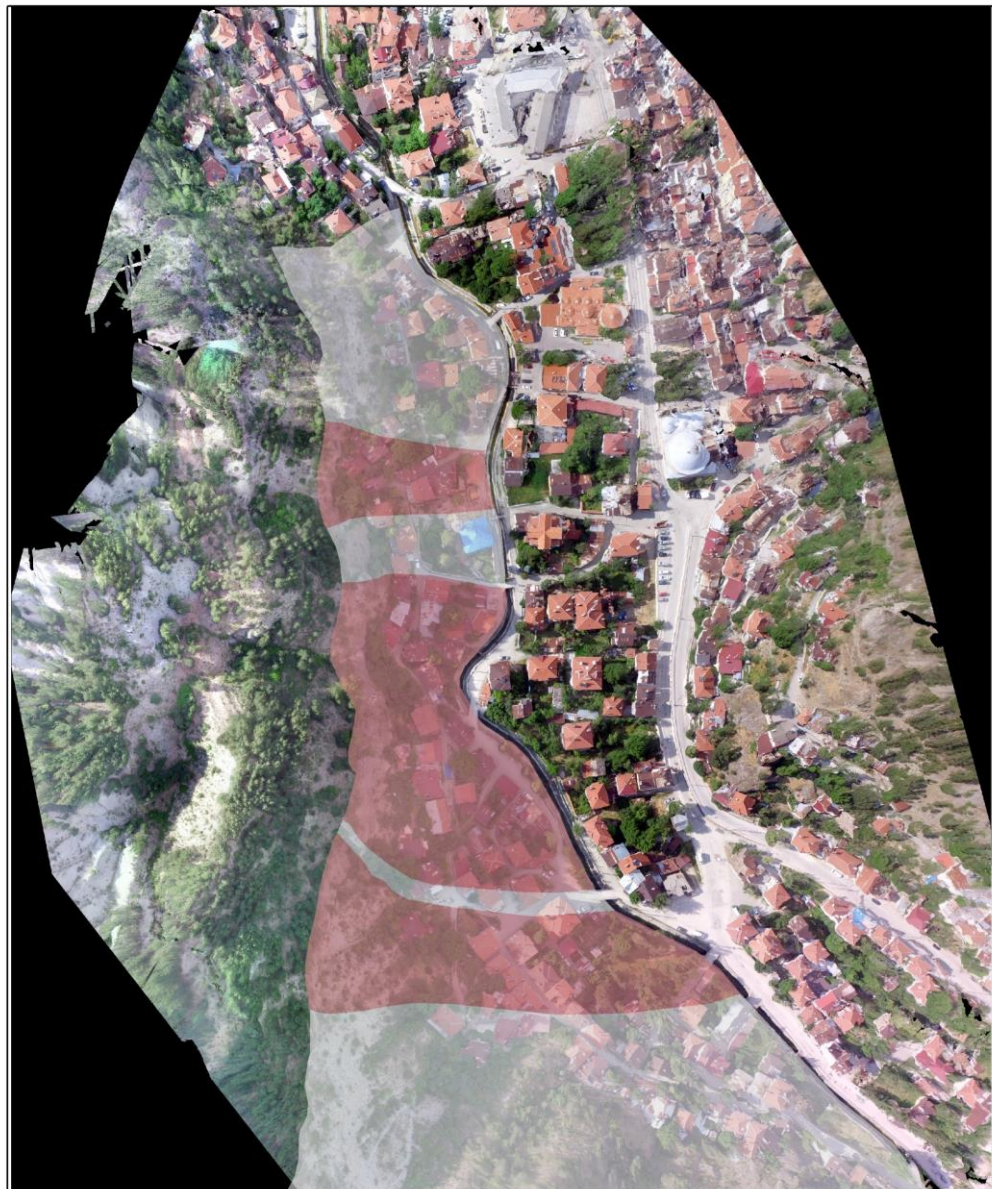


Legend
Rock slope failure hazard zone
High Moderate Low

0 20 40 80 120 160 Meters

Figure 100: Combined rock slope failure hazard zonation map on the western side of the Mudurnu valley

The stability analysis has revealed that introducing dynamic loading conditions also tends to increase the susceptibility to planar, wedge, and toppling failures. Therefore, the hazard potential originating due to seismicity will become higher. In the hazard assessment study, the dynamic loading conditions have been considered as a triggering factor. Different than the conventional methods, differentiating the dynamic loading between the sectors in terms of earthquake intensity or distance has been deemed to be unreasonable. Therefore, earthquake force was assumed to contribute to susceptibility by increasing the relative value of the temporal frequency of failure. Zones prone to planar, wedge, and toppling failures under dynamic loading are shown in Figures 101, 102, and 103, respectively. Note that these zones are associated with the possible number of events that was estimated qualitatively per sector. Hazard zonation maps that consider the dynamic loading conditions considering the TBEC (2019) are given in Figures 104, 105, and 106 for planar, wedge, and toppling failures, respectively.



Legend

High Medium None

0 15 30 60 90 120 Meters

Figure 101: Planar failure-prone zones of the study area under dynamic loading conditions

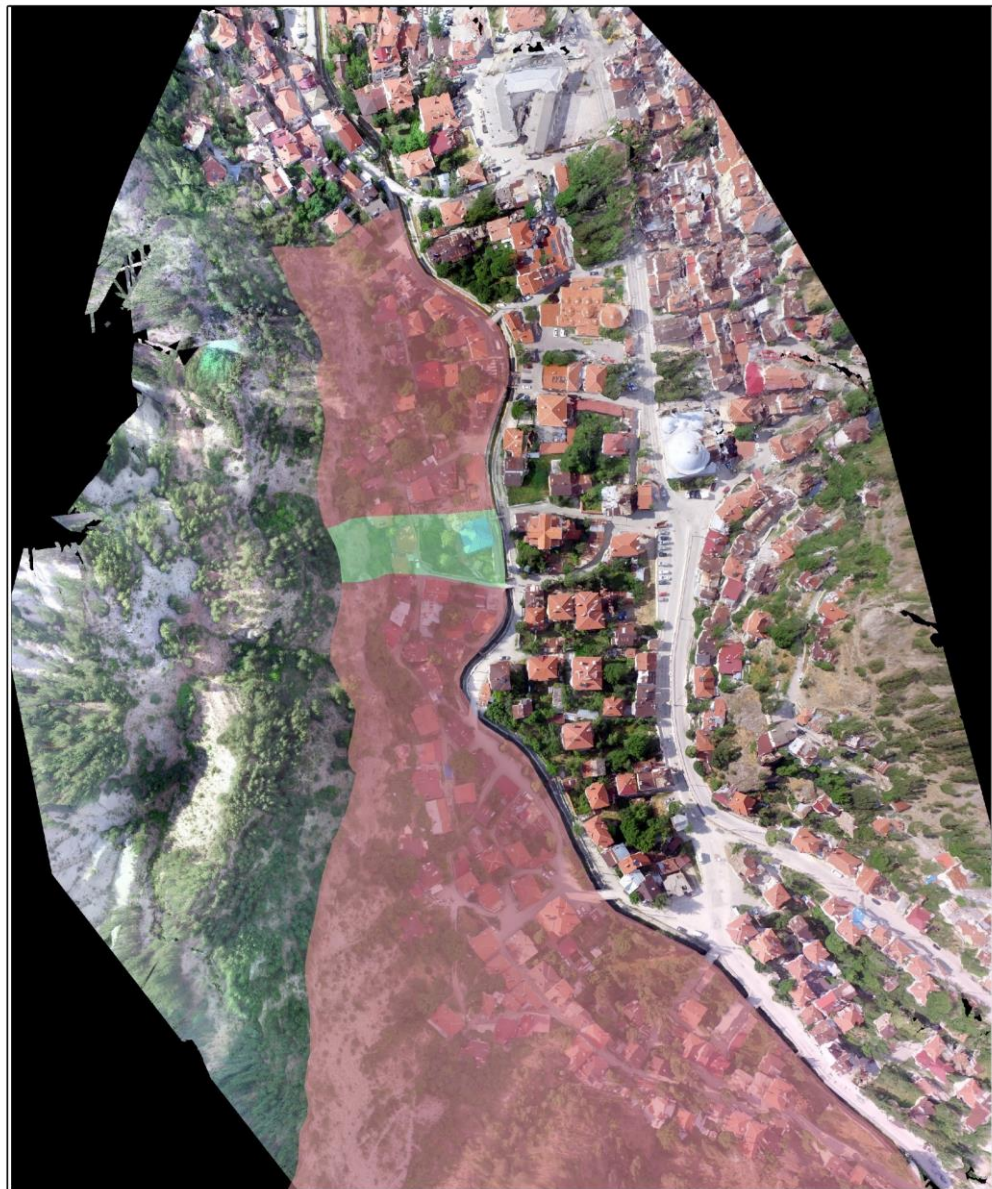


Legend

0 15 30 60 90 120 Meters

High Medium Low None

Figure 102: Wedge failure-prone zones of the study area under dynamic loading conditions

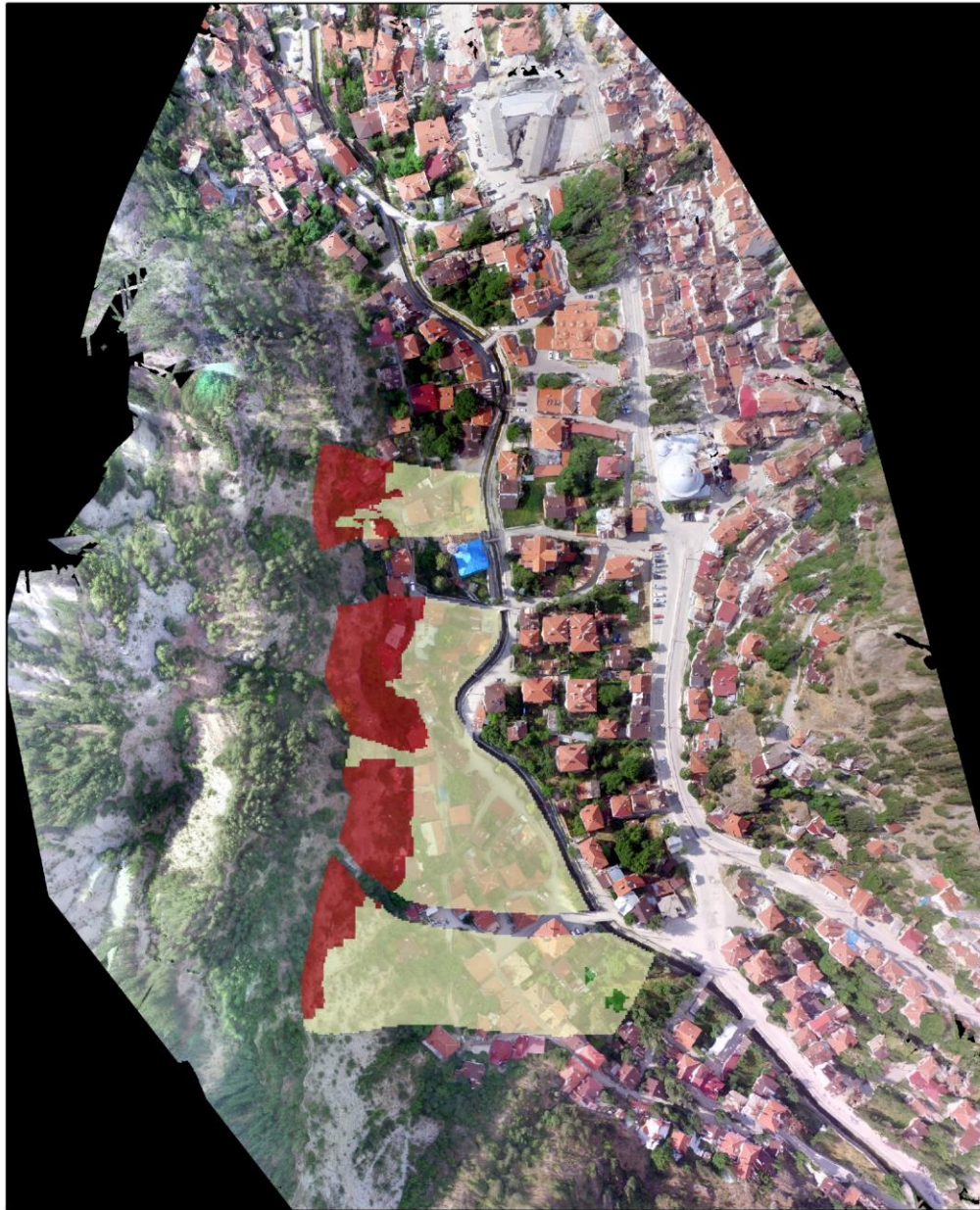


Legend

High Low

0 15 30 60 90 120 Meters

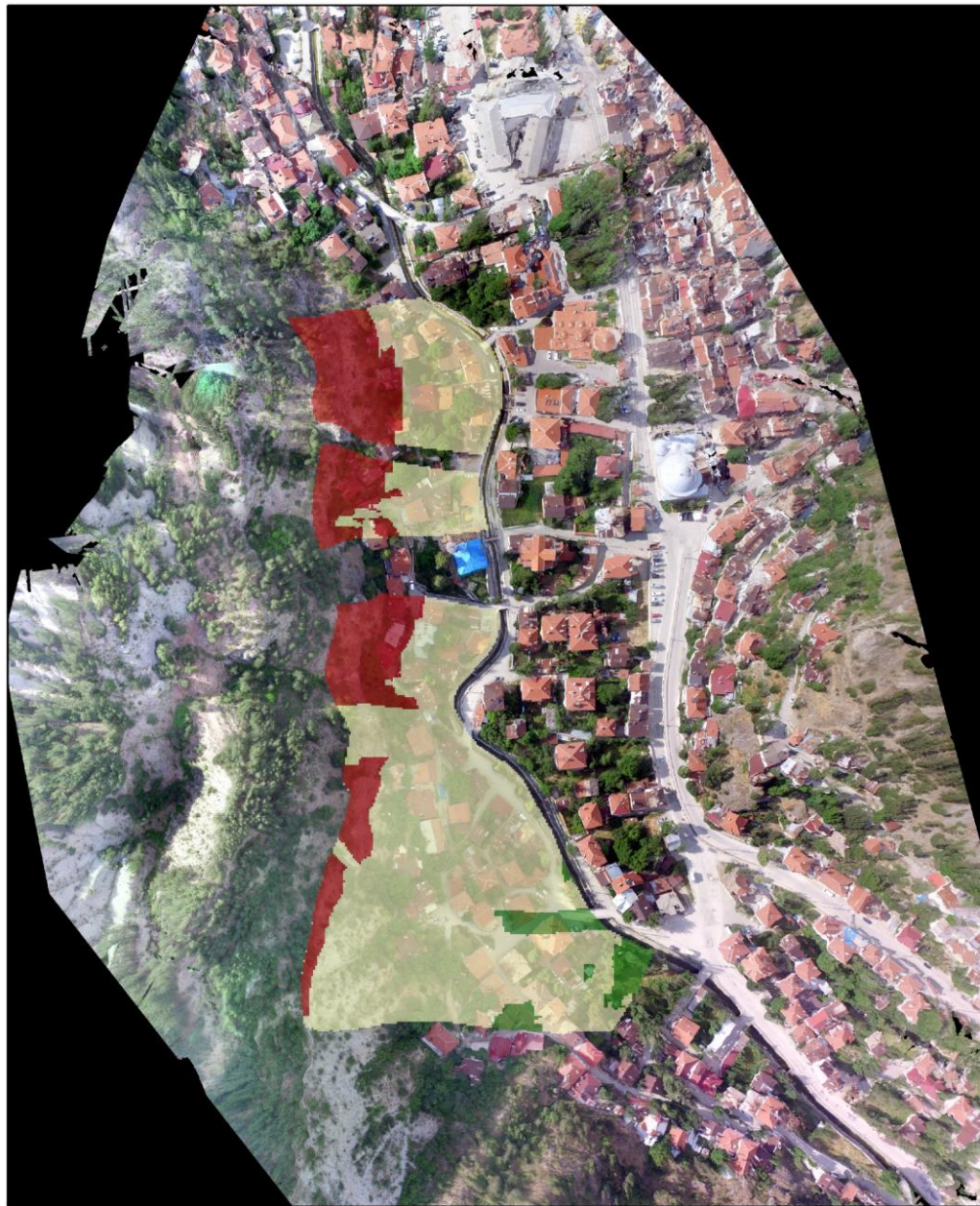
Figure 103: Toppling failure-prone zones of the study area under dynamic loading conditions



Legend
 Planar failure hazard zone under dynamic conditions
 High Moderate Low

0 20 40 80 120 160 Meters

Figure 104: Hazard zonation map of planar failure under dynamic loading conditions



Legend

Wedge failure hazard zone under dynamic conditions

- High Moderate Low

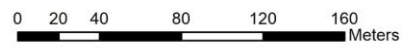


Figure 105: Hazard zonation map of wedge failure under dynamic loading conditions

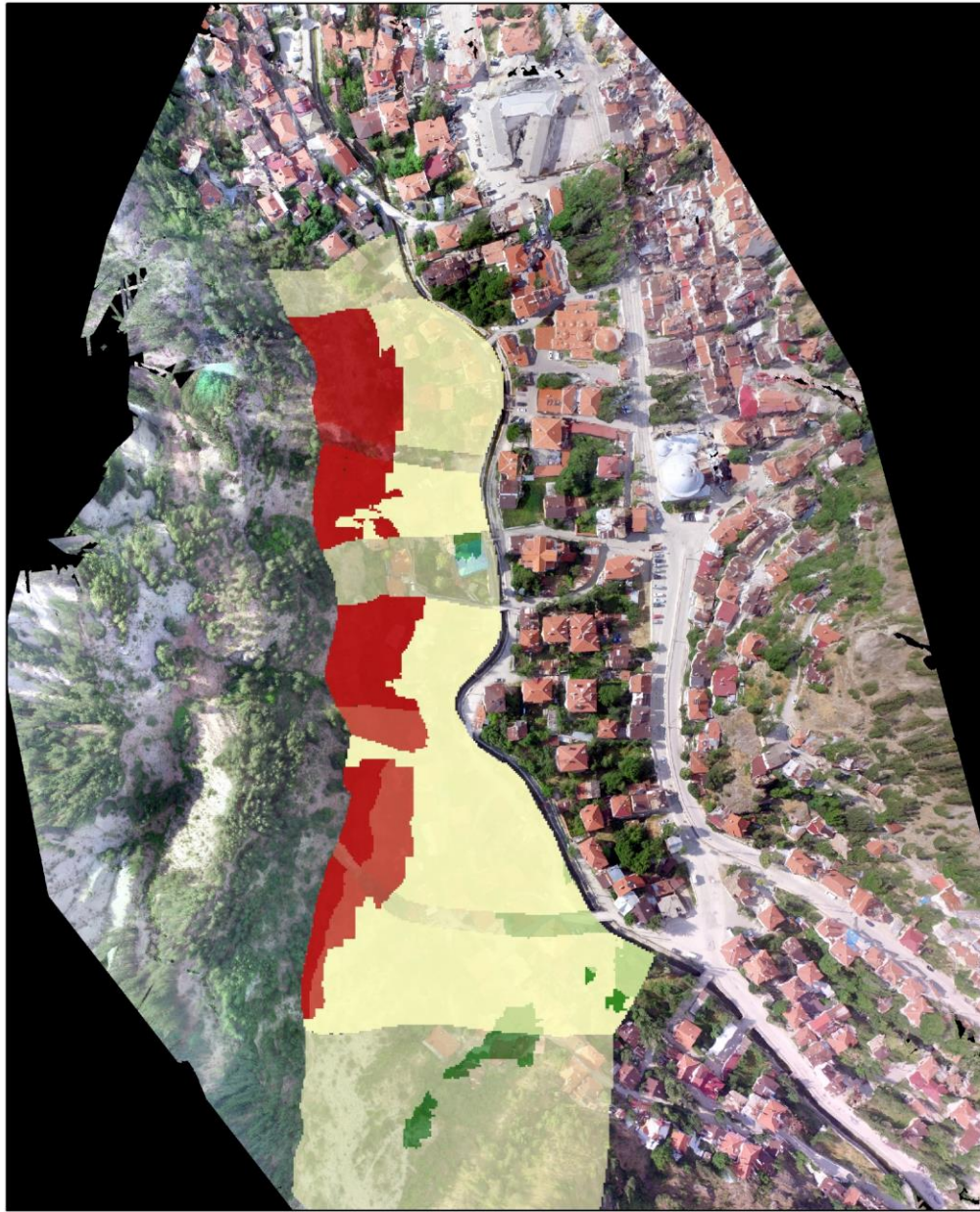


Legend
Toppling failure hazard zone under dynamic conditions
High Moderate Low

0 20 40 80 120 160 Meters

Figure 106: Hazard zonation map of toppling failure under dynamic loading conditions

When the seismic force is considered, high and moderate hazard zones cover a larger area. The change in the hazard classes is mainly observed in the southern part of the valley for wedge type of failure. In the northern part, wedge and toppling failure hazard zones shift into higher hazards. Unlike the static conditions, high hazard zones are distributed over the valley. A combined hazard map was prepared to evaluate the complex failures under dynamic loading conditions (Figure 107). Accordingly, the most critical sectors in terms of high hazards are Sectors 2, 4, 6, 8 and 10. These sectors are followed by Sectors 3, 5 and 9. Sectors 1, 7 and 11 have moderate hazard potential. Since the hazard possibility of the valley slopes increases under dynamic loading conditions, the associated risk is expected to become higher.



Legend
 Rock slope failure hazard zone under dynamic conditions
 High Moderate Low

0 20 40 80 120 160 Meters

Figure 107: Combined rock slope failure hazard zonation map on the western side of the Mudurnu valley under dynamic loading conditions

CHAPTER 6

CONCLUSIONS AND RECOMMENDATIONS FOR FUTURE RESEARCH

Mudurnu is a county of Bolu possessing natural and cultural values that has led it to its designation as an urban conservation site. There are many historical buildings (traditional houses/mansions, mosques from the Seljuk and Ottoman periods, a Turkish bath from the Ottoman period, and a wooden clock tower) in Mudurnu which has been nominated as a candidate for the UNESCO World Heritage List. Unfortunately, the county center suffers from regional rock instabilities originating from the rock masses of both the eastern and western sides of the valley slopes. The instabilities tend to introduce high hazard potential and create an associated high risk in Mudurnu as a consequence of the favorable position (i.e., exposure) of the elements at risk (i.e., human life, houses, buildings, small industrial facilities, and historically important structures). The purpose of this dissertation is to characterize the discontinuous rock masses that have the potential to create a hazard in the Mudurnu county center through geomechanical evaluation of the slope instability problems under static and dynamic loading conditions and then to identify the hazard zones on the western side of the Mudurnu Valley.

To accomplish this purpose, at first, the discontinuous rock mass (i.e., discontinuous pelagic limestone) that forms the rock slope instabilities at the western side of Mudurnu valley was characterized throughout the county center from an engineering geological point of view and geomechanically-uniform sectors were defined. To that end, field rock mass characterization utilizing scan-line surveys and Unmanned Aerial Vehicle (UAV) studies were conducted. Based on the field observations and the scan-line survey studies, the rock mass was characterized as pinkish gray to light gray limestone having three discontinuity sets; a Bedding plane (BP) and two Joint

sets (J1 and J2). The discontinuity sets had strong to very strong strengths according to the field identification. The limestone was slightly weathered in general although the degree of weathering was classified as moderate at several locations. The discontinuity surfaces were undulating rough to undulating smooth, and the apertures were generally classified as closed. Clay and silty clay infilling were observed where moderately wide and open apertures were present. Spacing of the discontinuities was close to moderate. Persistence was high. Block sizes varied between medium to large. Even though some color changes were detected at several locations, water was not observed during any of the field studies conducted at different seasons of the years. However, surface drainage flow through the slope face was encountered at one location in the spring season during snow melt. Hence, surface drainage was considered as a conditioning parameter in hazard assessment. Moreover, the rock mass indices and rock material parameters of the limestone were identified by field measurements and laboratory tests.

To accomplish a proper characterization, the rock mass was required to be studied spatially throughout the slope due to its non-uniform nature. However, most parts of the valley were not possible to be investigated during the field study due to the difficulties encountered in accessibility such as the steep nature of the area and the rather high elevation of the valley slopes. Therefore, an Unmanned Aerial Vehicle (UAV) was employed to overcome the physical limitations arising from performing the scan-line survey only at accessible locations and to overcome this bias as much as possible for rock mass characterization. The UAV survey was completed at the end of flights of a two-day long field study in Mudurnu county center by collecting 2053 images. Then, a high-density point cloud of the western side of the valley was generated. The overall resolution of the point cloud which possesses more than 35 million points is 7.8 cm. The 3D point cloud was employed to obtain the orientation, spacing, and persistence of the discontinuity sets by utilizing the Discontinuity Set Extractor (DSE) method. It should be noted that the method was verified prior to utilizing the DSE methodology to gather data from the entire valley. For this purpose,

the DSE method was initially applied to the parts (sectors) studied in the field (i.e., Sectors 2, 4, 6, 8, and 10). Then, the gathered data was controlled and validated with field observations. Since the data gathered from the point cloud and the data collected from the field were comparable, the 3D analysis method was applied to the entire valley.

Based on the gathering and evaluation of all the available data (i.e., the geological and geomechanical rock mass properties, scan-line survey measurements, photos taken during field studies, collected UAV images, and 3D point cloud), the western side of the valley was delineated into 11 geomechanical sectors. For the delineation, varying slope face orientations were considered. Then, the DSE methodology was applied to each sector to gather the distributions of the discontinuity set orientations, spacings, and apertures. Based on the spacing and persistence of the discontinuity sets obtained from the point cloud along with the number of discontinuity sets and their orientations, block sizes of the sectors were classified. Identification of block size was important since it is related to the mechanical behavior of the rock mass together with the inter-block shear strength. Therefore, the block size was considered as a conditioning parameter in hazard assessment.

The presence of different discontinuity sets together with the favorable orientation of the slope face at Mudurnu county center has led to the development of kinematically controlled failures. Two empirical rock mass classification systems, namely; Slope Mass Rating (SMR) and Q-Slope were considered to categorize the rock mass based on its geomechanical characteristics and to estimate the rock mass behavior and instability of the different sectors. Both of the methods indicated that all of the sectors except Sector 7 were capable of creating failures in varying degrees. A two-step process has been followed for the stability assessment in Mudurnu. First, kinematic analysis has been applied to identify possible modes of failure. Then, limit equilibrium analysis has been employed for the sectors that have a potential for

failure based on the kinematic analysis. The kinematic analyses revealed that planar, wedge, and toppling failures were possible throughout the study area. In the area, Joint set 1 (J1) has a potential of causing planar failures, the intersection of Joint set 1 (J1) and Joint set 2 (J2) may produce wedge failures and the Bedding Plane (BP) is capable of inducing toppling failure. According to the kinematic analysis results, planar, wedge, and toppling failures are possible in Sectors 2, 4, 5, 6, and 8. Both wedge and toppling failures are kinematically possible in Sectors 3 and 10. In Sectors 1 and 11, only toppling failure is possible, and in Sector 9 only wedge failure is possible. Moreover, the discontinuity sets are capable of creating complex kinematic failures by means of a combination of planar, wedge, and toppling failures in the area. The presence and characteristics of the complex kinematic failures are the reasons that make the study area a unique case study since it is difficult to separately identify the order or frequency of events originating from the different failure types that form complex failure. Assessment of rock slope stability is challenging because of the heterogeneous and anisotropic nature of the rock materials; difficulties in identifying the strength parameters of rock masses; the complexity of the rock behavior theories and models; difficulty to represent field conditions in the laboratory; and the complexity of field testing. By keeping these challenges in mind, back analyses were performed to determine the mobilized shear strength parameters through the identified failed blocks. The back analysis was performed on a total of 10 wedge blocks distributed over 5 different sectors (i.e., Sectors 2, 5, 6, 8, and 10) by using the equation proposed by Barton and Choubey (1977). As a result, friction angles along Joint set 1 and Joint set 2 were estimated. Then, limit equilibrium analysis has been applied in terms of planar and wedge types of failures at the kinematically possible sectors by utilizing the back-calculated friction angle values. For the limit equilibrium analysis, both probabilistic and deterministic approaches were utilized. In this dissertation, dynamic loading due to earthquakes was considered by pseudo-static analysis based on the TBEC (2019) for a return period of 475 years (i.e., the probability of exceedance in 50 years was considered to be 10%). The seismic load coefficient (k_h) of the study area was estimated as 0.24g to

evaluate the dynamic loading condition in the stability analysis. In addition, by considering the block geometry and base plane angle, the movement type of the blocks prone to toppling failure was identified as a “sliding and toppling” condition, which is concordant with the rock mass characteristics along the western side of the Mudurnu valley.

In terms of planar failure, the partially stable and unstable sectors identified by empirical methods were concordant with the sectors prone to kinematic failure. Limit equilibrium analyses revealed that the blocks were unstable in all of the sectors that showed a possibility of kinematic failure. In general, the probability of failure (POF) obtained from the limit equilibrium analyses was in good agreement with the empirical results. However, limit equilibrium analyses resulted in a higher POF in Sector 4 and a lower POF in Sector 5. Concerning wedge failure, the failure-prone sectors identified by empirical classification systems were concordant with the kinematically possible sectors except Sector 11. Kinematic analysis showed that there was no possibility of wedge failure in Sector 11. Limit equilibrium analyses revealed that the blocks were unstable in Sectors 2, 4, 5, 6, 8, and 10. From a kinematical point of view, Sectors 3 and 9 were stable in static conditions but unstable under dynamic loading conditions in Sector 3. In general, the probability of failure (POF) obtained from limit equilibrium analyses was lower than the empirical results. In the case of toppling failure, empirical methods revealed that Sector 7 was completely stable; Sectors 2, 3, 5, 8, 9, 10, and 11 were stable with some local block failures; Sectors 1, 4, and 6 were partially stable with the possibility of failure along some joints. Based on the kinematic analysis, toppling failure was possible along the Bedding plane in Sectors 1, 2, 3, 4, 5, 6, 8, 10, and 11. Although according to SMR, Sector 9 had a probability of failure of 0.2, the kinematic analysis showed no possibility of toppling failure for this sector.

In general, when the seismic force was introduced, the limit equilibrium analyses resulted in a higher probability of failure and a lower factor of safety as expected. Based on the results of the analysis, it was concluded that the influence of the dynamic loading was more intense for wedge failure as compared to planar failure. Moreover, the dynamic load has also been expected to change the stability of the toppling blocks significantly due to the geometry of blocks and the presence of the undermining effect. In conclusion, introducing dynamic force in the stability analysis tended to increase the susceptibility to planar, wedge, and toppling failures as expected. Thus, since the hazard potential originating from these failures is expected to be higher, dynamic loading conditions have been considered as a triggering factor in the hazard assessment study.

Since the scale of the study area was suitable and the engineering geological characteristics, as well as the stability, were assessed and considered in detail along the entire valley, using an heuristic approach in Mudurnu seemed to be reasonable. As a result, susceptibility zones for planar, wedge, and toppling failures were directly identified based on the field observations and stability assessment. To consider the influence of all of the possible factors that can be effective in the study area, and hence, to accomplish a complete hazard assessment, the heuristic method has been indirectly employed by utilizing maps of different parameters. These parameters were the geological and engineering geological parameters (i.e., lithology, degree of weathering, block size) and topographical parameters (i.e., slope angle, aspect, surface water) along with travel distance and temporal frequency. In addition, the seismic loading conditions were taken into account as a triggering factor. Then, weights were assigned to the parameters according to their relative importance in terms of hazard potential. Finally, high, moderate, and low hazard zones have been identified. According to the combined hazard map, Sectors, 6 and 8 were determined to be most critical in terms of high hazards. These sectors were followed by Sectors 2 and 4. Sectors 1 and 11 possessed moderate hazard potential, while Sector 7 was free from rock slope failure. Under dynamic loading conditions, the most critical

sectors in terms of high hazards were Sectors 2, 4, 6, 8, and 10. These sectors were followed by Sectors 3, 5, and 9. Sectors 1, 7, and 11 possessed moderate hazard potential. Since the hazard possibility of the valley slopes increases under dynamic loading conditions, the associated risk to human life and the structures located at the toe of the slopes is expected to become higher in Mudurnu. In accordance with the failure mechanisms, stability conditions and hazard potential of the rock mass, the remediation measures that can be recommended for the western side of the valley include systematic bolts. The rock bolts should be supported by wire mesh as surface protection. Also, dental concrete may be used to support the overhanging limestone blocks. Moreover, a durable surface drainage system is suggested to collect surface water. It should be emphasized that, for the risk studies that might be performed in the future, the hazard potential revealed in this dissertation should be utilized carefully. In the area, planar and wedge failures tend to create large to very large unstable blocks that are very critical in terms of their consequences. In addition, it needs to be noted that their frequency of occurrence is lower than the frequency of occurrence of toppling failures in the region. The unstable blocks prone to toppling failure are almost always associated with small to medium-sized blocks with a higher frequency of occurrence. Therefore, even if the susceptibility levels or hazard zones of different failure types are in the same category, the result will not be the same in terms of its consequences. In particular, planar and wedge failures associated with large to very large blocks tend to create a critical threat to those elements at risk (i.e., people, houses, historical structures, lifelines, etc.) and are expected to cause catastrophic results.

The studies completed and presented herein comprise a detailed engineering geological characterization case study applied to a discontinuous rock mass, identification of the rock slope failure probabilities of complex failures, and generation of hazard zonation maps. The results of the study are expected to serve as a basis for the future risk assessment studies since the results establish a pioneer hazard assessment study in the Mudurnu county center. In this regard, to achieve a

complete zonation, rock fall susceptibility of the eastern side of the valley should also be studied and hazard zones need to be defined. It should be noted that one of the major difficulties encountered during the hazard assessment was the unavailability of a well-documented inventory and thus, a proper magnitude-frequency relation of the previous events. Therefore, to create an inventory and to evaluate the return period of the events quantitatively, the application of a long-term remote sensing monitoring method such as laser scanning (Lidar), Electronic Distance Measurement (EDM), total station or systematic UAV flights; or in-situ monitoring methods such as Time Domain Reflectometry (i.e., optical fiber systems) would be useful to evaluate the risk by sophisticated methods.

REFERENCES

- Abdüselamoğlu, S. (1959). Almacıkdağı ile Mudurnu ve Göynük civarının jeolojisi, *İstanbul Üniversitesi, Fen Fakültesi Monografileri*, 14.
- Abramson, L. W., Lee, T. S., Sharma, S., & Boyce, G. M. (2002). Slope stability and stabilization methods, 2nd Edition, *Wiley, New York*, 736.
- Altiner, D., Kocuyigit, A., Farinacci, A., Nicosia, U., & Alessandra Conti, M. (1991). Jurassic-Lower Cretaceous stratigraphy and paleogeographic evolution of the southern part of north-western Anatolia (Turkey). *Geologica Romana*, 27, 13–80.
- Ambraseys, N. N. (1988). Engineering seismology. *Earthq. Engin. Struct. Dyn.*, 17, 1-105.
- Ambraseys, N. N. & Zatopek, A. (1969). The Mudurnu Valley, West Anatolia, Turkey, earthquake of 22 July 1967. *Bull. Seismol. Soc. America*, 59, 521-589.
- Ambraseys, N.N., Zapotek, A., Taşdemiroğlu, M. ve Aytun, A. (1968). The Mudurnu valley (West Anatolia) earthquake. *UNESCO Report*, 622, 1-74.
- Anbalagan, R. (1992). Landslide hazard evaluation and zonation mapping in mountainous terrain. *Engineering Geology*, 32, 269–277.
- Anderson, M. G. & Holcombe, E. (2013) Community-Based landslide risk reduction: Managing disasters in small steps. *World Bank Publications* 2013.
- Arslan, Kelam, A., Akgün, H., Koçkar, M.K. (2018). Evaluation of the complex kinematic failure mechanisms along Mudurnu valley, Bolu, Turkey through the utilization of UAV. *2nd International Discrete Fracture Network Engineering Conference DFNE 2018*.

- Arslan Kelam, A., Akgün, H., Bobet, A., Koçkar, M. K. (2021). Assessment of kinematic rock slope failures in Mudurnu Valley, Turkey. *EUROCK 2021 Mechanics and Rock Engineering from Theory to Practice*.
- Ayalew, L., & Yamagishi, H. (2005). The application of GIS-based logistic regression for landslide susceptibility mapping in the Kakuda-Yahiko Mountains, Central Japan. *Geomorphology*, 65(1–2), 15–31. <https://doi.org/10.1016/j.geomorph.2004.06.010>
- Azarafza, M., Ghazifard, A., Akgün, H., & Asghari-Kaljahi, E. (2018). Landslide susceptibility assessment of South Pars Special Zone, southwest Iran. *Environmental Earth Sciences*, 77(24). <https://doi.org/10.1007/s12665-018-7978-1>
- Bağcı, G., Yatman, A., Özdemir, S., Altın, N. (2000). Türkiye’de hasar yapan depremler. *Deprem Araştırma Bülteni*, 69 113-126.
- Barka, A. (1997). Neotectonics of the Marmara Region: In: Schindler, C., Pfister, M. (Eds.), *Active Tectonics of Northwestern Anatolia-The Marmara Poly-Project*, vdf Hochschulverlag AG an der ETH Zürich, 55-87.
- Barka, A. (1996). Slip distribution along The North Anatolian Fault associated with the large earthquakes of the period 1939 to 1967. *Bull. Seismol. Soc. America*, 86, 1238-1254.
- Barka, A., Akyüz, H.S., Altunel, E., Sunal, G. & Çakır, Z., (2002). The surface rupture and slip distribution of the 17 august 1999 izmit earthquake (M 7.4), north anatolian fault. *Bull. Seismol. Soc. America*, 92, 43–60.
- Barton, N.R. & Bandis, S.C. (1982). Effects of block size on the shear behaviour of jointed rock. *23rd U.S. Symp. on Rock Mechanics (Berkeley)*, 739-760.
- Barton, N. & Bar, N. (2015). Introducing the Q-slope method and its intended use within civil and mining engineering projects. In: Schubert, W. & Kluckner,

- A. (eds) Future development of rock mechanics; *Proceedings of the ISRM regional symposium, Eurock 2015 and 64th geomechanics colloquium, Salzburg, 7–10 October 2015*, pp 157–162.
- Barton, N.R. & Choubey, V. (1977) The shear strength of rock joints in theory and practice *Rock Mech.* 10 (1-2), 1-54.
- Barton, N.R., Lien, R. and Lunde, J. (1974). Engineering classification of rock masses for the design of tunnel support. *Rock Mech.* 6 (4), 189-239.
- Bieniawski, Z.T. (1989). Engineering rock mass classification. *Wiley, Chichester*, 251.
- Borgatti, L. and Soldati, M. (2010). Landslides as a geomorphological proxy for climate change: a record from the dolomites (northern Italy). *Geomorphology*, 120, 56-64.
<http://dx.doi.org/10.1016/j.geomorph.2009.09.015>
- Bozkır, A. S. , Nefeslioğlu, H. A. , Kartal, O. , Sezer, E., Gökçeoğlu, C. (2020). geological strength index prediction by vision and machine learning methods. *ISRM International Symposium - EUROCK 2020*.
- Bozkurt, E., & Mittwede, S. K. (2001). Introduction to the geology of Turkey - A synthesis. *International Geology Review*, 43(7), 578–594.
<https://doi.org/10.1080/00206810109465034>
- Brawner, C.O., and Milligan, V. (1971). Stability in open pit mining. *Society for Mining Metallurgy*, 242.
- Bromhead, E.N. (1992). The stability of slopes, *Black Academic & Professional, London*, 411.
- Can, T., Nefeslioglu, H. A., Gokceoglu, C., Sonmez, H., & Duman, T. Y. (2005). Susceptibility assessments of shallow earthflows triggered by heavy rainfall

- at three catchments by logistic regression analyses. *Geomorphology*, 72(1–4), 250–271. <https://doi.org/10.1016/j.geomorph.2005.05.011>
- Cascini, L. (2008). Applicability of landslide susceptibility and hazard zoning at different scales. *Engineering Geology*, 102(3–4), 164–177. <https://doi.org/10.1016/j.enggeo.2008.03.016>
- Corominas, J., & Moya, J. (2008). A review of assessing landslide frequency for hazard zoning purposes. *Engineering Geology*, 102(3–4), 193–213. <https://doi.org/10.1016/j.enggeo.2008.03.018>
- Corominas, J., van Westen, C., Frattini, P., Cascini, L., Malet, J. P., Fotopoulou, S., Catani, F., van den Eeckhaut, M., Mavrouli, O., Agliardi, F., Pitilakis, K., Winter, M. G., Pastor, M., Ferlisi, S., Tofani, V., Hervás, J., & Smith, J. T. (2014). Recommendations for the quantitative analysis of landslide risk. *Bulletin of Engineering Geology and the Environment*, 73(2), 209–263. <https://doi.org/10.1007/s10064-013-0538-8>
- Crosta, G. B., & Agliardi, F. (2003). Natural hazards and earth system sciences: a methodology for physically based rockfall hazard assessment. In *Natural Hazards and Earth System Sciences* (Vol. 3).
- Cruden, D. M. & Varnes, D. J. (1996). Landslide types and processes. In: A. K. Turner & R. L. Schuster (Eds.) *Landslides: Investigations and Mitigation*. Transportation Research Board Special Report, 247. National Research Council. Washington, D. C.: National Academy Press.
- D’Andrea, D. V., Fisher, R. L., Fogelson, D. E. (1964). Prediction of compression strength from other rock properties. *Colorado School of Mines Quarterly*, 59(4B), 623–640.
- Das, I., Stein, A., Kerle, N., Dadhwal, V.K. (2012). Landslide susceptibility mapping along road corridors in the Indian Himalayas using Bayesian logistic regression models. *Geomorphology*, 179, 116-125.

- Deere, D.U. & Miller, R.P. (1966). Engineering classification and index properties for intact rocks *Technical Report (New Mexico: Air Force Weapons Laboratory) AFNL-TR*, 65–116.
- Demirkol, C. (1973). Üzümlü-Tuzaklı (Bilecik) dolayının jeolojisi. *PhD Dissertation*, İstanbul Üniversitesi.
- Demirkol, C. (1977). Üzümlü-Tuzaklı (Bilecik) dolayının jeolojisi. *Türkiye Jeoloji Kurumu Bülteni*, 20(1).
- Duman, T. Y., Emre, O., Doğan, A., Özalp, S. (2005). Step-Over and bend structures along the 1999 Düzce earthquake surface rupture, North Anatolian Fault, Turkey. *Bull. Seismol. Soc. America*, 95, 1250 – 1262.
- Duman, T.Y., Çan, T., Emre, Ö. (2011). 1/1.500.000 ölçekli Türkiye Heyelan Envanteri Haritası. *Maden Tetkik ve Arama Genel Müdürlüğü Özel Yayınlar Serisi*, 27.
- Eker, A. M., Dikmen, M., Cambazoğlu, S., Düzgün, Ş. H. B., & Akgün, H. (2015). Evaluation and comparison of landslide susceptibility mapping methods: a case study for the Ulus district, Bartın, northern Turkey. *International Journal of Geographical Information Science*, 29(1), 132–158. <https://doi.org/10.1080/13658816.2014.953164>
- EM-DAT. (2022). *2021 Disasters in Numbers*. <https://doi.org/10.1787/eee82e6e-en>
- Emre, Ö., Doğan, A., Duman, T.Y. & Özalp, T. (2011). *1:250.000 scale active fault map series of Turkey*. General Directorate of Mineral Research and Exploration. Ankara-Turkey.
- Emre, Ö., Duman, T.Y., Özalp, S., Elmacı, H., Olgun, Ş., Şaroğlu, F. (2013). Açıklamalı Türkiye Diri Fay Haritası (1:1.250.000). *Maden Tetkik ve Arama Genel Müdürlüğü Özel Yayın Serisi*, 30.

- Emre, Ö., Erkal, T., Tchepalyga, A., Kazanci, N., Keçer, M. & Ünay, E. (1998). Doğu Marmara bölgesinin Neojen-Kuvaternerdeki evrimi, *Maden Tetkik ve Arama Dergisi*, 120, 233-258.
- Ercanoğlu, M. & Gökçeoğlu, C. (2004). Use of fuzzy relations to produce landslide susceptibility map of a landslide prone area (West Black Sea Region, Turkey). *Engineering Geology*, 75, 229–250.
- Erener, A. & Düzgün, H. S. B. (2010). Improvement of statistical landslide susceptibility mapping by using spatial and global regression methods in the case of More and Romsdal (Norway). *Landslides*, 7(1), 55–68. <https://doi.org/10.1007/s10346-009-0188-x>
- Ergin, K., Güçlü Ü. ve Uz, Z. (1967). Türkiye ve civarının deprem kataloğu (M.S. 11 1964): *İTÜ Arz Fiziği Enst. Yay.* 28, 74 s.
- Fell, R., Corominas, J., Bonnard, C., Cascini, L., Leroi, E., & Savage, W. Z. (2008). Guidelines for landslide susceptibility, hazard and risk zoning for land-use planning. *Engineering Geology*, 102(3–4), 99–111. <https://doi.org/10.1016/j.enggeo.2008.03.014>
- Fisher, R. (1953). Dispersion on a sphere. *Proc. Royal Society London*, A217, 295-305.
- Froude, M. J., & Petley, D. N. (2018). Global fatal landslide occurrence from 2004 to 2016. *Natural Hazards and Earth System Sciences*, 18(8), 2161–2181. <https://doi.org/10.5194/nhess-18-2161-2018>
- Gariano, S. L. & Guzzetti, F. (2016). Landslides in a changing climate, *Earth-Sci. Rev.*, 162, 227–252, <https://doi.org/10.1016/j.earscirev.2016.08.011>
- Ghosh, D. K. & Srivastava, M. (1991). Point-load strength: an index for classification of rock material. *Bull Int Assoc Eng Geol*, 44, 27–33.

- Glade, T. Landslide occurrence as a response to land use change: a review of evidence from New Zealand, *Catena*, 51, 297–314, [https://doi.org/10.1016/S0341-8162\(02\)00170-4](https://doi.org/10.1016/S0341-8162(02)00170-4), 2003.
- Glade, T., Anderson, M., & Crozier, M. J. (2005). *Landslide Hazard and Risk* (T. Glade, M. Anderson, & M. J. Crozier, Eds.). John Wiley & Sons, Ltd.
- Gokceoglu, C., Sonmez, H., Nefeslioglu, H. A., Duman, T. Y., & Can, T. (2005). The 17 March 2005 Kuzulu landslide (Sivas, Turkey) and landslide-susceptibility map of its near vicinity. *Engineering Geology*, 81(1), 65–83. <https://doi.org/10.1016/j.enggeo.2005.07.011>
- Gokceoglu, C. & Zorlu, K. (2004). A fuzzy model to predict the uniaxial compressive strength and the modulus of elasticity of a problematic rock. *Engineering Applications of Artificial Intelligence*, 17(1), 61–72.
- Gokce, O., Ozden, S., & Demir, A. (2008). *Türkiye’de Afetlerin Mekansal ve İstatistiksel Dağılımı Afet Bilgileri Envateri*.
- Göncüoğlu, M. C., Turhan, N., Şentürk, K., Uysal, Ş., Özcan, A., Işık, A. (1996). Orta Sakarya’da Nallıhan Sarıcakaya arasındaki yapısal birliklerin jeolojik özellikleri. *Maden Tetkik ve Arama Derleme Rapor*, 10094.
- Goodman, R. E. (1989). Introduction to rock mechanics. 2nd Edition, *John Wiley & Sons Ltd., New York*, 562.
- Gözübol, A.M. (1978). Mudurnu-Dokurcun-Abant (Bolu ili) alanının jeoloji incelemesi ve Kuzey Anadolu yarımının yapısal özellikleri. *PhD Dissertation*, İÜ Fen Fak. Uygulamalı Jeoloji Kürsüsü, 116.
- Greenwood, W., Zekkos, D., Lynch, J., Bateman, J., Clark, M., and Chamlagain, D. (2016). UAV-based 3-D characterization of rock masses and rock slides in Nepal. *50th U.S. Rock Mechanics/Geomechanics Symposium*.

- Harris, R.A., Dolan, J.F., Hartleb, R., Day, S.M. (2002). The 1999 Izmit, Turkey, earthquake: A 3D dynamic stress transfer model of intraequake triggering. *Bulletin of the Seismological Society of America*, 92 (1), 245-255. <https://doi.org/10.1785/0120000825>
- Hoek, E. & Bray, J.W. (1981). Rock slope engineering (Third edition). The *Institution of Mining and Metallurgy, London*.
- Hoek, E., and Karzulovic, A. (2001). Rock mass properties for surface mines. In *Slope Stability in Surface Mining* (Hustrulid, W.A., McCarter, M.K. and van Zyl, Littleton, D.J.A. Eds.), 59-70.
- Hungr, O., Leroueil, S., & Picarelli, L. (2014). The Varnes classification of landslide types, an update. In *Landslides* (Vol. 11, Issue 2, pp. 167–194). Springer Verlag. <https://doi.org/10.1007/s10346-013-0436-y>
- Hunt, R. E. (1996). Geotechnical engineering analysis and evaluation. *McGraw-Hill Book Co., New York*, 729.
- ISRM (2007). The complete ISRM suggested methods for rock characterization, testing and monitoring: 1974-2006 (R. Ulusay and J. A. Hudson, Eds.). *Commission on Testing Methods, International Society of Rock Mechanics, Ankara*, 628.
- Kahraman, S. & Günaydın, O. (2009). The effect of rock classes on the relation between uniaxial compressive strength and point load index test. *Bulletin of Engineering Geology and the Environment*, 68, 345–353. <https://doi.org/10.1007/s10064-009-0195-0>
- Kayabaşı, A. & Gökçeoğlu, C. (2022). An assessment on the correlations between uniaxial compression strength and point load index. *Arabian Journal of Geosciences*, 15, 268. <https://doi.org/10.1007/s12517-021-09391-3>
- Ketin, I. (1969). Über die Nordanatolische Horizontalverschiebung. *Bull Mineral Res. Explor. Inst. (MTA) Turkey*. 72, 1-28.

Kliche, C. A. (2018). *Rock slope stability*. SME.

Kohno, M. & Maeda, H. (2012). Relationship between point load strength index and uniaxial compressive strength of hydrothermally altered soft rocks. *International Journal of Rock Mechanics and Mining Science*, 50, 147–157.

Lettis, W., Bachhuber, J., Witter, R., Brankman, C., Randolph, C., Barka, A., Page, W. & Kaya, A. (2002). Influence of releasing step-overs on surface fault rupture and fault segmentation: Examples from the 17 August 1999 Izmit earthquake on the North Anatolian Fault, Turkey, *Bull. seism. Soc. Am.*, 92, 43–60.

Manousakis, J., Zekkos, D., Saroglou, F., Clark, M. (2016). Comparison of UAV-enabled photogrammetry-based 3D point clouds and interpolated DSMs of sloping terrain for rockfall hazard analysis. *Int. Arch. Photogramm. Remote Sens. Spatial Inf. Sci.*, XLII-2/W2, 71-77. <https://doi.org/10.5194/isprs-archives-XLII-2-W2-71-2016>

Mauldon, M. (1994). Intersection probabilities of impersistent joints. *Int. J. Rock Mech. Min. Sci. Geomech. Abstr.* 31, 107-115.

MTA (2003). *Atlas of North Anatolian Fault*. Special Publications Series, 2. MTA Press, Ankara.

Norrish, N.I, Wyllie, D.C. (1996). Rock slope stability analysis. In *Landslides: Investigation and Mitigation, Special Report No. 247 (Turner K.T. and Schuster, R.L., Eds.)*. Transportation Research Board National Research Council, Washington DC, 391-425.

Okalp, K., & Akgün, H. (2016). National level landslide susceptibility assessment of Turkey utilizing public domain dataset. *Environmental Earth Sciences*, 75(9). <https://doi.org/10.1007/s12665-016-5640-3>

- Okalp, K., & Akgün, H. (2022). Landslide susceptibility assessment in medium-scale: case studies from the major drainage basins of Turkey. *Environmental Earth Sciences*, 81(8). <https://doi.org/10.1007/s12665-022-10355-3>
- Omran, F., Mohamed, S., Abdalla, D., El-Hattab, M. (2021). Assessment of natural coastal hazards at Alexandria/Nile Delta interface, Egypt. *Environmental Earth Sciences*, 80, 3. <https://doi.org/10.1007/s12665-020-09329-0>
- Öztürk, A., İnan, S. & Tutkun, Z. (1985). Abant-Yeniçağa Yöresinin Tektoniği, *Bull. Earth Sci. Cumhuriyet Univ.*, 2, 35-52.
- Öztürk, H.S., Kocaman, S., Gökçeoğlu, C. (2019). A low-cost approach for determination of discontinuity orientation using smartphone images and application to a part of Ihlara Valley (Central Turkey). *Engineering Geology*, 254, 63-75. <https://doi.org/10.1016/j.enggeo.2019.04.011>
- Palmstrom, A. (2001). Measurement and characterization of rock mass jointing. In *In-Situ Characterization of Rocks* (Sharma, V.M. and Saxena, K.R., Eds.), A.A. Balkema Publishers, London, 97.
- Parise, M. (2002). Landslide hazard zonation of slopes susceptible to rock falls and topples. *Natural Hazards and Earth System Sciences*, 2, 37–49.
- Park, H. J., West, T. R. & Woo, I. (2005). Probabilistic analysis of rock slope stability and random properties of discontinuity parameters, Interstate Highway 40, Western North Carolina, USA. *Engineering Geology*, 79, 230-250.
- Piteau, D.R. and Peckover, F.L. (1978). Engineering of rock slopes. In *Landslides: Analysis and Control, Special Report No. 176* (Schuster R.L. and Krizek, R.J., Eds.). Transportation Research Board National Research Council, Washington DC, 192-234.

- Priest, S. D. (1993). Discontinuity analysis for rock engineering. In *Discontinuity Analysis for Rock Engineering*. Springer Netherlands. <https://doi.org/10.1007/978-94-011-1498-1>
- Priest, S. D. & Hudson, J.A. (1976). Discontinuity spacings in rock. *International Journal of Rock Mechanics and Mining Sciences & Geomechanics Abstracts*, 13(5), 135-148.
- Raetzo, .H., Lateltin, .O., Bollinger, .D., Tripet, J. (2002). Hazard assessment in Switzerland - Codes of Practice for mass movements. *Bull Eng Geol Environ*, 61, 263-268. <https://doi.org/10.1007/s10064-002-0163-4>
- Rencher, A.C., Christensen, W.F. (2012). Methods of multivariate analysis. *John Wiley & Sons*.
- Riquelme, A. J., Abellán, A., & Tomás, R. (2015). Discontinuity spacing analysis in rock masses using 3D point clouds. *Engineering Geology*, 195, 185–195. <https://doi.org/10.1016/j.enggeo.2015.06.009>
- Riquelme, A. J., Abellán, A., Tomás, R., & Jaboyedoff, M. (2014). A new approach for semi-automatic rock mass joints recognition from 3D point clouds. *Computers and Geosciences*, 68, 38–52. <https://doi.org/10.1016/j.cageo.2014.03.014>
- Riquelme, A., Tomás, R., Cano, M., Pastor, J. L., & Abellán, A. (2018). Automatic mapping of discontinuity persistence on rock masses using 3D point clouds. *Rock Mechanics and Rock Engineering*, 51(10), 3005–3028. <https://doi.org/10.1007/s00603-018-1519-9>
- Rocscience (2022). Dips: Graphical and statistical analysis of orientation data, *Rocscience Inc. Toronto, Canada*.
- Rocscience (2022). RocPlane: Planar & wedge analysis for slopes, *Rocscience Inc. Toronto, Canada*.

- Rocscience (2022). SWedge: Surface wedge analysis for slopes, *Rocscience Inc. Toronto, Canada*.
- Romana, M. (1985). New adjustment ratings for application of Bieniawski classification to slopes. *Proceedings of the International Symposium on the Role of Rock Mechanics in Excavations for Mining and Civil Works. International Society of Rock Mechanics, Zacatecas*, 49-53.
- Saroglu F., Emre, Ö.7 Boray, A. (1987). Türkiye'nin diri fayları ve depremsellikleri. *MTA Report no: 8174*, Ankara
- Saner, S. (1977). Geyve-Osmaneli-Taraklı alanının jeolojisi: eski çökeltme ortamları, çökeltmenin evrimi. *PhD Dissertation*, İstanbul Üniversitesi
- Saner, S. (1980). Mudurnu-Göynük havzasının Jura ve sonrası çökeltim nitelikleriyle paleocoğrafya yorumlaması. *Bulletin of Geological Society of Turkey*, 23, 39-52.
- Sengor, A.M.C. (1979). The North Anatolian transform fault: its age, offset and tectonic significance. *J. Geol. Soc. Lond.*, 136, 269-282
- Sipahioğlu, S. (1984). Earthquake activity of North Anatolian fault zone. Bulletin of Earthquake Research. *Earthquake Department Disaster and Emergency Management Authority of Turkey* (in Turkish).
- Soeters, R. and van Westen, C.J. (1996). Slope instability recognition analysis and zonation. In *Landslides: Investigation and Mitigation, Special Report No. 247* (Turner K.T. and Schuster, R.L., Eds.). Transportation Research Board National Research Council, Washington DC, 129-177.
- Sturzenegger, M. and Stead, D. (2009). Quantifying discontinuity orientation and persistence on high mountain rock slopes and large landslides using terrestrial remote sensing techniques. *Nat. Hazards Earth Syst. Sci.*, 9, 267-287. <https://doi.org/10.5194/nhess-9-267-2009>

- Syafril, N. S., Udin, W. S., & Achmad Bahar, A. M. (2020). GIS-Based Landslide Hazard Evaluation and Zonation of Kg. Chas, Kuala Betis, Gua Musang, Kelantan. *IOP Conference Series: Earth and Environmental Science*, 549(1). <https://doi.org/10.1088/1755-1315/549/1/012013>
- Topal, T. (2000). Problems faced in the applications of the point load index test. *Geological Engineering Journal*, 23/24(1), 73–86.
- Turkish Building Earthquake Code (TBEC) (2019). *Turkish Republic Ministry of Interior, Disaster and Emergency Management Presidency (AFAD) (Ankara Turkey)*.
- Turkish Earthquake Hazard Map (TEHM) (2018). *Turkish Republic Ministry of Interior, Disaster and Emergency Management Presidency (AFAD) (Ankara Turkey)*.
- Turkish Statistical Institute (TSI) (2019). *Address Based Population Registration System*.
- Turkish State Meteorological Service (2021). Meteorological data of Mudurnu Station. *Turkish State Meteorological Service (MGM)*. (unpublished)
- UN (2006). Global survey in early warning systems. Retrieved January 15, 2022 on https://www.preventionweb.net/files/3612_GlobalSurveyofEarlyWarningSystems.pdf
- Van Westen, C. J., Van Asch, T. W. J., & Soeters, R. (2006). Landslide hazard and risk zonation - Why is it still so difficult? *Bulletin of Engineering Geology and the Environment*, 65(2), 167–184. <https://doi.org/10.1007/s10064-005-0023-0>
- Varnes, D.J. (1978). Slope movement types and processes. In Special Report 176: Landslides: Analysis and Control (R. L. Schuster and R. J. Krizek, eds.), *Transportation and Road Research Board, National Research Council, Washington, D. C.*, 11-33.

- Wyllie, D. C. (2018). *Rock slope engineering: Civil applications*, (Fifth Edition), *CRC Press Taylor & Francis Group*.
- Yalçın, I., Can, R., Kocaman, S., Gökçeoğlu, C. (2022). A CNN architecture for discontinuity determination of rock masses with close range images. *The International Archives of the Photogrammetry, Remote Sensing and Spatial Information Sciences*.
- Yılmaz, Y., Tüysüz, O., Gözübol, A.M., Yiğitbaş, E. (1981). Abant (Bolu) - Dokurcun (Adapazarı) arasındaki Kuzey Anadolu fay zonunun kuzeyinde ve güneyinde kalan birliklerin jeolojik evrimi. *İstanbul Yer Bilimleri*, 2(3-4), 239-261.
- Zhang, L. (2005). Engineering properties of rocks. *Elsevier Geo-Engineering Book Series - Volume 4* (Hudson, J. A. Ed.), 288.

APPENDICES

A. Thin sections

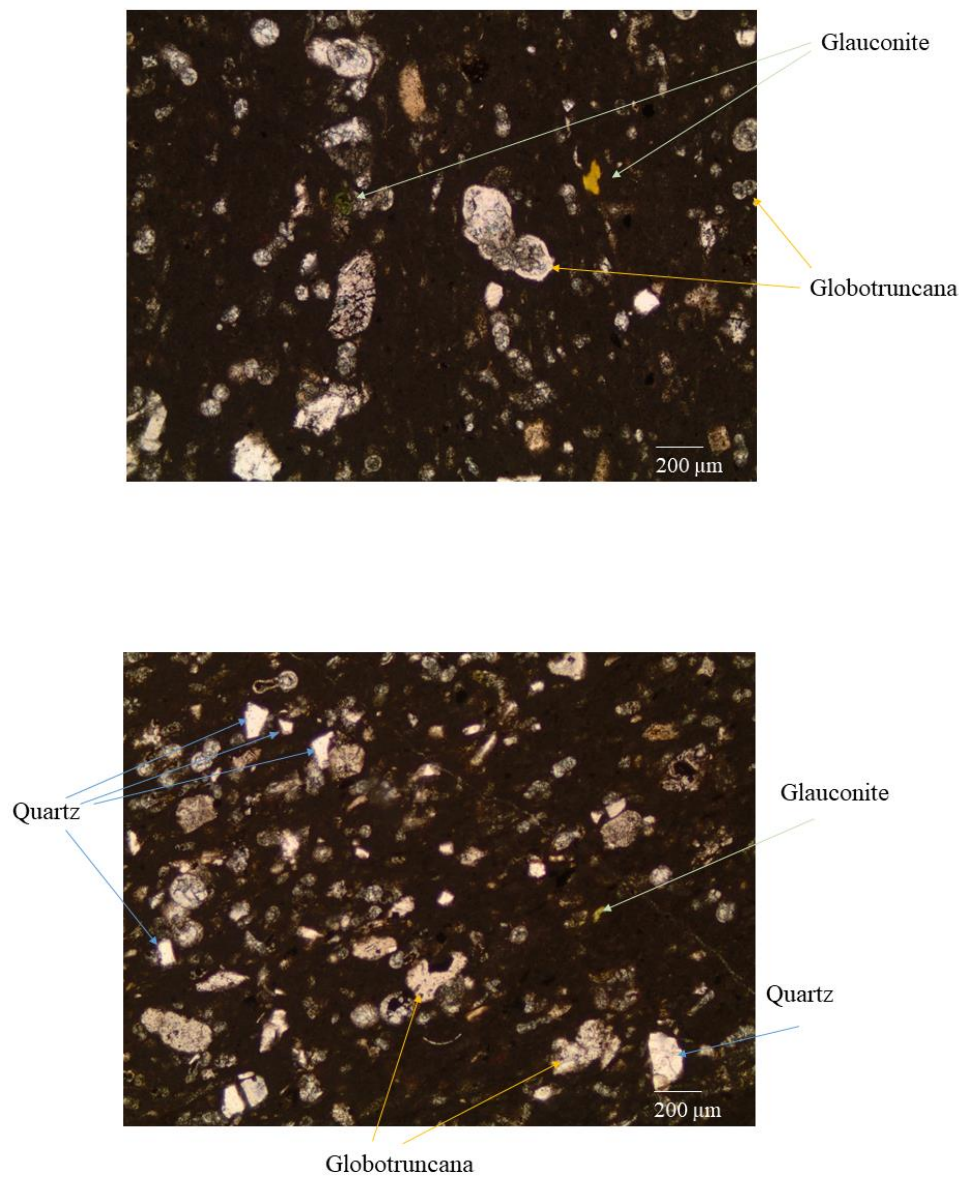


Figure A 1: Thin sections of the pelagic limestone of Sector 4 (under PPL - plane polarized light)

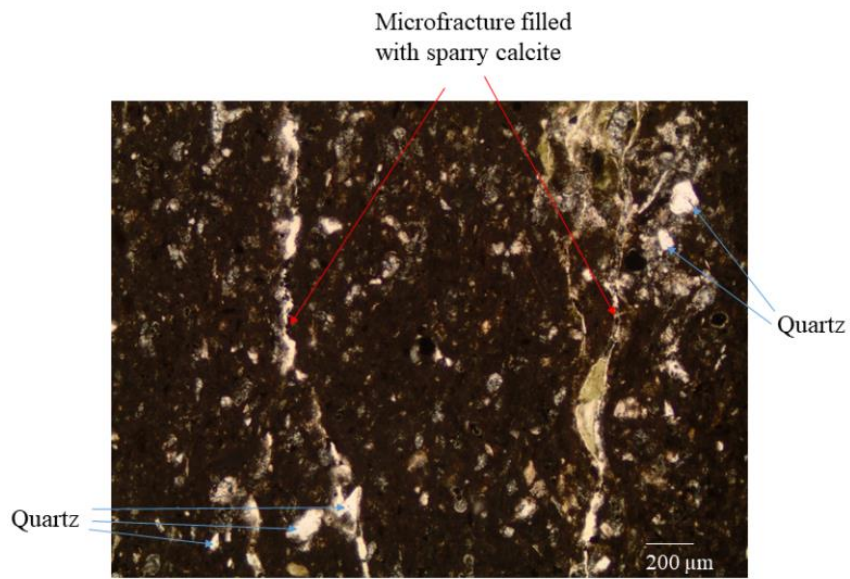


Figure A 2: Thin section of the pelagic limestone of Sector 10 (under PPL - plane polarized light)

B. Field survey measurements

Table B 1: Field scan-line survey measurements

Coordinates		Sector	Slope face orientation		Degree of weathering	Discontinuity plane orientation		Persistence (m)	Spacing (mm)	Aperture (cm)	Infilling	Roughness	Shape	JRC
Easting	Northing		Dip	Dip direction		Dip	Dip direction							
348258	4480725	2	54	90	slightly	44	270	very high	300	2	silty clay	undulating rough	4	6-8
348258	4480725	2	54	90	slightly	54	280	very high	600	close	no infill	undulating smooth	3	4-6
348294	4480720	2	54	90	slightly	45	280	very high	280	1.5	clay	undulating rough	5	8-10
348294	4480720	2	54	90	slightly	78	84	high	270	0.1	calcite	undulating smooth	2	2-4
348258	4480725	2	54	90	slightly	73	274	very high	300	close	no infill	smooth to rough	4	6-8
348294	4480720	2	54	90	slightly	40	285	very high	200	4	silty clay	undulating rough	4	6-8
348294	4480720	2	54	90	slightly	80	85	high	110	close	no infill	undulating smooth	3	4-6
348294	4480720	2	54	90	slightly	79	180	high	340	0.5	calcite	undulating smooth	3	4-6
348294	4480720	2	54	90	slightly	80	185	high	360	0.1	calcite	undulating smooth	4	6-8
348294	4480720	2	54	90	slightly	43	275	high	500	0.5	clay	undulating rough	4	6-8
348294	4480720	2	54	90	slightly	45	270	high	420	close	no infill	undulating smooth	4	6-8
348294	4480720	2	54	90	slightly	80	82	high	350	0.1	clay	undulating smooth	3	4-6
348294	4480720	2	54	90	slightly	78	80	high	420	0.2	clay	undulating smooth	3	4-6
348294	4480720	2	54	90	slightly	55	278	high	470	0.3	silty clay	undulating rough	4	6-8
348294	4480720	2	54	90	slightly	74	260	high	530	close	no infill	undulating smooth	5	6-8
348294	4480720	2	54	90	slightly	42	265	high	450	0.1	no infill	undulating rough	5	8-10
348294	4480720	2	54	90	slightly	80	168	high	650	0.3	clay	undulating smooth	3	4-6
348294	4480720	2	54	90	slightly	82	170	high	690	0.1	no infill	undulating smooth	2	2-4
348261	4480718	2	65	82	slightly	45	275	high	210	0.3	silty clay	undulating rough	4	6-8
348261	4480718	2	65	82	slightly	35	270	high	320	1	silty clay	undulating rough	4	6-8
348261	4480718	2	65	82	slightly	63	66	high	500	0.5	clay	undulating smooth	3	4-6
348261	4480718	2	65	82	slightly	64	75	high	360	0.8	clay	undulating smooth	3	4-6
348261	4480718	2	65	82	slightly	83	190	high	230	close	no infill	undulating smooth	2	2-4
348261	4480718	2	65	82	slightly	76	193	high	280	0.2	no infill	undulating smooth	4	6-8
348261	4480718	2	65	82	slightly	39	270	high	370	1.2	clay	undulating rough	4	6-8
348261	4480718	2	65	82	slightly	40	280	high	380	0.8	clay	undulating smooth	5	8-10
348261	4480718	2	65	82	slightly	55	70	high	180	0.1	no infill	undulating smooth	2	2-4
348261	4480718	2	65	82	slightly	50	69	high	200	close	no infill	undulating smooth	3	4-6
348261	4480718	2	65	82	slightly	80	180	high	350	close	clay	undulating rough	3	4-6
348261	4480718	2	65	82	slightly	85	175	high	300	close	clay	undulating rough	3	4-6
348261	4480718	2	65	82	slightly	42	262	high	430	close	no infill	undulating rough	4	6-8
348261	4480718	2	65	82	slightly	40	268	high	470	close	no infill	undulating rough	4	6-8
348261	4480718	2	65	82	slightly	80	92	high	430	0.2	clay	undulating smooth	3	4-6
348261	4480718	2	65	82	slightly	75	95	high	480	0.1	clay	undulating smooth	3	4-6
348261	4480718	2	65	82	slightly	68	170	high	800	close	no infill	undulating rough	4	6-8
348261	4480718	2	65	82	slightly	76	172	high	790	0.1	no infill	undulating rough	4	6-8
348261	4480718	2	65	82	slightly	45	270	high	550	0.3	clay	undulating rough	5	8-10
348261	4480718	2	65	82	slightly	38	275	high	500	close	no infill	undulating rough	5	8-10

Table B1 (cont'd): Field scan-line survey measurements

348261	4480718	2	65	82	slightly	82	102	high	390	close	no infill	undulating smooth	3	4-6
348261	4480718	2	65	82	slightly	74	95	high	435	0.2	clay	undulating rough	2	2-4
348261	4480718	2	65	82	slightly	72	183	high	920	close	no infill	undulating smooth	4	6-8
348261	4480718	2	65	82	slightly	64	180	high	1000	close	no infill	undulating smooth	4	6-8
348261	4480599	4	71	85	slightly	37	258	very high	200	0.1	no infill	undulating rough	4	6-8
348261	4480599	4	71	85	slightly	40	265	very high	140	close	no infill	undulating rough	5	8-10
348261	4480599	4	71	85	slightly	70	82	high	150	0.15	clay	undulating smooth	3	4-6
348261	4480599	4	71	85	slightly	62	75	high	400	0.12	clay	undulating smooth	3	4-6
348261	4480599	4	71	85	slightly	74	82	high	250	0.2	clay	undulating smooth	3	4-6
348261	4480599	4	71	85	slightly	72	80	high	130	0.15	clay	undulating smooth	2	2-4
348261	4480599	4	71	85	slightly	70	170	high	150	0.12	clay	undulating smooth	4	6-8
348261	4480599	4	71	85	slightly	65	162	high	180	0.1	no infill	undulating rough	3	4-6
348261	4480599	4	71	85	slightly	64	160	high	210	0.1	no infill	undulating rough	3	4-6
348261	4480599	4	71	85	slightly	60	175	high	200	close	no infill	undulating rough	4	6-8
348261	4480599	4	71	85	slightly	38	270	very high	250	close	no infill	undulating rough	5	8-10
348261	4480599	4	71	85	slightly	45	260	very high	300	close	no infill	undulating rough	5	8-10
348261	4480599	4	71	85	slightly	52	264	very high	120	0.1	no infill	undulating smooth	5	8-10
348261	4480599	4	71	85	slightly	45	260	very high	130	close	no infill	undulating smooth	5	8-10
348261	4480599	4	71	85	slightly	42	257	very high	200	0.1	clay	undulating rough	5	8-10
348261	4480599	4	71	85	slightly	62	83	high	260	close	no infill	undulating smooth	2	2-4
348261	4480599	4	71	85	slightly	65	80	high	140	close	no infill	undulating smooth	3	4-6
348261	4480599	4	71	85	slightly	66	75	high	320	0.1	no infill	undulating smooth	3	4-6
348261	4480599	4	71	85	slightly	60	74	high	410	close	no infill	undulating rough	3	4-6
348261	4480599	4	71	85	slightly	75	68	high	500	close	no infill	undulating rough	3	4-6
348261	4480599	4	71	85	slightly	71	167	high	90	close	no infill	undulating smooth	4	6-8
348261	4480599	4	71	85	slightly	72	172	high	130	close	no infill	undulating rough	4	6-8
348261	4480599	4	71	85	slightly	70	165	high	100	0.1	no infill	undulating rough	4	6-8
348261	4480599	4	71	85	slightly	35	272	very high	210	0.15	clay	undulating rough	4	6-8
348261	4480599	4	71	85	slightly	39	265	very high	350	0.3	clay	undulating rough	4	6-8
348261	4480599	4	71	85	slightly	50	263	very high	420	close	no infill	undulating rough	4	6-8
348261	4480599	4	71	85	slightly	46	255	very high	400	0.1	clay	undulating smooth	4	6-8
348261	4480599	4	71	85	slightly	48	260	very high	630	0.12	clay	undulating smooth	4	6-8
348261	4480599	4	71	85	slightly	65	80	high	120	0.1	clay	undulating smooth	3	4-6
348261	4480599	4	71	85	slightly	60	70	high	200	0.1	clay	undulating rough	3	4-6
348261	4480599	4	71	85	slightly	70	85	high	500	0.1	clay	undulating smooth	2	2-4
348261	4480599	4	71	85	slightly	72	177	high	150	close	no infill	undulating smooth	3	4-6
348261	4480599	4	71	85	slightly	70	168	high	110	0.1	clay	undulating rough	4	6-8
348261	4480599	4	71	85	slightly	62	160	high	130	0.2	no infill	undulating rough	4	6-8
348261	4480599	4	71	85	slightly	65	175	high	150	close	no infill	undulating rough	4	6-8
348261	4480599	4	71	85	slightly	42	270	very high	650	0.25	clay	undulating smooth	5	8-10
348261	4480599	4	71	85	slightly	40	265	very high	500	close	no infill	undulating rough	4	6-8
348261	4480599	4	71	85	slightly	71	85	high	100	close	no infill	undulating smooth	3	4-6
348261	4480599	4	71	85	slightly	60	80	high	110	close	no infill	undulating smooth	3	4-6
348261	4480599	4	71	85	slightly	70	64	high	150	0.18	clay	undulating smooth	2	2-4
348261	4480599	4	71	85	slightly	66	170	high	120	close	no infill	undulating rough	4	6-8

Table B1 (cont'd): Field scan-line survey measurements

348261	4480599	4	71	85	slightly	62	172	high	100	close	no infill	undulating rough	4	6-8
348261	4480599	4	71	85	slightly	65	163	high	80	0.15	clay	undulating smooth	4	6-8
348261	4480599	4	71	85	slightly	60	170	high	220	0.1	clay	undulating smooth	4	6-8
348261	4480599	4	71	85	slightly	68	164	high	200	0.15	clay	undulating rough	4	6-8
348283	4480896	6	65	92	slightly to moderately	40	265	high	400	0.15	silty clay	undulating rough	7	12-14
348283	4480896	6	65	92	slightly to moderately	74	62	high	350	0.15	silty clay	undulating rough	9	16-18
348283	4480896	6	65	92	slightly to moderately	86	160	high	400	close	no infill	rough to smooth	7	12-14
348280	4480905	6	65	92	slightly to moderately	48	255	very high	100	0.2	silty clay	undulating rough	7	12-14
348280	4480905	6	65	92	slightly to moderately	50	270	very high	150	close	no infill	undulating rough	7	12-14
348280	4480905	6	65	92	slightly to moderately	58	278	very high	250	0.3	silty clay	undulating smooth	7	12-14
348280	4480905	6	65	92	slightly to moderately	45	282	very high	320	0.1	clay	undulating smooth	7	12-14
348280	4480905	6	65	92	slightly to moderately	35	280	very high	460	0.12	clay	undulating rough	8	14-16
348280	4480905	6	65	92	slightly to moderately	72	80	high	500	close	no infill	undulating rough	10	18-20
348280	4480905	6	65	92	slightly to moderately	75	82	high	650	0.15	clay	undulating rough	9	16-18
348280	4480905	6	60	75	slightly	82	85	high	300	0.2	clay	undulating rough	8	14-16
348280	4480905	6	65	92	slightly to moderately	85	130	high	530	close	no infill	undulating rough	7	12-14
348280	4480905	6	65	92	slightly to moderately	76	132	high	500	0.15	clay	undulating rough	5	8-10
348280	4480905	6	65	92	slightly to moderately	80	135	high	650	0.12	clay	undulating smooth	7	12-14
348280	4480905	6	60	75	slightly	83	150	high	780	0.12	clay	undulating rough	7	12-14
348280	4480905	6	60	75	slightly	38	270	very high	430	0.15	clay	undulating rough	8	14-16
348280	4480905	6	60	75	slightly	44	263	very high	300	0.2	silty clay	undulating rough	8	14-16
348280	4480905	6	60	75	slightly	40	260	very high	450	0.1	clay	undulating rough	7	12-14
348280	4480905	6	65	92	slightly to moderately	54	95	high	100	0.4	silty clay	undulating smooth	8	14-16
348280	4480905	6	60	75	slightly	80	92	high	320	0.1	clay	undulating smooth	8	14-16
348280	4480905	6	60	75	slightly	75	96	high	700	0.12	clay	undulating rough	9	16-18
348280	4480905	6	60	75	slightly	59	93	high	200	0.5	silty clay	undulating rough	10	18-20
348280	4480905	6	65	92	slightly to moderately	83	115	high	300	0.3	clay	undulating rough	7	12-14
348280	4480905	6	65	92	slightly to moderately	80	140	high	420	close	no infill	undulating rough	7	12-14
348280	4480905	6	60	75	slightly	86	130	high	170	0.5	clay	undulating rough	6	10-12
348280	4480905	6	60	75	slightly	85	142	high	350	0.1	no infill	undulating rough	6	10-12
348280	4480905	6	60	75	slightly	42	262	very high	460	0.1	clay	undulating rough	7	12-14
348280	4480905	6	60	75	slightly	38	270	very high	350	close	no infill	undulating smooth	7	12-14
348280	4480905	6	60	75	slightly	65	77	high	360	close	no infill	undulating rough	9	16-18
348280	4480905	6	60	75	slightly	50	94	high	270	0.1	silty clay	undulating rough	9	16-18
348280	4480905	6	60	75	slightly	83	142	high	360	0.2	no infill	undulating smooth	5	8-10
348280	4480905	6	60	75	slightly	79	123	high	430	0.5	clay	undulating smooth	6	10-12
348280	4480905	6	60	75	slightly	35	265	very high	280	0.2	clay	undulating smooth	8	14-16
348280	4480905	6	60	75	slightly	50	274	very high	210	close	no infill	undulating rough	8	14-16
348280	4480905	6	60	75	slightly	44	270	very high	200	close	no infill	undulating rough	8	14-16
348280	4480905	6	60	75	slightly	52	265	very high	150	0.5	silty clay	undulating rough	8	14-16
348280	4480905	6	60	75	slightly	49	253	very high	400	0.15	silty clay	undulating rough	7	12-14
348280	4480905	6	65	92	slightly to moderately	64	76	high	180	0.12	silty clay	undulating rough	10	18-20
348280	4480905	6	65	92	slightly to moderately	68	75	high	250	2.5	silty clay	undulating rough	9	16-18
348280	4480905	6	60	75	slightly	68	80	high	150	close	no infill	undulating rough	10	18-20
348280	4480905	6	60	75	slightly	55	84	high	250	0.2	silty clay	undulating rough	9	16-18

Table B1 (cont'd): Field scan-line survey measurements

348280	4480905	6	60	75	slightly	80	135	high	1200	0.1	no infill	undulating rough	5	8-10
348280	4480905	6	60	75	slightly	82	140	high	1300	0.1	no infill	undulating rough	6	10-12
348174	4481083	8	85	138	slightly	35	230	high	520	5	clay	undulating rough	5	8-10
348174	4481083	8	85	138	slightly	64	58	high	760	0.5	no infill	undulating smooth	4	6-8
348174	4481083	8	85	138	slightly	85	138	high	900	3	no infill	smooth to rough	6	10-12
348174	4481083	8	85	138	slightly	36	244	very high	200	0.15	calcite	undulating rough	5	8-10
348174	4481083	8	85	138	slightly	32	240	very high	120	0.12	clay	undulating rough	5	8-10
348174	4481083	8	85	138	slightly	38	248	very high	450	close	no infill	undulating rough	6	10-12
348174	4481083	8	85	138	slightly	40	245	very high	460	close	no infill	undulating smooth	5	8-10
348174	4481083	8	85	138	slightly	44	232	very high	400	0.1	clay	undulating rough	5	8-10
348174	4481083	8	85	138	slightly	32	230	very high	350	0.1	clay	undulating rough	5	8-10
348174	4481083	8	85	138	slightly	60	65	high	190	0.2	no infill	undulating smooth	4	6-8
348174	4481083	8	85	138	slightly	57	70	high	310	0.1	no infill	undulating smooth	4	6-8
348174	4481083	8	85	138	slightly	75	70	high	420	0.1	clay	undulating smooth	4	6-8
348174	4481083	8	85	138	slightly	70	68	high	300	close	no infill	undulating smooth	5	8-10
348174	4481083	8	85	138	slightly	65	64	high	650	close	no infill	undulating rough	5	8-10
348174	4481083	8	85	138	slightly	64	76	high	760	0.12	clay	undulating smooth	4	6-8
348174	4481083	8	85	138	slightly	82	154	high	280	close	no infill	undulating smooth	6	10-12
348174	4481083	8	85	138	slightly	85	150	high	430	close	no infill	undulating smooth	6	10-12
348174	4481083	8	85	138	slightly	80	140	high	550	0.1	clay	undulating smooth	6	10-12
348174	4481083	8	85	138	slightly	78	142	high	380	0.12	clay	undulating smooth	5	8-10
348174	4481083	8	85	138	slightly	83	140	high	640	0.1	no infill	undulating rough	6	10-12
348174	4481083	8	85	138	slightly	84	140	high	870	0.1	clay	undulating smooth	6	10-12
348266	4480990	8	80	110	slightly	34	225	very high	280	0.2	silty clay	undulating rough	5	8-10
348266	4480990	8	80	110	slightly	30	230	very high	300	0.15	clay	undulating rough	6	10-12
348266	4480990	8	80	110	slightly	35	260	very high	480	close	no infill	undulating rough	6	10-12
348266	4480990	8	80	110	slightly	42	230	very high	500	close	no infill	undulating rough	5	8-10
348266	4480990	8	80	110	slightly	37	220	very high	150	0.1	silty clay	undulating rough	5	8-10
348266	4480990	8	80	110	slightly	66	62	high	600	0.2	no infill	undulating smooth	4	6-8
348266	4480990	8	80	110	slightly	62	67	high	400	close	no infill	undulating smooth	4	6-8
348266	4480990	8	80	110	slightly	64	80	high	800	0.1	clay	undulating smooth	5	6-8
348266	4480990	8	80	110	slightly	81	160	high	520	close	no infill	undulating smooth	6	10-12
348266	4480990	8	80	110	slightly	78	162	high	350	0.1	no infill	undulating rough	6	10-12
348266	4480990	8	80	110	slightly	85	165	high	1000	0.15	clay	undulating rough	5	8-10
348266	4480990	8	80	110	slightly	36	214	very high	450	0.15	clay	undulating rough	5	8-10
348266	4480990	8	80	110	slightly	32	210	very high	100	0.2	silty clay	undulating smooth	5	8-10
348266	4480990	8	80	110	slightly	71	82	high	330	0.15	silty clay	undulating smooth	4	6-8
348266	4480990	8	80	110	slightly	69	70	high	800	close	clay	undulating smooth	4	6-8
348266	4480990	8	80	110	slightly	86	133	high	940	0.2	no infill	undulating rough	6	10-12
348266	4480990	8	80	110	slightly	83	173	high	970	0.1	no infill	undulating rough	6	10-12
348266	4480990	8	80	110	slightly	38	234	very high	160	0.2	clay	undulating rough	5	8-10
348266	4480990	8	80	110	slightly	40	245	very high	350	0.5	silty clay	undulating rough	5	8-10
348266	4480990	8	80	110	slightly	64	72	high	240	close	no infill	undulating smooth	4	6-8
348266	4480990	8	80	110	slightly	60	75	high	770	close	no infill	undulating smooth	4	6-8
348266	4480990	8	80	110	slightly	88	173	high	840	close	no infill	undulating smooth	6	10-12

Table B1 (cont'd): Field scan-line survey measurements

348266	4480990	8	80	110	slightly	85	180	high	600	close	no infill	undulating smooth	6	10-12
348270	4481030	10	70	75	slightly	34	240	high	550	3	clay	undulating rough	7	12-14
348270	4481030	10	70	75	slightly	75	55	high	620	0.5	no infill	undulating rough	4	6-8
348270	4481030	10	70	75	slightly	83	140	high	670	0.5	silty clay	undulating rough	4	6-8
348270	4481030	10	70	75	slightly	38	210	very high	360	0.2	silty clay	undulating rough	6	10-12
348270	4481030	10	70	75	slightly	45	210	very high	490	0.12	silty clay	undulating rough	7	12-14
348270	4481030	10	70	75	slightly	30	225	very high	330	0.13	silty clay	undulating smooth	5	8-10
348270	4481030	10	70	75	slightly	42	235	very high	400	0.1	silty clay	undulating rough	6	10-12
348307	4481018	10	70	75	slightly	84	65	high	600	close	no infill	undulating smooth	4	6-8
348307	4481018	10	70	75	slightly	86	70	high	470	0.1	no infill	undulating smooth	4	6-8
348307	4481018	10	70	75	slightly	80	72	high	380	0.1	clay	undulating rough	3	4-6
348307	4481018	10	70	75	slightly	82	75	high	350	0.12	clay	undulating rough	5	8-10
348307	4481018	10	70	75	slightly	85	140	high	460	0.2	clay	undulating rough	3	4-6
348307	4481018	10	70	75	slightly	70	162	high	520	0.15	clay	undulating smooth	3	4-6
348307	4481018	10	70	75	slightly	72	160	high	550	0.13	clay	undulating smooth	4	6-8
348307	4481018	10	70	75	slightly	76	173	high	480	close	no infill	undulating rough	4	6-8
348307	4481018	10	70	75	slightly	74	145	high	650	close	no infill	undulating rough	4	6-8
348270	4481030	10	70	75	slightly	35	245	very high	720	close	no infill	undulating rough	6	10-12
348270	4481030	10	70	75	slightly	38	230	very high	680	close	no infill	undulating rough	6	10-12
348270	4481030	10	70	75	slightly	83	75	high	410	close	no infill	undulating rough	4	6-8
348270	4481030	10	70	75	slightly	75	80	high	370	close	no infill	undulating rough	5	8-10
348307	4481018	10	70	75	slightly	80	65	high	600	0.1	no infill	undulating rough	5	8-10
348270	4481030	10	70	75	slightly	86	160	high	400	0.1	no infill	undulating rough	3	4-6
348307	4481018	10	70	75	slightly	70	130	high	710	0.1	clay	undulating rough	4	6-8
348307	4481018	10	70	75	slightly	80	160	high	670	0.1	clay	undulating smooth	4	6-8
348270	4481030	10	70	75	slightly	42	232	very high	590	0.15	clay	undulating rough	6	10-12
348307	4481018	10	70	75	slightly	45	220	very high	430	0.1	clay	undulating rough	7	12-14
348307	4481018	10	70	75	slightly	34	225	very high	650	0.2	no infill	undulating rough	7	12-14
348307	4481018	10	70	75	slightly	37	250	very high	700	close	no infill	undulating rough	6	10-12
348307	4481018	10	70	75	slightly	78	70	high	520	0.15	clay	undulating smooth	4	6-8
348307	4481018	10	70	75	slightly	82	67	high	480	close	no infill	undulating rough	4	6-8
348307	4481018	10	70	75	slightly	76	65	high	510	0.14	clay	undulating rough	5	8-10
348270	4481030	10	70	75	slightly	74	165	high	350	close	no infill	undulating rough	4	6-8
348307	4481018	10	70	75	slightly	74	125	high	590	close	no infill	undulating smooth	3	4-6
348307	4481018	10	70	75	slightly	40	225	very high	760	close	no infill	undulating smooth	6	10-12
348307	4481018	10	70	75	slightly	38	235	very high	580	close	no infill	undulating smooth	5	8-10
348307	4481018	10	70	75	slightly	36	230	very high	460	0.1	no infill	undulating rough	7	12-14
348307	4481018	10	70	75	slightly	34	230	very high	670	0.13	clay	undulating rough	7	12-14
348270	4481030	10	70	75	slightly	67	69	high	330	close	no infill	undulating rough	3	4-6
348270	4481030	10	70	75	slightly	86	70	high	500	0.1	no infill	undulating rough	3	4-6
348307	4481018	10	70	75	slightly	85	72	high	650	0.15	clay	undulating rough	5	8-10
348307	4481018	10	70	75	slightly	83	68	high	400	0.2	no infill	undulating rough	4	6-8
348270	4481030	10	70	75	slightly	65	150	high	400	close	no infill	undulating rough	3	4-6
348270	4481030	10	70	75	slightly	70	170	high	290	close	no infill	undulating rough	3	4-6
348307	4481018	10	70	75	slightly	86	165	high	450	0.1	no infill	undulating rough	4	6-8

C. Laboratory test sheets

Table C 1: Density-Unit Weight Determination sheet of Sector 4, 6, and 10, respectively

METU - DEPARTMENT OF GEOLOGICAL ENGINEERING ENGINEERING GEOLOGY LABORATORY						DENSITY - UNIT WEIGHT DETERMINATION (Caliper Method)	
Date : 10.11.2021						Tested by : Arzu ARSLAN KELAM	
Specimen Number*	D (mm)	L (mm)	w (mm)	Volume (cm ³)	W (g)	Density (g/cm ³)	Unit Weight (kN/m ³)
MD4/2	29.51	42.50	39.98	50.14	133.28	2.66	26.08
MD 4/7	31.64	39.89	35.60	44.93	119.02	2.65	25.98
MD 4/8	27.32	41.26	31.54	35.55	94.39	2.65	26.04
MD 6/1	31.37	41.11	33.22	42.84	113.30	2.64	25.94
MD 6/2	29.17	43.15	39.54	49.77	132.18	2.66	26.06
MD 6/3	29.73	42.35	37.91	47.73	126.94	2.66	26.09
MD 6/4	24.72	31.3	30.37	23.50	62.24	2.65	25.98
MD 10/4	32.00	46.20	44.13	65.25	172.30	2.64	25.91
MD 10/8	35.23	43.15	41.22	62.66	166.10	2.65	26.00
MD 10/11	29.10	45.92	42.25	56.46	149.91	2.66	26.05

*MD4, MD6 and MD10 represent the samples from Sectors 4, 6 and 10, respectively

Note: D, L and w are the depth, length and width of the prismatic specimen



Figure C 1: The block samples of Sector 4 and Sector 10 before and after the Point Load Strength Index testing

Table C 2: Point Load Strength Index test sheet of Sector 4

METU - DEPARTMENT OF GEOLOGICAL ENGINEERING ENGINEERING GEOLOGY LABORATORY							POINT LOAD STRENGTH INDEX TEST					
Date : 14.11.2021							Tested by : Arzu ARSLAN KELAM					
Specimen Number	Test Type*	D (mm)	L (mm)	W ₁ (mm)	W ₂ (mm)	W (mm)	P (kgf)	P (kN)	D _c ²	I _s (MPa)	F	I _{s50} (MPa)
MD4/1	b //	35.15	43.06	40.53	38.10	39.32	1339	13.13	1759.52	7.4629	0.924	6.8958
MD4/3	b ⊥	32.04	51.34	40.58	40.54	40.56	2087	20.47	1654.63	12.3692	0.9113	11.2723
MD4/5	b ⊥	34.74	47.41	40.54	40.78	40.66	1634	16.02	1798.49	8.9097	0.9286	8.2734
MD4/6	b //	30.14	43.95	39.43	41.37	40.40	1069	10.48	1550.37	6.7618	0.8981	6.0726
MD4/7	b //	32.26	40.92	35.93	36.16	36.05	1002	9.83	1480.54	6.6370	0.8888	5.8990
MD4/9	b //	39.71	40.02	40.68	39.37	40.03	1007	9.88	2023.68	4.8799	0.9536	4.6532
MD4/10	b ⊥	39.12	41.90	41.61	40.88	41.25	1785	17.50	2054.38	8.5208	0.9568	8.1526
MD4/11	b ⊥	41.40	44.55	42.69	43.20	42.95	2020	19.81	2263.72	8.7508	0.9779	8.5575
MD4/12	b //	39.86	43.36	42.85	42.14	42.50	986	9.67	2156.68	4.4835	0.9673	4.3369
MD4/13	b //	40.06	45.76	42.49	41.53	42.01	1129	11.07	2142.76	5.1670	0.9659	4.9908
MD4/14	b ⊥	41.85	44.05	45.87	43.88	44.88	1558	15.28	2391.17	6.3897	0.9900	6.3260
MD4/16	b //	42.71	45.73	44.23	45.52	44.88	1473	14.45	2440.31	5.9194	0.9946	5.8873
MD4/17	b ⊥	41.23	42.74	41.67	41.96	41.82	1873	18.37	2195.11	8.3676	0.9712	8.1263
MD4/18	b ⊥	42.90	44.51	43.45	44.05	43.75	1222	11.98	2389.71	5.0147	0.9899	4.9641
MD4/19	b //	32.37	42.87	34.47	33.21	33.84	1350	13.24	1394.71	9.4923	0.8769	8.3242
MD4/20	b //	43.04	43.58	43.57	43.22	43.40	1520	14.91	2378.06	6.2682	0.9888	6.1981

*b=block, //parallel to plane of weakness, ⊥perpendicular to plane of weakness

Note: W is average width $((W_1+W_2)/2)$ of the specimen having unparallel dimension, D_c is equivalent core diameter, I_s is point load strength index of specimen tested, F is dimension correction factor, I_{s50} is corrected point load strength index for 50 mm

Table C 3: Point Load Strength Index test sheet of Sector 10

METU - DEPARTMENT OF GEOLOGICAL ENGINEERING ENGINEERING GEOLOGY LABORATORY							POINT LOAD STRENGTH INDEX TEST					
Date : 14.11.2021							Tested by : Arzu ARSLAN KELAM					
Specimen Number	Test Type*	D (mm)	L (mm)	W ₁ (mm)	W ₂ (mm)	W (mm)	P (kgf)	P (kN)	D _c ²	I _s (MPa)	F	I _{s50} (MPa)
MD10/1	b //	29.70	44.04	43.30	45.27	44.29	1552	15.22	1674.65	9.0884	0.9138	8.3049
MD10/2	b //	27.69	42.80	43.86	46.09	44.98	844	8.28	1585.64	5.2199	0.9026	4.7116
MD10/3	b //	31.39	48.67	44.79	44.26	44.53	605	5.93	1779.53	3.3340	0.9264	3.0885
MD10/4	b ⊥	32.92	46.37	45.25	46.75	46.00	714	7.00	1928.09	3.6315	0.9432	3.4254
MD10/5	b //	32.07	46.32	43.95	42.49	43.22	966	9.47	1764.79	5.3679	0.9246	4.9633
MD10/7	b //	41.15	44.39	42.56	42.93	42.75	2079	20.39	2239.57	9.1035	0.9756	8.8810
MD10/8	b //	36.02	44.43	42.30	41.34	41.82	1466	14.38	1917.95	7.4958	0.9421	7.0619
MD10/9	b //	32.95	43.29	43.86	41.27	42.57	1407	13.80	1785.74	7.7267	0.9271	7.1634
MD10/11	b ⊥	30.75	46.83	44.89	41.06	42.98	657	6.44	1682.56	3.8293	0.9148	3.5029
MD10/12	b //	32.09	44.80	37.28	36.08	36.68	989	9.70	1498.68	6.4715	0.8912	5.7677
MD10/13	b ⊥	31.55	41.05	38.81	38.16	38.49	655	6.42	1545.97	4.1549	0.8975	3.7290
MD10/15	b //	36.42	44.29	40.98	42.23	41.61	1176	11.53	1929.28	5.9777	0.9434	5.6391
MD10/17	b ⊥	30.77	43.58	40.56	39.32	39.94	881	8.64	1564.75	5.5214	0.8999	4.9690
MD10/19	b //	28.52	42.36	41.63	42.73	42.18	859	8.42	1531.67	5.4998	0.8956	4.9258
MD10/21	b ⊥	28.55	42.63	32.78	34.74	33.76	497	4.87	1227.21	3.9715	0.8521	3.3840

*b=block, //parallel to plane of weakness, ⊥perpendicular to plane of weakness

Note: W is average width $((W_1+W_2)/2)$ of the specimen having unparallel dimension, D_c is equivalent core diameter, I_s is point load strength index of specimen tested, F is dimension correction factor, I_{s50} is corrected point load strength index for 50 mm



Figure C 2: Slake Durability tested rock samples from Sectors 1, 2 and 4. The first column shows a view of specimens before the test, whereas the second and third columns present the condition of the specimen following the 1st and 2nd cycles, respectively

Table C 4: Slake Durability test sheet of Sector 1, Sector 2, Sector 4, Sector 6, and Sector 8

SLAKE DURABILITY TEST								
Specimen Number	Weight of Drum, C	Weight of Drum + Specimen, W_i (g)	Weight of Drum + Specimen after 1st Cycle, W_{f1} (g)	Weight of Drum + Specimen after 2nd Cycle, W_{f2} (g)	Slake Durability Index after 1st Cycle, I_{d1}	Slake Durability Index after 2nd Cycle, I_{d2}	Specimen Type after 1st Cycle*	Specimen Type after 2nd Cycle*
MD1	2079.2	2539.3	2536.2	2535.2	99.3	99.1	I	I
MD2	2079.2	2606.8	2603.2	2601.4	99.3	99.0	I	I
MD4	2079.2	2574.2	2570.9	2569.0	99.3	98.9	II	II
MD5	2099.0	2617.2	2613.8	2612.2	99.3	99.0	I	I
MD8	2099.0	2688.7	2685.1	2681.2	99.4	98.7	I	I

*Type I-Retained specimens remain virtually unchanged

Type II-Retained specimens consist of large and small fragments

Type III-Retained specimens are exclusively small fragments

D. Rock mass classification system tables

Table D 1: Rock Mass Rating (RMR) system table (Bieniawski, 1989) along with the values used for the discontinuous limestone

A. CLASSIFICATION PARAMETERS AND THEIR RATINGS								
Parameter		Ranges of Values						
1	Strength of intact rock material	Point-load strength index	>10 MPa	4 – 10 MPa	2 – 4 MPa	1 – 2 MPa	For this low range – uniaxial compressive test is preferred	
		Uniaxial compressive strength	>250 MPa	100 – 250 MPa	50 – 100 MPa	25 – 50 MPa	5 -25 MPa	1 – 5 MPa
	Rating	15	12	7	4	2	1	0
2	Drill core quality RQD (%)	90%– 100%	75 % - 90 %	50 % - 75 %	25 % - 50 %	<25 %		
	Rating	20	17	13	8	3		
3	Spacing of discontinuities	>2 m	0.6-2 m	200-600mm	60-200 mm	<60 mm		
	Rating	20	15	10	8	5		
4	Condition of discontinuities (See E)	Very rough surfaces	Slightly rough surfaces	Slightly rough surfaces	Slickensided surfaces or Gouge <5 mm thick or	Soft gouge >5 mm thick or Separation >5 mm Continuous		
		Not continuous	Separation <1 mm	Separation <1 mm	Separation 1- 5 mm Continuous			
		No separation Unweathered wall rock	Slightly weathered walls	Highly weathered walls				
Rating	30	25	20	10	0			
5	Ground water	Inflow per 10 m tunnel length (L/min)	None	<10	10 – 25	25 - 125	>125	
		(Joint water pressure)/(Major principal stress)	0	<0.1	0.1 – 0.2	0.2 – 0.5	>0.5	
	General conditions	Completely dry	Damp	Wet	Dripping	Flowing		
	Rating	15	10	7	4	0		
B. RATING ADJUSTMENT FOR DISCONTINUITY ORIENTATIONS (See F)								
Strike and dip orientations		Very favourable	Favourable	Fair	Unfavourable	Very unfavourable		
Ratings	Tunnels & mines	0	-2	-5	-10	-12		
	Foundation	0	-2	-7	-15	-25		
	Slopes	0	-5	-25	-50			
C. ROCK MASS CLASSES DETERMINED FROM TOTAL RATINGS								
Rating	100 - 81	80 - 61	60 - 41	40 - 21	<21			
Class number	I	II	III	IV	V			
Description	Very good rock	Good rock	Fair rock	Poor rock	Very poor rock			
D. MEANING OF ROCK CLASSES								
Class number	I	II	III	IV	V			
Average stand-up time	20 yrs for 15 m span	1 year for 10 m span	1 week for 5 m span	10 hrs for 2.5 m span	30 min for 1 m span			
Cohesion of rock mass (kPa)	>400	300 - 400	200 - 300	100 - 200	<100			
Friction angle of rock mass (deg)	>45	35 - 45	25 - 35	15 - 25	<15			
E. GUIDELINES FOR CLASSIFICATION OF DISCONTINUITY CONDITIONS *								
Discontinuity length (persistence)	<1 m	1 – 3 m	3 – 10 m	10 – 20 m	>20 m			
Rating	6	4	2	1	0			
Separation (aperture)	None	<0.1 mm	0.1 - 1.0 mm	1 - 5 mm	>5 mm			
Rating	6	5	4	1	0			
Roughness	Very rough	Rough	Slightly rough	Smooth	Slickensided			
Rating	6	5	3	1	0			
Infilling (gouge)	None	Hard filling <5 mm	Hard filling >5 mm	Soft filling < 5 mm	Soft filling >5 mm			
Rating	6	4	2	2	0			
Weathering	Unweathered	Slightly weathered	Moderately weathered	Highly weathered	Decomposed			
Ratings	6	5	3	1	0			
F. EFFECT OF DISCONTINUITY STRIKE AND DIP ORIENTATION IN TUNNELING **								
Strike perpendicular to tunnel axis				Strike parallel to tunnel axis				
Drive with dip – Dip 45 -90°		Drive with dip – Dip 20 -45°		Dip 45 -90°		Dip 20 - 45°		
Very favourable		Favourable		Very favourable		Fair		
Drive against dip – Dip 45 -90°		Drive against dip – Dip 20 -45°		Dip 0 -20° - Irrespective of strike				
Fair		Unfavourable		Fair				

Table D 2: Correction parameters and description of SMR classes (Romana, 1985)

Correction parameters for SMR related to joints						
Type of failure*	Correction parameter	Very favorable	Favorable	Normal	Unfavorable	Very unfavorable
P		>30°	30°-20°	20°-10°	10°-5°	<5°
W	A	>30°	30°-20°	20°-10°	10°-5°	<5°
T		>30°	30°-20°	20°-10°	10°-5°	<5°
P/W/T	F ₁	0.15	0.40	0.70	0.85	1.00
P	B	<20°	20°-30°	30°-35°	35°-45°	>45°
W	B	<20°	20°-30°	30°-35°	35°-45°	>45°
P/W	F ₂	0.15	0.40	0.70	0.85	1.00
T	F ₂	1.00	1.00	1.00	1.00	1.00
P	C	>10°	10°-0°	0°	0°-(-10°)	<(-10°)
W	C	>10°	10°-0°	0°	0°-(-10°)	<(-10°)
T	C	<110°	110°-120°	>120°	-	-
P/W/T	F ₃	0	-6	-25	-50	-60

*P=planar failure, W=wedge failure, T=toppling failure

Correction parameters for SMR related to methods of excavation	
Excavation method	F ₄
Natural slope	15
Presplitting	10
Smooth blasting	8
Blasting or mechanical	0
Deficient blasting	-8

Description of SMR classes					
Class	SMR	Description	Stability	Failures	Failure probability
I	81-100	Very good	Completely stable	None	0
II	61-80	Good	Stable	Some blocks	0.2
III	41-60	Normal	Partially stable	Some joints or many wedges	0.4
IV	21-40	Bad	Unstable	Planar or big wedges	0.6
V	0-20	Very bad	Completely unstable	Big planar or soil-like	0.9

Table D 3: Q-slope table (Barton and Bar, 2015)

Rock Quality Designation	description	RQD (%) ^a
A	Very poor	0-25
B	Poor	25-50
C	Fair	50-75
D	Good	75-90
E	Excellent	90-100

^a where RQD reported or measured as ≤ 10 (including zero), a nominal value of 10 is used to evaluate Q-slope. RQD intervals of 5, i.e., 100, 95, 90, etc., are sufficiently accurate

Joint set number	description	J_n
A	Massive, no or few joints	0.5-1
B	One joint set	2
C	One joint set plus random joints	3
D	Two joint sets	4
E	Two joint sets plus random joints	6
F	Three joint sets	9
G	Three joint sets plus random joints	12
H	Four or more joint sets, random, heavily jointed	15
J	Crushed rock, earthlike	20

Joint roughness number	description	J_r
(a)	Rock wall contact, (b) contact after shearing	J_r
A	Discontinuous joints	4
B	Rough or irregular, undulating	3
C	Smooth, undulating	2
D	Slickensided, undulating	1.5
E	Rough or irregular, planar	1.5
F	Smooth, planar	1
G	Slickensided, planar	0.5
(c)	No rock wall contact when sheared	
H	Zone containing clay minerals thick enough to prevent rock wall contact	1
J	Sandy, gravelly, or crushed zone thick enough to prevent rock wall contact	1

Descriptions refer to small-scale features and intermediate-scale features, in that order

Add 1.0 if mean spacing of the relevant joint set is greater than 3 m

$J_r = 0.5$ can be used for planar, slickensided joints having lineations, provided the lineations are favorably

oriented for minimum strength

J_r and J_n classification are applied to discontinuity set or sets that are least favorable for stability both from the

point of view of orientation and shear resistance τ , where $\tau = \sigma_n \tan^{-1}(J_r/J_n)$

Joint alteration number	description	J_a
(a)	Rock wall contact (no mineral filling, only coating)	
A	Tightly healed, hard, non-softening, impermeable filling, i.e., quartz or epidote	0.75
B	Unaltered joint walls, surface staining only	1
C	Slightly altered joint walls. Non-softening mineral coatings, sandy particles, clay free disintegrated rock, etc.	2
D	Silty- or sandy-clay coatings, small clay disintegrated rock, etc.	3
E	Softening or low friction clay mineral coatings, i.e., kaolinite or mica. Also chlorite, talc, gypsum, graphite, e 4 and small quantities of swelling clays	
(b)	Rock wall contact after some shearing (thin clay fillings, probable thickness $\approx 1-5$ mm)	
F	Sandy particles, clay-free disintegrated rock, etc.	4
G	Strongly over-consolidated, non-softening clay mineral fillings	6
H	Medium or low over-consolidation, softening, clay mineral fillings	8
J	Swelling clay fillings, i.e., montmorillonite. Value of J_a depends on percent of swelling clay-size particles and 8-12 access to water	
(c)	No rock wall contact when sheared (thick clay/crushed rock fillings)	
M	Zones or bands of disintegrated or crushed rock and clay (see G,H, I for description of clay condition)	6,8, or 8-12
N	Zones or bands of silty- or sandy-clay, small clay fraction (non-softening)	5
OPR	Thick, continuous zones or bands of clay (see G, H, J for description of clay condition)	10,13, or 13-20

Table D 3 (continued): Q-slope table (Barton and Bar, 2015)

O-factor description	Set A	Set B
Very favorably oriented	2	1.5
Quite favorable	1	1
Unfavorable	0.75	0.9
Very unfavorable	0.5	0.8
Causing failure if unsupported	0.25	0.5

Environmental and geological condition number

J_{wice}^a	Desert environment	Wet environment	Tropical storms	Ice wedging
Stable structure; competent rock	1	0.7	0.5	0.9
Stable structure; incompetent rock	0.7	0.6	0.3	0.5
Unstable structure; competent rock	0.8	0.5	0.1	0.3
Unstable structure; incompetent rock	0.5	0.3	0.05	0.2

^aWhen drainage measures are installed, apply $J_{wice} \times 1.5$, when slope reinforcement measures are installed, apply $J_{wice} \times 1.3$, and when drainage and reinforcement are installed, apply both factors $J_{wice} \times 1.5 \times 1.3$

SRF_a physical condition

Description	SRF _a
A Slight loosening due to surface location, disturbance from blasting or excavation	2.5
B Loose blocks, signs of tension cracks and joint shearing, susceptibility to weathering, severe disturbance from blasting	5
C As B, but strong susceptibility to weathering	10
D Slope is in advanced stage of erosion and loosening due to periodic erosion by water and/or ice-wedging effects	15
E Residual slope with significant transport of material downslope	20

SRF_b stress and strength

Description	σ_c / σ_1	SRF _b
F Moderate stress-strength range	50-200	2.5-1
G High stress-strength range	10-50	5-2.5
H Localized intact rock failure	5-10	10-5
J Crushing or plastic yield	2.5-5	15-10
K Plastic flow or strain softened material	1-2.5	20-15

SRF_c major discontinuity

SRF _c	Description	Favorable	Unfavorable	Very unfavorable	Causing failure if unstopped
L	Major discontinuity with little or no clay	1	2	4	8
M	Major discontinuity with $RQD_{100}=0^a$ due to clay and crushed rock	2	4	8	16
N	Major discontinuity with $RQD_{300}=0^b$ due to clay and crushed rock	4	8	12	24

^a $RQD_{100}=1m$ perpendicular sample of discontinuity, ^b $RQD_{300}=3m$ perpendicular sample of discontinuity

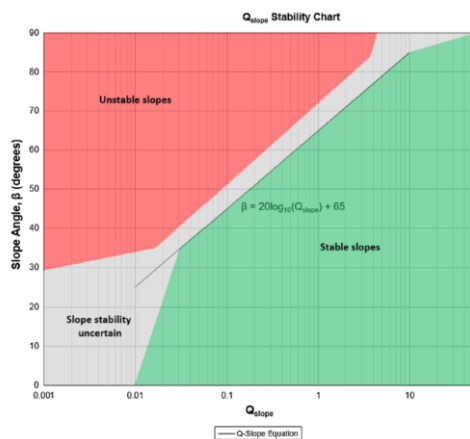


Figure D 1: Q-slope stability chart (Barton and Bar, 2015)

E. Back-calculated shear strength parameters

Table E 1: c - ϕ pairs of Sector 5 back-calculated by the Mohr-Coulomb failure criterion

ϕ (°)	c (kPa) of wedge 1	c (kPa) of wedge 2
25	3.6	6.8
27	3.4	6.4
30	3.2	5.7
35	2.8	4.5
38	2.6	3.8
41	2.3	3.1
44	2.0	2.3
46	1.8	1.7
51	1.3	0.2
55	0.8	

Table E 2: c - ϕ pairs of Sector 10 back-calculated by the Mohr-Coulomb failure criterion

ϕ (°)	c (kPa) of wedge 1	c (kPa) of wedge 2
25	5.0	7.5
27	4.7	7.0
30	4.3	6.1
35	3.5	4.8
38	3.0	3.9
41	2.5	2.9
44	1.9	1.8
46	1.5	0.9
48	1.0	0.1
51	0.3	

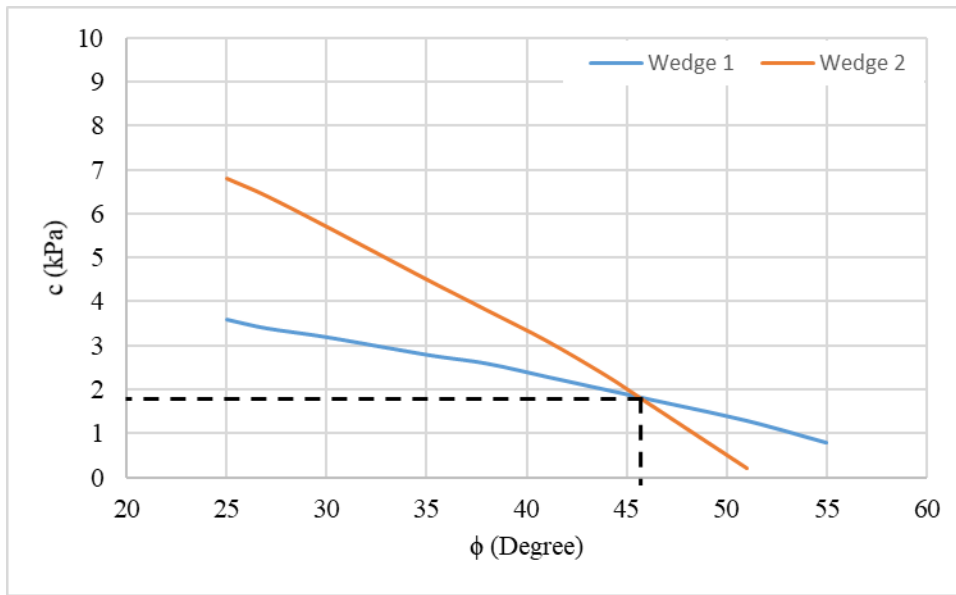


Figure E 1: Variation of the c - ϕ pairs in terms of the Mohr-Coulomb failure criterion where the intersection point identifies the back-calculated shear strength parameters of Sector 5

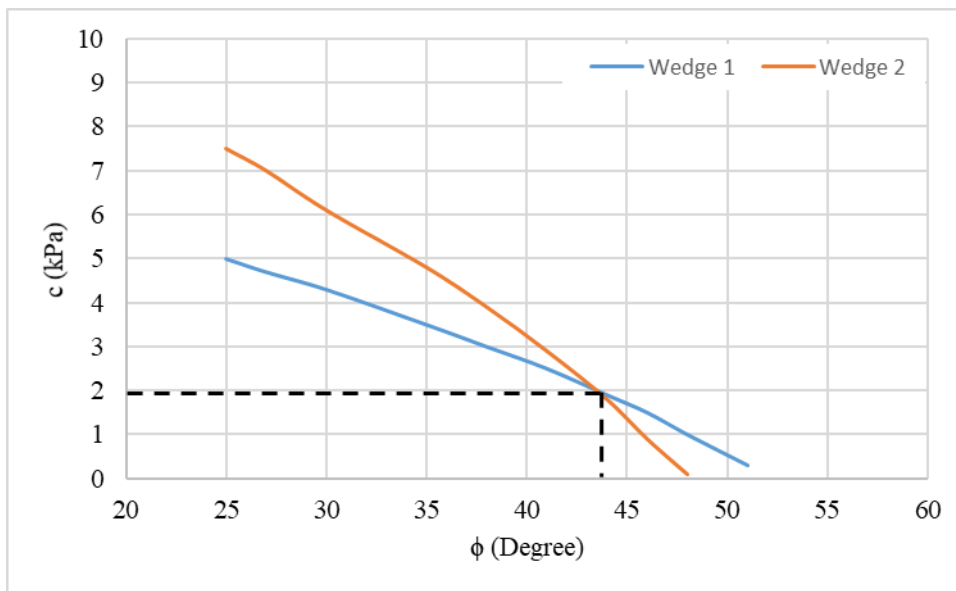


Figure E 2: Variation of the c - ϕ pairs in terms of the Mohr-Coulomb failure criterion where the intersection point identifies the back-calculated shear strength parameters of Sector 10

Table E 3: c - ϕ pairs of Sectors 5 and 10 back-calculated by the limit equilibrium solution proposed by Hoek and Bray (1981)

ϕ (°)	c (kPa) for wedge in Sector 5	c (kPa) for wedge in Sector 10
25	1.67	2.12
30	1.58	2.0
35	1.47	1.88
38	1.4	1.81
42	1.31	1.70
44	1.25	1.62
46	1.19	1.56

F. Report obtained from the application of the Seismic Hazard Map of Turkey

7/8/22, 4:58 PM

Sismik Tehlike Haritası Detay Raporu

AFAD



Türkiye Deprem Tehlike Haritaları İnteraktif Web Uygulaması

Kullanıcı Girdileri

Report Başlığı:	Mudurnu	
Deprem Yer Hareketi Düzeyi	DD-2	50 yılda eşilme olasılığı %10 (tekrarlanma periyodu 475 yıl) olan deprem yer hareketi düzeyi
Yerel Zemin Sınıfı	ZB	Az ayrışmış, orta sağlam kayalar
Enlem:	40.488506°	
Boylam	31.208324°	

Çıktılar

$S_g = 0.964$	$S_1 = 0.292$	$PGA = 0.398$	$PGV = 26.914$
---------------	---------------	---------------	----------------

S_g : Kısa periyot harita spektral ivme katsayısı [boyutsuz]

S_1 : 1.0 saniye periyot için harita spektral ivme katsayısı [boyutsuz]

PGA : En büyük yer ivmesi [g]

PGV : En büyük yer hızı [cm/sn]

Yerel Zemin Sınıfları

Yerel Zemin Sınıfı	Zemin Cinsi	Üst 30 metrede ortalama		
		$(V_s)_{30}$ [m/s]	$(N_{60})_{30}$ [darbe/30 cm]	$(C_u)_{30}$ [kPa]
ZA	Sağlam, sert kayalar	> 1500	-	-
ZB	Az ayrılmış, orta sağlam kayalar	760 - 1500	-	-
ZC	Çok sıkı kum, çakıl ve sert kil tabakaları veya ayrılmış, çok çatlaklı zayıf kayalar	360 - 760	> 50	> 250
ZD	Orta sıkı - sıkı kum, çakıl veya çok katı kil tabakaları	180 - 360	15 - 50	70 - 250
ZE	Gevşek kum, çakıl veya yumuşak - katı kil tabakaları veya $PI > 20$ ve $w > \% 40$ koşullarını sağlayan toplamda 3 metreden daha kalın yumuşak kil tabakası ($C_u < 25$ kPa) içeren profiller	< 180	< 15	< 70
ZF	Sahaya özel araştırma ve değerlendirme gerektiren zeminler : 1) Deprem etkisi altında çökme ve potansiyel göçme riskine sahip zeminler (sıvılaştırılabilir zeminler, yüksek derecede hassas killer, göçebilir zayıf çimentolu zeminler vb.), 2) Toplam kalınlığı 3 metreden fazla turba ve/veya organik içeriği yüksek killer, 3) Toplam kalınlığı 8 metreden fazla olan yüksek plastisiteli ($PI > 50$) killer , 4) Çok kalın (> 35 m) yumuşak veya orta katı killer.			

Yerel Zemin Etki Katsayıları

Yerel Zemin Sınıfı	Kısa periyot bölgesi için Yerel Zemin Etki Katsayısı F_S					
	$S_S \leq 0.25$	$S_S = 0.50$	$S_S = 0.75$	$S_S = 1.00$	$S_S = 1.25$	$S_S \geq 1.50$
ZA	0.8	0.8	0.8	0.8	0.8	0.8
ZB	0.9	0.9	0.9	0.9	0.9	0.9
ZC	1.3	1.3	1.2	1.2	1.2	1.2
ZD	1.6	1.4	1.2	1.1	1.0	1.0
ZE	2.4	1.7	1.3	1.1	0.9	0.8
ZF	Sahaya özel zemin davranış analizi yapılacaktır.					

Yerel Zemin Sınıfı ZB ve $S_S=0.964$ için $F_S=0.900$

Yerel Zemin Sınıfı	1.0 saniye periyot için Yerel Zemin Etki Katsayısı F_1					
	$S_1 \leq 0.10$	$S_1 = 0.20$	$S_1 = 0.30$	$S_1 = 0.40$	$S_1 = 0.50$	$S_1 \geq 0.60$
ZA	0.8	0.8	0.8	0.8	0.8	0.8
ZB	0.8	0.8	0.8	0.8	0.8	0.8
ZC	1.5	1.5	1.5	1.5	1.5	1.4
ZD	2.4	2.2	2.0	1.9	1.8	1.7
ZE	4.2	3.3	2.8	2.4	2.2	2.0
ZF	Sahaya özel zemin davranış analizi yapılacaktır.					

Yerel Zemin Sınıfı ZB ve $S_1=0.292$ için $F_1=0.800$

Tasarım Spektral İvme Katsayıları

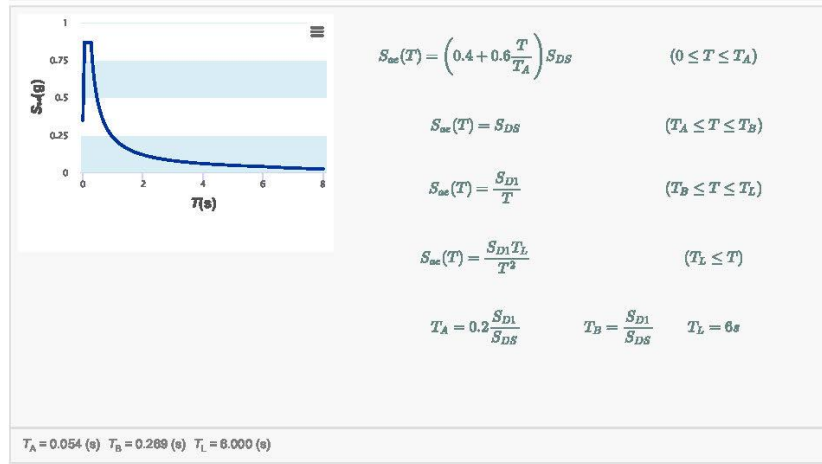
$$S_{DS} = S_S F_S = 0.964 \times 0.900 = 0.868$$

$$S_{D1} = S_1 F_1 = 0.292 \times 0.800 = 0.234$$

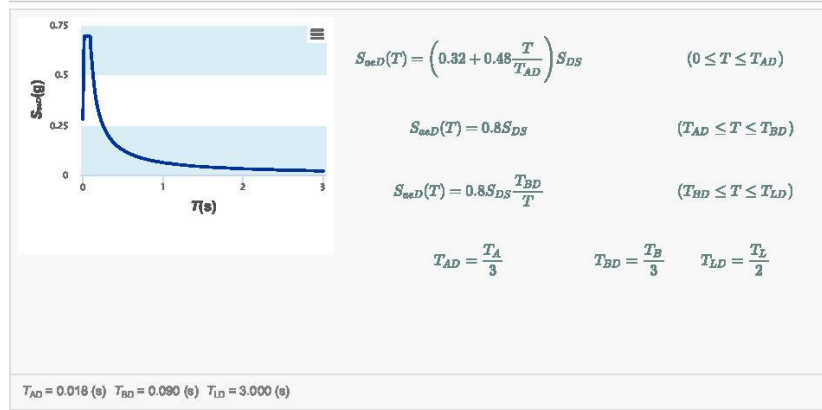
S_{DS} : Kısa periyot tasarım spektral ivme katsayısı [boyutsuz]

S_{D1} : 1.0 saniye periyot için tasarım spektral ivme katsayısı [boyutsuz]

Yatay Elastik Tasarım Spektrumu



Düsey Elastik Tasarım Spektrumu



G. Hazard assessment flow chart

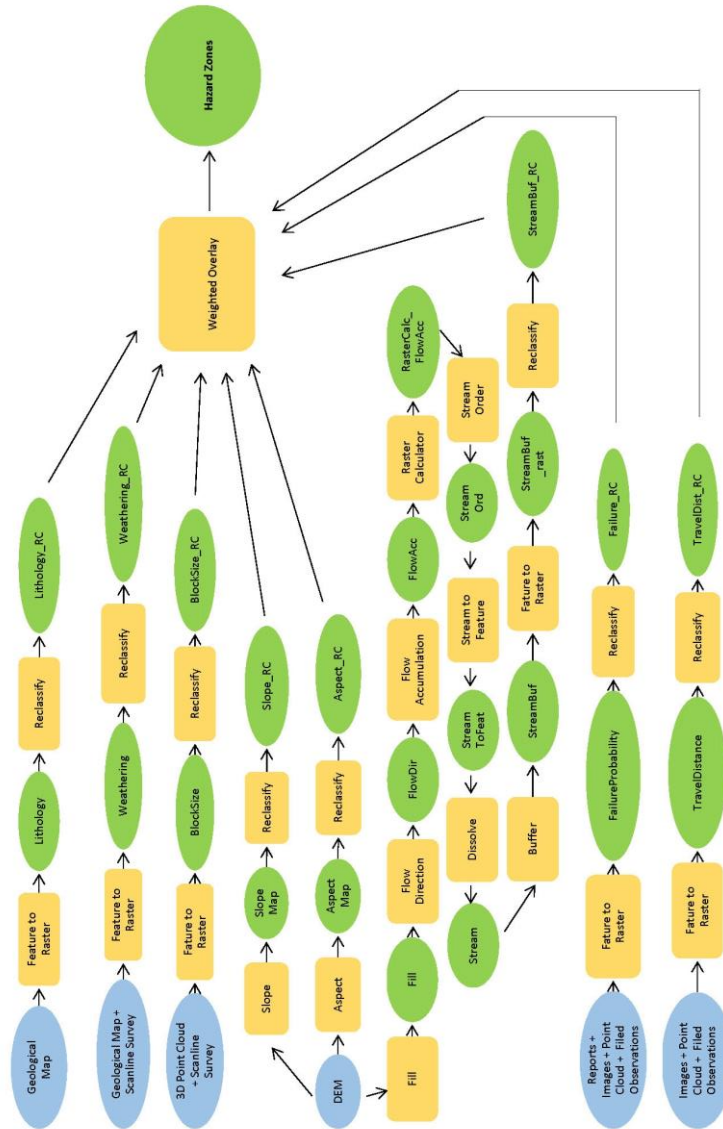


Figure G 1: Details of the process followed for the preparation of the hazard assessment layers in ArcGIS software

CURRICULUM VITAE

PERSONAL INFORMATION

Surname, Name: Arslan Kelam, Arzu
Nationality: Turkish (TC)

EDUCATION

Degree	Institution	Graduation Year
MS	METU Geological Engineering	2015
BS	METU Geological Engineering	2012
High School	Aydınlıkevler High School, Ankara	2007

LANGUAGE SKILLS

English: TOEFL IBT: 95 (2013); IELTS: 7 (2013)

WORK EXPERIENCE

Year	Affiliation	Title
2013-2022	METU Dept. of Geological Eng.	Research Assistant
2012-2013	METU Dept. of Geological Eng.	Student Assistant

ACADEMIC STUDIES

Journal Papers

1. Arslan Kelam A., Akgün H., Koçkar M. K., 2022. Application of an Optical Fiber-based System for Mass Movement Monitoring. Environmental Earth Sciences. 81:170. <https://doi.org/10.1007/s12665-022-10289-w>
2. Arslan Kelam A., Karimzadeh S., Yousefibavil K., Akgün H., Askan A., Erberik M. A., Koçkar M. K., Pekcan, O., Çiftçi, H., 2022. An Evaluation of Seismic Hazard and Potential Damage in Gaziantep, Turkey Using Site specific Models for Sources, Velocity Structure and Building Stock. Soil Dynamics and Earthquake Engineering. 154:107129. <https://doi.org/10.1016/j.soildyn.2021.107129>

3. Akgün, H., Günal Türkmenoğlu, A., Arslan Kelam, A., Yousefi-Bavil, K., Öner, G., Koçkar, M. K., 2018. Assessment of the Effect of Mineralogy on the Geotechnical Parameters of Clayey Soils: A Case Study for the Orta County, Çankırı, Turkey. *Applied Clay Science*. Vol. 164, pp. 44-53. DOI: 10.1016/j.clay.2017.08.029.
4. Arslan Kelam A., Koçkar M. K., Akgün H., 2016. Utilization of Optical Fiber System for Mass Movement Monitoring. *Disaster Science and Engineering*. Vol. 2(1), pp. 19-24.
5. Arslan A., Kelam M. A., Eker A. M. Akgün H., Koçkar M. K., 2014. Optical Fiber Technology to Monitor Slope Movement. *Engineering Geology for Society and Territory* (eds. G. Lollino et al.), Vol. 2, pp. 1425-1429. DOI: 10.1007/978-3-319-09057-3_252.

M. S. Thesis

Arslan A., 2015. Generation of an Early Warning System for Landslide and Slope Instability by Optical Fiber Technology. Middle East Technical University, 134 pages.

Conference Papers

1. Arslan Kelam, A., Koçkar, M. K., Akgün, H., 2021, Determination of Hazard Zones of Mudurnu Rock Slopes Under Seismic Loading Conditions, 6th International Conference on Earthquake Engineering and Seismology (6. ICEES), 13-15 October 2021, Gebze/Kocaeli, Turkey.
2. Arslan Kelam, A., Akgün, H., Bobet, A., Koçkar, M. K., 2021, Assessment of kinematic rock slope failures in Mudurnu Valley, Turkey, EUROCK 2021 Mechanics and Rock Engineering from Theory to Practice, 21 – 24 September 2021, Turin, Italy.
3. Arslan Kelam, A., Koçkar, M. K., Akgün, H., 2020, Application of an Optical Fiber Based Monitoring System to a Mass Movement Area, 54th US Rock Mechanics/Geomechanics Symposium, 28 June - 01 July 2020, Colorado, USA.
4. Arslan Kelam, A., Koçkar, M. K., Akgün, H., 2019, Application of a Landslide Monitoring System to an Earthquake Prone Region by Using Optical Fiber Technology, 5. International Conference on Earthquake Engineering and Seismology (5. ICEES), 08-11 October 2019, Ankara, Turkey.
5. Arslan Kelam, A., Koçkar, M. K., Akgün, H., 2019, An Optical Fiber Early Warning System for Monitoring Mass Movements and for Assessing the Effect of the Triggering Factors, ENGGE0'2019: National Symposium on Engineering Geology and Geotechnics, 03-05 October 2019, Denizli, Turkey.

6. Arslan Kelam, A., Akgün, H., Öner, G., Koçkar, M. K., 2019, Bentonite Enhancement of Clayey Soils of Konya for Geotechnical Applications, 18th National Clay Symposium, 25 - 28 September 2019, Kocaeli, Turkey.
7. Arslan Kelam, A., Koçkar, M. K., Akgün, H., 2019, An Optical Fiber Based Early Warning System for Large Landslides, EGU2019, 7-12 April 2019, Vienna, Austria.
8. Arslan Kelam, A., Akgün, H., Koçkar, M. K., 2018, A UAV Supported Evaluation of the Complex Kinematic Failures for the Discontinuous Rock Masses of Mudurnu Valley, 2. International Symposium on Natural Hazards and Disaster Management (ISHAD2018), 4-6 May 2018, Sakarya, Turkey.
9. Arslan Kelam, A., Akgün, H., Koçkar, M. K., 2018, Evaluating Modes of Failure Zones of Rock Masses Along Mudurnu Valley (Turkey) by Using an Unmanned Aerial vehicle, EGU2018, 8-13 April 2018, Vienna, Austria.
10. Arslan Kelam, A., Koçkar, M. K., Akgün, H., 2017, Heyelan Hareketlerinin Fiber Optik Sistemlerle İzlenmesi ve Değerlendirilmesi, Uluslararası Katılımlı 7. Geoteknik Sempozyumu, 22-24 Kasım 2017, İstanbul, Turkey. TMMOB IMO Publication No: E/17/05, ISBN No: 978-605-01-1103-3, 843-852 (in Turkish).
11. Arslan Kelam A., Koçkar M. K., Akgün H., 2017. Monitoring and Evaluation of the Effect of Seismic Activity and Precipitation Condition on Landslide Movement by Optical Fiber Systems. 4. International Conference on Earthquake Engineering and Seismology (4ICEES). Eskişehir, Turkey.
12. Akgün, H., Günel Türkmenoğlu, A., Arslan Kelam, A., Yousefi-Bavil, K., Öner, G., Koçkar, M. K., 2017. Mineralogical Characteristics of the Orta Clay. 17. National Clay Symposium, Mugla, Turkey.
13. Arslan A., Koçkar M. K., Akgün H., 2016. Utilization of Optical Fiber System for Mass Movement Monitoring. International Symposium on Natural Hazards and Hazard Management, Karabük University, Karabük.
14. Arslan A., Akgün H., Koçkar M. K., Eker A. M., Kelam M. A., 2015. Slope Movement Monitoring with Optical Fiber Technology. EUROCK 2015 & 64th Geomechanics Colloquium (Ed. Schubert), Salzburg, Austria.
15. Arslan A., Kelam M. A., Eker A. M. Akgün H., Koçkar M. K., 2015. Usage of Optical Fiber Technology for Monitoring Slope Instabilities. Turkey's Disaster Risk Management, 17th Round Table Meeting, METU Cultural and Conventional Center, Ankara.
16. Arslan A., Kelam M. A., Eker A. M. Akgün H., Koçkar M. K., 2014. Optical Fiber Technology to Monitor Slope Movement, IAEG – International Association for Engineering Geology and Environment, XII Congress Torino, Italy
17. Kelam M. A., Eker A. M., Akgün H., Arslan A., Koçkar M. K., 2013. A New Method for Monitoring Landslide and Slope Stability: Optical Fiber Technology.

66th Geological Congress of Turkey, METU Cultural and Conventional Center, Ankara.

Projects

Laboratory Testing of Hazards and Risks Caused by Landslides Triggered by Earthquakes Through Utilizing Fiber Optic Methods and Development of a Real-Time Landslide Early Warning System as a Consequence of Field Monitoring (HEUSIS-NET). Researcher in TUBITAK 1001 Project (October 2021 – Present).

Investigation of the Fracture Network Enhancement Mechanism and the Parameters through Hydro-Mechanical Modelling with the Incorporation of the Geomechanical Properties of the Menderes Massif Marble unit and the In-Situ Principal Stresses. Scholar in TUBITAK 1001 Project (November 2020 - Present).

Monitoring Landslide Movements by Early Warning Systems in Kocaeli, Investigation of the Effects and Sensitivity of Earthquake Seismicity and Other Factors (Hydrogeological, Hydrological, Precipitation Effects) on Mass Movement Deformation. Scholar in Republic of Turkey Prime Ministry Disaster and Emergency Management Authority (AFAD), National Earthquake Research Program (UDAP) Project (December 2017 - April 2021).

Bentonite Enhancement of Konya Clayey Soils in Order to be Utilized as a Compacted Landfill Liner Material. Researcher in Middle East Technical University, Scientific Research Project (BAP) (May 2018 - November 2019).

Characterization of the Rock Masses, Determination and Modelling the Slope Instability Mechanisms and Proposal of Remedial Measures in Mudurnu, Bolu, Turkey. Researcher in Middle East Technical University, Scientific Research Project (BAP) (January 2017 - December 2018).

Assessment and Justification of the Deformational Characteristics of Slopes in Landslide Areas. Researcher in Middle East Technical University, Scientific Research Project (BAP) (January 2016-December 2017).

Correlation of the Mineralogical and Geotechnical Parameters of Clayey Soils: A Case Study for Orta County, Çankırı. Researcher in Middle East Technical University, Scientific Research Project (BAP) (January 2015- December 2016).

Optical Fiber Technology to Monitor Slope Movement in Kocaeli. Scholar in Republic of Turkey Prime Ministry Disaster and Emergency Management Authority (AFAD), National Earthquake Research Program (UDAP) Project (April 2014-April 2017).

AWARDS

- 2019 Scholarship of ‘International Research Fellowship Program for PhD Students’ given by the Scientific and Technological Research Council of Turkey (TÜBİTAK)
- 2019 Scholarships of Japan Student Services Organization (JASSO) and Tokyo Institute of Technology Fellowship
- 2017 Academic Incentive Award for the academic studies completed in 2017 which is given by the Council of Higher Education of Turkey
- 2016 Academic Incentive Award for the academic studies completed in 2016 which is given by the Council of Higher Education of Turkey

COURSES ASSISTED AT METU – DEPT. OF GEOLOGICAL ENGINEERING

- GEOE 407: Engineering Geology
- GEOE 414: Environmental Geology
- GEOE 425: Computer Applications in Geological Engineering
- GEOE 437: Geomechanics
- GEOE 491: Geological Engineering Design I
- GEOE 492: Geological Engineering Design II
- GEOE 542: Mechanical Behavior of Earth Materials
- GEOE 544: Stability of Soil Slopes in Engineering Practice